Charged Dust Dynamics in Saturn's Rings

Maria-Joy T. Mace

A thesis submitted to the University of Bristol
in accordance with the requirements of the degree of
Doctor of Philosophy
in the Faculty of Science

School of Physics,
H.H. Wills Physics Laboratory,
Tyndall Avenue,
Bristol,
BS8 1TL

January 2021

$\sim 38,000$ words

Abstract

Dust is ubiquitous throughout the Solar System and beyond. In the main rings of Saturn, dust becomes electrically charged through interactions with sunlight and the plasma environment, leading to complex phenomena for which many questions still remain to be answered. Key issues are introduced in Chapter 1, through examples of the elusive spokes of the B ring, streaming particles from the outer rings, and ring rain.

The dynamics of dust in the presence of planetary magnetic and gravitational fields is studied using numerical simulations of grain trajectories in Chapter 2; electromagnetic forces are added to an existing N-body code and novel adaptive integration methods are implemented. In Chapter 3, a constant charge-to-mass ratio is assumed, in order to test the numerical method and independently verify the theoretical and simulation results of older and more recent literature. The planet is treated as spherical, with an aligned and centred magnetic dipole, so that analytical boundaries for stability can be derived for the radial, azimuthal and vertical motions of dust. Depending on the launch location and their positive or negative surface potential, grains can remain in orbit, collide with the planet at low latitudes, climb up magnetic field lines to collide at higher latitudes, or escape the ring system. The full extent of radial distances from the innermost to the outermost parts of the ring system are considered, for both positive and negative grain potentials, covering a wide range of charge-to-mass ratios that encompass the gravitationally- and electromagnetically-dominated regimes.

The effects of random discrete charging events on nanodust dynamics are of paramount importance. In Chapter 4, with the numerical method verified, the assumption of constant grain surface potential is relaxed and a novel stochastic charging algorithm is developed so that the dynamics of nanograins can be studied. The periodic modulating effect on the grain's charge as it transits the planetary shadow is included as this can have a significant destabilising effect.

In Chapter 5, attention is then directed back to ring rain, the precipitation of dusty material from the rings onto the planet's ionosphere. Results are presented that corroborate the hypothesis that ring rain may not be a cleaning mechanism, whereby the rings preferentially rain out pollutants, leaving the young age of Saturn's rings a possibility. The need for a systematic sensitivity analysis to fully explore the chaotic nature of grain trajectories under the full range of environmental and grain parameters is described in Chapter 6.

Acknowledgements

I have made it this far through the generous help of many people. Firstly, I would like to express my gratitude to my supervisors, Dr Zoë Leinhardt and Prof Mark Birkinshaw, for their help and guidance during my PhD, and their unwavering optimism. Special thanks, too, to past and present members of the Bristol Astrophysics group: Phil Carter, Gibwa Musoke, Crispin Logan, Ben Henderson, Thomas Denman, Rhys Morris and Malcolm Bremer.

There have been numerous others who have supported me through this journey. Their kindness and other qualities have been a wonderful reminder of all that we can be. I'm so glad to know them. I thank Olivia Donnelly, for all that she showed me. I will always carry what I have learnt from my time with her. It is partly because of this that I am able to express myself so earnestly here! I thank Gemma Murray and Fiona Kelly for their expertise and compassion. I thank Dave Sibley, who has been a place of stability during some difficult periods and who has helped me to stay afloat. I thank Fran Hathorn for her support and good advice. I thank Laura Brown, whose conversations have been so real and understanding and kind. I thank Ven. Jinho Shi, whose generosity, encouragement and teachings have helped me immeasurably in all aspects of existence. I thank my friends for their humour and companionship; especially Ivan Batchelor, who has literally provided a place of shelter these last few months.

I hope to pay it forward. Finally, I thank my parents and the rest of my family for their support and love throughout my life. I cannot fully express here what they mean to me, except to say that they are very special.

"That light," said the Chaplain, "is it going up or coming down?"
"It's coming down," said Lord Asriel, "but it isn't light. It's Dust."
Something in the way he said it made Lyra imagine *Dust* with a capital letter, as if this wasn't ordinary dust. The reaction of the Scholars confirmed her feeling, because Lord Asriel's words caused a sudden collective silence, followed by gasps of incredulity.

– Philip Pullman
His Dark Materials: Northern Lights, Chapter 2

But still, like dust, I'll rise.

– Maya Angelou
And Still I Rise: A Book of Poems

Declaration

I declare that the work in this dissertation was carried out in accordance with the requirements of the University's *Regulations and Code of Practice for Research Degree Programmes* and that it has not been submitted for any other academic award. Except where indicated by specific reference in the text, the work is the candidate's own work. Work done in collaboration with, or with the assistance of, others, is indicated as such. Any views expressed in the dissertation are those of the author.

Mia T. Mace

4th January 2021

Contents

Declaration xi

Table of Contents xiii

List of Figures xvii

List of Tables xxiii

List of Acronyms and Symbols xxv

1 Introduction **1**

1.1 Saturnian Ring System 4

1.1.1 The Rings of Saturn 4

1.1.2 Inner Magnetosphere and Plasma Environment 11

1.2 Charged Dust in Planetary Rings 16

1.2.1 Spokes of Saturn 16

1.2.2 Dust Streams 24

1.2.3 Ring Rain 29

1.3 Physical Processes Acting on Dust in Planetary Rings 41

1.3.1 Gravitational and Magnetic Planetary Fields 42

1.3.2 Comparison to Other Forces on Circumplanetary Dust 51

2 Numerical Methods **58**

2.1 Parallel k-Dimensional Tree Gravity Integrator 59

2.1.1 Local Shearing Patch Simulations 61

2.1.2 Modifying Code to Include Planetary Magnetic Field 64

2.1.3 Global Simulations 68

2.2 Adaptive Runge-Kutta 69

2.3 Gragg-Bulirsch-Stoer . . . 72
2.4 Testing the Numerical Integrators . . . 73

3 Orbital Motions of Charged Dust **80**
3.1 Background . . . 81
3.2 Numerical Simulation Results . . . 84
3.2.1 Some Example Trajectories . . . 84
3.2.2 Stability Maps of Saturn and Jupiter . . . 89
3.3 Hamiltonian and Potential . . . 91
3.4 Azimuthal Motion . . . 95
3.4.1 Guiding Centre Approximation . . . 95
3.4.2 Drifts . . . 97
3.4.3 Orbital Velocity of the Guiding Centre . . . 100
3.5 Radial Motion . . . 103
3.5.1 Gyroradius . . . 103
3.5.2 Local Radial Stability . . . 105
3.5.3 Global Radial Stability . . . 107
3.6 Vertical Motion . . . 114
3.6.1 Mirror Motion . . . 114
3.6.2 Local Vertical Stability . . . 116
3.7 Timescales . . . 120
3.8 Summary and Discussion of Stability Boundaries . . . 122

4 Time-Variable Charging of Dust **128**
4.1 An Approach to Modelling Time-Variable Charging . . . 129
4.1.1 Plasma Currents . . . 129
4.1.2 Continuous Charging Model . . . 130
4.1.3 Discrete Charging Model . . . 136
4.1.4 Stochastic Charging Algorithm: Randomising Timestep & Particle Type 137
4.1.5 Simulation Results . . . 141
4.2 Charging Algorithm Using Poisson Processes . . . 144
4.2.1 Binary Tree Traversal for Charge Distribution . . . 148
4.2.2 Applying the Binary Tree Traversal Algorithm . . . 155

4.3 Planetary Shadow 158

5 Dynamical Modelling of Ring Rain **164**

5.1 Open Questions 164

5.1.1 Silicate-to-Water-Ice Ratio and Latitudinal Water Deposition 165

5.1.2 Ring Structure and Electromagnetic Erosion 166

5.1.3 The Effect of Ring Rain on the Perceived Age of the Rings 168

5.2 Literature Review of Ring Rain Dynamical Studies 170

5.2.1 Constant $\frac{q_d}{m_d}$ and Keplerian Launch Velocities: Liu & Ip (2014) 170

5.2.2 Constant $\frac{q_d}{m_d}$ and Vertical Launch Velocities: Ip et al. (2016) 172

5.2.3 Variable $\frac{q_d}{m_d}$ and Ejecta Launch Velocities: Hsu et al. (2018a) 173

5.2.4 Variable $\frac{q_d}{m_d}$, Ejecta Launch Velocities and Plasma Model: Hsu et al. (2018b) 175

5.3 Ring Rain Simulation Method 178

5.4 Ring Rain Simulation Results 180

6 Conclusions **196**

6.1 Summary of Work 196

6.2 Future Work 198

List of Figures

1.1 Terrella experiments. 2
1.2 Huygens' sketches of Saturn's rings. 4
1.3 Keeler (1895)'s sketch of Doppler measurements of Saturn's rings. 5
1.4 Early images of Saturn's rings from space. 6
1.5 Sketch of Saturn's ring system. 7
1.6 *Cassini NAC* image of main rings. 8
1.7 *Cassini NAC* image of F ring. 8
1.8 Optical depth of main rings. 8
1.9 *Cassini VIMS* imaging of A ring. 10
1.10 Saturn's magnetosphere. 12
1.11 *Cassini* measurements of plasma densities and temperatures near the main rings 13
1.12 *Cassini NAC* images of spokes. 17
1.13 Seasonality of spokes. 22
1.14 Ring electric polarity. 23
1.15 Ring-ionosphere configuration, Fig. 1 of Wilson & Waite (1989). 32
1.16 Ring rain conjugate locations, Fig. 1 of Connerney (1986). 33
1.17 Forces on a highly charged grain, Fig. 1 of Connerney (2013). 34
1.18 H_3^+, opacity, and optical observations as a function of radius of Saturn's main rings, Fig. 4 of O'Donoghue et al. (2017). 36
1.19 Latitudinal profiles of ring rain, Fig. 4 of Hsu et al. (2018b). 38
1.20 Impact rate profiles measured by *CDA*, Fig. 3 of Hsu et al. (2018b). 39
1.21 Spherical harmonics 44
1.22 Comparison of forces on dust grains. 52

1.23 Ratio of solar radiation pressure force to gravitational force, Fig. 7b of Burns et al. (1979). . . . 53
1.24 Enceladus plumes, Fig. 6 of Porco et al. (2006). . . . 54

2.1 Tree method of force calculation in PKDGRAV. . . . 60
2.2 Sketch of shearing patch model. . . . 62
2.3 Shearing patch simulation snapshot. . . . 64
2.4 Reproducing the results of Matthews & Hyde (2004) using shearing patch simulations. . . . 67
2.5 Reproducing the results of Matthews & Hyde (2004) using global simulations. . . 68
2.6 Mesh used in the Gragg-Bulirsch-Stoer method. . . . 72
2.7 Richardson extrapolation, from Press et al. (2007). . . . 73
2.8 Fractional energy change over time for PKDGRAV, RKDP and GBS methods. . . 76
2.9 Mirror motion of a charged grain in stable orbit. . . . 78
2.10 Conservation of the first adiabatic invariant for adaptive integrators. . . . 79

3.1 Grain trajectory with low-latitude oscillations. . . . 85
3.2 Grain trajectory in 2:1 (radial:vertical) resonance. . . . 86
3.3 Vertically unstable grain trajectory. . . . 87
3.4 Grain trajectory with large vertical oscillations. . . . 88
3.5 Stability maps for Saturn and Jupiter, with $\vec{B}$ modelled as an aligned and centred dipole. . . . 90
3.6 The guiding centre model. . . . 95
3.7 $\vec{F} \times \vec{B}$ drifts. . . . 97
3.8 Summary of drifts, from Alfvén (1950). . . . 99
3.9 Drift rates for highly charged grains launched close to R_{syn} around Saturn. . . . 101
3.10 Drift rates for highly charged grains launched further from R_{syn} around Saturn. 102
3.11 Radial range of grains around Saturn. . . . 104
3.12 Potential wells illustrating orbital escape. . . . 109
3.13 Critical quartic method for determining radial escape. . . . 110
3.14 Potential wells (notional peaks within R_p) illustrating collision with planet. . . 111
3.15 Potential wells (peaks outside R_p) illustrating collision with planet. . . . 112
3.16 Critical quartic method for determining collision with planet. . . . 113

3.17 Grain moving along $\vec{B}$ field line, varying the ratio of gravitational to centrifugal force. . . . 117
3.18 Roots of $\Omega_b^2 = 0$. . . . 119
3.19 Characteristic time periods for negatively charged grains around Saturn and Jupiter 121
3.20 Analytical and semi-analytical solutions for stability boundaries around Saturn and Jupiter. . . . 123
3.21 Stability maps for Saturn and Jupiter, with analytical solutions. . . . 126

4.1 Continuous charging example of a grain in a H^+ plasma. . . . 133
4.2 Continuous charging example of a grain in an Ar^+ plasma. . . . 134
4.3 Reproducing charging timescale and charge number results of Goree (1994). . . . 135
4.5 Charge number time series for a $10\,\mathrm{nm}$ grain. . . . 142
4.6 Charge number time series for a $100\,\mathrm{nm}$ grain. . . . 142
4.7 Power spectrum, reproducing Cui & Goree (1994). . . . 143
4.8 Dust charging currents in Saturn's main rings. . . . 145
4.9 Poisson probability distribution example. . . . 147
4.10 Binomial probability distribution example. . . . 149
4.11 Binary tree for a single current example. . . . 149
4.12 Timestep traversal using binary trees. . . . 150
4.13 Binary tree for a single current example, with timestep traversal. . . . 151
4.14 Testing the stochastic charging algorithm for a single current. . . . 151
4.15 Weighted binomial probability distribution example. . . . 152
4.16 Binary tree for multiple currents example. . . . 153
4.17 Testing the stochastic charging algorithm for multiple currents. . . . 154
4.18 Reproducing Cui & Goree (1994), using the novel stochastic charging algorithm 155
4.19 Checking the long-term stability of the stochastic charging algorithm. . . . 156
4.21 Reproducing literature results for continuous charging in the presence of a planetary shadow. . . . 158
4.22 Numerical simulation of charged dust during shadow passage, Fig. 3 of Hamilton & Krüger (2008). . . . 159
4.23 Continuous charging example with Saturn's shadow. . . . 160
4.24 Stochastic charging example with Saturn's shadow. . . . 160
4.25 As Figure 4.24, but using a different random seed. . . . 161

4.26 As Figure 4.24, but using a different random seed. . . . 161
4.27 As Figure 4.24, but using a different random seed. . . . 162
4.28 As Figure 4.24, but using a different random seed. . . . 162

5.1 Radial structure of Saturn's main rings. . . . 167
5.2 Latitudinal deposition angle as a function of charge-to-mass ratio and launch position, Fig. 5 of Liu & Ip (2014). . . . 171
5.3 Example trajectories of positive grains with an initial vertical velocity boost, Fig. 2 of Ip et al. (2016). . . . 173
5.4 Latitudinal deposition of $10\,\mathrm{nm}$ grains as a function of plasma density, Fig. 2 of Hsu et al. (2018a). . . . 174
5.5 Plasma model used by Hsu et al. (2018b). . . . 175
5.6 Modelled grain number density in (r, z) space, Fig. 1B of Hsu et al. (2018b). . . . 176
5.7 Latitudinal deposition of $20\,\mathrm{nm}$ dust ejecta compared to H_3^+ emission, Fig. S6 of Hsu et al. (2018b). . . . 177
5.8 Grain trajectory example, launched outside the instability region at local noon: collision with ring plane. . . . 182
5.9 Grain trajectory example, launched outside the instability region at local midnight: collision with ring plane. . . . 183
5.10 Grain trajectory example, launched outside the instability region at local midnight: eventual collision with planet at mid-southern latitude. . . . 184
5.11 Grain trajectory example, launched outside the instability region at local midnight: collision with planet at low latitude. . . . 185
5.12 Grain trajectory example, launched outside the instability region at local noon: collision with planet at mid-southern latitude. . . . 186
5.13 Grain trajectory example, launched within the instability region at local midnight: collision with the main rings. . . . 187
5.14 Grain trajectory example, launched within the instability region at local noon: collision with planet's equatorial region. . . . 188
5.15 Grain trajectory example, launched within the instability region at local noon: eventual collision with the planet at mid-southern latitude. . . . 189
5.16 Grain trajectory example, launched within the instability region at local midnight: collision with the planet at mid-southern latitude. . . . 190

5.17 Grain trajectory example, launched inside of the instability region at local noon: collision with main rings. 191
5.18 Grain trajectory example, launched inside of the instability region at local noon: rapid collision near planet's equator. 192
5.19 Grain trajectory example, launched inside of the instability region at local midnight: collision with planet at mid-southern latitude. 193
5.20 Grain trajectory example, launched inside of the instability region at local midnight: collision with planet at mid-southern latitude. 194
5.21 Grain trajectory example, launched inside of the instability region at local noon with larger vertical boost: collision with planet at mid-northern latitude. 195

List of Tables

1.1 Planetary parameters. 25
1.2 Properties of streaming particles, Table 1 of Hamilton & Burns (1993). 26
1.3 Legendre polynomials up to degree-3. 44
1.4 Older literature Gauss-Schmidt quasi-normalised spherical harmonic coefficients 48
1.5 *Cassini* Gauss-Schmidt quasi-normalised spherical harmonic coefficients. . . . 49

2.1 Butcher tableau for RKDP method. 71

4.1 Reproducing charging coefficients of Cui & Goree (1994). 132

5.1 Ring rain simulation results 181

List of Acronyms and Symbols

The following list describes acronyms and symbols that will be widely used within the body of the document.

Acronyms for *Cassini* instruments

CAPS CAssini Plasma Spectrometer

CDA Cosmic Dust Analyzer

CIRS Composite InfraRed Spectrometer

HRD *CDA*'s High Rate Detector

IMS Ion Mass Spectrometer

INCA Ion and Neutral CAmera

INMS Ion and Neutral Mass Spectrometer

ISS Imaging Science Subsystem

MAG MAGnometer

MAPS Magnetospheric And Plasma Science

MA Mass Analyzer, a linear impact time-of-flight mass spectrometer: a subsystem of the *CDA*.

MIMI Magnetosphere IMaging Instrument

NAC Narrow Angle Camera, part of *ISS*

RPWS Radio and Plasma Wave Science

UVIS	UltraViolet Imaging Spectrograph	
VIMS	Visible and Infrared Mapping Spectrometer	
WAC	Wide Angle Camera, part of *ISS*	

Greek Symbols

ϵ	Accuracy tolerance for RKDP method	
κ_ν	Photoelectric efficiency factor	
κ_c	Epicyclic Frequency	
λ	Expected rate for Poisson distribution	
λ_{mfp}	Collisional mean free path	
λ_D	Debye length	
μ	Magnetic moment of grain (first adiabatic invariant)	
Ω_{K}	Keplerian angular frequency	
Ω_{S}	Spin frequency of Saturn	$1.622 \times 10^{-4}\,\text{rads}^{-1}$
ω_c	Angular velocity of guiding centre	
Ω_{gc}	Gyrofrequency evaluated at guiding centre	
Ω_{gL}	Gyrofrequency evaluated at launch location	
Ω_g	Gyrofrequency	
Ω_p	Spin frequency of planet	
ϕ	Azimuth coordinate	
ϕ_{eq}	Equilibrium dust grain surface electric potential	
Φ_B	Magnetic scalar potential	
Φ_g	Gravitational scalar potential	
ϕ_d	Dust grain surface potential	
Ψ	Electric potential	

ρ Cylindrical coordinate, $\rho = \sqrt{x^2 + y^2}$

ρ_c Distance from planet to guiding centre

ρ_d Mass density of dust grain

Σ Surface mass density of planetary rings

σ Electrical conductivity

τ Optical depth of planetary rings

τ_c Characteristic charging timescale

θ Colatitude coordinate

Latin Symbols

$\ddot{\vec{r}}_n$ Acceleration of a particle on the n^{th} integration timestep

$\dot{\vec{r}}_n$ Velocity of a particle on the n^{th} integration timestep

$\mathcal{U}^e$ Effective potential

$\vec{A}$ Magnetic vector potential

$\vec{B}$ Magnetic field

$\vec{E}$ Electric field

$\vec{g}$ Gravitational field

$\vec{j}$ Current density

$\vec{m}$ Dipole magnetic moment of planet

$\vec{r}_n$ Position of a particle on the n^{th} integration timestep

$\vec{v}_\nabla$ $\vec{\nabla}B$ drift velocity

$\vec{v}_E$ $\vec{E} \times \vec{B}$ drift velocity

$\vec{v}_G$ Gravitational drift velocity

$\vec{v}_p$ Plasma velocity

a Distance of shearing patch to planet

a_d	Dust grain radius	
g_n^m, h_n^m	Normalised Gauss-Schmidt coefficients	
H	Hamiltonian, note $\mathcal{H} = H/m_d$	
h	Numerical integration timestep	
I_α	Plasma current of type $\alpha = \{e, i\}$	
I_{sec}	Secondary electron emission current	
J_2	Planetary gravity oblateness coefficient	$J_2^S = 0.0163$
K_ϕ	Electric grain surface potential coefficient	
K_{τ_c}	Charging timescale coefficient	
K_q	Charge coefficient	
L	Distance of $\vec{B}$ field line from centre of planet measured in R_p	
L_*	Dimensionless charge-to-mass ratio	
M_{J}	Mass of Jupiter	$1.898 \times 10^{27}\,\text{kg}$
M_{S}	Mass of Saturn	$5.685 \times 10^{26}\,\text{kg}$
m_d	Mass of dust grain	
m_i	Mass of plasma ion	
M_p	Mass of planet	
N	Number of particles in an N-body simulation	
n	Number density	
N_{eq}	Equilibrium charge number	
n_c	Keplerian angular frequency evaluated at the guiding centre	
n_e, n_i	Plasma number density of electron and ion species, respectively	
n_L	Keplerian angular velocity at launch location	
p_ρ, p_ϕ, p_z	Canonical conjugate momenta	

P_n	Legendre polynomials	
P_n^m	Associated Legendre polynomials	
q	Power law slope	
q_d	Charge of dust grain	
q_i	Plasma ion charge	
r	Radial position, $r = \sqrt{x^2 + y^2 + z^2}$	
R_{B}	Random number drawn from a uniform distribution: $R_{\mathrm{B}} \sim U(0, 1]$, to be compared to the binomial distribution to randomly assign charging events across substeps	
R_{J}	Radius of Jupiter	$71,372\,\mathrm{km}$
R_{P}^{α}	Random number drawn from a uniform distribution: $R_{\mathrm{P}}^{\alpha} \sim U(0, 1]$, to be compared to the Poisson distribution for each α current type	
R_{syn}	Synchronous orbit position, where $\Omega_K = \Omega_p$	
R_{S}	Radius of Saturn	$60,268\,\mathrm{km}$
r_g	Gyroradius	
r_L	Launch position	
R_p	Planetary radius	
T_ν	Characteristic temperature of photoelectron current	
T_{K}	Keplerian time period	
T_e, T_i	Plasma electron and ion temperatures, respectively	
U	Scalar potential	
$v_\parallel, v_\perp$	Velocity parallel and perpendicular to the magnetic field direction, respectively	
v_{esc}	Escape velocity	
v_{K}	Keplerian velocity	
v_c	Velocity of guiding centre	

$X(t)$	Integrated solution to equations of motion: position and velocity
Y_n^m	Spherical harmonics
Z_i	Electronic charge number of positive ions

Miscellaneous Acronyms

GBS	Gragg-Bulirsch-Stoer, extrapolates solution for timestep H
IVP	Initial Value Problem
PKDGRAV	Parallel k-Dimensional Tree Gravity Integrator
RKDP	Runge-Kutta with Dormand Prince coefficients
SED	Saturn Electrostatic Discharge
SKR	Saturn Kilometric Radiation

Physical Constants

ϵ_0	Vacuum permittivity	$8.8541878128 \times 10^{-12}\,\mathrm{F\,m^{-1}}$
e	(Roman) Euler's constant	$2.71828\ldots$
c	Speed of light	$299,792,458\,\mathrm{m\,s^{-1}}$
e	(Italicised) Charge of electron	$1.602176634 \times 10^{-19}\,\mathrm{C}$
G	Universal gravitational constant	$6.67430 \times 10^{-11}\,\mathrm{N\,m^2\,kg^{-2}}$
k_B	Boltzmann constant	$1.380649 \times 10^{-23}\,\mathrm{J\,K^{-1}}$
m_e	Mass of electron	$9.1093837015 \times 10^{-31}\,\mathrm{kg}$
amu	Atomic mass unit	$1.66053906660 \times 10^{-27}\,\mathrm{kg}$

1

Introduction

Charged dust is ubiquitous throughout the universe and, more locally, in our Solar System: present in planetary rings, the surface of the Moon and other bodies, the atmospheres of planets, comets, and the space in between. The interaction of charged dust with its varying environments results in beautiful displays, including the spokes of Saturn (Smith et al. 1981), lunar horizon glow and streamers (Rennilson & Criswell 1974; McCoy & Criswell 1974), and striated features in comet tails (Price et al. 2019). Ringed planets provide a local analogy for other cosmic systems, like planet-forming disks and galaxies. The particles' modest size ($\mathrm{nm} - \mu\mathrm{m}$) makes dust subject to a complex interplay of different forces, not solely contingent on gravity. Given the prevalence of dust in regions around young stars, a greater understanding of the charging conditions and dynamics of dust could provide fresh insights into planet formation (e.g. Okuzumi 2009; Steinpilz et al. 2020).

The focus of this thesis is charged dust in planetary rings, principally Saturn's, whose ring system is arguably the most striking and beautiful of all. The Saturnian system is complex and involves dynamical and chemical connections between the planet, its rings, numerous satellites and various dust, neutral and plasma populations (André et al. 2008). The components of these relevant to the study of charged dust dynamics and the physical properties of the main inner rings

and their environment are presented in §1.1. The variety of phenomena are demonstrated through key examples of charged dust in planetary ring systems (§1.2), which motivate the importance of understanding their dynamics and developing a model for which the most relevant forces are considered in §1.3. It will become apparent how modelling the fate of circumplanetary dust leads to greater understanding of the complexities surrounding the age of Saturn's rings (Crida et al. 2019), which is described in the Chapter 5.

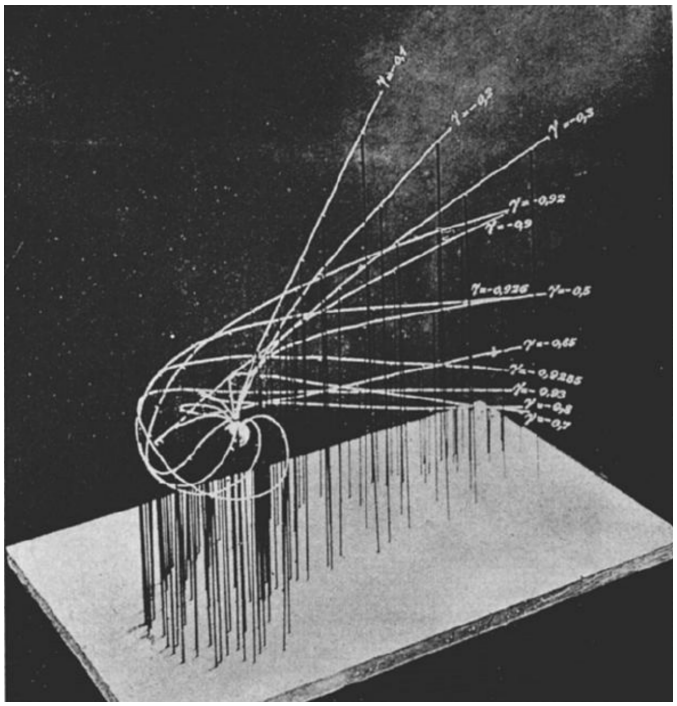

(a) Trajectories of electrons causing aurora borealis, solved by numerical integration and presented as a thread model (Størmer 1930). The γ labels are constants of integration.

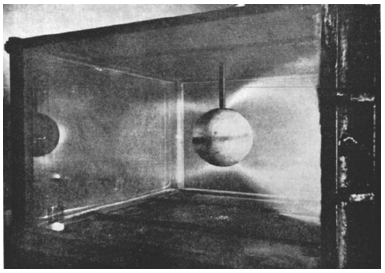

(b) Regions of forbidden toroidal space (Birkeland 1913), theorised by Størmer (1930).

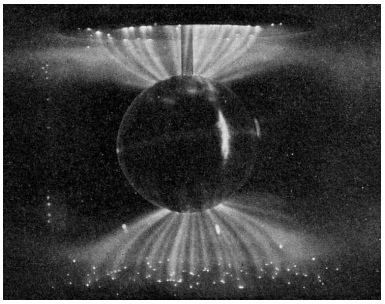

(c) Birkeland currents generating auroral-like displays (Birkeland 1913).

Figure 1.1: Early experimental and theoretical work on charged particle dynamics. Terrella experiments (b,c) involved firing cathode rays at a sphere containing an electromagnet inside a vacuum chamber, representing the Earth and its magnetic field in space.

The study of charged particles in planetary magnetic fields began in earnest in the late nineteenth century with various physicists and meteorologists studying the Earth's aurorae. Following the discovery of X-rays (Röntgen 1895), Birkeland was inspired to study the influence of magnets on cathode rays inside vacuum chambers. At the turn of that century, the Norwegian Polar Expedition, organised by Birkeland, established a network of observatories to collect magnetic field data in high-latitude regions in order to study the electric current pattern in such polar regions

(Birkeland 1913). Størmer became interested in Birkeland's theory of the polar aurorae and they began collaborating in 1903, with Størmer constructing numerical methods to determine the trajectories of high-energy charged particles, pictured in Figure 1.1a. It was through terrella experiments, shown in Figure 1.1b and 1.1c, that Birkeland developed his theory for aurorae – high-energy electrons ejected from sunspots travel towards Earth, where they are guided to polar regions by the geomagnetic field.

Measurements of magnetic field perturbations during polar expeditions, led Birkeland (1913) to propose that currents were flowing along geomagnetic field lines, shown in Figure 1.1c. These field-aligned currents, which came to be known as Birkeland currents, are explained further in §1.1.2 where the electromagnetic environment of Saturn is described. The early work on aurorae and charged particle dynamics has relevance for the study of charged particles interacting with planetary atmospheres, besides aurorae in other planets (e.g. Stallard et al. 2008), such as the ring rain of Saturn (e.g. O'Donoghue et al. 2013) described in §1.2.3. The ring-planet connection works both ways, with Jones et al. (2006) hypothesising that the spokes of Saturn (§1.2.1) are formed by lightning-induced electron beams originating in the atmosphere. Indeed, the spokes of Saturn and ring rain could be different manifestations of the same dust population, with the Collisional Cascade model presented in Jontof-Hutter (2012) raising some interesting questions about whether spoke particles could rain from the rings onto Saturn.

1.1 Saturnian Ring System

Saturn's rings are a rich and complex system, and to establish the broader context of charged dust, their structure is described in §1.1.1, and the wider electromagnetic environment in which they are situated is described in §1.1.2, which provides an overview of the key regions of Saturn's magnetosphere, plasma, and radiation belts in relation to the main rings. A brief description is provided in the following sections; for further detailed descriptions refer to the reviews of e.g. Graps & Grün (2002), André et al. (2008), Gombosi et al. (2009), Gombosi & Ingersoll (2010), Dougherty et al. (2009), Esposito (2014), Baines et al. (2018), Tiscareno & Murray (2018).

1.1.1 The Rings of Saturn

a) Structure of Rings and History of Observations

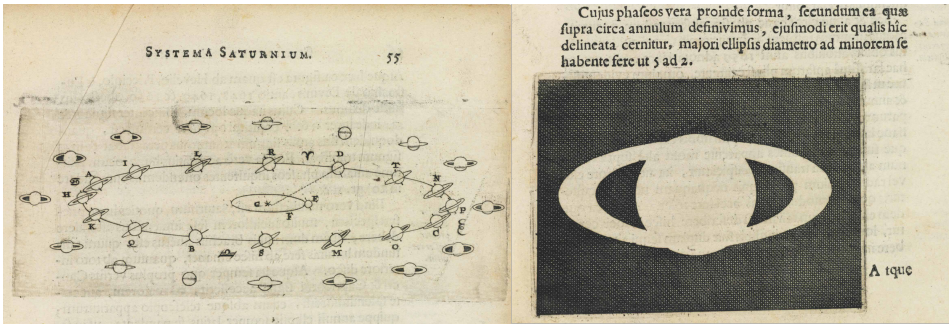

Figure 1.2: A page (adapted to fit horizontally) from Christiaan Huygens' work *Systema Saturnium*, explaining the changing appearance of Saturn's rings.

Galileo first observed Saturn using a telescope in 1610. He spoke of the rings as 'ears' of Saturn and drew three separate bodies to represent the Saturnian system, stating they are *'arranged in a row along the zodiac, the middle one being three times larger than the lateral ones, and they are situated in this form: oOo'*. Half a century later, Huygens used his telescope's improved resolving power to discern that Saturn was surrounded by a ring, Figure 1.2. Then in 1675, Cassini observed that the singular ring was actually composed of smaller rings with gaps between them, corroborated by Laplace's calculation that a uniform solid ring would be unstable and therefore the system could instead be comprised of a number of solid ringlets (Laplace 1966). Maxwell

(1859) deduced that this ringlet structure would be unstable, as would a continuous fluid ring. Kovalevskaya worked with Laplace's assumption, and presented her work as part of three papers for her dissertation (Kovalevskaya 1948; Polyakhova 2004), becoming the first woman to gain a doctorate in mathematics in 1874. Spectroscopic analysis of the rings confirmed that the rings were not orbiting as a solid uniform body but comprised of a multitude of orbiting particles (Keeler 1895), Figure 1.3.

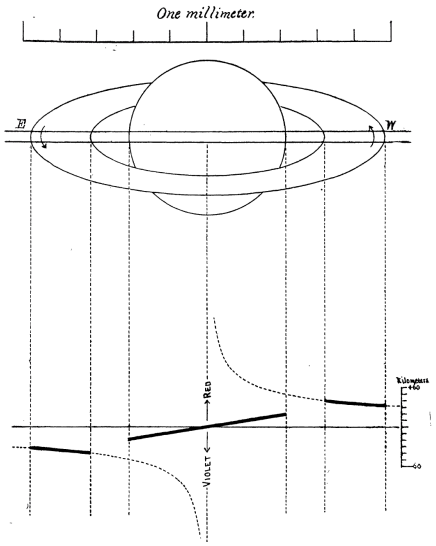

Figure 1.3: Sketch by Keeler (1895) shows the spectroscopic method of using Doppler shifts to determine how the planet rotates as a solid body while the rings of Saturn obey Kepler's Third Law, indicated by the dashed curve.

Following these Earth-bound observations, Saturn's rings have to date been observed from the vicinity of the planet by four spacecraft. The first to do so was *Pioneer 11* in 1979, see Figure 1.4a, which imaged several moons and discovered the F ring. In the early 1980s *Voyager 1* and *2* studied the atmosphere of Saturn, aurorae and giant moon Titan, which was known to have an atmosphere of its own. Radial bicycle spoke-like features in the rings were also observed, Figure 1.4b; these are describe in greater detail in §1.2.1. Then *Cassini-Huygens* entered into orbit around Saturn in 2004, with *Huygens* landing on Titan in early 2005. The huge volume of scientific discoveries made about the Saturnian system using *Cassini* data is reviewed in Dougherty et al. (2009) and the Cassini Final Mission Report (NASA/JPL 2019), with the latest *Grand Finale* results covered by special issues of *Science* (Smith 2018) and *Geophysical Review Letters* (Spilker 2019).

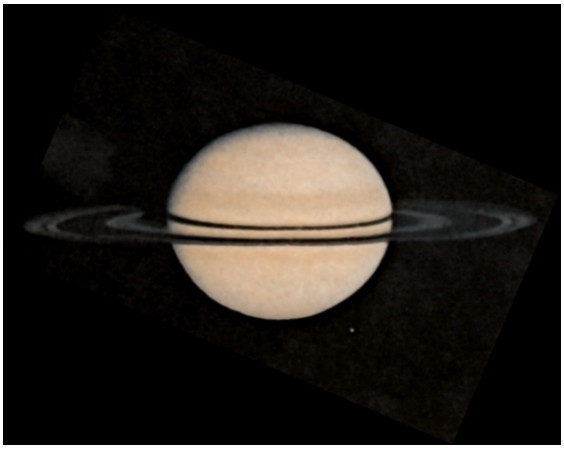

(a) *Pioneer* image of Saturn, the satellite Rhea can be seen to the lower right of the planet. Image credit: NASA/JPL.

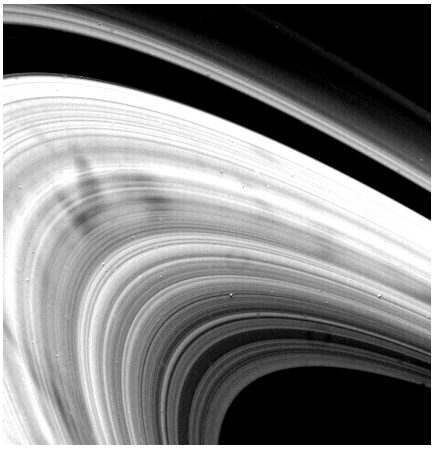

(b) *Voyager 2* image of spokes in the B ring, 22 August 1981. Image credit: NASA/JPL/CICLOPS.

Figure 1.4: Early images of Saturn and its rings from space. Spokes are described further in §1.2.1.

The rings of Saturn, Figure 1.5, can be divided broadly into two categories: the dense A, B, C rings (detailed in Figure 1.6, and which will be referred to as the main rings throughout this work, with optical depths $\tau > 0.1$), and the tenuous D, E, G rings ($\tau < 10^{-3}$). The F ring is more difficult to categorise being very narrow with kinks and knots, a dense core enveloped in a broad sheet of dust (Colwell et al. 2009b), shown in Figure 1.7. The size distribution of particles in the main rings follows a power law distribution in radius, a_d, and can be expressed in terms of the particle number density, n, as

$$n(a_d, a_d + da_d) = n_0 a_d^{-q} da_d, \tag{1.1}$$

where the slope q and maximum and minimum radius limits vary with ring location, but generally $q \sim 3$ and $a_d^{\min} \sim 1-30\,\mathrm{cm}$, $a_d^{\max} \sim 2-20\,\mathrm{m}$ (Cuzzi et al. 2009). The main rings extend out to just within the F ring's orbit at $\sim 140,000\,\mathrm{km}$, but are only metres thick based on the brightness asymmetry of dynamical models of self gravity wakes (French et al. 2007), spiral wave dispersion (Colwell et al. 2009a) and thermal model fitting to *Cassini CIRS*[1] data (Reffet et al. 2015). These dense rings lie inside the Roche limit, where tidal forces overcome an orbiting

[1] *Composite InfraRed Spectrometer*. Refer to the List of Acronyms and Symbols for subsequent acronyms of other instruments on-board *Cassini*.

body's self-gravity, with dusty rings and Saturn's larger moons orbiting further out.

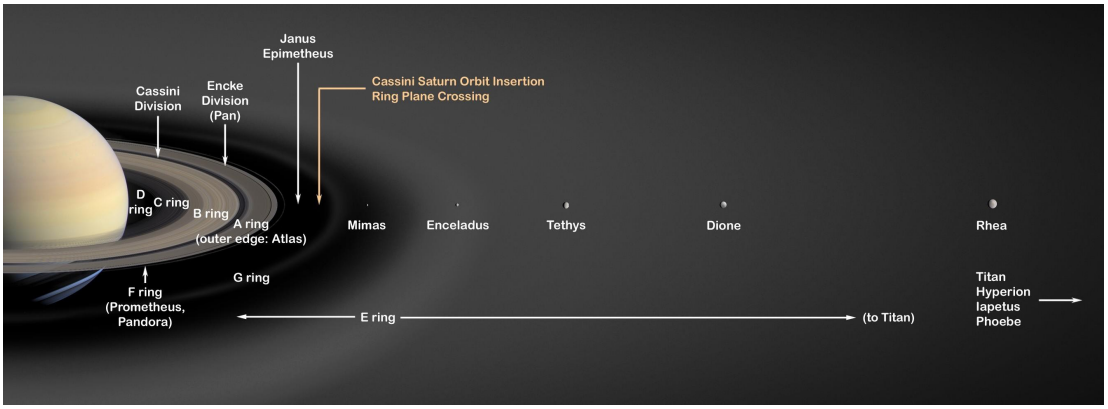

Figure 1.5: Artist's concept of Saturn's rings and major moons. Orbital dynamics of dust grains originating from the main A, B and C rings will be the focus of this work. Image credit: NASA/JPL (PIA03550).

Smaller irregular moons clear gaps within the rings, and yet smaller moonlets produce disturbances in the ring material dubbed 'propellers' due to their morphology (Tiscareno et al. 2006). Orbiting outside of the main dense rings, the moon Mimas is in a 2:1 orbital resonance with ring particles to generate the Cassini Division (Hamilton & Burns 1993; Hedman et al. 2009), which separates the A and B rings, and other resonances with that moon generate waves in the rings, such as the 5:3 bending wave. Numerous density and bending waves are caused by satellites exciting ring particles.

Figure 1.8 shows the dense rings, the most massive of which is the B ring, with the highest opacity and greatest variation in its brightness and density (Colwell et al. 2009b). The A ring, the outermost of the main rings, has intermediate opacity, with waves excited by moons. Lying interior to the B ring, the C ring has lower opacity with several gaps and narrow ringlets. Stellar occultations, where starlight passing through the rings is measured, enable the ring structure and opacity to be analysed as shown by the *Cassini UVIS* data in Figure 1.8.

During its *Grand Finale* phase, *Cassini* passed between the rings and the planet, measuring the gravity of the rings so that their mass could be determined: $0.41 \pm 0.13\, M_{\text{Mimas}}$ (Iess et al. 2019). This relatively low mass, a fraction of the $400\,\text{km}$ wide moon, has consequences for the age of the rings, discussed further in Chapter 5.

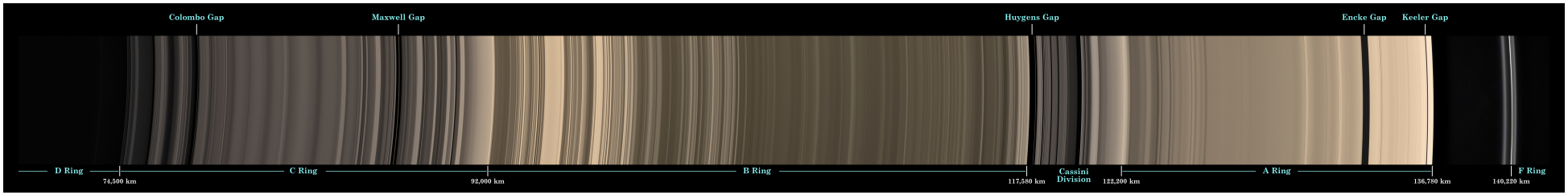

Figure 1.6: Natural colour mosaic of the unilluminated side of the main rings taken by *Cassini's NAC*. Image credit: NASA/JPL/Space Science Institute (PIA08389).

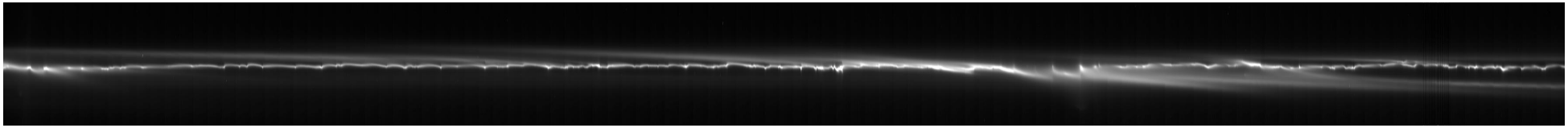

Figure 1.7: The F ring unfurled, covering $255°$ longitude. Mosaic of images taken by *Cassini's NAC*. Image credit: NASA/JPL/Space Science Institute (PIA08412).

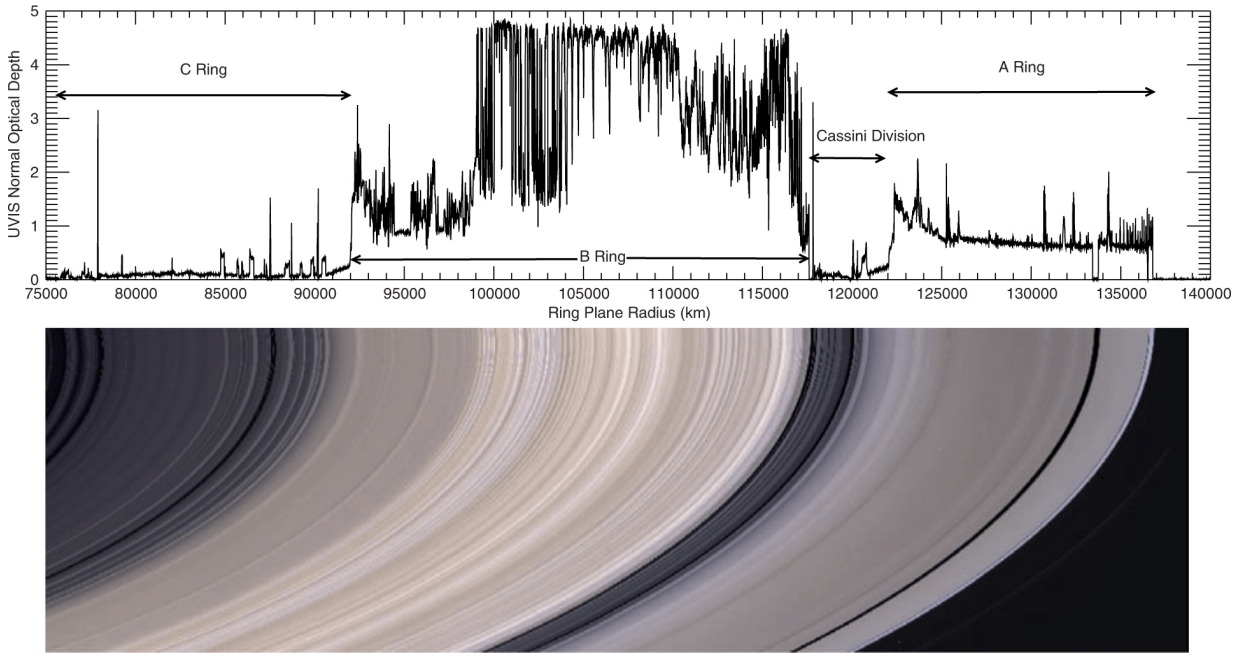

Figure 1.8: *Cassini* imaging of the main rings (the faint F ring is also visible outside of the A ring): *UVIS* stellar occultation data (top panel) and *ISS* mosaic (lower panel). Optically thick regions, such as those in the B ring, appear brighter than thinner regions due to the viewing geometry.
Image credit: Colwell et al. (2009b) and NASA/JPL/Space Science Institute.

b) Composition of Rings

Since before the first spacecraft visited Saturn, it has been known that the rings are comprised principally of water-ice, measured through near-infrared and microwave spectra (Pilcher et al. 1970; Clark & McCord 1980; Epstein et al. 1984; Poulet & Cuzzi 2002). In fact, water was the only molecule detected, although subsequently measured spectral characteristics, including reddening between 0.3 and 0.7 μm, indicate that other substances are also present, and additionally, the albedos of the A, B and C rings are not high enough to be consistent with a composition of pure water-ice (Poulet & Cuzzi 2002). More recent work, using *Cassini VIMS'* UV, visible and near-infrared reflectance spectra, confirms that the main rings are mostly water-ice with a small fraction of non-icy material (Ciarniello et al. 2019), and a similar composition would be expected for charged dust in the rings. However, there is a difference in the observed fraction of non-icy charged dust that rains out of the rings along magnetic field lines onto Saturn compared to the main rings (Hsu et al. 2018b); this *ring rain* is described in greater detail in §1.2.3, and the questions it raises with regard to broader open subjects, such as the age of Saturn's rings, is discussed in Chapter 5.

The non-icy constituent could be organic solids acting as a strong UV and blue wavelength absorber (Cuzzi & Estrada 1998; Poulet et al. 2003; Cuzzi et al. 2018) or nanophase particles of iron oxides (Clark et al. 2012), as well as a spectrally neutral absorber component assumed to be carbon (Cuzzi & Estrada 1998). Poulet & Cuzzi (2002), through analysing Clark & McCord (1980)'s reference spectrum of Saturn's rings and applying scattering theory (Shkuratov et al. 1999), conclude that the icy ring particles contain tholins[2], and that there is a small fraction of coarse amorphous carbon separated from the bulk water-ice material.

Based on *VIMS* data, an example shown in Figure 1.9, the UV absorber seems to take the form of inclusions within the individual water-ice grains with the abundance increasing as distance to Saturn decreases (Nicholson et al. 2008; Hedman et al. 2013; Filacchione et al. 2014). The neutral absorber is thought to present as separate particles in close proximity to the icy grains, described as a 'salt and pepper' mixture with the highest abundance in the C ring and Cassini Division (Hedman et al. 2013). This is also shown by the *Grand Finale* data of *Cassini* (Tiscareno et al. 2019), which shows that the ice-bands were deepest in the outer regions of the A

[2]Tholins are reddish brown compounds formed by UV or cosmic ray irradiation of cosmically abundant material such as methane, carbon dioxide, ethane, nitrogen and water.

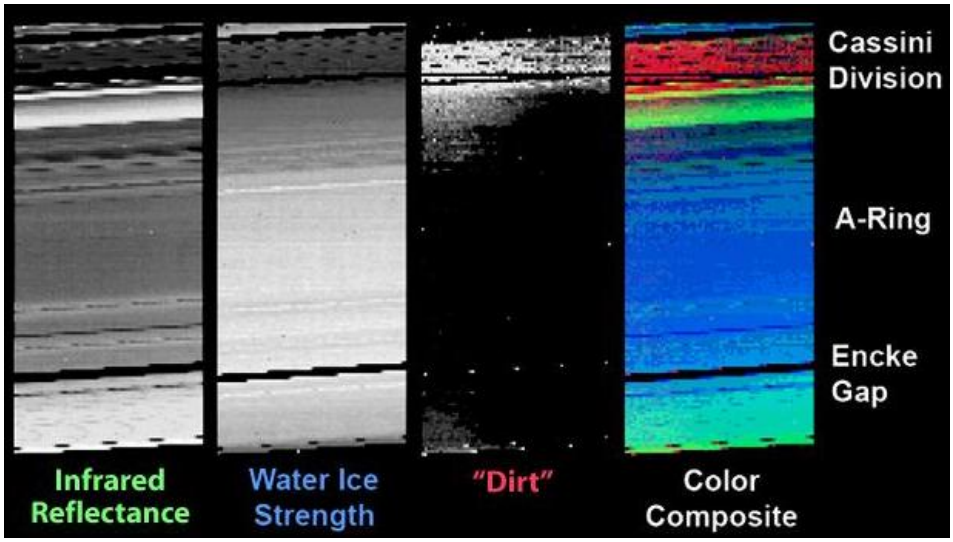

Figure 1.9: *Cassini VIMS* imaging of the A ring, radial distance from Saturn increases vertically downward. The infrared reflectance (leftmost) shows the brightness of scattered light transmitted through the rings: thinner parts appear brighter. Water-ice appears to peak in the outer A ring, with dirty material being most prevalent in the most tenuous parts of the ring such as the Cassini Division. The colour composite (rightmost) uses three colours to represent different compositions: blue is water-ice, red is organic material, and yellow/green indicates a mixture. Image credit: NASA/JPL (PIA06350).

and B rings, and thinnest in the Cassini Division and inner C ring.

Extrinsic meteoritic pollutants are transported radially through the *ballistic transport* mechanism, and can explain certain structural and compositional properties of the main rings (Durisen et al. 1989; Cuzzi & Estrada 1998; Estrada et al. 2015). The composition of the rings has deep implications for their formation and evolution, as it is thought that the organic UV absorbing material is primordial, whilst the silicate/iron neutral absorber may be due to bombardment by interplanetary debris polluting the almost pure water-ice rings. This is explored further in Chapter 5.

1.1.2 Inner Magnetosphere and Plasma Environment

The existence of a magnetic field around Saturn was discovered by the *Pioneer 11* flyby in 1979, which first explored the magnetosphere and trapped radiation belts (Van Allen et al. 1980; Fillius et al. 1980). This was followed in the early 1980s by the two *Voyager* flybys, which enabled the magnetosphere to be investigated in more detail (Krimigis et al. 1981, 1982), found auroral activity at mid- to high-latitudes (Broadfoot et al. 1981; Sandel et al. 1982), and observed spokes in the B ring (Smith et al. 1981, §1.2.1). Saturn's magnetosphere has since been studied in greater detail by *Cassini-Huygens*, which entered into orbit around the planet in 2004, eventually plunging into the atmosphere in 2017 after its *Grand Finale*, a series of proximal orbits diving between the inner D ring and planetary surface.

Saturn's magnetic moment is ~ 30 times weaker than Jupiter's and ~ 580 times stronger than Earth's (Russell 1993). The shape of the inner magnetic field is dipolar and its axis almost perfectly aligned with Saturn's rotational axis. At $6 < r < 15\,R_{\mathrm{S}}$, the ring current distorts the field and it becomes quasi-dipolar, and beyond $15\,R_{\mathrm{S}}$, it describes a warped magnetodisk (e.g. Baines et al. 2018). The nature of Saturn's internal magnetic field, including its negligible tilt and northward offset, will be described in greater detail for the main ring region in §1.3.1. Saturn's dynamo-generated internal field deflects the solar wind, creating a region composed of plasma around the planet called the magnetosphere, shown in Figure 1.10 to demonstrate the scale of the main planetary rings to the magnetospheric components. The plasma within the magnetosphere differs significantly from the solar wind's stream of ionised particles, with several possible plasma sources at Saturn, including the ionosphere, Titan, the rings, and inner icy moons (Gombosi et al. 2009), with Enceladus being the dominant mass source of magnetospheric plasma (Waite et al. 2006). The planetary magnetic field traps the plasma generated by these internal sources and it becomes entrained around the planet by its rapid rotation, with the centrifugal force confining the plasma towards the equatorial plane as a thin disc (André et al. 2008).

The size of the magnetosphere is governed by the balance between the magnetic field pressure and the solar wind, which in turn depends on solar activity. The magnetopause, the boundary separating the plasma of the solar wind from that within the magnetosphere (Figure 1.10), can extend anywhere from $22 - 27\,R_{\mathrm{S}}$ (Arridge et al. 2006). The corotation electric field, described in §1.3.1, dominates inside a few tens of R_{S} (Gombosi et al. 2009) and therefore for the main

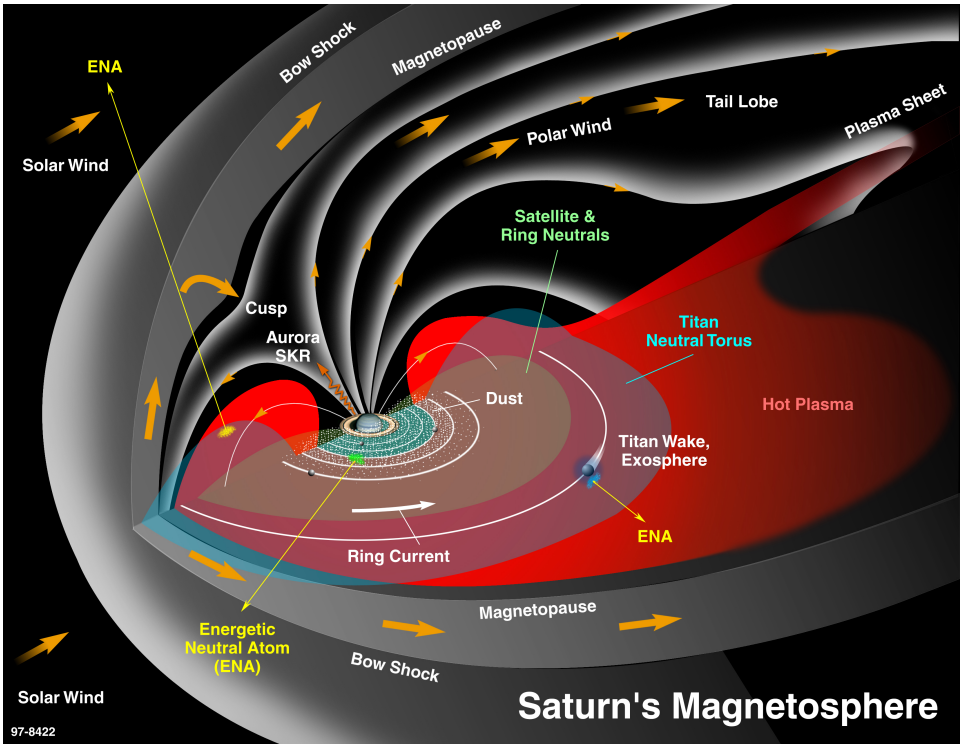

Figure 1.10: Illustration of Saturn's magnetosphere. The main ring system, shown in beige, lies well within the ring current and hot plasma region, figure reproduced from *Cassini MIMI* team.

rings, extending out to only $\sim 2.3\,R_S$ and lying well within the magnetopause, the plasma can be treated as corotating with the planet.

Birkeland currents, introduced at the beginning of this chapter, which are field-aligned currents that arise due to plasma heating caused by magnetic reconnection of the solar wind's and planet's magnetic fields, drive accelerated electrons into the upper atmosphere, exciting atoms there, which radiate as they drop energy levels and results in the observed aurorae. Saturn Kilometric Radiation (SKR, Figure 1.10), powerful low frequency radio emission originating from the planet, is related to aurorae as it is considered to be generated by the Cyclotron Maser Instability of electrons in auroral regions. It was thought that SKR was modulated by Saturn's true rotation period, and that the spokes in Saturn's rings, charged dust levitating away from the ring plane in approximately radial clouds (§1.2.1), shared the same periodicity (Porco & Danielson 1982); however, later a small but significant drift was observed in the SKR period over time (details in Kurth et al. 2009). This countered Porco & Danielson (1982)'s theory that spoke activity

was associated with a particular magnetic field sector.

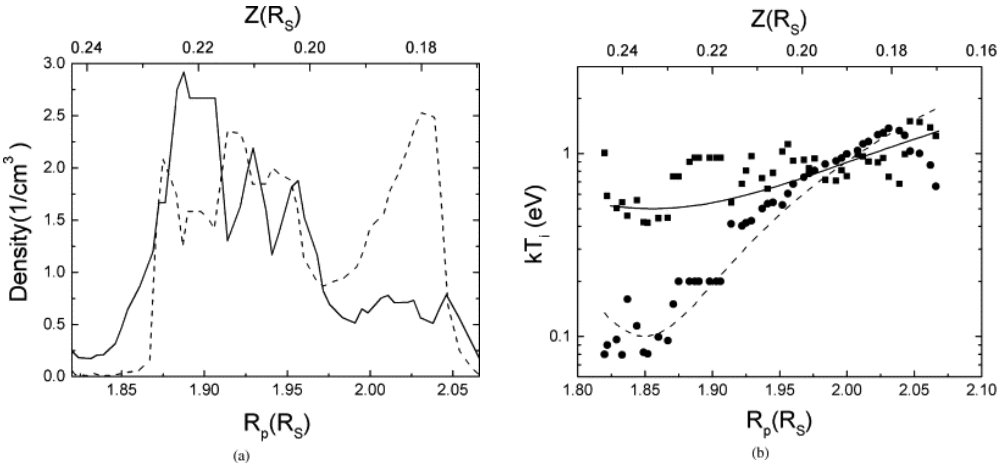

Figure 1.11: Measurements by CAPS (at a spacecraft altitude Z) of oxygen ions taken north of the ring plane, while the Sun was 23.6° south of the ring plane. (a) O^+ (solid) and O_2^+ (dashed) plasma densities versus equatorial distance. (b) Measured ion temperatures for O^+ (squares) and O_2^+(dots) versus equatorial distance. Lines are model temperatures described in Tokar et al. (2005). Image credit: Johnson et al. (2006, Fig. 1), adapted from Tokar et al. (2005).

During the *Cassini* mission, the existence of a tenuous plasma layer close to the main rings was discovered by *INMS* and *CAPS* measurements (Waite et al. 2005; Young et al. 2005) and *RPWS* electron density measurements (Gurnett et al. 2005). Water-related ions originating from icy ring material creates this *ring ionosphere*. Taking measurements over the A and B rings, Tokar et al. (2005), Waite et al. (2005) and Young et al. (2005) found that this tenuous plasma layer consists of O^+ and O_2^+, Figure 1.11. These oxygen ions are likely produced by UV photo-sputtering of the icy surfaces, then subsequent photoionisation of the molecular oxygen produced by the decomposition of water, a process modelled by Johnson et al. (2006). Hydrogen is also produced by the decomposition of water in the rings but more readily escapes the system. The contribution of energetic particles to the decomposition of ice in the main rings appears to be low (Johnson et al. 2006). Outside of the A ring, charged-particle sputtering from the magnetospheric plasma dominates over photo-sputtering, which is discussed below in relation to the radiation belts. Such collisions between an ion and an icy surface tends to lead to the liberation of water molecules and a small fraction of dissociation products, including O_2^+ and H_2^+, although such ions can be produced directly.

André et al. (2008) used the suite of magnetospheric instruments during *Cassini's* Saturn orbit

insertion of 2004 to give a unified description of the structure of the magnetosphere, identifying different regions. They summarise the single-instrument findings of previous studies, including the work of Tokar et al. (2005), Waite et al. (2005) and Young et al. (2005) described above: *MIMI*, *MAG*, *CAPS*, and *RPWS* (refer to the List of Acronyms, p. xxv). From a comparison of the regions observed by the the full suite of *MAPS* instruments (refer *ibid.*), they divide the magnetosphere into four regions; the first of these lies within 3 R_S and is of most relevance, containing the main rings. These rings block the radiation belts (described below), so that neutral particles and plasma can be produced only via other mechanisms: UV and low-energy particle irradiation or micrometeorite bombardment of the rings. This neutral population forms a ring exosphere, while the plasma forms a tenuous ring ionosphere. André et al. (2008) find that the ring system region is characterised by strong coupling between plasma, gas, and ring particles, and is essentially void of energetic particles due to absorption by main ring particles.

A planet's dipole magnetic field can trap charged particles to form radiation belts. Like the Van Allen belts around Earth, Saturn is surrounded by radiation belts of high energy protons and electrons in the keV - MeV range (Baines et al. 2018). However, there are key differences: they develop independently of the solar wind, instead originating from the moons (Kollmann et al. 2017); and the main ion radiation belts of Saturn (located outside of the F-ring) are clearly separated from each other and the rest of the magnetosphere by the moons Janus, Mimas, Enceladus and Tethys, which orbit outside of the F-ring. These moons are efficient at sweeping up charged particles in their orbital paths. The electron radiation belts on the other hand, are only weakly depleted at the moon orbits due to their magnetic drift being directed in the opposite sense of the corotational drift, such that their azimuthal velocity relative to the moons is lower and hence they are not absorbed as readily. Since the moons and main rings block sources of charged magnetospheric particles that would be radially transported inward, the dominant source is the decay of secondary neutrons produced by cosmic ray impacts onto the rings (Cooper 1983). During *Cassini*'s Saturn Orbit Insertion, *MIMI* and *INCA* measured energetic neutral atoms originating between the D ring and Saturn's atmosphere, evidence of a narrow inner radiation belt (Roussos et al. 2008, 2018). This inner belt extends across the D ring and is comprised of protons produced through the same cosmic ray albedo neutron decay mechanism of the outer radiation belts (Fillius et al. 1980).

As well as a ring ionosphere, there is also a ring exosphere: a layer of neutral molecules around

the main ring plane (Ip 2005). Since the *Voyager* flybys, the possibility of a ring atmosphere has been investigated (Ip 1984, 1995). The ring system, offering a large surface area, receives a high influx of interplanetary meteoroids, interstellar dust, and grains originating from satellites. These high-velocity impacts create water vapour (Ip 1997) alongside particulate ejecta, which dissociates (through either solar photons or electron impacts) into H_2 and O_2 molecules (Ip 2005). The measurements by the *Cassini CAPS* and *INMS* instruments of a population of O^+ and O_2^+ above the main rings (Tokar et al. 2005; Waite et al. 2005; Young et al. 2005), is consistent with the prediction of a ring atmosphere of O_2 molecules (Ip 1995). *HST* and *Cassini* have observed a neutral atmosphere of water molecules and their dissociation products that fill an extended region (Shemansky et al. 1993; Esposito et al. 2005), and it is the ionisation of this material by solar photons or electrons that is the primary source of plasma in Saturn's magnetosphere (Gombosi et al. 2009).

Another key element of the Saturnian system to consider is the planet's ionosphere – cold dense plasma (Wahlund et al. 2018) – which is produced by solar radiation photodissociation/photoionization or energetic electron impacts on the otherwise neutral atmosphere (McElroy 1973; Nagy et al. 2009). The solar extreme ultra-violet radiation acts across the dayside, while electron impact ionisation acts in auroral regions (O'Donoghue et al. 2016). Models predict that H^+ and H_3^+ dominate (Nagy et al. 2009), with H^+ dominating at higher altitudes and H_3^+ at lower altitudes between 900 and $3000\,\mathrm{km}$ altitude (O'Donoghue et al. 2016). Observations of H_3^+ emission, which was initially observed concentrated near the poles of the planet (Stallard et al. 1999) and later at low/mid-latitudes (Stallard et al. 2012; O'Donoghue et al. 2013), yields valuable insights into the ring-planet connection, described further in §1.2.3.

1.2 Charged Dust in Planetary Rings

To introduce physical and dynamical concepts relating to circumplanetary charged dust, it is useful to consider a few specific examples and relate them back to the environment of Saturn's rings: the spokes of the B ring (§1.2.1), streaming particles (§1.2.2), and ring rain (§1.2.3).

1.2.1 Spokes of Saturn

Spokes remain enigmatic, and a variety of approaches have been proposed to explain their formation and transient appearance, Figures 1.4b and 1.12. Spokes are filamentary structures, orbiting for hours at a time, appearing against Saturn's B ring. A journey through the literature brings up several properties of spokes that must be explained in a successful theory and which can be used to critically evaluate a theory's efficacy:

- Morphology – radially extended, generally with dimensions of 2000 by 10 000 km^2 (e.g. Carbary et al. 1982), with a characteristic wedge shape that has the narrowest portion at synchronous orbit.
- Rapid formation – a 6000 km spoke was observed to form within at least a short duration of 5 minutes (Smith et al. 1982). Spoke complexes develop over a couple of hours and usually fade within a planetary rotation.
- Active radial edge – most spokes are near-radial or tilting away from radial in a Keplerian sense (Smith et al. 1981), that is, spokes appear to form radially in a reference frame corotating with the planetary magnetic field (Terrile et al. 1981); the radial edge was thought to corotate with Saturn, surviving Keplerian shear (Hill & Mendis 1981). Porco & Danielson (1982) suggest that the observed shear $< 50°$ indicates that either spoke particles' orbital motion departs from Keplerian, or spokes are refreshed each rotation so that any large shearing is overprinted.
- Most spoke activity occurs in the outer B ring, with spokes appearing to originate near to synchronous orbit (e.g. Tagger et al. 1991; Graps et al. 2008).
- Longitudinal asymmetry in activity – there is a preponderance of spoke activity in the dawn (east) ansa (Porco & Danielson 1982; McGhee et al. 2005).
- Seasonal variation – spokes fade when the ring opening angle increases (Mitchell et al. 2006).

It is established that spokes are comprised of charged dust grains levitated tens of kilometres away from the ring plane (e.g. Graps et al. 2008), their phase angle dependence betraying their sub-micron size, as shown in Figure 1.12. However, initial ideas proposed that spokes were an optical brightness effect caused by the orientation of grains within the ring plane. These different paradigms share a commonality – both rely on electromagnetic effects to position the grains: one proposing that the spokes are changes in the albedo of material within the ring due to the polarisation and alignment of grains, the other proposing spokes are distinct structures from the main rings, lofted by electromagnetic forces.

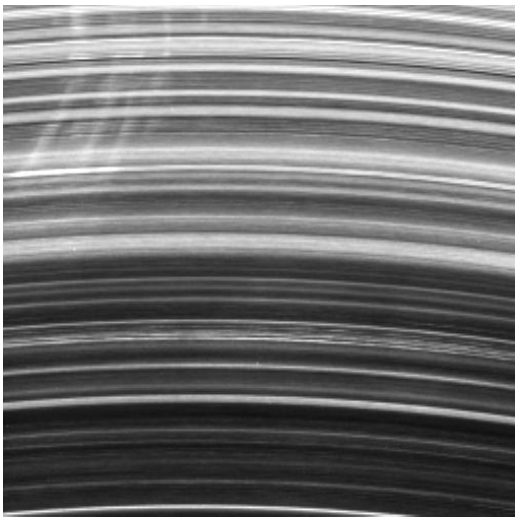

(a) A group of bright spokes appear in the upper left of this image of the B ring on 28 September 2006; the direction towards Saturn is downward, orbital motion to the left. Image credit: NASA/JPL/Space Science Institute (PIA08288).

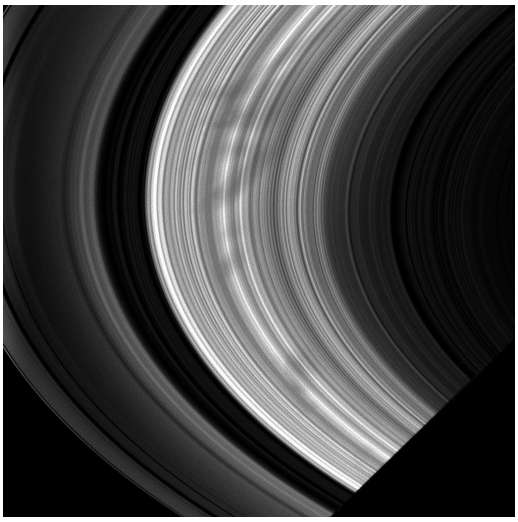

(b) The morning ansa of Saturn shows a group of dark spokes emerging from the planetary shadow on 2 November 2008.
Image credit: NASA/JPL/Space Science Institute (PIA10539).

Figure 1.12: Spokes appear bright at high phase angles and dark at low phase angles. Images taken by *Cassini's NAC* show spokes in **(a)** forward-scattered light taken when the phase angle (between Sun-Saturn-*Cassini*) was 147° and **(b)** back-scattered light at a phase angle of 37°.

Grain orientation theories rely on non-spherical grains being aligned by radial electric fields, resulting in a change in brightness within the ring plane, which are observed as spokes. An advantage of such theories is that no mass motion of grains on the large scales of spoke-lengths is invoked, thus requiring no rapid transport mechanisms for the dust (Grün et al. 1983, $\geq 20\,\mathrm{km\,s^{-1}}$), which can be problematic. It is not the dust itself which propagates, but rather its

optical properties. This idea of a velocity of something less tangible than the observed micron-sized dust, which drives the rapid formation timescales of the observed spokes, also occurs in the Collisional Cascade model presented in Jontof-Hutter (2012), which is discussed towards the end of this sub-section. In a short letter, Bastin (1981) argues that no physical electromagnetic field could evacuate and replenish dusty material over the observed distances in such a short time, and proposes the albedo changes are due to a local electromagnetic field anomaly, and parenthetically mentions an alternative theory of electrostatically induced clustering and dispersal of grains. However, that model does not explain the wedge-shaped spoke morphology, or why spokes have a radial active edge, and it does not develop a theory for the origin of such a required local electromagnetic field.

Carbary et al. (1982) developed a theory for local radial electric fields, which could polarise dust grains, altering their light scattering properties and resulting in spokes. These fields are distinct from the global corotational electric field. Such an azimuthally uniform global electric field, derived in §1.3.1 and described by Eq. 1.37, could not explain the localised structure of spokes, nor their variability and confinement to the B ring. Instead, Carbary et al. (1982) suggest that a polarising radial potential across the B ring is generated from zonal ionospheric winds establishing electric fields which drive Birkeland currents that flow along magnetic field lines from the planet to the ring plane, where they align grains. Carbary et al. (1982) associate spokes with Saturn's electrostatic discharges (SEDs), which are powerful episodic bursts of radio emission (Warwick et al. 1981), a notion proposed by Smith et al. (1981). SEDs have a periodicity close to that of Saturn Kilometric Radiation, §1.1.2 and described further below. Carbary et al. (1982) calculated that the power released by such SED bursts was comparable to that resulting from their model current flowing radially through the B ring. The uncertainty in SED periodicity allowed for tentative corroboration. However, several findings subsequently disputed this. Weinheimer & Few (1982) argued that water-ice did not have the ferroelectric properties to result in the necessary torque to polarise the grains, and, moreover, the poor conductivity of ice grains could not explain the short spoke formation timescales.

Handel & James (1983) attempted to recover the grain alignment model by suggesting that some grains are able to transition to a ferroelectric state by exploiting the properties of ice at B ring temperatures in the shadow of the planet. These grains become polarised, which increases the local electric field strength (since the grains' electric dipole moments align with the electric

field), leading to the polarisation of more grains, which in turn increase the electric field strength, thus creating a polarisation catastrophe, which Handel & James (1983) argue is the mechanism responsible for the SEDs. However, this attempt to link spoke activity with the SEDs via a polarisation catastophe has since fallen out of favour as the electric discharges are now thought to originate in Saturn's atmosphere rather than the rings (Warwick 1989). Moreover, Porco & Danielson (1982) found that spoke activity peaked at the same longitude as Saturn Kilometric Radiation (SKR), intense auroral radio emission generated by accelerated electron beams via the cyclotron maser instability (Lamy et al. 2008), and more recently the periodicity of spoke activity matches more closely the *Cassini* measurements of SKR periodicities than SED periodicities (Mitchell et al. 2011).

Grain orientation theories for spoke formation have been abandoned in favour of grain levitation models, in which spokes are formed from clouds of charged dust, which are lofted away from the ring plane by electromagnetic forces. However, it should be noted that Meyer-Vernet (1984) states some caveats, taking into account physical processes that were previously ignored by other authors. When the dielectric properties of ice are included, the (attractive) polarisation force can overcome the electrostatic ejection of grains, and the constraint on grain size based on electrostatic disruption alone is modified by accounting for the grains' centrifugal disruption because of their spin.

Hill & Mendis (1981) propose a model for spoke formation where loosely bound regolithic dust on ring boulders is charged by Birkeland currents flowing from the magnetotail into auroral regions to generate electric fields in the ionosphere driving currents into the ring plane. Such electron beams charge up both the ring bodies and dust negatively on the night side and the grains become electrostatically repulsed and lofted away from the ring plane. Their model can explain the increased spoke activity in the dawn ansa, as the dust discharges as it orbits in sunlight (refer to §4.2) and therefore the spokes shear out and dissipate as the day progresses and the grains orbit closer to Keplerian velocities. In order to explain the discrete nature of spokes, the model of Hill & Mendis (1981) relies on the electron currents being localised, which Tagger et al. (1991) argues is difficult to explain, stating that the electron beams' source in the magnetosphere would need to be unphysically confined in longitude and extended in latitude. Moreover, the active spoke region is magnetically-connected to lower latitudes on Saturn than those that are connected to the magnetotail, which is the supposed source of dust-charging electron beams

(Graps et al. 2008).

Instead, Tagger et al. (1991) suggest that spokes are magnetosonic (compressional) waves driven by, for example, electron beam impacts (cf. Hill & Mendis 1981) or meteor impacts (cf. Goertz & Morfill 1983), that yield large-scale, long-wavelength spiral instabilities with a pattern speed equal to the corotational frequency of the magnetic field. Although this model can explain the rapid radial extension of spokes, it relies on extremely high charge-to-mass ratios to explain a spoke's persistent radial active edge. Another challenge to Hill & Mendis (1981)'s model, which was initially levelled at Carbary et al. (1982), is that of the poor conductivity of ice as this requires high electrostatic potentials to levitate grains and to sustain corotational motion of the spokes' radial edge.

A popular grain levitation theory for spoke formation, proposed by Goertz & Morfill (1983), involves a dense plasma cloud, generated by meteor impacts on the B ring, that charges up dust on the ring bodies so they escape the gravity of the ring. Goertz & Morfill (1983) argue that the rapid radial motion of dust grains is energetically problematic and the spokes are actually a manifestation of radially perturbed plasma. As in the work of Hill & Mendis (1981) and Thomsen et al. (1982), Goertz & Morfill (1983) argue that the spokes consist of negatively-charged dust, based on the observed spoke shapes. The negatively-charged plasma moves radially due to an $\vec{E} \times \vec{B}$ drift, described by Eq. 3.20 . The azimuthal electric field is generated by the relative motion of the corotating plasma and the negatively-charged dust orbiting at close-to-Keplerian velocities, which flows via field-aligned currents to the ionosphere and sets up an azimuthal electric field that maps back onto the ring plane. The peak in spoke activity at dawn can be explained by the meteor impact model, as Cuzzi & Durisen (1990) find that meteor impact speeds peak around solar midnight, thus generating more dust which can be seen as it orbits into sunlight. However, in the Hill & Mendis (1981) model the formation of spokes is suppressed in sunlight as the solar photoelectron current discharges the negatively-charged grains (§4.2). Farmer & Goldreich (2005) argue that the relatively high velocity of the plasma invoked by Goertz & Morfill (1983) to explain the rapid spoke formation timescales is not within the range expected by the difference between the corotational and Kepler velocities. Morfill & Thomas (2005) review the physics of the meteor impact model in light of more recent dusty plasma research and argue that a complex structured plasma cloud can easily reach the required $20\,\mathrm{km\,s^{-1}}$ radial drift (Grün et al. 1983).

Jones et al. (2006) propose a model of spoke formation in which currents arising in Saturn's atmosphere travel down magnetic field lines into the ring plane, a theory not dissimilar to that of Carbary et al. (1982), who suggested zonal winds in the ionosphere generate currents flowing into the rings. In the model of Jones et al. (2006), an electron avalanche is triggered by cosmic rays above thunderclouds and beamed along magnetic field lines which map onto the B ring. The induced negative charging causes large ring particles to electrostatically repel dust. Saturn's ionospheric density reaches a minimum close to dawn, so that electron beams can more easily propagate to the rings, explaining the longitudinal asymmetry of spoke activity. Spokes form almost instantly along the outline of the magnetic field lines that cross the ring, and it is the shape of the electron beam in the atmosphere and how it maps onto the midplane that determines the shape of the spokes (Horányi et al. 2010). They state that a meridional arc at the top of the atmosphere will map onto a radial segment in the ring plane magnified by a factor of $2(L-1)^{\frac{1}{2}}L$, while an azimuthal arc gets magnified by a factor $L^{\frac{3}{2}}$, where L is the distance from the magnetic field line in question to the centre of Saturn in units of R_{S}. This results in a requirement that the electron beams have to be very elongated along the direction of lines of longitude to produce the thin radial spokes (a circular electron beam results in a elliptical footprint with aspect ratio 1.4), as well as there being no positive correlation of thunderstorms at suitable planetocentric latitudes and spokes yet confirmed.

The Collisional Cascade model proposed by Hamilton (2006) and studied by Jontof-Hutter (2012) bears certain similarities to the Goertz & Morfill (1983) model as it involves meteor impacts, but in this case it is the dynamics of the ejected dust that trigger spoke formation, rather than dense plasma. And the spokes are not electrostatically levitated grains but rather the visible evidence of a cascade of unseen high velocity impacts of smaller dust. The grains are rapidly accelerated to high velocities by the magnetic field and are transported both vertically and radially. Upon returning to the ring plane after being mirrored up magnetic field lines (§3.6.1), the grains strike larger bodies there, generating new debris particles at different radial locations and micron-sized ones become visible as spokes, while smaller faster grains continue the collisional cascade. This theory, like Goertz & Morfill (1983)'s, can explain the greater spoke activity near dawn by the highest rate of meteor impacts occurring near solar midnight (Cuzzi & Durisen 1990), although Jontof-Hutter & Hamilton (2012a) think it could be due to Saturn's shadow casting an azimuthal asymmetry onto the plasma density. There are some issues with the Collisional Cascade model, such as requiring $<$ nm-sized grains in their cascades, given their

choice of plasma parameters, which prohibits the production of micron-sized spoke particles, as well as their acknowledgement of the plasma's seasonal variation having a significant effect on the progression of a cascade chain. An update on the status of the Collisional Cascade model (Hamilton et al. 2020) was unfortunately postponed due to the COVID-19 pandemic.

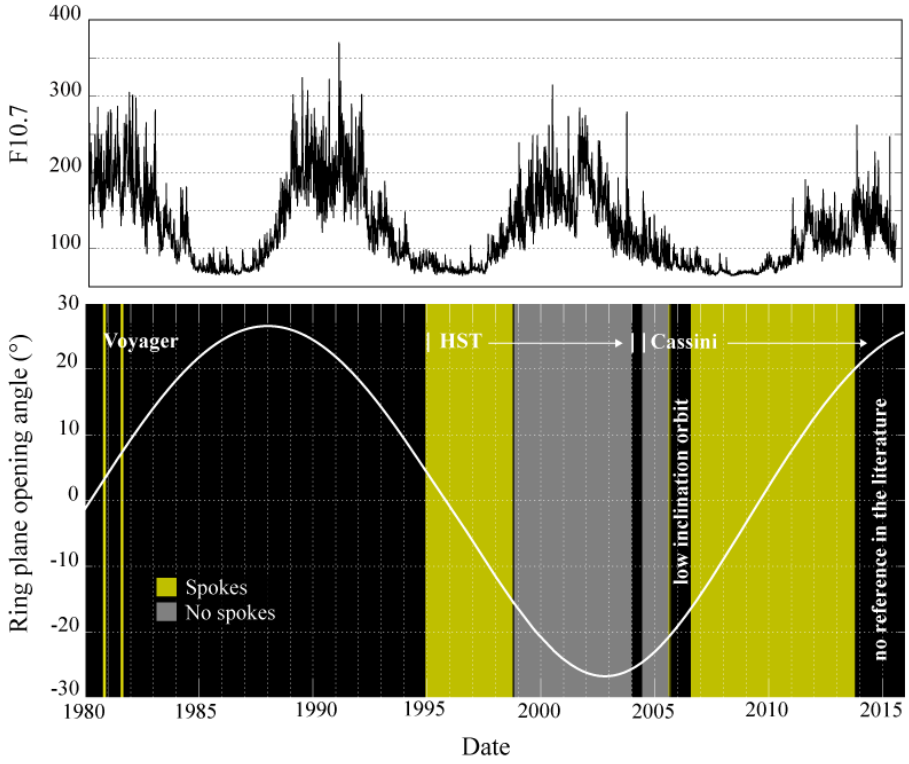

Figure 1.13: The ring plane opening angle (solar elevation angle) is approximately sinusoidal over time as Saturn orbits the Sun every $\sim$ 30 years. Solar activity, indicated by the F10.7 index in solar flux units, is generally higher for periods of no spokes. Spokes *were* seen during the *Voyager* flybys in the 1980s even though it appears that solar activity was quite high, probably due to the rings being almost edge-on at that time. Using F10.7 data from the National Geophysical Data Center (now part of the National Centers for Environmental Information) and spoke seasonality data from Horányi et al. (2009, Fig. 16.8).

Although the triggering mechanism for spokes is still open to debate, the seasonal variability of spokes after they have formed is better understood. *HST* data showed periods when spoke activity disappeared. Scattering calculations, taking into account viewing geometry, predicted that spoke contrast decreased with increasing ring plane opening angles (McGhee et al. 2005). This suggested that spokes could still be forming, but the viewing geometry was such that it was

just not possible to see them. However, when *Cassini* arrived at Saturn in 2004 and was in a position to observe good spoke contrast, spokes were still not seen. Therefore, it is thought that the angle between the Sun and the ring plane must play an important role in the charging of the background plasma environment and whether the dust can be charged and overcome cohesive and gravitational forces (Nitter et al. 1998; Mitchell et al. 2006). Figure 1.13 shows the ring plane opening angle and solar activity over periods of spoke activity.

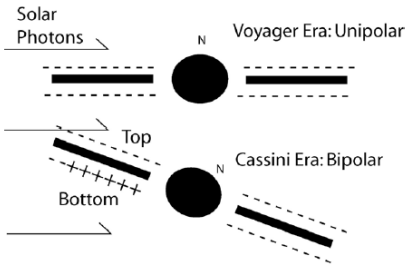

Figure 1.14: Comparing the ring electric configuration in the early 1980s (*Voyager* Era) and 2000s (*Cassini* Era). Image credit: Farrell et al. (2006, Fig. 2).

An idea put forward by Farrell et al. (2006) to explain the seasonality of spokes relies on the changing electrical nature of the rings. The background plasma density above the rings is dependent on the angle that the ring plane makes to the incoming solar wind and insolation, as shown in Figure 1.14. When the Sun is at a lower angle so that fewer photons impinge on the rings, then the plasma electron current (§4.1.1) dominates and the disk is charged to a negative potential thus repelling the grains (assumed to be negatively charged) leading to the production of spokes. When the rings are more open to the Sun, the increased photon flux kicks out electrons and the exposed side of the ring plane becomes positively charged and hence spokes do not form, as indicated by the grey shading on Figure 1.13. There is also a link between the photoemission current and the diurnal variability of spoke activity – more spokes are seen on the dawn ansa, emerging out of the nightside (Smith et al. 1981; Porco & Danielson 1982; Mitchell et al. 2013). The planetary shadow effect on grain charging is explored in greater detail in §4.3.

There are several models for spoke formation, and it remains an open question. One promising avenue is Hamilton et al. (2020)'s Collisional Cascade model, which shares elements with models of ring rain (§1.2.3), namely the high-velocity dust ejecta produced by micro-meteoroid bombardment of the main rings.

1.2.2 Dust Streams

Charged dust ejected from the ring systems of Saturn and Jupiter has been detected. A description of these so-called *dust streams* is included as they allow various useful concepts to be introduced, and are of interest for several reasons outlined in Hsu et al. (2010), including being the fastest solid bodies known in the Solar System. Although hypothesised in the 1980s (e.g. Johnson et al. 1980), it was not until about a decade later that direct observations were made. First observed in the Jovian system by the *DUST* instrument sensitive to submicrometre- and multimicrometre-sized particles aboard *Ulysses* (Grün et al. 1992, 1993), these periodic, high-velocity bursts of submicron-sized dust were subsequently detected by *Galileo* (Grün et al. 1996) and *Cassini* (Graps et al. 2001), and later also found in the Saturnian system (Kempf et al. 2005).

Grains become positively charged within Jupiter's plasma environment, and the corotational electric field (§1.3.1) accelerates these grains radially outward (Horányi et al. 1993a,b). Initially the origin of the dust streams was unknown, and Io (Horányi et al. 1993b), the Gossamer ring (Hamilton & Burns 1993), or Shoemaker-Levy 9 (Grün et al. 1994) were considered as sources. Following the analysis of Hamilton & Burns (1993) for Jupiter, the velocity of escaping particles from a ring system can be calculated from energy considerations, restricting orbits to the equatorial plane and considering only the dominant components of the magnetic and gravitational fields for a grain with constant charge q_d and mass m_d.

The escape velocity of a grain can be calculated in the following manner – the kinetic energy of an escaped grain from a planet of mass M_p will equal the total energy of a grain on an initially circular orbit of radius r, such that

$$v_{\text{esc}} = \sqrt{\frac{2GM_p}{r}\left(L_* - \frac{1}{2}\right)}, \tag{1.2}$$

as the total energy is the kinetic energy of a grain orbiting at Keplerian velocity $\left(\frac{1}{2}\frac{GM_pm_d}{r}\right)$ plus the gravitational and electric potential energy of such a grain $\left(-\frac{GM_pm_d}{r}(1-L_*)\right)$. L_* is the ratio of the Lorentz force due to the corotational electric field, explained in §1.3.1 (Eq. 1.37), to gravity,

$$L_* = \frac{q_d \Omega_p g_1^0 R_p^3}{m_d G M_p}, \tag{1.3}$$

following Hamilton & Burns (1993); Jontof-Hutter (2012), assuming a magnetic dipole $B = g_1^0 \left(\frac{R_p}{r}\right)^3$, for a general planet denoted by subscript p and dust grain by subscript d. Equation 1.3 is used in place of a charge-to-mass ratio $\frac{q_d}{m_d}$ (§3.1).

Planet	Saturn	Jupiter
M_p/kg	5.685×10^{26} (Hsu et al. 2018b)	1.898×10^{27} (NASA/JPL 2020)
R_p/km	$60,268$ (Cao et al. 2012)	$71,372$ (Acuña et al. 1983)
$g_1^0/\ \mathrm{T}$	2.1191×10^{-5} (Cao et al. 2012)	4.218×10^{-4} (Acuña et al. 1983)
Ω_p/s^{-1}	1.622×10^{-4} (Ye et al. 2016)	1.758×10^{-4} (Archinal et al. 2018)

Table 1.1: Planetary parameters.

Substituting in Jupiter's values (Table 1.1) and using the expressions for surface grain potential $\phi_d = \frac{q_d}{4\pi\epsilon_0 a_d}$ and grain mass density $\rho_d = \frac{m_d}{\frac{4}{3}\pi a_d^3}$, and then converting to more useful units gives

$$L_*^J = 0.21 \frac{q_d}{m_d} = 0.0057 \left(\frac{\mu\mathrm{m}}{a_d}\right)^2 \left(\frac{\phi_d}{V}\right) \left(\frac{\mathrm{g\,cm^{-3}}}{\rho_d}\right), \tag{1.4}$$

where superscript J refers to Jupiter. In order to enforce the realness of v_{esc} in Eq. 1.2, $L_* > \frac{1}{2}$. Thus the escaping grains are positively charged. Substituting this condition into Eq. 1.4 with reference values $\phi_d = 3\,V, \rho_d = 1\,\mathrm{g\,cm^{-3}}$, limits on the spherical grain properties can be obtained: $a_d^J < a_d^{J,\max} \sim 0.2\,\mu\mathrm{m}$, $m_d^J \lesssim 3 \times 10^{-14}\,\mathrm{g}$. Any grains larger than $a_d^{J,\max}$ are gravitationally dominated and hence remain in orbit around Jupiter. Electromagnetically dominated grains, those with the highest charge-to-mass ratios (smallest in size), also remain in orbit around Jupiter because they gyrate tightly around the planet's field lines. Intermediate-sized grains, satisfying $a_d^J > a_d^{J,\min}$, exhibit larger gyro-orbits, refer to Eq. 3.26, because the electromagnetic forces are weaker; when the gravitational force is relatively weak at larger orbital distances so that the forces do not balance, positively-charged grains are accelerated away by the radial electric field.

Hamilton & Burns (1993) ran numerical simulations of grains with initial launch locations chosen to represent potential sources of dust in Jupiter's magnetosphere: the gossamer ring and Io. Their critical (dimensionless) charge-to-mass ratio, $L_{\rm crit}$, which can yield the size of the smallest escaping grains via Eq. 1.4, was found by determining the stability boundary from simulations with different L_* for the orbital locations of interest. Their results are given in Table 1.2:

Source region	$R(R_J)$	$L_{\rm crit}$	$r_g^{\rm min}$ (μm)	$m_g^{\rm max}/m_g^{\rm min}$	v_∞ (km s^{-1})
Near synchronous orbit	2.25	4.4	(0.062)	26	<77
Outer gossamer ring	3.0	22	(0.028)	290	<150
Io	5.9	200	(0.009)	8,000	<340

Possible source regions and their distances from Jupiter in jovian radii ($R_J \sim 71{,}500$ km) are shown, followed by $L_{\rm crit}$, the numerically-determined force ratio for the smallest escaping grains. The size of these smallest grains ($r_g^{\rm min}$) is determined from equation (2) using $L = L_{\rm crit}$, $\rho_g = 1$ g cm^{-3}, and $\Phi_g = +3$ V. The mass ratio $m_g^{\rm max}/m_g^{\rm min}$ is found by solving equation (2) for r_g^3, using first $L = 1/2$ (which corresponds to the largest escaping grain regardless of source) and then $L = L_{\rm crit}$. The final column lists numerically determined escape speeds which agree well (to within a few per cent) with those found from equation (1). With the exception of the minimum grain size, all quantities in this table are independent of the assumed grain charge and density.

Table 1.2: Properties of particles escaping from Jupiter, from Hamilton & Burns (1993, Tab. 1).

The size of the smallest escaping grains $a_d^{\rm min}$ is determined from substituting $L_{\rm crit}$ into Eq. 1.4, with $\phi_d = 3\,V$, $\rho_d = 1\,{\rm g\,cm^{-3}}$, and the corresponding grain mass is found assuming a sphere of constant density. Similarly, the mass of the largest escaping grain is found by setting $L_* = \frac{1}{2}$, so that the ratio of the masses of the largest to smallest escaping grains can be determined. Their numerically determined escape speeds agree well with Eq. 1.2.

Hamilton & Burns (1993) tried to explain the 1992 *Ulysses* measurements by proposing an origin for the dust particles in Jupiter's gossamer ring, suggesting that the periodicity in the signal was due to the periodicity of the grains' vertical acceleration, causing their paths to intersect with the spacecraft trajectory at specific intervals. However, further measurements of the dust streams by *Galileo*, *Cassini*, and *Ulysses* corroborated Horányi et al. (1993b)'s hypothesis of Io as the source of dust. Periodicities in the dust impact signal, compatible with Io's orbital period, confirmed this origin (Krüger et al. 1998, 2003). Furthermore, the quantity, composition and size of the

dust grains are consistent with particles that can escape from a typical Io volcanic plume and rule out impact ejecta (Graps et al. 2000; Postberg et al. 2006). Time-frequency analysis by Graps et al. (2001) demonstrated that Io is a localised source of the dust streams.

Detailed analysis through numerical simulations found that the dust stream particles move faster and are smaller in size than was previously suggested. Theoretical analysis by Zook et al. (1996) gave a size distribution of $5 \leq a_d^J \leq 15\,\mathrm{nm}$, $m_d^J \sim 10^{-18}\,\mathrm{g}$ and escape speeds $v_{\mathrm{esc}}^J \geq 100\,\mathrm{km\,s^{-1}}$, which differed from quantities previously obtained by Grün et al. (1993) from the measured impact data: $20 \leq v_{\mathrm{esc}}^J \leq 56\,\mathrm{km\,s^{-1}}$ and $1.6 \times 10^{-16} \leq m_d^J \leq 1.1 \times 10^{-14}\,\mathrm{g}$ (assuming the average density of water-ice: $0.03 \leq a_d^J \leq 0.1\,\mu\mathrm{m}$). Due to a lack of calibration for that parameter range, the estimates of Grün et al. (1993) remained uncertain. Observations from *Galileo* (Horányi 2000) fell within the ranges for the dust particles derived by Zook et al. (1996).

A similar mechanism for dust streams was suggested for Saturn (Horányi 2000) and indeed high-velocity bursts of dust particles escaping from the Saturnian system have been detected by *Cassini's CDA* (Kempf et al. 2005; Hsu et al. 2010). Potential sources for the dust streams are the dense A ring outside synchronous orbit, the E ring, and dust clouds around Dione and Rhea (Kempf et al. 2005). There is evidence from the *CAPS* instrument to suggest the cryovolcanic plumes from Enceladus (Jones et al. 2009), which also feed the E ring, in an analogous setup to that of Io for the Jovian system. There are key differences between the magnetic fields of Jupiter and Saturn, namely the strength and alignment. As described in §1.1.2, Saturn's magnetic moment is ~ 30 times weaker than Jupiter's, and whilst Jupiter's magnetic dipole is tilted relative to its rotational axis at just under $10°$, the magnetic and rotational axes of Saturn are closely aligned and therefore dust particles will remain closely confined to the equatorial plane, as there is no radial component of $\vec{B}$ to cross with $\vec{v}$ to provide vertical motion.

Saturn's weaker magnetic field results in differing escape velocities and grain sizes for the stream particle populations. Following a similar approach to Hamilton & Burns (1993), the ratio of the corotational electric field to gravity can be expressed for Saturn (denoted by superscript S) using parameters from Table 1.1 as

$$L_*^S = 0.020\frac{q_d}{m_d} = 0.00053\left(\frac{\mu\mathrm{m}}{a_d}\right)^2\left(\frac{\phi_d}{V}\right)\left(\frac{\mathrm{g\,cm^{-3}}}{\rho_d}\right). \tag{1.5}$$

Taking the ratio of Equations 1.4 and 1.5, it can be seen that the grains in Jupiter's rings have higher charge-to-mass ratios than Saturn's, for a fixed grain type, size and charging environment, largely due to its higher field strength. As was the case for Jupiter, the charge-to-mass ratio has to be sufficiently large to overcome the planet's gravity. This sets an upper limit on the radius for an escaping grain, such a maximum grain size for Saturn can be estimated following the method of Hamilton & Burns (1993), based on Equations 1.2 and 1.5: $a_d^S < a_d^{S,\max} \sim 0.06\,\mu\mathrm{m}$, that is, grains no larger than about $60\,\mathrm{nm}$ would be expected to be ejected from Saturn, under the simplifying assumptions noted above.

Considerations of the various charging processes, described in greater detail in Chapter 4, including the collection of plasma ions and electrons, and the emission of photo- and secondary electrons by the grains, allows the equilibrium surface potential of grains to be calculated based on a model of the magnetosphere of Saturn's plasma parameters (Kempf et al. 2005). It was found that there are only two regions where the surface potential is expected to be positive, a necessary prerequisite for ejection from the system by the corotational electric field: on the outskirts of the A ring and beyond the orbit of Dione.

The escape velocity of grains leaving the Saturnian system can be estimated and compared to those of Jupiter. Following the analysis of Horányi et al. (2009) and equating the work done by the corotating electric field on positively charged grains to the kinetic energy of the ejected grain (ignoring the initial gravitational binding energy) gives

$$\int_{r_0}^{r_{\mathrm{esc}}} q_d E dr = \frac{1}{2} m_d v_{\mathrm{esc}}^2, \tag{1.6}$$

which can be re-arranged for the escape velocities of the respective planets:

$$v_{\mathrm{esc}} = \sqrt{\frac{6\epsilon_0 \phi_d \Omega_p g_1^0 R_p^3}{\rho_d a_d^2} \int_{r_0}^{r_{\mathrm{esc}}} r^{-2} dr}. \tag{1.7}$$

Substituting values into Eq. 1.7, assuming that Jovian dust particles are accelerated out from Io and Saturnian dust particles start at Dione's orbit until they reach the edge of their respective

magnetospheres:

$$v_{\text{esc}}^{J} = 3 \left(\frac{\mu\text{m}}{a_d} \right) \text{km}\,\text{s}^{-1}, \tag{1.8a}$$

$$v_{\text{esc}}^{S} = 0.6 \left(\frac{\mu\text{m}}{a_d} \right) \text{km}\,\text{s}^{-1}. \tag{1.8b}$$

The faster velocities at Jupiter are largely due to its stronger magnetic field strength.

Kempf et al. (2005) inferred that the mass and impact speed of Saturnian stream particles are at least comparable to those of Jovian particles because of the similarity in both the rise time and amplitude of their impact signals. However, they noted that the measurements were well outside the calibrated range, and referred to theoretical considerations of Zook et al. (1996) to conclude that the Saturnian grains had $v_{\text{esc}} \geq 100\,\text{km}\,\text{s}^{-1}$ and $a_d \lesssim 6\,\text{nm}$. Based on *CDA* observations, Hsu et al. (2010) constrain the size of grains to $2 - 9\,\text{nm}$ and their ejection speed to $\sim 70\,\text{km}\,\text{s}^{-1}$.

1.2.3 Ring Rain

This section describes the relevant background theory and observations relating to ring rain, an important pathway of interaction between the rings and planet. In Chapter 5, this leads onto discussing the complexities involved in determining the age of Saturn's rings, through considering the water-ice to non-icy ratio of ring rain and the effect of the low mass of the rings on their evolution.

Ring rain is the precipitation of particles from the main rings of Saturn onto the planet. Moore et al. (2015) make the distinction between a flux of neutrals (e.g. H_2O) and ions (e.g. O_2^+). The neutral source is interpreted as water plumes ejected from Enceladus, whilst the ion source is thought to arise from a series of chemical reactions in the rings. When referring to *ring rain*, Moore et al. (2015) refer to the ionised source; in contrast, Miller et al. (2020) uses the term to refer to all material flowing from the rings onto Saturn. In this thesis, *ring rain* refers to charged dust grains precipitating from the ring plane onto the planet, with a focus on physical dynamics rather than chemistry.

Theory predicted a lower temperature and higher peak electron density for Saturn's ionosphere than is observed, reviewed by Nagy et al. (2009). The ionospheric electron density profiles (Atreya & Waite 1981; Atreya et al. 1984) observed by Pioneer (Kliore et al. 1980) and Voyager (Tyler et al. 1981, 1982) radio occultation observations were an order of magnitude smaller than early predictions. In order to reduce the modelled electron densities, two mechanisms were proposed, which share in common the conversion of long-lived atomic H^+ into short-lived molecular ions. Radiative recombination with H^+ is a very slow process and therefore electrons must be removed from the ionosphere via other faster recombination and quenching events. The removal of H^+, which would survive many planetary rotations, is also required to account for the large diurnal variation of ionospheric electron density (Kaiser et al. 1984). McElroy (1973) suggested that H^+ can be lost, via charge exchange, to vibrationally excited H_2, which is produced from collisions with electrons or via H_3^+ recombination, and is subsequently quenched via collisions with (thermal or photo-) electrons and H, H_2 and H^+ (Nagy et al. 2009). Chen (1983) calculated that vibrational temperatures of thousands of degrees would be required to ensure H_2 was excited to its fourth or higher vibrational level so that the reaction was exothermic, which was unlikely outside of the auroral zone since there are lower rates of high energy particle bombardments.

The other mechanism to convert H^+ into short-lived molecular ions was proposed by Shimizu (1980), who suggested that oxygen-hydrogen compounds could be sputtered from ring particles and reach the upper atmosphere of Saturn, where, through a series of reactions the H^+ ions produce water ions, whose rapid recombination rate subsequently lowers the electron density in the ionosphere. The interaction between rings and ionosphere had been considered earlier by Atreya & Donahue (1975), but lack of knowledge of the presence of a strong magnetic field stymied anything beyond speculation at that point. Chen (1983) argued for the theory proposed by Shimizu (1980), noting that by comparison with Jupiter, whose measured peak electron densities are of the same order as those predicted by theoretical calculations using the same fundamental physical and chemical processes as those for Saturn, there must be some difference operating in Saturn's system. Such a difference is readily available through the unique presence of many potential sources of ice, including small moons or the rings themselves.

Connerney & Waite (1984) built upon this model in which water plays a major role. Their series of chemical reactions differ to those suggested by Shimizu (1980), and are largely based on

work on comet models (Giguere & Huebner 1978; Huebner & Carpenter 1979). The same idea persists though: removal of H^+ ions via charge exchange with oxygen-hydrogen compounds and subsequent electron recombination. Emission of the H_3^+ ion is a proxy for water influx onto Saturn, Eqs. 1.9a – 1.9h. The full table of chemical reactions along with rates in Saturn's ionosphere can be found in Connerney & Waite (1984), of which the most important are stated below:

$$H_2 + h\nu \rightarrow H + H^+ + e \tag{1.9a}$$
$$\rightarrow H_2^+ + e \tag{1.9b}$$
$$H_2O + H^+ \rightarrow H_2O^+ + H \tag{1.9c}$$
$$H_2O^+ + H_2 \rightarrow H_3O^+ + H \tag{1.9d}$$
$$H_3O^+ + e \rightarrow H_2O + H \tag{1.9e}$$
$$\rightarrow H_2 + OH \tag{1.9f}$$
$$\rightarrow H + H + OH \tag{1.9g}$$
$$H_2^+ + H_2 \rightarrow H_3^+ + H. \tag{1.9h}$$

The major constituent of the ionosphere is H^+, resulting principally from photodissociation of H_2 (1.9a), which is lost via charge exchange with water (1.9c). The H_2O^+ ion reacts with H_2 to produce H_3O^+ (1.9d), which is rapidly removed via electron recombination (1.9e) - (1.9g), leading to the observed lower electron densities. H_3^+ is produced from the reaction of H_2^+ ions, present through photoionisation of H_2 (1.9b), with H_2 via (1.9h). H_3^+ is observed primarily from discrete ro-vibrational emission lines in the infrared (O'Donoghue et al. 2013, 2014). It is a useful probe of upper atmosphere/ionospheric conditions (e.g. Stallard et al. 2012), being approximately in local thermodynamic equilibrium with its surroundings, although the focus in this work is on the connection between H_3^+ and the ring system.

Wilson & Waite (1989) used a time independent kinetic plasma to determine the densities, drift velocities and temperatures for two ion species; the ionospheric H^+ and ring-originating O^+, refer to §1.1.2 and see Figure 1.15, with the caveat that O^+, OH^+ and H_2O^+ can all result from reactions of $H_2O + h\nu$ (refer to Table 1 of Connerney & Waite (1984)) and choosing any such ring ions does not greatly change the results. Their model results showed that the influx of

water-derived ions from the rings could be $> 2 \times 10^7\,\mathrm{cm}^{-2}\,\mathrm{s}^{-1}$, in keeping with the required $\sim 4 \times 10^7\,\mathrm{cm}^{-2}\,\mathrm{s}^{-1}$ calculated by Connerney & Waite (1984), to reduce the ionospheric electron densities for latitudes magnetically connected to the B ring.

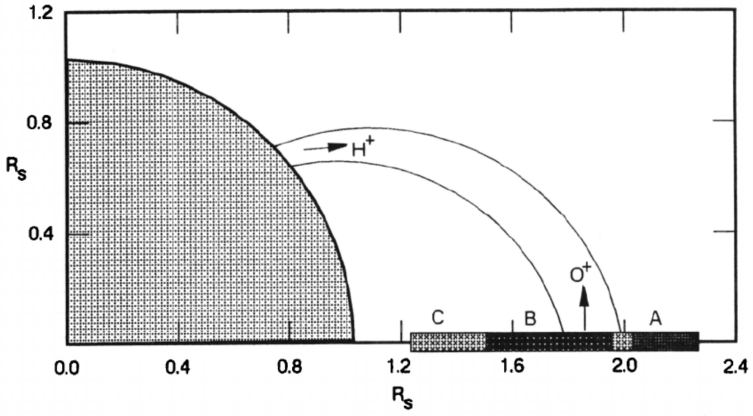

Figure 1.15: Meridian plane diagram illustrating the ring-ionosphere connection. H^+ ions originate in the ionosphere, while O^+ (or likewise, OH^+ or H_2O^+) ions originate from the rings. Image credit: Wilson & Waite (1989, Fig. 1).

Alongside the higher than expected electron densities at Saturn, a further unexpected observation was the north-south variation in peak electron densities. The production mechanism is extreme ultraviolet radiation from the Sun and therefore a maximum should be observed close to the equator. However, the highest density was found at a latitude of 73°S, and the lowest at 36°N (Atreya et al. 1984). The work of Connerney & Waite (1984) on chemical reactions and water influx rates was developed by Connerney (1986), who mapped features observed in Voyager images at specific ionospheric latitudes to their counterpart ring locations, via magnetic field lines. They proposed that the latitudinal asymmetry was due to the north-south asymmetry of Saturn's vertically offset dipole magnetic field (§1.3.1). Measurements of spatially resolved methane absorption band reflectivity (West et al. 1982) showed dark bands indicating a removal of haze, revealing several atmospheric features mapping to particular boundaries within the rings (Connerney 1986). In Figure 1.16, a double band near 50°N, indicated by arrows labelled (1) and (2), maps to two instability boundaries ($1.525\,R_S$ and $1.62\,R_S$) in the B ring, which is discussed further below, observed in numerical results presented in Chapter 3, and explored further in Chapter 5. Prangé et al. (2006) use spatially-resolved ultraviolet spectra to study hydrocarbon abundances and find results consistent with water flowing into Saturn's ionosphere at latitudes magnetically connected to the main rings.

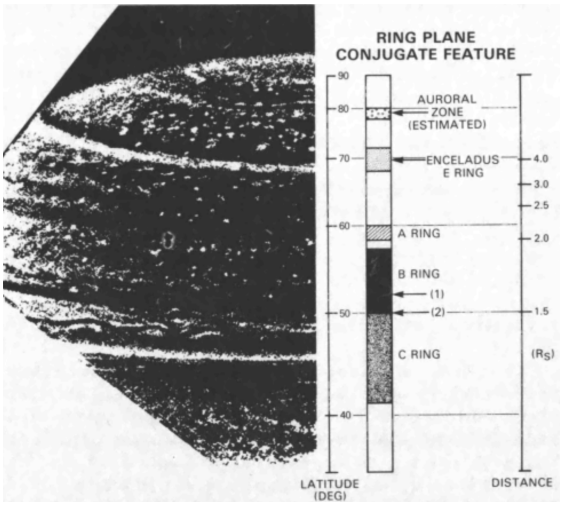

Figure 1.16: *Voyager 2* high contrast image of Saturn's northern hemisphere. From left to right, a latitude scale, the corresponding ring plane conjugates, and a ring plane distance scale are shown. Image credit: Connerney (1986, Fig. 1).

The first direct measures of H_3^+ emission from Saturn's ionosphere, indicative of ring rain, were made by O'Donoghue et al. (2013) in the form of near-infrared spectral data obtained by the 10-m W. M. Keck II telescope using the NIRSPEC (Near InfraRed Spectrograph) instrument. They found that a majority of H_3^+ emission peaks map via planetary magnetic field lines to gaps in the rings, and troughs in emission map to dense ring sections. O'Donoghue et al. (2013) proposed that charged material from the water-product atmosphere surrounding the rings must be streaming along field lines into Saturn's ionosphere, producing the modulation in H_3^+ emissions.

O'Donoghue et al. (2013) initially thought that a greater depletion of H_3^+ emission would be observed at latitudes with higher water influx, based on charge-exchange reactions with water ions, but by considering the various loss channels for H_3^+, described in Moore et al. (2015) which states that the dominant loss channel for H_3^+ is dissociative recombination with electrons, O'Donoghue et al. (2017) found that a greater depletion of H_3^+ emission is observed at latitudes with *lower* water influx. Indeed, O'Donoghue et al. (2013) report an 'anomalous' peak in H_3^+ emission for the instability region $1.52 - 1.62\,R_S$, where they had expected higher water influx and therefore greater depletion of H_3^+ through charge-exchange, but this can be readily explained by how H_3^+ is lost to electrons more readily than to water ions, that is, an influx of (positive) water ions decreases electron densities thereby decreasing the dominant loss channel for H_3^+. Any theory to explain an increase in H_3^+ emission must involve some alternative quenching

channel in order to remove electrons and reduce H_3^+ loss rates.

Following orbital insertion, *Cassini* detected a ring ionosphere comprised of O^+ and O_2^+ (Tokar et al. 2005; Waite et al. 2005), produced by the photoionisation of the O_2 ring atmosphere, itself a product of solar UV-decomposed water-ice (Johnson et al. 2006), §1.1.2. These ring-derived O_2^+ and O^+ ions are the most likely to precipitate into the planet's atmosphere, being the dominant species (Moore et al. 2015). Oxygen-bearing molecules charge-exchange with H^+, then those resulting charge-exchange products subsequently rapidly recombine, which leads to the observed reduction in electron densities. As a result there is an increase in H_3^+ emission due to a decrease in H_3^+ loss rates.

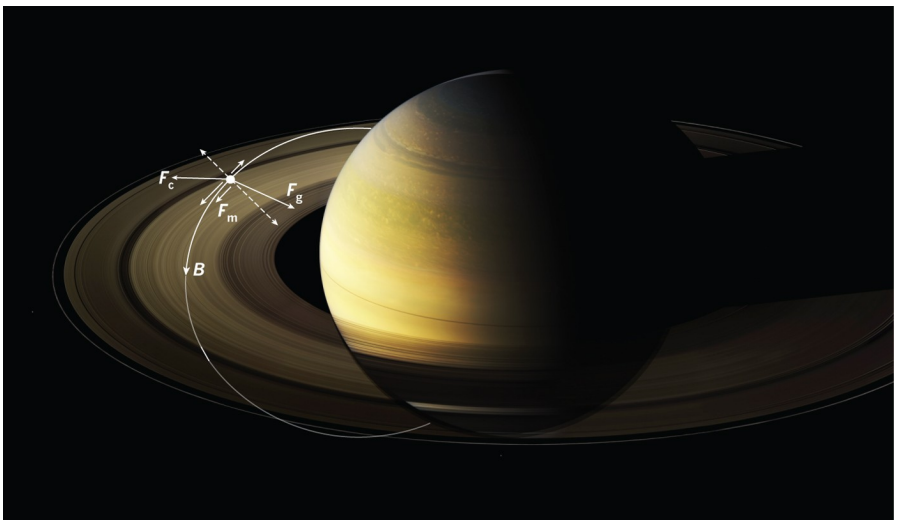

Figure 1.17: A highly charged dust grain is constrained to move along a magnetic field line, illustrated by the solid white curve, like a bead on a wire. It responds to the gravitational force, $\vec{F}_g$, centrifugal force, $\vec{F}_c$, and magnetic mirror force, $\vec{F}_m$, with components parallel to $\vec{B}$, indicated by small solid arrows, causing the grain to slide up and down the field line. The perpendicular-to-$\vec{B}$ components of $\vec{F}_g$ and $\vec{F}_c$, indicated by dashed vectors, are responsible for gyromotion (§§3.4.1 and 3.6.1). Image credit: Connerney (2013, Fig. 1).

As described in Connerney (2013) and Figure 1.17, the motion of charged grains in planetary rings is a problem of classical mechanics. Charged grains gyrate around magnetic field lines due to the perpendicular Lorentz force, and slide along the field lines in response to the parallel components of the gravitational and centrifugal forces and the magnetic mirror force, which points towards the magnetic equator (towards weaker field strength), §3.6.1. In the case of a planet with a tilted dipole magnetic field, such forces would disperse charged grains. However, Saturn has highly aligned magnetic and rotation axes, and so there are unique pairs of conjugate

north and south latitudes that map to specific radial distances in the rings. The northward-offset of the magnetic dipole relative to the geographic equator means there is an asymmetry to the north/south latitudes for a given radial distance mapping, hence observations show features occurring at higher latitudes in the north than in the south (e.g. Connerney 1986; O'Donoghue et al. 2013).

One such latitude region showing a suppression in electron emission (and a peak in H_3^+ emission) corresponds to the inner region of the B ring ($1.525 - 1.625\,R_S$). A theory of charged particle motion in the ring plane, developed by Northrop & Hill (1982, 1983), which explains regions of instability (§§3.5.2, 3.5.3 and 3.6.2), can explain the inner edge of the B ring at $1.525\,R_S$ and the major increase in optical depth beginning at $1.625\,R_S$, refer to Figure 1.8 which shows an increase in optical depth at $\sim 98,000\,\mathrm{km}$. Consider the forces on a charged grain shown in Figure 1.17. Grains with zero magnetic moment are unstable for $r < 1.625\,R_S$, as gravity overwhelms the centrifugal force resolved along $\vec{B}$ and such grains fall onto Saturn, while outside of $1.625\,R_S$, the centrifugal force overcomes gravity and returns grains to the ring plane (for the bead on a wire picture imagine the bead travelling along the magnetic field line to the point of largest radial extent).

Northrop & Hill (1982)'s method of deriving an expression for the marginal stability radius is described in §3.6.2, where Eq. 3.55 predicts a vertical instability boundary for Saturn at about $1.625\,R_S$. Kepler launched grains will also experience an outward magnetic mirror force, which is directed towards the ring plane as this where the magnetic field strength is weaker for a given B field line, so that the force balance location is moved inward to $1.525\,R_S$, as gravity increases with decreasing distance to match the centrifugal and magnetic mirror forces; the nonzero gyroradius and magnetic moment has a stabilising effect (Northrop & Hill 1983; Northrop & Connerney 1987). This so-called marginal stability boundary is observed in Figure 3.5 and described further in §3.6.2 and §5.1.2. Plotting the potential in which highly charged grains move along a magnetic field line showed that any grains inside of the inner B ring fall onto Saturn along magnetic field lines, as particles at $r < 1.525\,R_S$ have no potential well to reside in and therefore no stable orbit (Northrop & Connerney 1987), §3.6.2. Such an electromagnetic erosion mechanism could explain the relative scarcity of material in the C ring observed through its low optical thickness and also provide a physical basis for making an estimate of the age of the rings, a question that will be addressed in Chapter 5. The increase in optical depth outward of

1.625 R_S, refer to Figure 1.8, occurs at the stability limit of grains (Northrop & Hill 1982) so that any orbits of highly charged grains outside of this radial distance are stable and therefore increase the observed opacity of the rings, whilst decreasing the precipitation onto the planet.

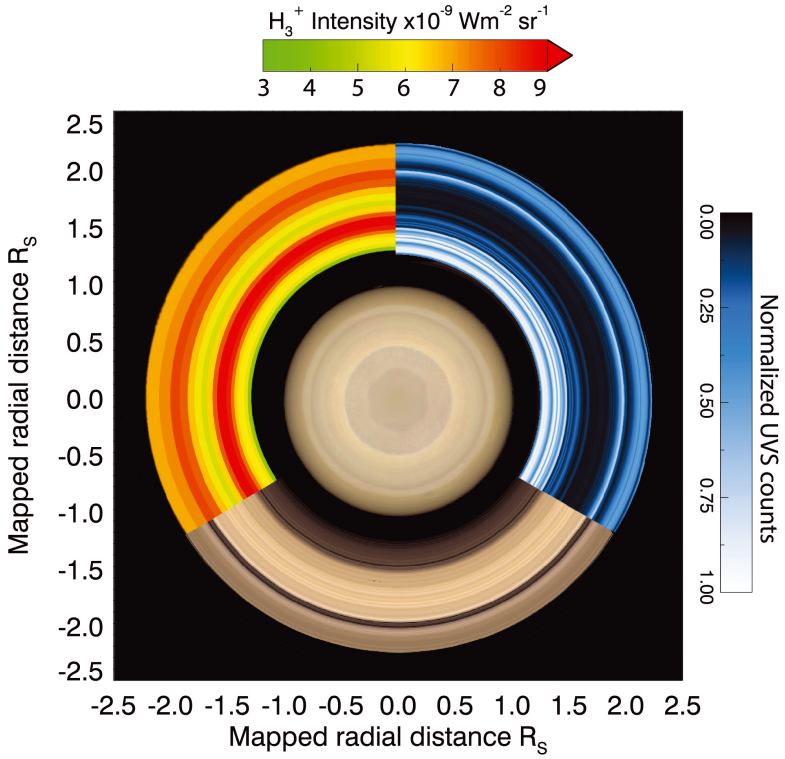

Figure 1.18: Saturn and its ring system shown above the northern hemisphere. Both axes indicate radial distances from the planet's centre. H_3^+ intensities from spectral line measurements (cut-off at $9\,\mathrm{nW\,m^{-2}\,sr^{-1}}$) are mapped via the magnetic field to their conjugate radial distances in the ring plane on the upper left of the rings (over an arbitrary longitude range). On the top right, opacity measured by the *Voyager 2 Ultraviolet Spectrometer* is shown (Lillie et al. 1977; Lane et al. 1982), with a value of 0 indicating rings are sufficiently dense enough to block all light, while a value of 1 indicates light passes through unattenuated. At the bottom, the main rings observed in reflected light are shown. Image credit: O'Donoghue et al. (2017, Fig. 4).

The statement by Connerney (2013), that gaps in the rings are weak sources of ring rain, as there is little material therein to be eroded, does not quite tell the whole story. It is such scarcity of ring material, which is indicative of unstable orbits propelling grains onto the planet, that corresponds to higher levels of ring rain, provided that there is a supply of grains to that region. At 1.525 R_S, there is both a supply of grains from the optically thick B ring and an unstable potential, such that there can be a high flux of water grains from the rings onto the planet (O'Donoghue et al.

2017).

The initial observations of Saturn's midlatitude ionospheric H_3^+ emissions recorded in 2011 (O'Donoghue et al. 2013) were followed up and confirmed by higher resolution observations recorded in 2013 by O'Donoghue et al. (2017). The more recent emissions were dimmer across latitudes, probably due to lower upper-atmospheric temperatures as measured by (Koskinen et al. 2015). The ring plane opening angle, which varies according to season (Figures 1.13 and 1.14), was larger in 2013 compared to 2011 and therefore the rings were subject to higher levels of solar radiation. This was thought to explain the larger contrast between bright and dim features in H_3^+ emission, as the production of charged grains would be larger and increase water precipitation onto Saturn. O'Donoghue et al. (2017) provide a clear visualisation of the relationship between H_3^+ and ring structures, Figure 1.18, which will be explored further in Chapter 5.

Mitchell et al. (2018) note that ring rain, precipitating onto the planet at the feet of magnetic field lines cannot access equatorial regions, yet these are the same regions where ionospheric electron densities are observed to be lowest (Kliore et al. 2014; Wahlund et al. 2018). In order to reconcile this, Mitchell et al. (2018) invoke atmospheric drag to de-orbit dust and model grains precipitating into Saturn's equatorial atmosphere from the inner edge of the D-ring. They used *MIMI* onboard *Cassini* to detect and characterise neutral grains and find a dust population tightly confined near the equator. Hsu et al. (2018b) observe a latitudinal variation in nanograin impact rate, Figure 1.19, with a high fraction around the ring plane, which can be explained by the time-variable stochastic charging of such small grains sometimes resulting in low charge-to-mass ratios such that they are are not confined to move along magnetic field lines, refer to Chapters 4 and 5.

Water is the dominant constituent for the main rings, §1.1.1b), (Pilcher et al. 1970; Clark & McCord 1980), with the remaining material in the form of either organics (tholins), metallic iron or hematite (Miller et al. 2020), or inorganics such as silicate (Hsu et al. 2018b). Miller et al. (2020) use *INMS* to analyse the composition of material flowing from the D ring into Saturn's atmosphere, identifying various organic compounds, water and ammonia. They use the term *ring rain* to refer to all material flowing into Saturn's rings (rather than only material flowing along magnetic field lines). These compounds are also found in Serigano et al. (2020)'s *INMS* results. Hsu et al. (2018b) used *CDA* measurements obtained during *Cassini's Grand Finale* mission to collect material between the planet and the D ring. They found that the region

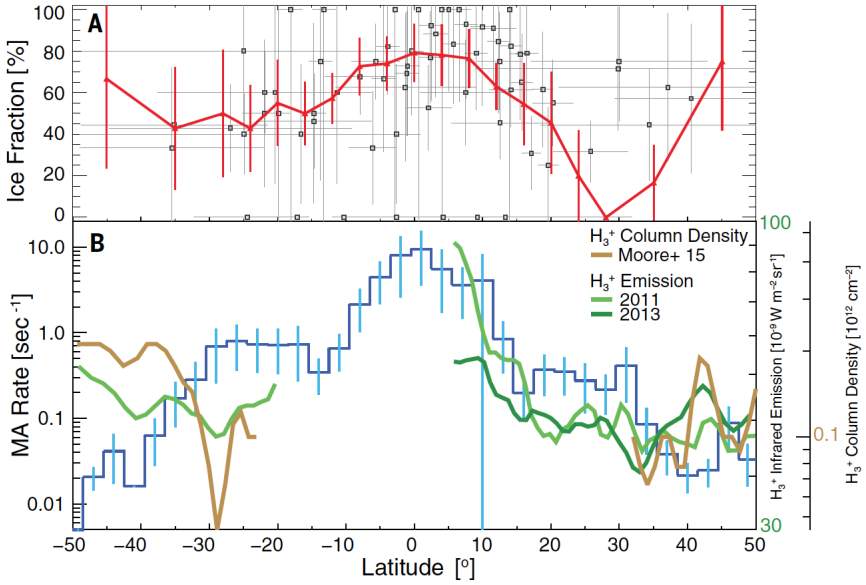

Figure 1.19: Latitudinal profiles. (A) Plotting fraction of water-ice spectra against latitude. There is a dependence on latitude with a peak around the ring plane. Horizontal bars indicate the latitude range of contributing spectra, with squares indicating the dead-time–corrected water-ice fractions for 50 consecutive spectra. (B) Nanograin impact rate (blue histogram) and H_3^+ observations (curves). The green curves show the H_3^+ infrared emission from Saturn's atmosphere described in the work of O'Donoghue et al. (2013) and O'Donoghue et al. (2017). The gold curve shows the corresponding column density (Moore et al. 2015). Image credit: Hsu et al. (2018b), further details are described in the original caption of their Fig. 4.

within the innermost ring is largely free of micron-sized grains and populated principally by grains with radii of a few tens of nanometres.

This dust population is assumed to be the ejecta generated by hypervelocity collisions between interplanetary dust particles and the main rings. The *CDA Dust Analyzer* recorded nearly 3000 impact mass spectra, of which 78% were too faint or showed only the target or its known contaminant spectra. Hsu et al. (2018b) allow for the possibility of organic molecules by noting that due to the high impact velocities onto the *CDA*, there could be overlaps in signals between organic fragments and known carbon contamination. From the spectra with sufficient signal-to-noise for an analysis, Hsu et al. (2018b) identified two types: water-ice and silicate, all within $\pm 50^\circ$ latitude of the ring plane.

Hsu et al. (2018b) report an ice-to-silicate number ratio of 2:1 based on their identified 422 water-ice-type and 214 silicate-type spectra. They explain in their supplementary material how

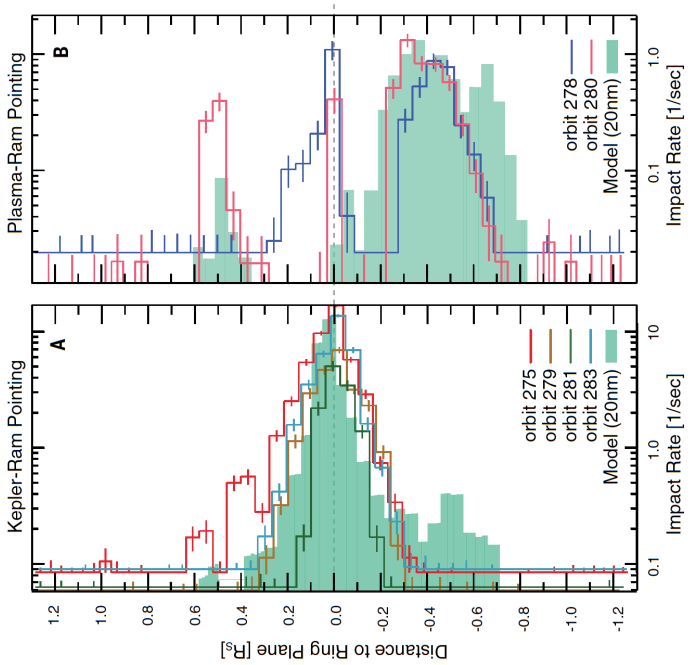

Figure 1.20: Vertical density profiles measured by the *CDA*. The *Mass Analyzer*, a linear impact time-of-flight mass spectrometer, impact rate is plotted (lines) as a function of the distance from the ring plane during (A) Kepler ram and (B) plasma ram orbits. The green histograms are results of model calculations for 20 nm grains. Image credit: Hsu et al. (2018b), Fig. 3A & B – the figure has been rotated to display the distance to the ring plane horizontally.

they convert this into a mass ratio of between 2:1 and 11:1 (30% and 8% silicate respectively) – the number fraction is taken to be the upper limit of the silicate mass fraction, while a lower bound to the silicate mass fraction can be estimated from the number of impact events measured by the sum of the *QI* signal of silicate grains compared to *all* grains, compositionally identified or not, given in Table S2 of Hsu et al. (2018b): $\frac{208}{2651} \approx 8\% \rightarrow$ water-ice: silicate $\approx 11:1$.

The *CDA* dust impacts can be classified into Kepler ram or plasma ram directions, where the impact direction is of grains moving in circular prograde orbits or the direction of plasma co-rotating with the magnetic field respectively. The profiles depend on the instrument's orientation relative to dust flow, as shown by the difference between the subplots of Figure 1.20: the impact rate peaks at $0\ R_S$ for all orbits with Kepler ram orientation (A), whereas the plasma ram orientation shows two broader peaks either side of the ring plane peak and centred at similar north and south magnetic latitudes (B). This is the ring rain signature of charged grains funnelled from the main rings along magnetic field lines onto the planet. The southern dust peak is stronger and

broader than the northern dust peak in Figure 1.20 (B), which can be attributed to the northward offset of Saturn's dipole – the radial component of $\vec{B}$ at the ring plane crossed with a velocity in the azimuthal direction generates a vertical Lorentz force acceleration.

Due to the high impact speeds of the nanograins, which lie outside the *CDA* calibration range, the mass cannot be obtained directly from the impact waveforms. Instead, a proxy for the grain mass is used, in the form of the number of charges produced in an impact (under the assumption that each grain impinges on the detector with the same speed), which is measured by the *CDA Ion Grid QI* signal (Srama et al. 2004). Hsu et al. (2018b) plot the charge distributions for water-ice and silicates, described by power laws with very similar slopes, indicating that the grain types have similar mass distributions. The grain mass is expected to be linearly proportional to the impact charge amplitude (Göller & Grün 1989), yet the impact charge yield varies with grain composition – silicate grains are more efficient in impact charge production than water-ice (Koschny & Grün 2001); and therefore similar impact charge distributions could mean that the water-ice grains are more massive than the silicate grains to achieve the same yield, rather than similar mass distributions between the two types based on the similar power slopes. However, Hsu et al. (2018b) note that due to sodium contamination from the E ring and Enceladus plumes on the *CDA* target, which acts as a signal amplifier regardless of grain composition, there could be tiny ice grains whose signals are boosted to levels similar to that of tiny silicate grains so that the effect of a less efficient charge yield for water-ice is countered by sodium amplification.

Hsu et al. (2018b) find a variation in water-ice fraction with latitude, Figure 1.19. They show a peak of $70 - 90\%$ close to the ring plane dropping to $\sim 40\%$ at 30° latitude, and a similarity between the nanograin density profile and H_3^+ emission. Such variation in latitude of water-ice deposition onto the planet could indicate that the water-ice grains are more massive or larger and therefore are less affected by the Lorentz force so that they are concentrated close to the ring plane. However, Hsu et al. (2018b) argue that their results are consistent with silicate and water-ice having similar masses/sizes, and this means that the ice-to-silicate ratio of ring rain and the latitudinal profiles are *not* due to grain dynamics, but rather arise from material processes during ejection and transportation. For example, the photo-evaporation of ice grains could explain the high silicate fraction in ring rain (compared to bulk rings), and as grains take a longer time to reach higher latitudes (Hsu 2020) this could also explain the higher ice fraction close to the ring

plane, Figure 1.19.

Hsu et al. (2018b) argue that there is no dynamical selection effect for the ring rain material, finding that the ratio between the dust originating from the B ring and that from the C ring measured by the *CDA* is almost constant, and therefore the variation in latitude of the water-ice fraction cannot be explained by the difference between the main rings' composition (the B ring has a higher water-ice fraction than the C ring). So it appears to *not* be the case that more material from the C ring is deposited at higher latitudes, which might have explained the lower ice fraction away from the ring plane observed in Figure 1.19. And in fact the bulk C ring has a higher ice fraction, up to $\sim 90\%$ (Zhang et al. 2017b), than the $\frac{2}{3}$ observed by the *CDA* for the nanograins so that the ring rain material is somehow sorted, either physically through ejection mechanisms or chemically, in the process of travelling from the rings to the planet and is therefore different from the main ring composition.

In Chapter 5, this question of why the overall silicate mass fraction in ring rain is higher than the concentration of non-ice components in the main rings is returned to, alongside the question of the varying latitudinal water-ice deposition. Chapter 5 also discusses the structure of the rings themselves and the effect that ring rain could have on the interpretation of their age.

1.3 Physical Processes Acting on Dust in Planetary Rings

Before commencing a description of the forces that act on dust grains in planetary rings, it is necessary to acknowledge the importance of their electric charge and how that affects their motion through the Lorentz force. The various charging processes and how they vary in time are discussed in detail in Chapter 4. For the purposes of this section, the grains are assumed to hold a representative constant charge (depending on their size and an assumed potential) so that the respective strengths of electromagnetic forces on a grain can be compared to radiation pressure, gravity and various drag forces, to quantify more directly the varying effects of the different forces and their relative strengths.

1.3.1 Gravitational and Magnetic Planetary Fields

The dynamics of a charged grain in planetary rings is significantly affected by the presence of the planetary gravitational and magnetic fields. The gravitational field can be expressed as the gradient of a scalar potential,

$$\vec{g} = -\vec{\nabla}\Phi_g, \tag{1.10}$$

and provided there is an absence of local currents ($\nabla \times B = 0$), the magnetic field can be expressed as

$$\vec{B} = -\vec{\nabla}\Phi_B. \tag{1.11}$$

Laplace's equation is applied to find the gravitational and magnetic potentials at a point outside the central body's surface (that is, outside of the mass and dynamo core sources). Spherical harmonics, Eq. 1.12, which are solutions to Laplace's equation in spherical coordinates are a useful tool to describe these fields, and are essentially an adaptation of Fourier analysis to a spherical surface. The plasma environment (§1.1.2) around a rotating planet gives rise to a corotational electric field term, which will be discussed following the description of the magnetic field.

The Laplace equation in spherical polar coordinates is

$$\frac{1}{r^2}\frac{\partial}{\partial r}\left(r^2\frac{\partial \Phi}{\partial r}\right) + \frac{1}{r^2 \sin\theta}\frac{\partial}{\partial \theta}\left(\sin\theta\frac{\partial \Phi}{\partial \theta}\right) + \frac{1}{r^2 \sin^2\theta}\frac{\partial^2 \Phi}{\partial \phi^2} = 0. \tag{1.12}$$

Any function Φ which satisfies Laplace's equation is a harmonic function. If there is a rotational asymmetry, like in the case of non-spheroidal planets and tilted magnetic dipoles, the solution to Eq. 1.12 varies with azimuth ϕ, as well as radius r and colatitude θ. The radial and angular dependence are separable, and the full solution is given by a summation over all possible degree n and order m. For grains orbiting in the rings around a central mass, contributions from external sources can be disregarded. Therefore only terms in inverse powers of r of the gravitational and magnetic potentials due to the internal sources of the mass and planetary dynamo are required (e.g. Connerney 1993; Wieczorek 2015):

$$\Phi_g = -\frac{GM_p}{R_p}\sum_{n=0}^{\infty}\left(\frac{R_p}{r}\right)^{n+1}\sum_{m=0}^{n} Y_n^m(\theta,\phi)_g, \tag{1.13}$$

$$\Phi_B = R_p\sum_{n=1}^{\infty}\left(\frac{R_p}{r}\right)^{n+1}\sum_{m=0}^{n} Y_n^m(\theta,\phi)_B. \tag{1.14}$$

The spherical harmonic functions for each of the fields are

$$Y_n^m(\theta,\phi)_g = [\bar{c}_n^m \cos m\phi + \bar{s}_n^m \sin m\phi]\bar{P}_n^m(\cos\theta), \tag{1.15}$$

$$Y_n^m(\theta,\phi)_B = [\bar{g}_n^m \cos m\phi + \bar{h}_n^m \sin m\phi]\bar{P}_n^m(\cos\theta), \tag{1.16}$$

and are expressed in terms of the associated Legendre polynomials, $P_n^m(\cos\theta)$, and the $c_n^m, s_n^m, g_n^m, h_n^m$ coefficients which characterise the respective fields and have different normalisations, with a bar above a given variable referring to its normalised form. The first few spherical harmonics are illustrated in Figure 1.21. The geomagnetic convention, used here, is to apply Schmidt quasi-normalisation:

$$\bar{P}_n^m(\cos\theta) = \sqrt{(2-\delta_m^0)\frac{(n-m)!}{(n+m)!}}P_n^m(\cos\theta), \tag{1.17}$$

which leaves the sum $\sum_{m=0}^{n}[(\bar{g}_n^m)^2+(\bar{h}_n^m)^2]$ invariant under an arbitrary rotation of the magnetic field. Table 1.3 gives the first few values of the Schmidt quasi-normalised associated Legendre functions and the unassociated functions.

$P_n(\cos\theta)$	$\bar{P}_n^m(\cos\theta)$
$P_0 = 1$	$P_0^0 = 1$
$P_1 = \cos\theta$	$P_1^0 = \cos\theta$ $P_1^1 = \sin\theta$
$P_2 = \frac{3}{2}(\cos^2\theta - \frac{1}{3})$	$P_2^0 = \frac{3}{2}(\cos^2\theta - \frac{1}{3})$ $P_2^1 = \sqrt{3}\cos\theta\sin\theta$ $P_2^2 = \frac{\sqrt{3}}{2}\sin^2\theta$
$P_3 = \frac{5}{2}\cos\theta(\cos^2\theta - \frac{9}{15})$	$P_3^0 = \frac{5}{2}\cos\theta(\cos^2\theta - \frac{9}{15})$ $P_3^1 = \frac{5\sqrt{3}}{2\sqrt{2}}\sin\theta(\cos^2\theta - \frac{3}{15})$ $P_3^2 = \frac{\sqrt{15}}{2}\cos\theta\sin^2\theta$ $P_3^3 = \frac{\sqrt{5}}{2\sqrt{2}}\sin^3\theta$

Table 1.3: Legendre polynomials up to degree-3.

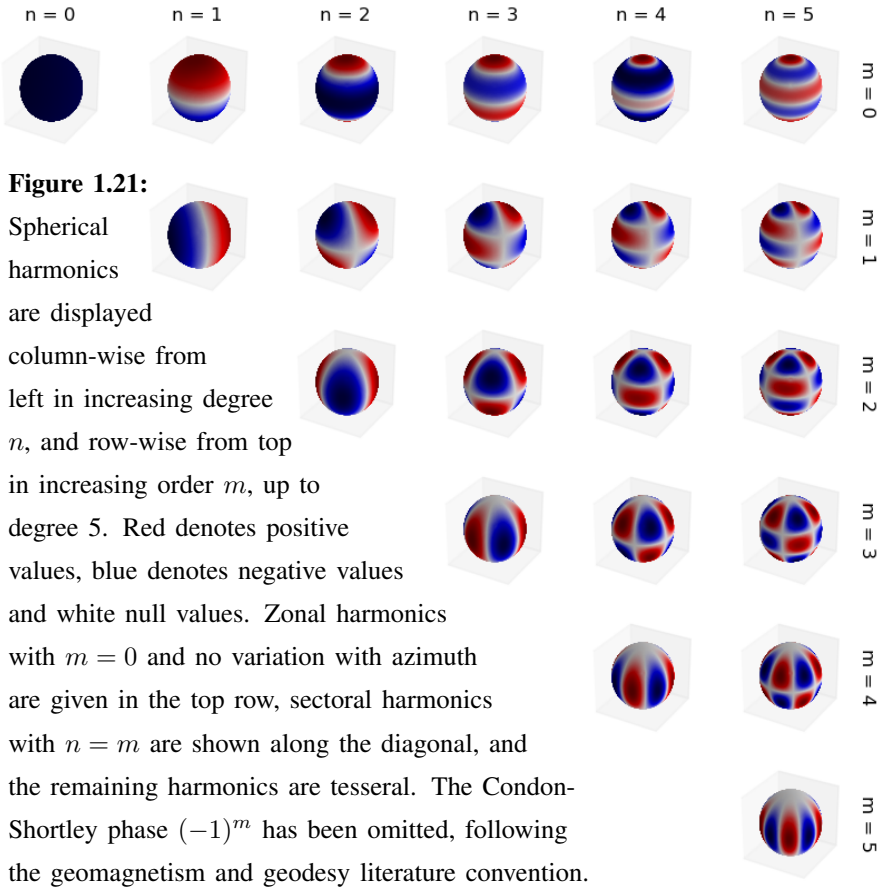

Figure 1.21: Spherical harmonics are displayed column-wise from left in increasing degree n, and row-wise from top in increasing order m, up to degree 5. Red denotes positive values, blue denotes negative values and white null values. Zonal harmonics with $m = 0$ and no variation with azimuth are given in the top row, sectoral harmonics with $n = m$ are shown along the diagonal, and the remaining harmonics are tesseral. The Condon-Shortley phase $(-1)^m$ has been omitted, following the geomagnetism and geodesy literature convention.

Substituting the spherical harmonic functions, Eq. 1.15, into the potential, Eq. 1.13, and restricting attention to rotationally symmetric cases, such as fast rotating planets, yields

$$\Phi_g = -\frac{GM_p}{r}\sum_{n=0}^{\infty}\left(\frac{R_p}{r}\right)^n P_n(cos\,\theta)\bar{c}_n^0, \tag{1.18}$$

where the gravitational potential is expressed solely using zonal terms, as illustrated by the top row of Figure 1.21. Note for $m = 0$ that the associated Legendre functions reduce to the unassociated polynomials $P_n^0 \triangleq P_n$). Furthermore, there is no physical difference between northern and southern hemispheres ($P_n(\cos\theta)$ is an odd function for odd n, as can be seen in the top row of Figure 1.21), and so only even n are included, so that

$$\Phi_g = -\frac{GM_p}{r}\left[1 - \sum_{n=1}^{\infty} J_{2n}\left(\frac{R_p}{r}\right)^{2n} P_{2n}(\cos\theta)\right], \tag{1.19}$$

where the so-called gravitational moments $J_n \triangleq -\bar{c}_n^0$. For Saturn, the higher order J_{2n} are not significant, e.g. $\frac{J_4}{J_2} \approx 0.05$, and therefore the acceleration ($g_r = -\frac{\partial\Phi_g}{\partial r}, g_\theta = -\frac{1}{r}\frac{\partial\Phi_g}{\partial\theta}, g_\phi = -\frac{1}{r\sin\theta}\frac{\partial\Phi_g}{\partial\phi}$) can be written as

$$\begin{aligned} g_r &= -\frac{GM_p}{r^2}\left[1 - \frac{3}{2}\frac{J_2R_p^2}{r^2}(3\cos^2\theta - 1)\right] \\ g_\theta &= \frac{3GM_pJ_2R_p^2}{r^4}\cos\theta\sin\theta \\ g_\phi &= 0. \end{aligned} \tag{1.20}$$

The J_2 coefficient, known as the *dynamical form factor* or *ellipticity coefficient*, describes the oblateness of the planet. Including it in the planet's gravitational field accounts for the effect of the equatorial bulge, so that for a grain in orbit around the planet there is a reduced gravitational acceleration over the poles ($\theta = 0, \pi$) compared to the equator ($\theta = \frac{\pi}{2}$). Saturn is the most oblate planet in our solar system, with a flattening (the ratio of the difference between the polar and equatorial radii to the equatorial radius) of 9.8% (Cao et al. 2019).

The components of gravity in spherical coordinates, Eq. 1.20, can be expressed in the planet-centred inertial frame using

$$\begin{bmatrix} g_x \\ g_y \\ g_z \end{bmatrix} = \begin{bmatrix} \sin\theta\cos\phi & \cos\theta\cos\phi & -\sin\phi \\ \sin\theta\sin\phi & \cos\theta\sin\phi & \cos\phi \\ \cos\theta & -\sin\theta & 0 \end{bmatrix} \begin{bmatrix} g_r \\ g_\theta \\ g_\phi \end{bmatrix}, \tag{1.21}$$

so that

$$\vec{g} = -\frac{GM_p}{r^3}\left[x\hat{x} + y\hat{y} + z\hat{z} + \frac{3}{2}J_2\left(\frac{R_p}{r}\right)^2\left[\left(1 - 5\frac{z^2}{r^2}\right)(x\hat{x} + y\hat{y}) + \left(3 - 5\frac{z^2}{r^2}\right)z\hat{z}\right]\right]. \tag{1.22}$$

Substituting the spherical harmonic functions from Eq. 1.16 into Eq. 1.14 yields the magnetic potential:

$$\Phi_B = R_p\sum_{n=1}^{\infty}\left(\frac{R_p}{r}\right)^{n+1}\sum_{m=0}^{n}[\bar{g}_n^m\cos m\phi + \bar{h}_n^m\sin m\phi]\bar{P}_n^m(\cos\theta). \tag{1.23}$$

The magnetic field terms are obtained by applying Eq. 1.11, so that

$$\begin{aligned} B_r &= -\frac{\partial\Phi_B}{\partial r} = \sum_{n=1}^{\infty}(n+1)\left(\frac{R_p}{r}\right)^{n+2}\sum_{m=0}^{n}[g_n^m\cos m\phi + h_n^m\sin m\phi]\bar{P}_n^m(\cos\theta), \\ B_\theta &= -\frac{1}{r}\frac{\partial\Phi_B}{\partial\theta} = -\sum_{n=1}^{\infty}\left(\frac{R_p}{r}\right)^{n+2}\sum_{m=0}^{n}[g_n^m\cos m\phi + h_n^m\sin m\phi]\frac{\mathrm{d}\bar{P}_n^m(\cos\theta)}{\mathrm{d}\theta}, \\ B_\phi &= -\frac{1}{r\sin\theta}\frac{\partial\Phi_B}{\partial\phi} = \frac{1}{\sin\theta}\sum_{n=1}^{\infty}\left(\frac{R_p}{r}\right)^{n+2}\sum_{m=0}^{n}m[g_n^m\sin m\phi - h_n^m\cos m\phi]\bar{P}_n^m(\cos\theta). \end{aligned} \tag{1.24}$$

Pioneer 11 measurements of Saturn's intrinsic field found it to be very nearly aligned with its rotational axis (Smith et al. 1980; Acuña & Ness 1980), subsequent measurements by *Voyager 1* and *2* found similar close alignment (Ness et al. 1981, 1982), and more recently this has been attested by *Cassini* data (Dougherty et al. 2018). An aligned centred dipole ($n = 1$) is the simplest physical case for a planetary magnetic field. This can be expressed (e.g. Connerney 1993; Jontof-Hutter 2012) as

$$\vec{B}(\vec{r}) = -\frac{\vec{m}}{r^3} + \frac{3(\vec{m}\cdot\vec{r})\vec{r}}{r^5} \equiv \frac{3(\vec{m}\cdot\hat{r})\hat{r} - \vec{m}}{r^3} \tag{1.25}$$

where $|\vec{m}| = g_1^0 R^3$ is the scalar strength of the planetary dipole moment at the equator. The magnetic field components are obtained using Eq. 1.24:

$$B_r = 2\frac{|\vec{m}|}{r^3}\cos\theta, \tag{1.26}$$

$$B_\theta = \frac{|\vec{m}|}{r^3}\sin\theta, \tag{1.27}$$

$$B_\phi = 0. \tag{1.28}$$

The change-of-basis matrix can be used to convert to Cartesian coordinates for simulation purposes, so that

$$\begin{aligned} B_x &= \frac{3|\vec{m}|xz}{r^5}, \\ B_y &= \frac{3|\vec{m}|yz}{r^5}, \\ B_z &= \frac{|\vec{m}|(3z^2 - r^2)}{r^5}, \end{aligned} \tag{1.29}$$

Connerney et al. (1982) found that the so-called Z_3 model – zonal harmonic model of degree 3 – was sufficient to describe Saturn's field as measured by *Voyager 1* and *2*. The components of such a field, with axisymmetric dipole, quadrupole and octupole magnetic moment contributions (g_1^0, g_2^0 & g_3^0 respectively) derived from Eq. 1.24 and transformed into Cartesian coordinates are

$$\begin{aligned} B_x &= 3g_1^0\frac{R_p^3}{r^5}xz + g_2^0\frac{R_p^4}{r^4}\left[\frac{15z^2x}{2r^3} - \frac{3x}{2r}\right] + g_3^0\frac{R_p^5}{r^5}\left[\frac{35z^3x}{2r^4} - \frac{15xz}{2r^2}\right], \\ B_y &= 3g_1^0\frac{R_p^3}{r^5}yz + g_2^0\frac{R_p^4}{r^4}\left[\frac{15z^2y}{2r^3} - \frac{3y}{2r}\right] + g_3^0\frac{R_p^5}{r^5}\left[\frac{35z^3y}{2r^4} - \frac{15yz}{2r^2}\right], \\ B_z &= g_1^0\frac{R_p^3}{r^5}(3z^2 - r^2) + g_2^0\frac{R_p^4}{r^4}\left[\frac{15z^3y}{2r^3} - \frac{9z}{2r}\right] + g_3^0\frac{R_p^5}{r^5}\left[\frac{35z^4}{r^4} - \frac{15z^2}{r^2} + \frac{3}{2}\right]. \end{aligned} \tag{1.30}$$

The dipole field described by Eq. 1.30 has a small but non-negligible vertical offset. This distance can be calculated by finding the location where $\vec{B}$ points solely along the $\hat{z}$ direction in

the equatorial plane, that is setting Eq. 1.30's $B_x = B_y = 0$:

$$\frac{z}{R_p} = \frac{g_2^0}{2g_1^0}, \tag{1.31}$$

where the weaker g_3^0 coefficient has been ignored in the analytic calculation. Dougherty et al. (2018) find the northward offset of Saturn's magnetic equator from the planetary equator is $2808\,\mathrm{km}$. The relevant Legendre functions of the offset dipole model can be found in Table 1.3, with $n = 1, 2, 3, m = 0$. More recent work since have refined the coefficients, and a comparison is presented in Tables 1.4 and 1.5.

	Connerney et al. (1982)		Cao et al. (2011)
R_p (km)	$60,000$	$60,268$	$60,268$
g_1^0	21535	21248	21191
g_2^0	1642	1613	1586
g_3^0	2743	2683	2374

Table 1.4: Some literature values of Gauss-Schmidt quasi-normalised spherical harmonic coefficients in nT for Saturn's Z_3 model. The fits of Connerney et al. (1982) originally used $R_p = 60,000$ km (left column) and were transformed by Cao et al. (2011) to use $R_p = 60,268$ km for direct comparison (middle column). The h_n^0 coefficients do not exist, because in those cases $\sin m\phi = 0$ in Eq. 1.24 and those terms do not contribute.

For Saturn, there is a measurable vertical offset in the field, but negligible tilt (with an upper limit of $\sim 0.007°$, as revealed by the *Cassini Grand Finale* measurements (Cao et al. 2019)). The nearly-perfect axisymmetry of Saturn's dipole is disconcerting because Cowling's antidynamo theorem states that no axisymmetric magnetic field can be sustained by a dynamo (Cowling 1933). Stevenson (1982) proposed a mechanism that can resolve this conflict and axisymmetrise the observed field outside Saturn's dynamo region. 3D numerical models based on this theory have resulted in more symmetric fields (Christensen & Wicht 2008; Stanley 2010; Stanley & Bloxham 2016). In order to reproduce the stability maps of Jontof-Hutter (2012)'s Figures 3.13 and 4.12 for Saturn's aligned dipole and Z_3 magnetic fields, the values of $g_{1,2,3}^0$ of Connerney et al. (1982) with $R_p = 60,000$ km were used (given in Table 1.4). The more recent *Cassini* measurement of $g_1^0 = 0.21141$ Gauss obtained from its *Grand Finale* data (Cao et al. 2019) does not differ significantly to the value used by Jontof-Hutter (2012).

Another field term of significance to consider is the corotational electric field due to the rotating

	Dougherty et al. (2018)	Cao et al. (2019)
g_1^0	21140	21141
g_2^0	1581	1583
g_3^0	2260	2262
g_4^0	91	95
g_5^0	12.6	10.3
g_6^0	17.2	17.4
g_7^0	−59.6	−68.8
g_8^0	−10.5	−15.5
g_9^0	−12.9	−24.2
g_{10}^0	15	9.0
g_{11}^0	18	11.3
g_{12}^0	–	−2.8
g_{13}^0	–	−2.4
g_{14}^0	–	−0.8

Table 1.5: As Table 1.4, but the latest *Cassini* results which include Gauss coefficients up to degree 11 and 14 ($R_S = 60,268\,\mathrm{km}$). Reproduced from Cao et al. (2019).

magnetic field in the plasma environment. This has been observed via the charged dust streams reported in e.g. Horányi (2000). Bunce et al. (2003) state that the *Voyager* plasma data at Saturn suggests that the plasma angular velocity at inner radii declines from almost rigid corotation with the planet to sub-corotation values in outer regions. As the main ring region is the focus here, it can be assumed that the plasma is corotating with the planet and any difference from Ω_p can be neglected. It should be noted that there is no electric field directly induced by a 'moving' uniform magnetic field, but there is an electric field associated with a moving plasma. Therefore, even in Saturn's case with its dipole aligned along its spin axis, there is a corotational electric field.

Beginning with the generalised form of Ohm's law,

$$\vec{j} = \sigma(\vec{E} + \vec{v}_p \times \vec{B}), \tag{1.32}$$

where $\vec{j}$ is the current density, and $\vec{v}_p$ is the velocity of the plasma. Given that the conductivity,

σ, is high in a plasma, then Eq. 1.32 states

$$\vec{E} = -(\vec{v}_p \times \vec{B}). \tag{1.33}$$

That is, in a frame where the plasma is moving, there is an electric field. In the corotating frame (denoted by $'$), the electric field vanishes, as can be seen by the (non-relativistic limit of) the transformation equation:

$$\vec{E}' = E + \vec{v}_p \times \vec{B}, \tag{1.34}$$

and substituting Eq. 1.37 into Eq. 1.34 gives $\vec{E}' = 0$ (noting that a frame rotating about the planet-centred frame can be treated as two *instantaneously* inertial frames and therefore the Lorentz transformation of the field can be applied). This is consistent with the plasma moving at the $\vec{E} \times \vec{B}$ drift velocity (§3.4.2):

$$\vec{v}_E = \frac{\vec{E} \times \vec{B}}{B^2}, \tag{1.35}$$

as substituting Eq. 1.35 into Eq. 1.34 and using the vector triple product gives

$$\vec{E}' = \vec{E} + \frac{1}{B^2}[-B^2\vec{E} + (\vec{B} \cdot \vec{E})\vec{B}] = 0. \tag{1.36}$$

The result of Eq. 1.36 holds as $\vec{E} \cdot \vec{B} = 0$: the conductivity along magnetic field lines is large as charges flow easily in that direction, so that $\vec{B}$ field lines can be considered as electric equipotentials. In the frame corotating with the plasma, which is rotating rigidly with the planet, the corotational electric can thus be written as

$$\vec{E} = -(\vec{\Omega}_p \times \vec{r}) \times \vec{B}, \tag{1.37}$$

and is directed radially outward. Equation 1.37 encapsulates the equivalence of a rotating magnetic field in an inertial frame with a radial electric field and stationary magnetic field in the rotating frame.

1.3.2 Comparison to Other Forces on Circumplanetary Dust

In addition to the planetary gravitational and electromagnetic forces described in §1.3.1, by Equations 1.22, 1.30 and 1.37, there are several other forces acting on the grain to consider in turn: gravity of satellites, radiation forces (pressure and Poynting-Robertson drag), and plasma drag (e.g. Grün et al. 2006). The gravitational forces exerted by the moons on dust grains has been excluded from this work, on the basis that the region of study is restricted to the main rings, and only small moons orbit within the Roche Limit.

Dust in circumplanetary space is affected by forces due to incident solar radiation; having large surface-area-to-mass ratios means that the absorption, emission or scattering of photons by the grains can be significant. Grains are repelled from the Sun by radiation pressure due to the momentum carried by solar photons (e.g. Burns et al. 1979). The radiation pressure force can be written as

$$\vec{F}_{\text{RP}} = -\beta \frac{GM_{\odot}}{r_{\text{sp}}} \hat{s}, \tag{1.38}$$

where r_{sp} is the Sun-planet distance, $\hat{s}$ is a unit vector pointing from the planet to the Sun and β is the dimensionless ratio of the radiation force to the gravitational force of the Sun (with mass $M_{\odot}$ and luminosity $L_{\odot}$), which can be written as

$$\beta = \frac{3L_{\odot}}{16\pi GM_{\odot}c} \frac{Q_{\text{pr}}}{\rho_d a_d}, \tag{1.39}$$

where Q_{pr} is a dimensionless coefficient representing the radiation pressure efficiency factor, and ρ_d, a_d are the grain's density and radius respectively (Burns et al. 1979; Mignard 1984). The radiation pressure force exerted is radial with an intensity that goes according to the solar flux, which drops off quadratically with distance. Therefore, in the vicinity of a planet, the solar radiation pressure is approximately constant in magnitude, but the direction varies slowly during the planet's orbit around the Sun (Burns et al. 2001). The forces described thus far are plotted in Figure 1.22.

Given that Saturn's orbital period is about thirty years, but the relevant dynamical timescales are < 0.1 years (Jontof-Hutter 2012), the solar radiation pressure has been omitted as it is a

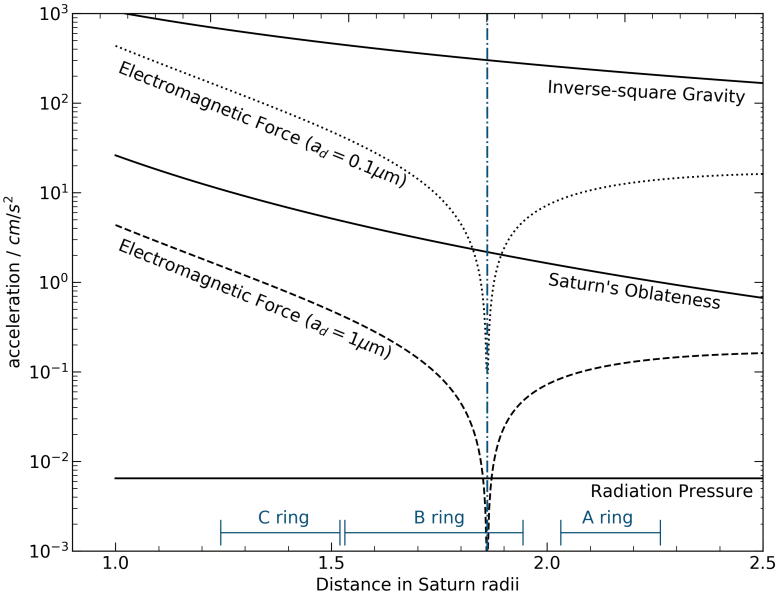

Figure 1.22: Following the example of Burns et al. (2001), a comparison of the relevant forces around Saturn for a dust grain charged to -5 V are plotted: the gravitational pull of Saturn (both spherical and oblate terms), the Lorentz force for different-sized grains, and the radiation pressure force. The radiation pressure force is plotted for a totally absorbing ($\beta = 1$) grain. The radial distance over which the forces are calculated has been restricted to the main rings, which extend out to $\sim 2.3\,R_S$ and the range of grain sizes has been expanded to include sub-micron dust (nanograins are subject to stochastic charging and therefore have been omitted, refer to Chapter 4 for further details). The synchronous orbit location, R_{syn}, is shown by the vertical dash-dot line.

relatively slowly varying modulation on top of the other stronger forces on the grain. The dust particles' orbital periods are much shorter than that of the planet and so the solar direction can be assumed to be constant. Moreover, for grains less than a tenth of a micron, the ratio of the solar radiation force to the solar gravitational force, β, drops sharply (Mignard 1984) as shown by the Mie scattering calculations of Burns et al. (1979), Figure 1.23.

Poynting - Robertson drag, which arises from a drop in the grain's angular momentum due to the subsequent anisotropic re-radiation of the incident solar energy when viewed from the solar frame of reference, acts tangentially and causes dust particles to fall inward (Burns et al. 1979, 2014). Hamilton (1993) states that it is small compared to the radiation pressure and can usually be neglected in a first approximation. This is the approach taken here, noting also that the

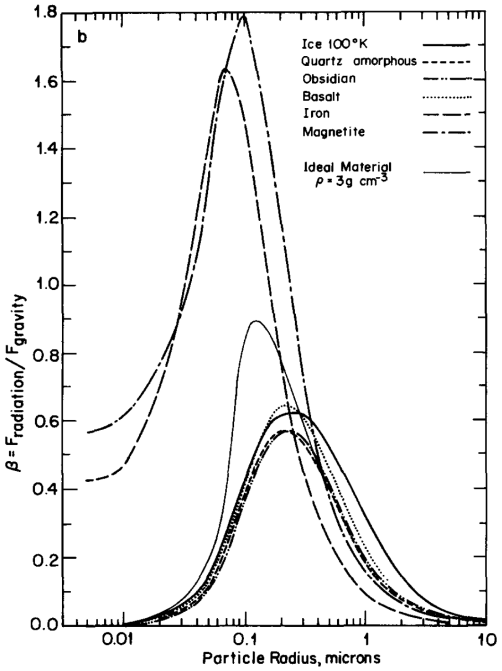

Figure 1.23: The ratio of solar radiation pressure force to gravitational force, β, as a function of particle radius, a_d for six cosmically significant substances and an ideal material. Very small grains are unaffected by the solar radiation pressure because the relatively long wavelength cannot cause much absorption or scattering, due to its low energy. Image credit: Burns et al. (1979, Fig. 7b)

timescale for a 1-micron grain orbiting at $1.8\,R_S$ around Saturn is $\sim 10^5$ years , which is much larger than the orbital timescales considered here.

As dust travels through a plasma (refer to Chapter 4), the grains exchange momentum with the ions and electrons and a drag is exerted on the dust (e.g. Grün 1984). As with any drag force, it is a function of velocity; here, the relative velocity of the grain with respect to the corotating plasma: $\sim \sqrt{\frac{GM_p}{r}} - r\Omega_p$. The effects of plasma drag on the orbital elements of grains have been studied in detail by, for example, Grün et al. (1984), Northrop & Birmingham (1990) and Havnes et al. (1992b). Essentially, the eccentricities and inclinations are damped and the grains take on the circular and uninclined orbits of the impacting plasma particles. Grains inside synchronous distance orbit faster than the plasma, and lose energy via collisions with the slower particles and therefore spiral into the planet, whereas grains outside synchronous distance orbit slower than the plasma, gaining energy via collisions and therefore drift away from the planet. The orbital evolution timescale, which is approximately proportional to grain radius, for a 1-micron grain at

1.8 R_p from Saturn is $\sim 10^{5\pm1}$ years (Burns et al. 2001). As in the case of Poynting-Robertson drag, this is orders of magnitude longer than the timescales over which the dust grains are studied here (refer to Chapters 3, 4, 5) and therefore the effects of plasma drag are ignored. Hamilton & Krivov (1996) also ignore slowly acting forces such as plasma drag and Poynting-Robertson drag, stating that their typical grain lifetimes are $\lesssim 1000$ years. Outside of the main rings of study in this work, plasma drag has been instrumental in outward dust transport from Enceladus (e.g. Havnes et al. 1992b; Horányi et al. 2008), pictured in Figure 1.24.

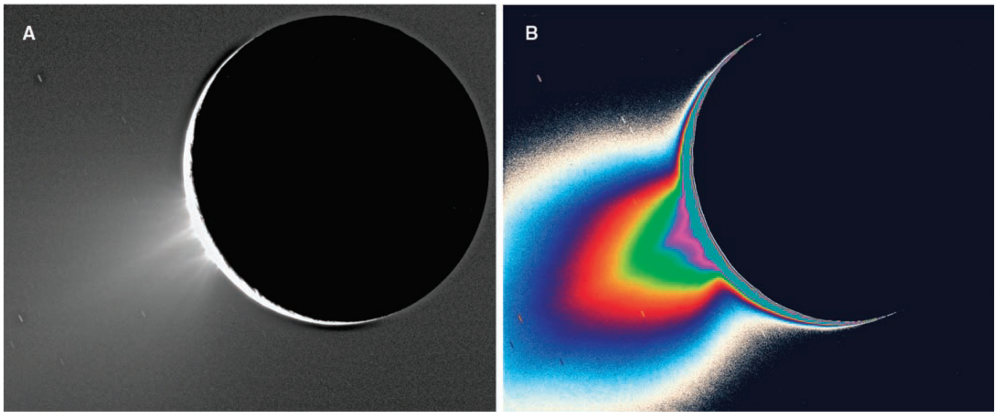

Figure 1.24: Geysers on the geologically active south polar region (lower left) of Enceladus provide most of the dusty E ring's material. Plasma drag is responsible for grains reaching the outskirts of Saturn's magnetosphere, as modelled by Horányi et al. (2008). (A) Clear-filter image of Enceladus' plumes, and (B) a colour-coded version to enhance visibility of fainter components. Image credit: Porco et al. (2006, Fig. 6).

As well as the plasma drag caused by direct collisions between plasma particles and dust grains, there is also a Coulomb drag due to the electrostatic forces exerted between the charged particles. Northrop & Birmingham (1990) studied Coulomb drag in detail, noting that it had previously been calculated for a test charge moving in a plasma (ignoring collective effects) by analogy to Chandrasekhar's gravitational *dynamical friction* on a star moving though a Maxwellian distribution of background stars (Spitzer 1962; Draine & Salpeter 1979), which they generalise to include large scattering angles and collective effects. Grün et al. (1984) and Morfill et al. (1980) find that distant Coulomb interactions increase the plasma drag force for subsonic grains in charge equilibrium with the plasma by a factor in the range $\sim 10-100$ (depending on plasma conditions for sub-micron – micron-sized grains), and therefore the momentum loss time due to plasma drag is decreased by an order or two in magnitude, which is still much larger than the orbital timescales of study in this work.

The drag forces described above, cause slow monotonic changes in the orbital semimajor axes, eccentricities and inclinations of dust (Burns 1991) through secular changes in the orbital energy and angular momentum of the grains, but can be largely ignored because of their weaker strength and longer timescales (Burns et al. 2001) than the gravitational and electromagnetic forces due to the planet. For times of less than tens of years considered here, it is legitimate to follow the approach of Hamilton (1993) and ignore these weak forces.

Atmospheric drag arises in an analogous fashion to plasma drag, but instead of collisions with plasma particles, the atmospheric drag of grains is due to collisions with neutral molecules or atoms in the atmosphere and exosphere of the planet. As with plasma drag, atmospheric drag is approximately proportional to grain radius but also depends strongly on the distance from the planet as the density and temperature profile varies with altitude (Burns et al. 2001). Broadfoot et al. (1986) studied the exosphere of Uranus and found that atmospheric drag plays an important role in rapidly depleting the inner Uranian ring system of small particles. Due to Broadfoot et al. (1986, 1989)'s findings of high temperatures in the outer atmospheres of Uranus and Neptune, it was thought that atmospheric gases could extend to significant altitudes for all giant planets and therefore gas drag may be relevant for the inner parts of their ring systems, including Saturn's. However, Uranus has an unusually bloated exosphere, extending several Uranian radii (Herbert & Sandel 1999). Perry et al. (2018) note that Saturn's tenuous exosphere only extends to the inner edge of the D ring, with Mitchell et al. (2018) showing, through simulations of collisions between dust and the H, H_2 exospheric populations and in situ measurements with *MIMI* during *Cassini's Grand Finale* orbits, that dust is precipitating onto Saturn from the inner D ring through atmospheric drag. In this thesis, a full atmospheric model (Koskinen et al. 2015; Mitchell et al. 2018) will not be employed, as the resulting chemical reactions are beyond the scope of this work.

As Hamilton & Krivov (1996) state, in many applications a single perturbation dominates and the orbital dynamics can be well approximated by neglecting the weaker forces, an approach taken here by neglecting radiation pressure, plasma drag, Coulomb drag, Poynting-Robertson drag, and atmospheric drag. In addition to the simplifications with regard to forces described above, the question arises of whether collective effects, in the sense both of inter-grain collisions and of the dusty plasma, need to be considered. In regions of significant dust density, the charge on a dust grain can be reduced compared to an isolated grain in the same plasma environment

(e.g Goertz & Ip 1984; Havnes et al. 1984). As described in Chapter 4, an orbital motion theory approach is taken in this work, in which the dust in plasma can be treated as isolated grains because their radius, a_d, is much smaller than the Debye length, λ_D, which is smaller than the average intergrain distance:

$$a_d \ll \lambda_\mathrm{D} < \lambda_\mathrm{mfp}, \tag{1.40}$$

where λ_mfp is the collisional mean free path of the dust grains. The Debye length for an electron plasma with number density n_e and temperature T_e is

$$\lambda_\mathrm{D} = \sqrt{\frac{\epsilon_0 k_\mathrm{B} T_e}{e^2 n_e}}, \tag{1.41}$$

where $e = 1.602\cdots\times10^{-19}\,C$, $\epsilon_0 = 8.854\cdots\times10^{-12}\,\mathrm{C^2\,N^{-1}\,m^{-2}}$ and $k_\mathrm{B} = 1.380\cdots\times10^{-23}\,\mathrm{J\,K^{-1}}$. Substituting in some example values for the plasma parameters in the vicinity of the main rings from Hsu et al. (2018b) gives $\lambda_\mathrm{D} \sim 10\,\mathrm{m}$. If a representative value (or at least an upper or lower bound) for the collisional mean free path of the dust grains present in the main rings can be taken from the F ring's population of submicron – micron grains, which Mendis et al. (1982) estimates to be $\sim 10^3\,\mathrm{m}$, based on optical depth observations, then the condition for isolated dust grains (1.40) holds. More recently, Hsu et al. (2018b) have made in situ measurements of dust between the D ring and Saturn's atmosphere using the *MA* instrument and the *HRD* foil detector (p. xxv) on-board *Cassini*. These gave a nanograin number density of $3.5 - 8.5\times10^{-2}\,\mathrm{m^{-3}}$ and a submicron-grain number density of $(2\pm1)\times10^{-4}\,\mathrm{m^{-3}}$, which corresponds to $\lambda_\mathrm{mfp} \sim \frac{1}{n\pi a_d^2} \approx 10^{15} - 10^{17}\,\mathrm{m}$, which readily upholds the condition of Eq. 1.40. So following the orbital evolutions of single test grains, as they do not interact but are effectively shielded from each other, seems to be a legitimate approach, and in fact one used by numerous authors (e.g. Mendis et al. 1982; Northrop & Morfill 1984; Hsu et al. 2011; Jontof-Hutter & Hamilton 2012b).

The dynamics of dust in a planetary ring system embedded in a magnetosphere, subject to the solar wind, impacts and varying plasma conditions (temperature, composition and density), is complex. Each grain will be sensitively influenced by its material composition, (irregular) shape, density, strength, conductivity, reflectivity etc., characteristics which are not constant in time but subject to change by sublimation, sputtering and shattering. Although certainly important for

dust, the direct interaction with a spatially- and temporally-variable plasma environment will not be investigated because a detailed plasma model is beyond the scope of this project. In addition, the plasma environment affects the charging of the grain and therefore sensitively affects the grain's dynamics (Chapters 4, 5), and so rather than enforcing a set of finely-tuned assumptions onto the plasma environment, instead a focus in this work is on the forces which dominate over the timescales of interest based on representative plasma values.

Having described physical processes of importance for dust in the main rings of Saturn and the circumplanetary environment, and introduced concepts of relevance through the example of charged dust phenomena and identified several open questions, work can proceed in the following manner. In the next chapter, the numerical method used to integrate the equations of motion is described and tested, then in Chapter 3 the characteristic motions of charged grains are described and the stability of circumplanetary dust with constant charge is studied, both numerically and analytically. In Chapter 4, the assumption of constant charge is relaxed and time-variable charging algorithms are described and analysed. Chapter 5 returns to the questions raised by ring rain.

2

Numerical Methods

In order to follow the trajectories of charged dust grains in a planet's gravitational and magnetic fields, the equations of motion are solved numerically, as even for a dipole field the problem is not analytically integrable and the epicyclic approximation (§3.4.1) does not hold for all q_d/m_d, namely grains exhibiting large radial excursions (§3.5.1). This requires solving an initial value problem (IVP):

$$\dot{\vec{X}}(t) = f(t, \vec{X}), \quad \vec{X}_0 = \begin{pmatrix} \vec{r}(t_0) \\ \dot{\vec{r}}(t_0) \end{pmatrix}, \tag{2.1}$$

where $\vec{X} = \begin{pmatrix} \vec{r}(t) \\ \dot{\vec{r}}(t) \end{pmatrix}$ is the solution sought, given some function f and the initial conditions $\vec{X}_0$.

Initially an approach using an existing N-body code, PKDGRAV, is described. The symplectic nature of this leapfrog integrator is broken through the addition of a velocity-dependant force and therefore a higher-order approach is adopted in the form of adaptive Runge-Kutta and Bulirsch-Stoer methods.

2.1 Parallel k-Dimensional Tree Gravity Integrator

The Parallel k-Dimensional Tree Gravity code (PKDGRAV) is an N-body code that is used in multiple astrophysical situations, including planet formation, granular dynamics and rubble-pile disruptions. PKDGRAV is a parallelised N-body code (Richardson et al. 2000; Stadel 2001), which uses a second order leapfrog integrator for temporal evolution and a binary tree partitioning method with multipole expansion, similar to the oct-tree in the Barnes-Hut algorithm (Barnes & Hut 1986), to calculate inter-particle gravity.

The leapfrog integrator updates the positions and velocities by employing an operator splitting technique that permits the construction of a symplectic integrator (Saha & Tremaine 1992), that is, an integrator which enforces certain conservation laws characteristic of Hamiltonian dynamics (Sanz-Serna 1992). It uses the *Kick Drift Kick* formalism (which is more efficient than the equivalent *Drift Kick Drift* method within a multistepping code) that kicks the velocities forward for a half-step $\left(\frac{h}{2}\right)$ while the positions are fixed under the potential energy component of the Hamiltonian, drifts the positions forward for a step (h) while the velocities are held constant under the kinetic energy component of the Hamiltonian, then kicks the velocities forward for a half-step. More formally, the kick operator (that evolves the system under the potential generating the accelerations), K, and the drift operator (that evolves the system under kinetic energy), D, are combined $K(\frac{h}{2})D(h)K(\frac{h}{2})$ to advance the system by a full step:

$$\dot{\vec{r}}_{n+\frac{1}{2}} = \dot{\vec{r}}_n + \frac{h}{2}\ddot{\vec{r}}(\vec{r}_n), \tag{2.2a}$$

$$\vec{r}_{n+1} = \vec{r}_n + h\dot{\vec{r}}_{n+\frac{1}{2}}, \tag{2.2b}$$

$$\dot{\vec{r}}_{n+1} = \dot{\vec{r}}_{n+\frac{1}{2}} + \frac{h}{2}\ddot{\vec{r}}(\vec{r}_{n+1}). \tag{2.2c}$$

For a grain on its n^{th} timestep, the initial half-step kick of 2.2a updates the velocity given the acceleration evaluated at the start of the step, using $\vec{r}_n$. This is followed by evolving the grain's position according to the updated velocity, expressed in 2.2b. The velocity is then evolved to the end of the timestep, that is the start of the next step, $n+1$, using the just-updated velocity and acceleration, $\dot{\vec{r}}_{n+\frac{1}{2}}$ and $\ddot{\vec{r}}(\vec{r}_{n+1})$ by 2.2c.

The hierarchical tree algorithm used in PKDGRAV reduces computational expense by approximating the gravitational forces that N particles exert on each other in a system. A naïve direct summation force approach is $\mathcal{O}(N^2)$. The k-D tree algorithm approach, described in detail in Richardson (1993b) and Stadel (2001), which is similar to the Barnes-Hut algorithm of $\mathcal{O}(N \log N)$, places particles in a tree-like hierarchy of cells and replaces the direct forces with a multipole expansion (up to hexadecapole order) about the centre of mass for those cells which are small enough or far enough away from the particle in question. A simplified 2-D quad-tree example is sketched in Figure 2.1.

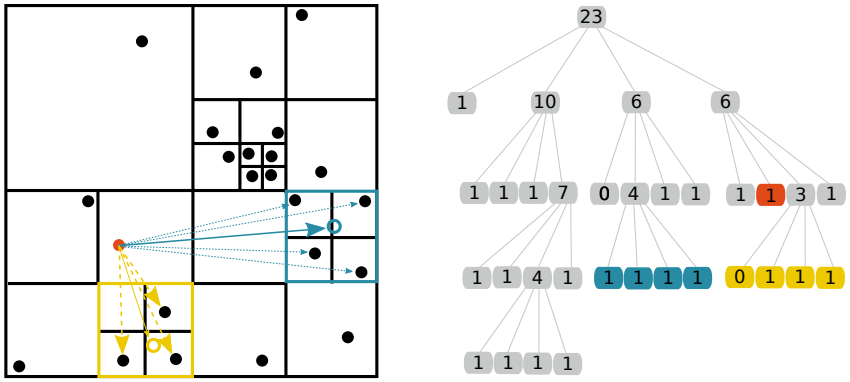

Figure 2.1: Sketch of a simple system of particles for illustrative purposes: a distribution of 23 particles in a box on the left, with its 2D quad-tree representation on the right. The full domain is divided and the number of particles in each quadrant is placed at the next level (the tree is populated starting from the left upper quadrant and proceeding clockwise). This process advances for each quadrant: it is divided into subquadrants if there is more than one particle contained, and force calculations are carried out according to the prescription detailed in the main text of this section. The dashed arrows indicate direct particle-particle force calculations, the solid arrows indicate centre-of-mass approximations. The yellow cell is opened whilst the blue is not (the larger arrows indicate the force calculations that *are* carried out based on whether or not the cell is opened).

In order to estimate the interparticle gravitational forces, PKDGRAV traverses the tree of particles in cells and checks whether each cell needs to be *opened* or not, if the cell is opened then the cell's children are added to the interaction list. This is illustrated in the simplified example of Figure 2.1: during the force calculation of the red particle (the source of the arrows), the tree algorithm will check whether the yellow cell's centre of gravity (open yellow circle) is sufficiently far away. As it is not, the code proceeds to look at all subcells and performs the individual force calculations marked by the (larger) dashed yellow arrows. When the algorithm considers the blue cell, however, it finds that this cell is far enough away and will therefore only perform one

centre-of-mass force calculation (larger solid blue arrow) and will not calculate deeper into this cell (dashed blue arrows). I later use an analogous tree-like structure, although temporal rather than spatial, when designing an algorithm for time-variable charging (Chapter 4).

2.1.1 Local Shearing Patch Simulations

To use PKDGRAV to study inter-particle forces in ring systems, it is necessary to restrict the computational volume to a smaller region (patch), where realistic surface densities can be modelled within a tractable timeframe. The local patch code was developed separately, based on the local planetary ring simulations by Wisdom & Tremaine (1988), and known as `box_tree` (Richardson 1993a, 1994), before being integrated into PKDGRAV, which was originally a cosmological code. `box_tree` incorporates a fourth-order force polynomial integration method with individual time-steps for close encounters based on a technique by Aarseth et al. (1985) and a full hierarchical tree algorithm (cf. Barnes & Hut 1986) to deal with inter-particle gravitational interactions.

The local shearing patch model is built upon the premise that a ring is self-similar azimuthally and the patch size is much smaller than the orbital distance (so that there is no curvature) but much larger than the radial mean free path of the particles (so that collisional dynamics can be followed). In the following, the discussion is restricted to Saturn and therefore $\Omega_p \rightarrow \Omega_\mathrm{S}$. For Saturn's rings there is no risk of violating these assumptions, since typical particle sizes are in the range $1\mathrm{cm} - 1\mathrm{m}$ (Marouf et al. 1983) compared to an average orbital distance of $10^8\,\mathrm{m}$ for the main rings and the particles are densely packed (optical depth $\gtrsim 1$ in B ring), so the radial mean free path is small, $\lesssim$ particle size (Schmidt et al. 2009), and the largest box sizes are just a few km on a side.

A natural coordinate system to use in such a case is one centred on the patch and rotating with it, with v pointing in the direction of motion and u pointing radially outward from Saturn (w in the sense according to the RH rule). It was developed by Julian & Toomre (1966) in the context of disk galaxies and first applied to rings by Wisdom & Tremaine (1988). To avoid unphysical edge–effects the patch is surrounded by replicas, so-called *ghost patches*, to account for the boundary conditions, as illustrated in Figure 2.2.

Particles that leave the patch wrap around to reappear on the other side with the same physical

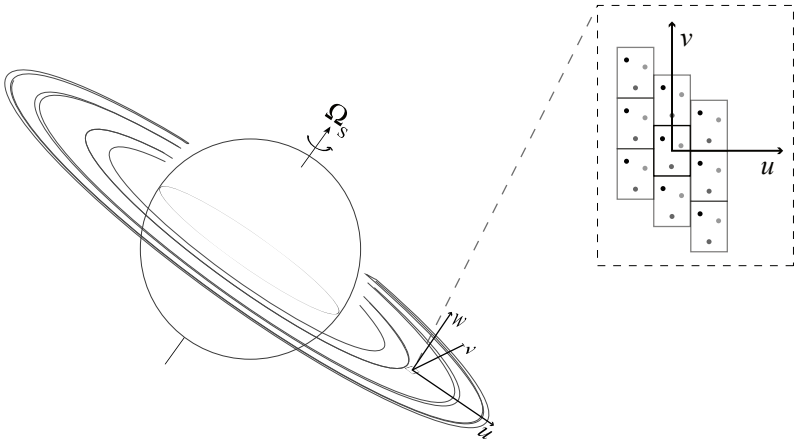

Figure 2.2: Sketch of the shearing patch model. The patch is orbiting the centre of Saturn with an angular velocity of $\Omega_{\rm K}$. The spin of Saturn, Ω_S, and the vertical axis, w, are parallel. Eight ghost patches surround the patch in question.

properties (total number of particles is conserved). If a particle passes through a radial boundary, then it is given an adjusted v-velocity to account for Keplerian shear. Under the conditions just described, it is valid to linearise the equations of motion (as first derived by Hill (1878) in the context of the Earth-Sun-Moon problem), and shown below for completeness, following Richardson (1993b) who provides a derivation in the context of planetesimals orbiting the Sun.

Let $\vec{\mathcal{R}}_i$ denote the relative position vector of a particle expressed in the Saturn-centred inertial frame. Seen in the rotating patch frame (denoted with subscript r), the relative position vector is the same $\vec{\mathcal{R}}_r = \vec{\mathcal{R}}_i = \vec{\mathcal{R}}$ at any given time. A particle will feel the gravitational pull of Saturn, and also the gravitational pull of all the other particles in the patch $\vec{\nabla}\Phi = -(\mathcal{F}_u, \mathcal{F}_v, \mathcal{F}_w)$, which is handled by the tree part of PKDGRAV described above:

$$\ddot{\vec{\mathcal{R}}}_i = \frac{-GM_{\rm S}}{\mathcal{R}^3}\vec{\mathcal{R}} - \vec{\nabla}\Phi. \tag{2.3}$$

The acceleration expressed in the patch frame, $\ddot{\vec{\mathcal{R}}}_r$, will have additional non-inertial terms. In order to obtain $\ddot{\vec{\mathcal{R}}}_r$, apply an operator (Goldstein et al. 2014):

$$\left(\frac{d}{dt}\right)_i = \left(\frac{d}{dt}\right)_r + \vec{\Omega}_{\rm K}\times \ , \tag{2.4}$$

which relates the time rate of change of a quantity in an inertial frame to its counterpart in the rotating frame, twice to $\vec{\mathcal{R}}_i$. Then, assuming a constant $\vec{\Omega}_{\rm K} = \Omega_{\rm K}\hat{w}$, and re-arranging:

$$\ddot{\vec{\mathcal{R}}}_r = \ddot{\vec{\mathcal{R}}}_i - 2(\vec{\Omega}_{\rm K} \times \dot{\vec{\mathcal{R}}}_r) - \vec{\Omega}_{\rm K} \times (\vec{\Omega}_{\rm K} \times \vec{\mathcal{R}}), \tag{2.5}$$

with the additional terms being due to the Coriolis and centrifugal forces. Since it is assumed that the patch is orbiting at a fixed distance $\vec{a}$ (so that $\Omega_{\rm K} = \sqrt{\frac{GM_{\rm S}}{a^3}}$) and that calculations are going to be done *in* the rotating patch, it follows to write $\vec{\mathcal{R}}_r = \vec{a} + \vec{d}$, where $\vec{d} = (u, v, w)$ is relative to the origin of the rotating frame. Standing inside the rotating frame, $\vec{a}$ does not look to change with time and so $\dot{\vec{\mathcal{R}}}_r = \dot{\vec{d}}$ and $\ddot{\vec{\mathcal{R}}}_r = \ddot{\vec{d}}$. Substituting in for $\ddot{\vec{\mathcal{R}}}_i$ from Eq. 2.3 yields:

$$\ddot{\vec{d}} = \frac{-GM_{\rm S}(\vec{a} + \vec{d})}{|\vec{a} + \vec{d}|^3} - \vec{\nabla}\Phi - 2(\vec{\Omega}_{\rm K} \times \dot{\vec{d}}) - \vec{\Omega}_{\rm K} \times [\vec{\Omega}_{\rm K} \times (\vec{a} + \vec{d})] \tag{2.6}$$

Considering each component in turn, expanding out the cubic term in the denominator using the binomial approximation, and dropping all terms smaller than $\frac{d}{a}$, yields the complete set of linearised equations of motion in the rotating patch frame:

$$\begin{aligned} \ddot{u} &= \mathcal{F}_u + 3\Omega_{\rm K}^2 u + 2\Omega_{\rm K}\dot{v}, \\ \ddot{v} &= \mathcal{F}_v - 2\Omega_{\rm K}\dot{u}, \\ \ddot{w} &= \mathcal{F}_w - \Omega_{\rm K}^2 w. \end{aligned} \tag{2.7}$$

The velocity-dependant terms can be recognised as Coriolis accelerations and the $\Omega_{\rm K}^2$ terms as centrifugal accelerations.

The presence of the velocity-dependent terms in Eq. 2.7 requires a modification to PKDGRAV's leapfrog method such that a *predicted* velocity is used to estimate the acceleration at the end of the step (Quinn et al. 2010). This would not be time reversible and would therefore destroy the symplectic nature of leapfrog. However, Quinn et al. (2010) derives a symplectic integrator for this system by separating the Hamiltonian into a position-independent (i.e. free particle, in

the sense of not acting under a potential), momentum-independent, and mixed term. The first two terms of the separated Hamiltonian can be straightforwardly solved, and the latter mixed term gives equations of motion that can be solved exactly. Quinn et al. (2010) thereby construct a second-order symplectic integrator. This method is executed in PKDGRAV as external forces, involving the Coriolis and centrifugal forces, in a separate function that is called at the appropriate point in the Kick-Drift-Kick procedure.

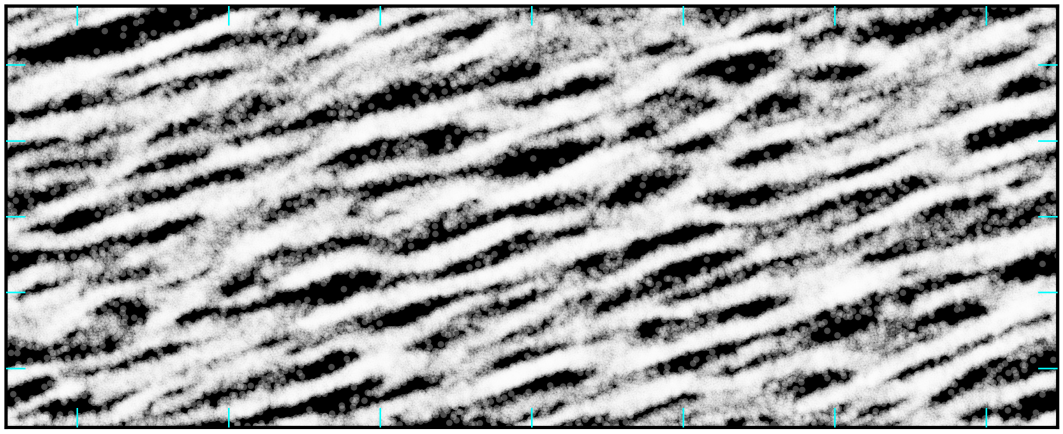

Figure 2.3: Snapshot of an $\sim 300 \times 700 \times 20\,\mathrm{m}$ patch after approximately 7.4 hours, each semi-transparent point represents a single particle. Ticks indicate $50\,\mathrm{m}$ intervals in the radial u-direction (vertically down the page), $100\,\mathrm{m}$ in the azimuthal v-direction (horizontal along the page). The wakes are tilted to the orbital direction in the trailing sense, due to the differential shear rate across the patch. The following simulation parameters were used: $N \sim 60,000$; $h = 45\,\mathrm{s}$; $a = 100,000\,\mathrm{km}$; $(T_\mathrm{K} \sim 9\,\mathrm{h})$; $\Sigma \sim 1000\,\mathrm{kg/m^2}$; $\tau \sim 1$.

An example snapshot of a patch is shown in Figure 2.3, with simulation parameters specified in the caption. The coefficient of restitution for particle collisions within the patch was set to be a function of impact velocity, following Borderies et al. (1984). The particles' mutual gravitational attraction and dissipation of energy during collisions leads to clumps which shear out to form transient trailing structures called self-gravity wakes. The typical radial separation between wakes can be estimated from Toomre (1964)'s critical wavelength $\lambda_\mathrm{crit} = \frac{4\pi^2 G\Sigma}{\Omega_\mathrm{K}^2}$ ($\sim 70\mathrm{m}$ for the run shown in Figure 2.3).

2.1.2 Modifying Code to Include Planetary Magnetic Field

In order to study charged dust in Saturn's rings, the gravitational code must be modified to include the effect of the planetary magnetic field, $\vec{B}$. A grain of mass m_d and charge q_d experiences

an acceleration due to the Lorentz force:

$$\ddot{\vec{d}}_{\text{Lorentz}} = \frac{q_d}{m_d}(\vec{E} + \dot{\vec{d}} \times \vec{B}). \tag{2.8}$$

The rotation of the planet induces an electric field in the plasmasphere (§1.3.1); the plasma is coupled to the planetary magnetic field lines and thus corotates with the planet at $\vec{\Omega}_{\text{S}}$, producing a plasma polarisation electric field, $\vec{E}$. In the synchronously rotating frame where the plasma is at rest, the magnetically-induced electric field is zero. The electric field term in Eq. 2.8 is:

$$\vec{E} = [(\vec{\Omega}_{\text{K}} - \vec{\Omega}_{\text{S}}) \times \vec{d}] \times \vec{B}, \tag{2.9}$$

recalling $\vec{d}$ is relative to the origin of the rotating frame orbiting at Ω_{K}. So the Lorentz acceleration in the rotating patch frame can be written:

$$\ddot{\vec{d}}_{\text{Lorentz}} = \frac{q}{m}[(\vec{\Omega}_{\text{K}} - \vec{\Omega}_{\text{S}}) \times \vec{d} + \dot{\vec{d}}] \times \vec{B}, \tag{2.10}$$

where, as you would expect, away from synchronous location, it is the *relative* motion of the charged grains to the rigidly rotating magnetic field lines that is important, plus any additional motion within the patch frame, $\dot{\vec{d}}$. Straightforwardly performing the cross products yields (under the assumption that the spin vector is about the vertical w-axis):

$$\begin{aligned}
\ddot{u}_{\text{Lorentz}} &= \frac{q_d}{m_d}[(\Omega_{\text{K}} - \Omega_{\text{S}})(a+u)B_w + (\dot{v}B_w - \dot{w}B_v)] \\
\ddot{v}_{\text{Lorentz}} &= \frac{q_d}{m_d}[(\Omega_{\text{K}} - \Omega_{\text{S}})vB_w + (\dot{w}B_u - \dot{u}B_w)] \\
\ddot{w}_{\text{Lorentz}} &= \frac{q_d}{m_d}[-(\Omega_{\text{K}} - \Omega_{\text{S}})(vB_v + (a+u)B_u) + (\dot{u}B_v - \dot{v}B_u)],
\end{aligned} \tag{2.11}$$

where a is the radial distance to the patch as before. This agrees with Matthews (1998)'s Equation 4.25 under the assumption that $(a+u)B_w \to a(1+\frac{u}{a})B_w \simeq aB_w$, and $(a+u)B_u \to a(1+\frac{u}{a})B_u \simeq aB_u$, which is realistic as the patch is small so $u \ll a$. However, Eq. 2.11 differs slightly from the results as given in Matthews & Hyde (2003, 2004):

$$\begin{aligned}
\ddot{u}_{\text{Lorentz}} &= \frac{q_d}{m_d}[(\Omega_{\text{K}} - \Omega_{\text{S}})aB_w + \dot{v}B_w - \dot{w}B_v], \\
\ddot{v}_{\text{Lorentz}} &= \frac{q_d}{m_d}[\dot{w}B_u - \dot{u}B_w], \\
\ddot{w}_{\text{Lorentz}} &= \frac{q_d}{m_d}[-(\Omega_{\text{K}} - \Omega_{\text{S}})aB_u + \dot{u}B_v - \dot{v}B_u].
\end{aligned} \tag{2.12}$$

The differences between Eq. 2.11 terms and Matthews & Hyde (2003, 2004)'s Equation 2.12 arise due to the differences in patch size that are used. They were studying the F ring and thus the patch size could be larger: 2000 km versus the few hundred metres of a B ring patch illustrated in Figure 2.3 (Matthews divides up the F ring into $\sim$ 400 patches). As a particle travels through their large F ring patch from one end to the other it would experience a change in the v-component of acceleration it feels, however by symmetry the magnitude of the polarisation electric field (-$(\vec{\Omega}_{\text{S}} \times \vec{d}) \times \vec{B}$) should be approximately constant around a ring in the azimuthal direction. Therefore, they appear to drop the troublesome $(\Omega_{\text{K}} - \Omega_{\text{S}})vB_w$ and $-(\Omega_{\text{K}} - \Omega_{\text{S}})vB_v$ terms that would otherwise cause the magnitude of the induced electric field to change unphysically through the patch as v increases. There would not be such an issue with the smaller B ring patch.

The magnetic field components for Saturn's northward offset dipole as found in (§1.3.1), were substituted into the Lorentz force expression of Eq. 2.11 and implemented in PKDGRAV's shearing patch code as external forces in a separate function call. In order to match Connerney (1993)'s best-fit for the g_1^0, g_2^0, $R_{\text{S}} = 60\,000\,\text{km}$. As shown in Figure 2.4, there is good agreement with Matthews & Hyde (2004), except vertical displacements are inverted relative to their labelled $\frac{q_d}{m_d}$: given that $\Omega_{\text{K}} < \Omega_{\text{S}}$ in Saturn's F Ring and that $B_u < 0$ (due to the dominating $-\frac{3}{2}g_2^0\left(\frac{R_p}{r}\right)^4$ factor of B_r in Eq. 1.24), then $\ddot{w}_{\text{Lorentz}} < 0$ for $\frac{q_d}{m_d} > 0$ (substituting into Eq. 2.11). In Figure 2.4, the azimuthal values are adjusted for the mean motion of the guiding centre (§ 3.4.1) and unfurled across boundaries - i.e. for negatively charged grains, the equilibrium point is displaced inward so that $\omega_c > \Omega_{\text{K}}$ and grains pass through the positive azimuthal $(+v)$ boundary, and vice versa for positively charged grains.

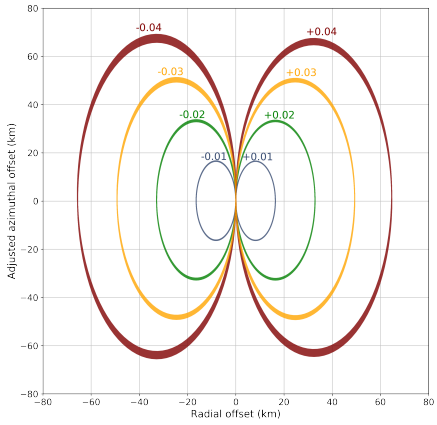

(a) Results reproducing Matthews & Hyde (2004).

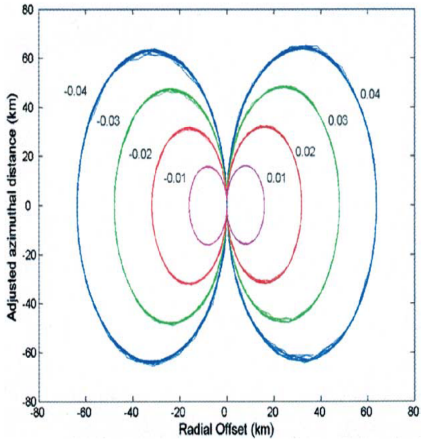

(b) Matthews & Hyde (2004)'s Figure 2.

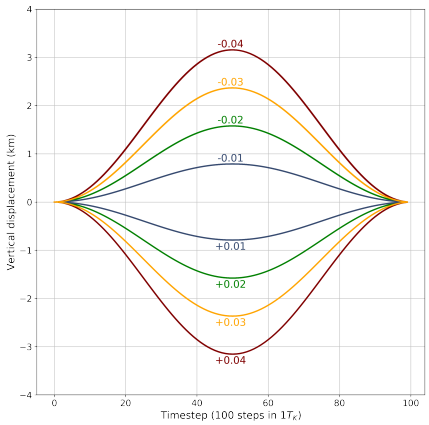

(c) Results reproducing Matthews & Hyde (2004). Using timestep as a proxy for longitude y.

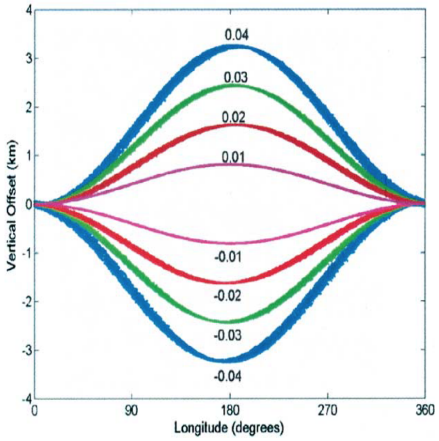

(d) Matthews & Hyde (2004)'s Figure 3.

Figure 2.4: (a), (b): Epicyclic orbits in the (horizontal) uv-plane of charged grains over 10 orbital periods in a dv (azimuthally) periodic patch – with no u nor w ghost patches due to the thinness of the F ring, orbiting the planet at $\Omega_K = 1.168 \times 10^{-4}\,\mathrm{rad\,s^{-1}}$. **(c), (d)**: Vertical (w) lofting of charged grains, caused by the radial (quadrupole) component of Saturn's magnetic field. Labels indicate the charge-to-mass ratio of a grain in $\mathrm{C\,kg^{-1}}$.

2.1.3 Global Simulations

As well as the local shearing patch frame mode, PKDGRAV can be used in a global non-rotating frame with the origin at the central body and coordinate system denoted (x, y, z). The Lorentz force due to the planetary magnetic field for charged grains for such a reference frame can be written (under the assumption that the planet is spinning about the z axis):

$$\begin{aligned}
\ddot{x}_{\text{Lorentz}} &= \frac{q_d}{m_d}[(\dot{y} - x\Omega_{\text{S}})B_z - \dot{z}B_y], \\
\ddot{y}_{\text{Lorentz}} &= \frac{q_d}{m_d}[\dot{z}B_x - (\dot{x} + y\Omega_{\text{S}})B_z], \\
\ddot{z}_{\text{Lorentz}} &= \frac{q_d}{m_d}[(\dot{x} + y\Omega_S)B_y - (\dot{y} - x\Omega_{\text{S}})B_x].
\end{aligned} \tag{2.13}$$

Due to the presence of the velocity-dependent terms in the Lorentz force, it was necessary to use a predicted velocity so that the accelerations due to the Lorentz force and due to gravity were aligned in the step according to the Kick-Drift-Kick scheme. This involved a modification to the code that breaks the symplectic nature of the leapfrog.

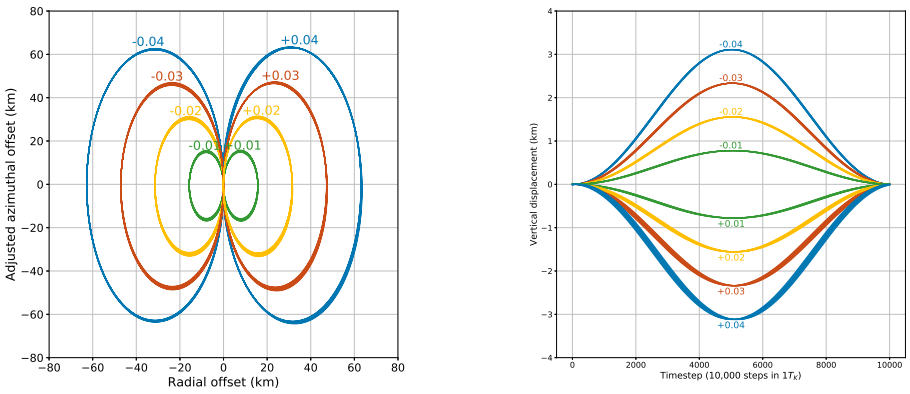

(a) Epicyclic orbits of charged grains.

(b) Vertical motion of charged grains.

Figure 2.5: Reproducing the results of Matthews & Hyde (2003, 2004) for orbits in the F ring using PKDGRAV's global simulations with the Lorentz force modification. Labels indicate the charge-to-mass ratio of a grain in $\mathrm{C\,kg^{-1}}$.

Similar tests for the global code modifications were run to reproduce Matthews & Hyde (2003, 2004), and these results, Figure 2.5, agree with Figure 2.4. The global and patch methods

are consistent. The x and y coordinates have been adjusted to match the rotating patch frame (u, v, w), i.e. the radial displacement relative to the centre of the F ring and the azimuthal positions adjusted for the mean motion of the guiding centre, respectively. The grains undergo out-of-plane motion due to the cross product of the in-plane magnetic field components of Saturn's northward offset dipole with the grains' velocities.

2.2 Adaptive Runge-Kutta

It is clear that in adapting the PKDGRAV local and global codes to include the Lorentz force, the symplectic nature of the leapfrog integrator is broken due to the introduction of predicted velocities. Due to the higher accuracy of the Runge-Kutta method and the low-N requirements for the simulations of interest (test grain trajectories will be investigated, rather than ring systems), an adaptive Runge-Kutta method was chosen over modifying the existing PKDGRAV code to include the velocity-dependent Lorentz force, which would have involved following a Hamiltonian splitting technique such as that used by Quinn et al. (2010) in the context of a local shearing patch.

To apply a higher order integrator to dust grain trajectories first meant solving a well-known problem in numerical integration – that the choice of step size must be optimised in order to avoid both truncation errors and wasting computational resources. A given step size may be appropriate for the start of an integration, however later prove to be unsuitable. A simple gravitational example to illustrate this would be a grain that is launched on a distant orbit that later destabilises and causes the grain to plunge into the planet: initially a larger step size, say a few hundredth of a Keplerian period, would be suitable as the gravitational force is weaker and the orbital curvature is smaller, however as the grain approaches the planet, such a step size would cause the grain to over-step where it should be leading to an erroneous drift.

Adaptive Runge-Kutta methods estimate the truncation error at each step and use this to adjust the step size so that the solution remains within prescribed limits. This enables a range of physical parameters to be studied (e.g. different charge-to-mass ratios and varying orbital distances). The Runge-Kutta formulae and Dormand-Prince method are well-documented (e.g. Press et al. 2007; Dormand & Prince 1980), but for completeness a description of the formulae implemented in the code is included.

It is widely accepted that the Runge-Kutta embedding technique is an efficient method for the solution of non-stiff initial value problems (stiff problems occur if some terms in the solution vector vary more rapidly than others and these require special care beyond the scope of this section). In the embedding technique for Dormand-Prince (RKDP), formulae are obtained which share the same function evaluations, i.e. they share the same coefficients (Dormand & Prince 1980). The Runge-Kutta formulae of order five for the initial value problem (2.1) with a timestep h are:

$$\begin{aligned} \vec{k}_0 &= h\vec{f}(t, \vec{X}), \\ \vec{k}_i &= h\vec{f}\left(t + A_i h, \vec{X} + \sum_{j=0}^{i-1} B_{ij}\vec{k}_j\right), \quad i = 1, 2, \ldots, 6 \end{aligned} \tag{2.14}$$

$$\vec{X}_5(t+h) = \vec{X}(t) + \sum_{i=0}^{6} C_i \vec{k}_i, \tag{2.15}$$

and the embedded fourth-order formula is:

$$\vec{X}_4(t+h) = \vec{X}(t) + \sum_{i=0}^{6} D_i \vec{k}_i. \tag{2.16}$$

The coefficients A_i, B_{ij}, C_i, D_i of Equations 2.15 and 2.16, given in Table 2.1, are not unique – Dormand & Prince (1980) chose the coefficients of their method to minimise the error of the fifth-order solution, $\vec{X}_5$, in contrast to Fehlberg (1969) who minimised the error in the fourth-order solution, $\vec{X}_4$.

RKDP has seven stages, but it has only six function evaluations per step due to its property of *First Same As Last*, where the last stage for the n^{th} step is evaluated at the same point as the first stage of the $n + 1^{\text{th}}$ step. The solution is advanced using the fifth-order formula of 2.15.

The difference between the fourth- and fifth-order formulae (2.15 – 2.16) estimates the error of the solution:

$$\vec{E}(h) = \sum_{i=0}^{6} (C_i - D_i)\vec{k}_i \tag{2.17}$$

i	A_i	B_{ij}						C_i	D_i
0	—	—	—	—	—	—	—	$\frac{35}{384}$	$\frac{5179}{57600}$
1	$\frac{1}{5}$	$\frac{1}{5}$	—	—	—	—	—	0	0
2	$\frac{3}{10}$	$\frac{3}{40}$	$\frac{9}{40}$	—	—	—	—	$\frac{500}{1113}$	$\frac{7571}{16695}$
3	$\frac{4}{5}$	$\frac{44}{45}$	$-\frac{56}{15}$	$\frac{32}{9}$	—	—	—	$\frac{125}{92}$	$\frac{393}{640}$
4	$\frac{8}{9}$	$\frac{19372}{6561}$	$-\frac{25360}{2187}$	$\frac{64448}{6561}$	$-\frac{212}{729}$	—	—	$-\frac{2187}{6784}$	$-\frac{92097}{339200}$
5	1	$\frac{9017}{3168}$	$-\frac{355}{33}$	$\frac{46732}{5247}$	$\frac{49}{176}$	$-\frac{5103}{18656}$	—	$\frac{11}{84}$	$\frac{187}{2100}$
6	1	$\frac{35}{384}$	0	$\frac{500}{1113}$	$\frac{125}{192}$	$-\frac{2187}{6784}$	$\frac{11}{84}$	0	$\frac{1}{40}$

Table 2.1: Butcher tableau for RKDP method. A_i are the nodes, B_{ij} is the Runge-Kutta matrix, and C_i, D_i are the weights.

Noting that the error $\vec{E}(h)$ is a vector, with components representing the errors in the dependent variables $\vec{X} = \begin{pmatrix} \vec{r} \\ \dot{\vec{r}} \end{pmatrix} = (x, y, z; \dot{x}, \dot{y}, \dot{z})$, a choice is made to use the root-mean-square error for the error measure:

$$\bar{E}(h) = \sqrt{\frac{1}{n}\sum_{i=0}^{n-1} E_i^2(h)}, \quad n = \text{number of first-order equations.} \tag{2.18}$$

Error control is achieved in the following manner by adjusting h, so that the error-per-step is approximately equal to some prescribed tolerance ϵ: suppose an integration step with h' that resulted in an error $\bar{E}(h')$ is performed, the step size h'' that ought to be used to obtain a tolerance can be estimated, noting that the truncation error is $\mathcal{O}(h^5)$ so that,

$$h'' \approx 0.9h' \left[\frac{\epsilon}{\bar{E}(h')}\right]^{\frac{1}{5}}, \tag{2.19}$$

where a 0.9 factor has been introduced as a safety measure to account for the crude approximations. If $h'' \geq h'$, the step is accepted as the error is below the tolerance, however if $h'' < h'$, the step is rejected and re-attempted with h''. Once a particle moves away from a region of rapid change, the step size is increased according to the tolerance of Eq. 2.19 because the value in the denominator, $\bar{E}(h)$, decreases. Whilst adjustments to the step size are necessary to accurately resolve the motion, in, for example, regions of strong magnetic field close to the planet, excessive changes in step size are avoided by constraining $\frac{1}{10} \leq \frac{h''}{h'} \leq 10$.

A caveat to note with regard to the error control measures discussed above is that $\bar{E}(h)$ is the error in a single integration step. The global truncation error is the accumulation of these per-step errors, however it is usually satisfactory to use these errors interchangeably as $\bar{E}(h)$ is a conservative estimate, unless the number of integration steps is very large.

2.3 Gragg-Bulirsch-Stoer

In order to verify the RKDP solutions, an independent adaptive integrator method was used. The Gragg-Bulirsch-Stoer (GBS) method (Gragg 1964; Bulirsch & Stoer 1966) was chosen as it provides high-accuracy solutions (e.g. Press et al. 2007) to smooth IVPs, Eq. 2.1, and as Chambers (1999) notes, it is generally robust for N-body problems. The GBS method relies on the use of the modified midpoint method to advance the solution, together with Richardson extrapolation. These concepts are explained in greater detail in Press et al. (2007); Stoer & Bulirsch (2013) but for completeness, the method is outlined below.

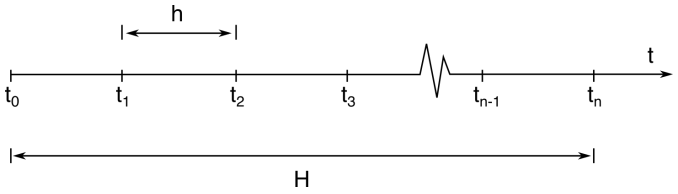

Figure 2.6: Mesh used in the Gragg-Bulirsch-Stoer method. The interval of integration is divided into n steps of length $h = \frac{H}{n}$. The solution is advanced in stages of length H, using the modified-midpoint method with Richardson extrapolation (described in Figure 2.7) to perform the integration in each stage.

A numerical solution becomes increasingly accurate as the stepsize used in the approximation decreases. In the GBS method, this property is exploited by solving the IVP, Eq. 2.1, several times with the modified midpoint method, each time using more sub-steps as described in Figure 2.6. As the solutions with increasingly fine stepsizes asymptote to the true value, an analytic function can be fitted. It turns out that rational function fits remain good approximations to analytic functions even for large H (Stoer & Bulirsch 2013). Deuflhard (1983) found that straightforward polynomial extrapolation is slightly more efficient than rational function extrapolation provided there are no rapid variations in the function. This act of taking the limit as $h \to 0$ in order to asymptote to the result with infinitely small steps is known as Richardson extrapolation, illustrated in Figure 2.7. Richardson extrapolation considers the solution to the

initial value problem as being an analytic function of the adjustable stepsize parameter, h.

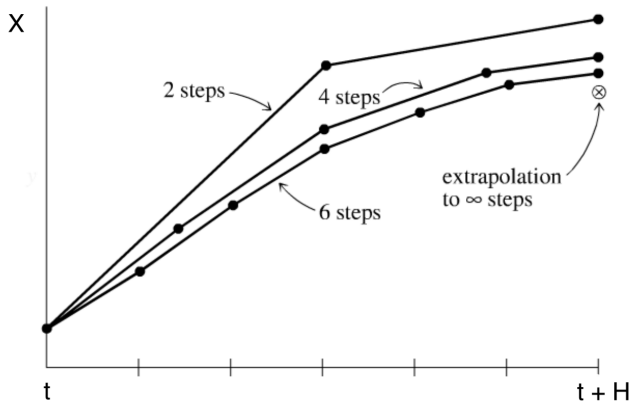

Figure 2.7: Richardson extrapolation. The large interval H is spanned by different sequences of substeps, with the numerical integrations done by the modified midpoint method. The polynomials fitted to those datapoints are a function of h and the solution for which $h \to 0$ is extrapolated (indicated by the $\otimes$). From Press et al. (2007) with minor adjustments.

The modified mid-point method is chosen as the integration method within the GBS algorithm as it has the property that its error function is strictly even, which allows the rational function (or polynomial function) of the Richardson extrapolation method to be expressed in terms of h^2 rather than h (Gragg 1964, 1965). The accuracy increases two orders at a time, by combining steps from separate attempts to traverse H with increasing numbers of substeps h, to eliminate higher order error terms.

2.4 Testing the Numerical Integrators

The numerical integrators described previously, PKDGRAV (§2.1), RKDP (§2.2), and GBS (§2.3), were tested in the context of the dynamics of charged grains in planetary gravitational and magnetic fields. The fractional energy error should be close to zero for effective integrators. It is known that over *long* integration periods, the leapfrog method, which is used by PKDGRAV, behaves better than Runge-Kutta methods for gravitational problems (Springel 2016) due to conserving phase space volume over time (Liouville's Theorem). However, in the context of this work other issues must be considered. The inclusion of electromagnetic forces introduces other characteristic timescales, namely the gyroperiod, mirror bounce period, and guiding

centre orbital period, so that the behaviour of the integrators on these timescales as well as the Kepler timescale must be examined. These periods are described in greater detail in §§3.5.1 and 3.6.2.

As described in §2.1, the addition of the Lorentz force to PKDGRAV's source code via a naïve approach broke the time reversible symmetry of the leapfrog method. Although it could be possible to construct a system of equations that enables a time-reversible invocation of the Lorentz force within the Kick Drift Kick formalism by splitting the Hamiltonian in a similar manner as performed by Quinn et al. (2010) in the context of the shearing patch (§2.1.1), this approach was not pursued due to there being multiple timescales of interest requiring an adaptive integrator. Moreover, variations in a dust grain's charge (Chapter 4) can alter its trajectory over rapid timescales (Jontof-Hutter 2012) and therefore the ability to decrease and increase the step size is a necessity. In addition, Jontof-Hutter (2012), studying the stability of charged grain orbits, notes that all relevant dynamical timescales are < 0.1 years, therefore the benefit of no secular energy drift over very long time periods for the leapfrog method is no longer of paramount importance.

It is necessary to check that the fractional energy error of the adaptive methods (RKDP and GBS) do not grow over the timescales of interest for the problem of a charged grain in planetary gravitational and magnetic fields. The GBS method was implemented alongside to give an independent verification of the RKDP solutions. The orbital energy includes the gravitational potential and kinetic energy terms, plus an additional term due to the corotational electric field. Of course, the magnetic field does no work on the charged grain and so there is no magnetic energy term. The corotational energy term can be expressed as the work done on the grain by the electric field: $q_d \int_{\vec{r}_L}^{\vec{r}} \vec{E} d\vec{r}$, so that the total energy can be written

$$E = \frac{1}{2} m_d v^2 - \frac{G M_p m_d}{r} - \frac{q_d \Omega_p g_{10} R_p^3}{r}. \tag{2.20}$$

Fractional energy errors for the three integrators are plotted in Figure 2.8. The RKDP method performs better than PKDGRAV, which is to be expected as it is a fifth order method compared to a second order method. Likewise, the GBS method performs better than PKDGRAV as the stepsize varies such that the error remains within prescribed boundaries. The maximum energy error for the adaptive methods, RKDP and GBS, remain constant. The tolerance for the RKDP

method example illustrated in Figure 2.8 was chosen to define an average stepsize large enough to illustrate energy drift in the broken-symplectic fixed-timestep PKDGRAV method (§2.1). The RKDP and GBS methods are able to achieve $\epsilon = 1 \times 10^{-10}$, with the coarser tolerance shown here to illustrate the behaviour of the methods. In order to make a direct comparison between the three integration methods, the same (average) stepsize was used: $\bar{h} \approx h \approx 250\,\mathrm{s}$, which corresponds to $\sim 0.0009\,\mathrm{T_K}$, or about 0.05% of the gyroperiod, at the launch position.

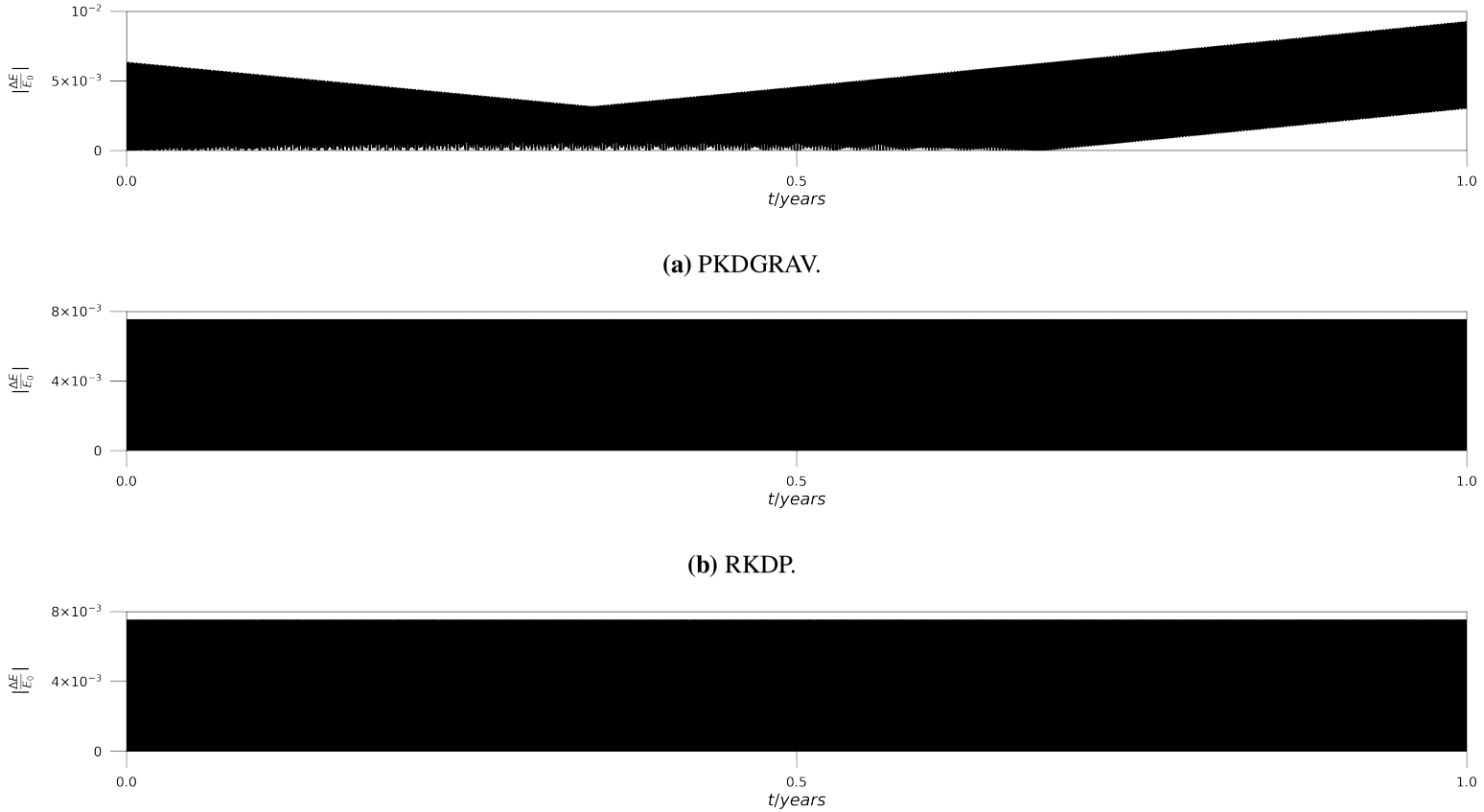

(a) PKDGRAV.

(b) RKDP.

(c) GBS.

Figure 2.8: Fractional energy change over time for the three integration methods described in §§2.1, 2.2 and 2.3, for a grain launched around Saturn at $r_L = 2\,R_p$ with an $L_* = -0.1$. A tolerance for the RKDP method, $\epsilon = 0.01$, was chosen to define an average stepsize large enough to illustrate energy drift in the broken symplectic fixed-timestep PKDGRAV method. The same average stepsize for the adaptive methods and fixed stepsize for the leapfrog method was used, $\bar{h} \approx h \approx 250\,\mathrm{s}$, to compare the integrators.

In addition to energy, there is another important conserved quantity to consider when testing the accuracy and stability of the numerical integrators in the context of charged grain motion in planetary magnetic fields: the first adiabatic invariant or magnetic moment (Eq. 3.47), $\mu = \frac{m_d v_\perp^2}{2|\vec{B}|}$, which is derived in §3.6.1. As the case for using adaptive integrators has been argued previously in this section, only the RKDP and GBS methods are tested with this μ parameter, and the fixed-timestep PKDGRAV method is relinquished.

More highly charged grains were analysed as these test the integrators are able to resolve gyromotion where the Guiding Centre Approximation (§3.4.1) holds. The trajectory of such a grain, with $L_* = 10$ (the Lorentz force dominates the gravitational) and $r_L = 1.5\,R_p$, is illustrated in Figure 2.9. The grain's magnetic moment is plotted in Figure 2.10, which shows that the fractional error in μ remains bounded and therefore the integrators perform well for highly charged grains with rapid gyromotion, that is, the epicyclic motion is resolved.

As can be seen from Figure 2.9, the test grain exhibits bounce motion which takes it from regions of weaker magnetic field strength in the equatorial plane, to regions of stronger field strength nearer to the poles (§3.6). Note also how the gyroradius decreases in size as the grain moves closer to the planet in Figure 2.9. Since the gyrofrequency varies with time as the grain encounters varying field strength, by Eq. 3.7, it is not possible to average over an integer number of gyrations when plotting out the first adiabatic invariant and therefore some fluctuations occur. However, in order to minimise this effect, the average was taken over a bounce period so that the full range of gyrofrequencies were sampled as the grain completed a full vertical oscillation. As explained in §2.3, the GBS method advances the solution by a large step H, where H is held constant as the number of substeps h varies to achieve the prescribed accuracy. This means that the output of the GBS method is sparser and therefore fewer gyrations were averaged over, resulting in larger fluctuations, as can be seen in Figure 2.10b.

Having demonstrated that the adaptive methods of integration are stable to their stated accuracy, the GBS and RKDP methods can be applied to the study of charged dust.

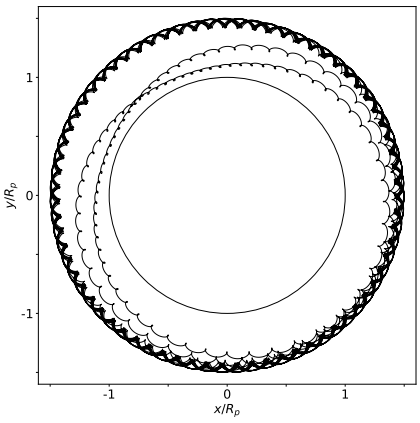

(a) Plan view, with Jupiter denoted by circle.

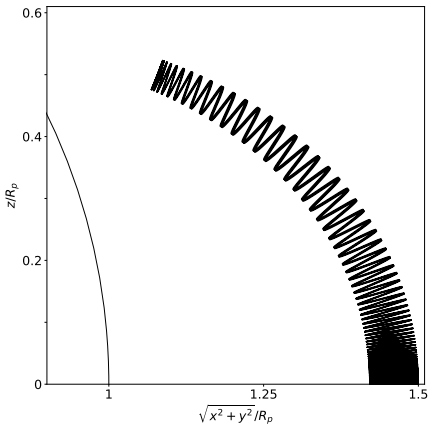

(b) Vertical displacement against cylindrical radial distance, with Jupiter drawn as arc.

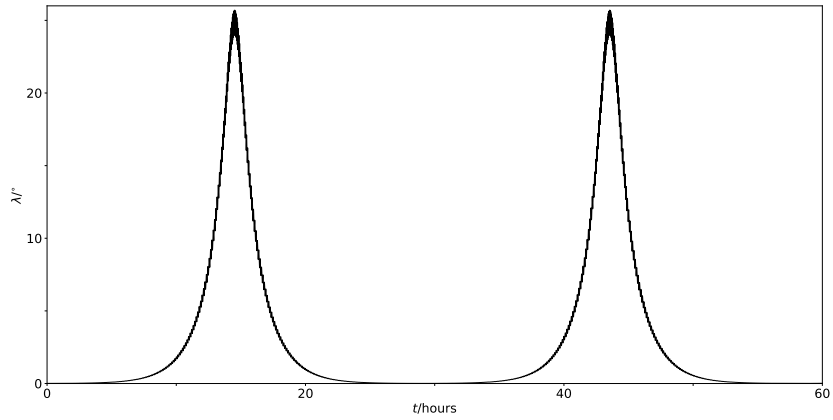

(c) Latitude over time.

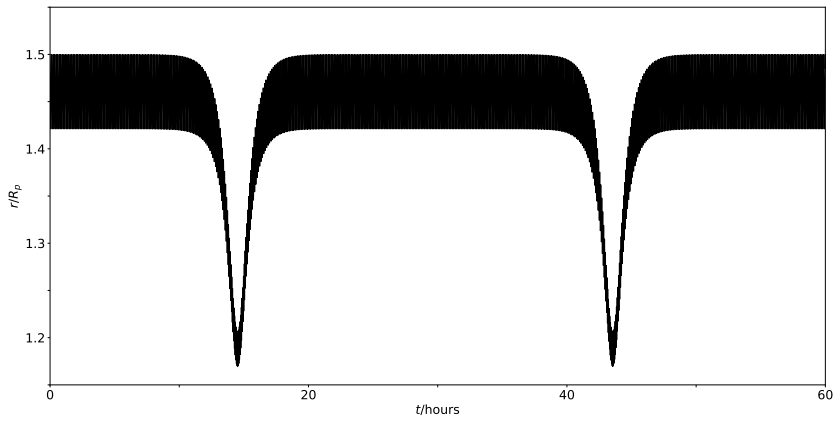

(d) Radial range over time.

Figure 2.9: The first 60 hours of a stable grain's trajectory around Jupiter, with grain parameters equal to those shown in Figure 2.10: $L_* = 10.0$, $r_L = 1.5\,R_p$.

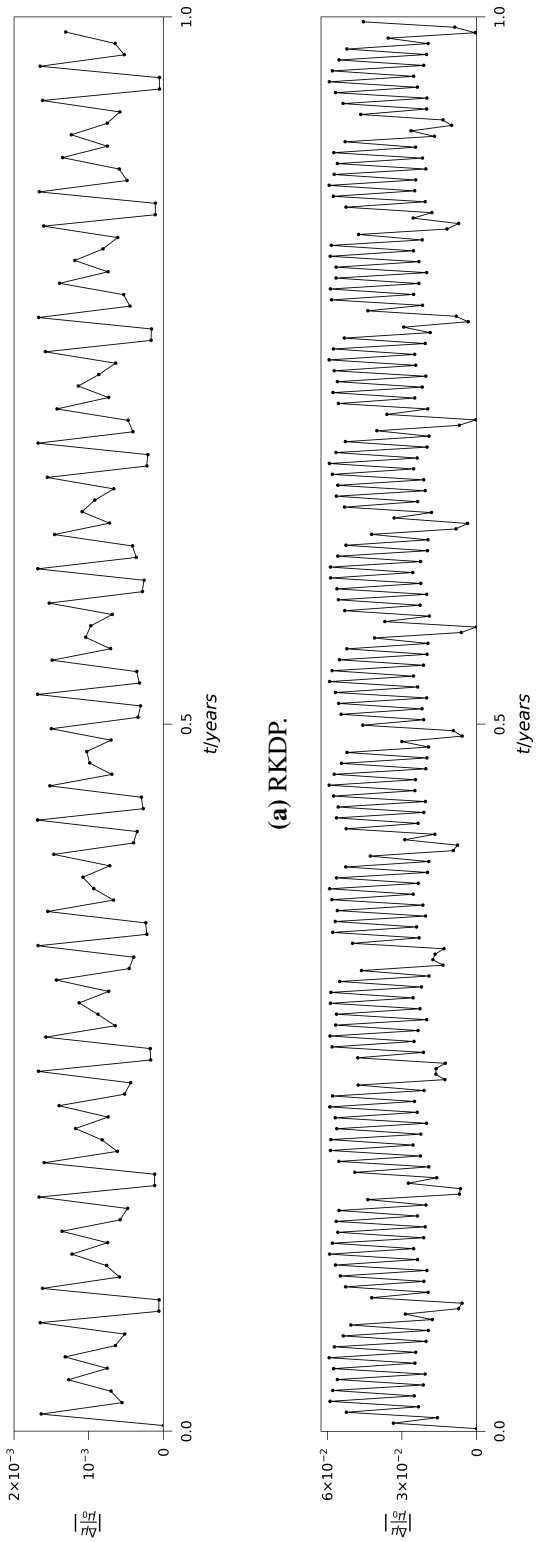

(a) RKDP.

(b) GBS.

Figure 2.10: Fractional change in the first adiabatic invariant over time for the adaptive integration methods described in §§2.2 and 2.3, for a grain launched around Jupiter at $r_L = 1.5\,R_p$ with an $L_* = 10$. The RKDP results are averaged over a full vertical oscillation, resulting in smaller fluctuations, whereas the sparser output of the GBS method necessitates a smaller sample size for the averaging, resulting in larger fluctuations, nevertheless the fractional change is bounded indicating that the integrators are robust.

3

Orbital Motions of Charged Dust

This chapter lays out the relevant background and theory from literature to explain the dynamics of charged grains in planetary gravitational and magnetic fields. It develops the theory, in particular following Jontof-Hutter (2012), to find analytical expressions for the motions that can be compared to numerical results using the codes developed in Chapter 2, to further test the numerical methods and to extend the work of investigating regions of stability around Saturn. The work of Jontof-Hutter (2012) has been published in two papers: Jontof-Hutter & Hamilton (2012a) and Jontof-Hutter & Hamilton (2012b), but for the purposes of this chapter, reference will primarily be made to Jontof-Hutter (2012).

In order to elucidate the relevant physical concepts, the planetary magnetic field is modelled as an aligned dipole, the gravitational field includes only first order terms ($n = 0$, cf. Figure 1.21) and the grain charge is held constant. Later, these simplifying assumptions will be relaxed: in Chapter 4, the grain's charge will vary in time according to the various currents it encounters in Saturn's environment as well as the planet's shadowing effect, and in Chapter 5, a more realistic Saturnian magnetic and gravitational field model will be applied.

The sections have been structured to consider the orbits of dust grains through analysis in the principal directions: azimuthal (§3.4), radial (§3.5), and vertical (§3.6), introducing the relevant

physical concepts of drifts, gyro-orbits and mirror motion. The vertical and radial motions of a charged grain launched near the equatorial plane are initially decoupled and may be considered independently (e.g. Northrop & Hill 1982). The physical parameter L_*, which describes the ratio of the gravitational to electromagnetic force is introduced in §3.1 (previously referenced in §1.2.2). The results of the simulations enable sets of trajectories to be characterised in §3.2.1, so that stable and unstable regions in (L_*, r_L) parameter space can be mapped out in §3.2.2.

There are several regions of instability within the parameter space that are studied in §§3.5.2, 3.5.3 and 3.6.2. The grain could escape the system, strike the planet at low or high latitude, or remain in orbit. Such orbital outcomes can be studied through a local or global stability analysis, depending on the distance to an equilibrium point. Stability boundaries can be determined (semi–) analytically by working out for which parameters there exists an energetic barrier that prevents the grain from colliding with the planet or escaping the system thus maintaining the grain in orbit. Therefore, prior to describing the radial and vertical stability boundaries, the potential in which the grain moves is described in §3.3. Following the study of the physical parameters associated with the grain motions, the timescales of relevance are presented in §3.7 followed by a summary of the stability regions in §3.8.

Throughout this chapter, subscript g refers to gyromotion, c to guiding centre motion, L to launch location and p to planet.

3.1 Background

Alfvén (1940, 1950) developed a perturbation theory describing guiding centre motion. For highly charged grains, the essential features of motion can be described by a circular epicycle superimposed on the drift of a guiding centre (e.g. Lehnert 1964). This theory is described in §3.4.1.

Alongside a description of the relevant motions and physical quantities in the guiding centre approximation, this chapter studies the stability of orbits of charged dust grains launched from parent bodies in planetary ring systems. The act of seeking to compare the analytic and numerical results necessitates the following simplifications: the dust grain charge q_d is constant, the magnetic field B is an aligned dipole, and only motion close to the equatorial plane is considered for stability analysis. Once the simulation code (Chapter 2) has been verified by semi-analytical

solutions, more complicated physical scenarios for which there are no analytical solutions, for example stochastic charging (Chapter 4), can be studied numerically.

The orbital outcomes of various dust populations will be studied numerically using the approach of Jontof-Hutter (2012), by varying the parameters affecting the relative strengths of the gravitational and electromagnetic forces: the launch distance of the dust grain from the planet, r_L, and the charge-to-mass ratio, q_d/m_d, of the dust grain. In this way, the behaviour of a dust grain can be tracked systematically from a gravity-dominated regime through to an electromagnetic-dominated regime. Interesting behaviour emerges in the intermediate regime, where limiting cases do not apply and the guiding centre approximation breaks down (§3.4.1).

Before proceeding, a key physical parameter to consider is the ratio of the electromagnetic and gravitational forces, this can be expressed in a variety of units. A straightforward choice is $\mathrm{C/kg}$, used by Northrop & Hill (1982). However, this can be unwieldy as the charge-to-mass ratio varies with grain size, a_d, for a given grain potential, ϕ_d (Eqs. 1.4, 1.5). Other authors make this distinction and assume some constant grain potential across a range of different-sized grains, for example (Howard et al. 1999; Mitchell et al. 2003):

$$\frac{q_d}{m_d} = \frac{10^6 \phi_d}{4\pi \rho_d a_d^2} \mathrm{esu\,g^{-1}},$$

and, Schaffer & Burns (1994):

$$\frac{q_d B}{m_d c} = 2.6 \times 10^{-6} \frac{(\phi_d/\mathrm{V})(B/\mathrm{Gauss})}{(a_d/\mu\mathrm{m})^2 (\rho_d/\mathrm{g\,cm^{-3}})},$$

where ρ_d is the density of the grain. Alternatively, the frequencies associated with the principal motions of a charged grain can be used in the discussion of the transition from gravitionally dominated to electromagnetically dominated motion (Mendis et al. 1982), namely the gyrofrequency Ω_g, guiding centre frequency ω_c, and planetary spin frequency Ω_p (at which the magnetic field lines are assumed to rigidly rotate).

In this work, an approach following Hamilton & Burns (1993) and Jontof-Hutter (2012) is chosen, taking the ratio of the electric and gravitational forces as described in Eq. 1.3 and repeated here,

$$L_* = \frac{q_d g_0^1 R_p^3 \Omega_p}{m_d G M_p},$$

which is dimensionless[1] and independent of distance. Choosing a value for L_* is equivalent to choosing an electric potential, ϕ_d, grain size, a_d, and grain density, ρ_d.

[1] As it is the ratio of two forces, it is dimensionless, noting that a Tesla (the unit for g_0^1) can be expressed in SI-derived units as $\mathrm{kg\,A^{-1}\,s^{-2}}$.

3.2 Numerical Simulation Results

In order to give the analytical discussion of this work some context, it is helpful to initially present numerical results, which were produced using the codes described in Chapter 2. In this chapter, the L_* of the grains were held constant, although time-variable charging will be considered in Chapter 4. In order to study the long-term behaviour of charged dust grains acting under planetary gravitational and magnetic fields, their trajectories were integrated for up to 0.1 years. Even in the simplest case of a constant-charge spherical grain in orbit around a spherical homogeneous central planet with a centred aligned dipole magnetic field there are complex regions of instability. Therefore, the simulation results are presented first in §§3.2.1 and 3.2.2, which can be compared directly to the analytical/semi-analytical solutions, derived in §§3.5.2, 3.5.3 and 3.6.2.

3.2.1 Some Example Trajectories

To map out the behaviour of grains across a range of charge-to-mass ratios, L_* (Eq. 1.3), and launch positions, r_L, it is helpful to first characterise some grain trajectories. The dynamics of grains around Jupiter have also been included here, in addition to Saturn, for two reasons. Firstly, so that any observed differences and similarities can serve to elucidate the important physical processes at work, and secondly, so that the numerical method is checked against the literature as Jupiter was the primary focus of Jontof-Hutter (2012)'s study. Figures 3.1 - 3.4 show some illustrative trajectories for both Saturn and Jupiter, and for which their L_*, r_L values have been marked onto the stability maps of Figure 3.5 for reference. Figure 3.1 shows a reasonably highly charged grain which remains in stable orbit close to the ring plane. An interesting resonance is shown in Figure 3.2, where both the vertical and radial frequencies display beats. There are also conditions which are unstable. Figure 3.3 shows a grain that collides with the planet at high latitude, due to its high L_* causing it to spiral up magnetic field lines. It is also possible for a grain to be excited to high latitudes and remain in stable orbit, an example of which is shown in Figure 3.4.

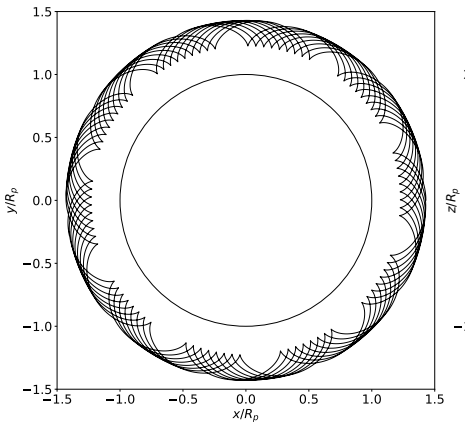

(a) Plan view, with Saturn denoted by circle.

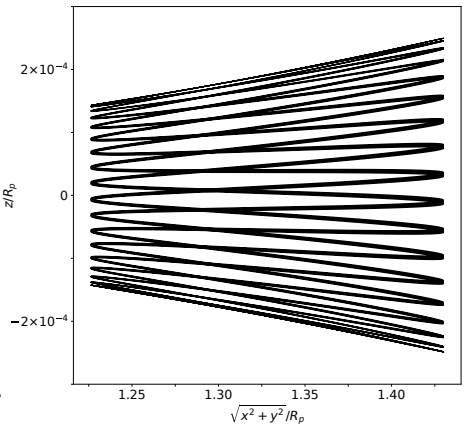

(b) Vertical displacement against cylindrical radial distance.

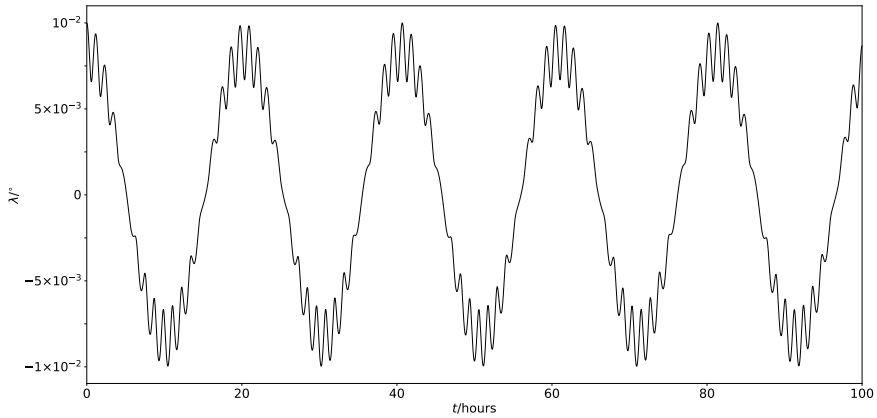

(c) Latitude over time.

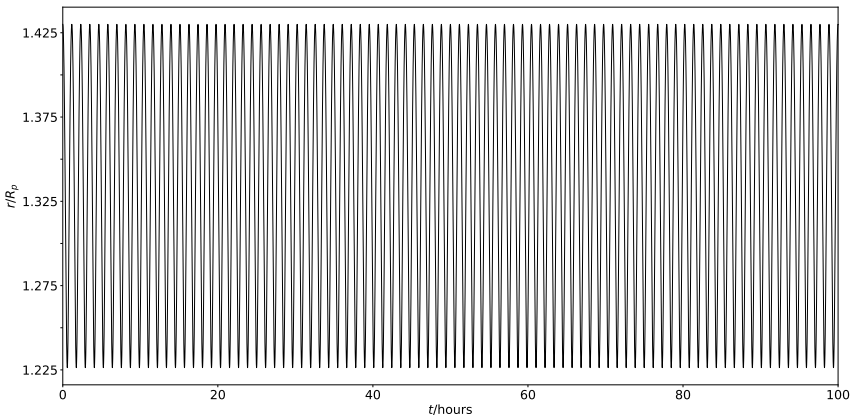

(d) Radial range over time.

Figure 3.1: Trajectory of a stable grain around Saturn, with charge-to-mass ratio of $L_* = 4.01$, and initial launch position of $r_L = 1.43\,R_p$. The grain's bounce period is just under twenty times longer than the gyroperiod.

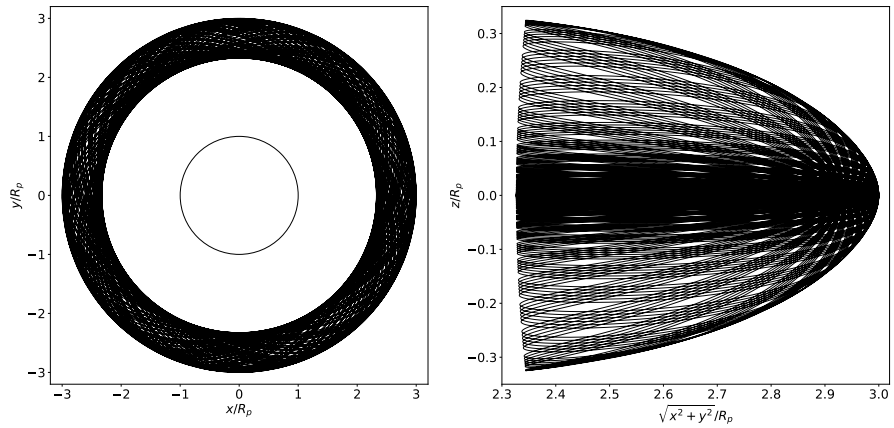

(a) Plan view, with Saturn denoted by circle.

(b) Vertical displacement against cylindrical radial distance.

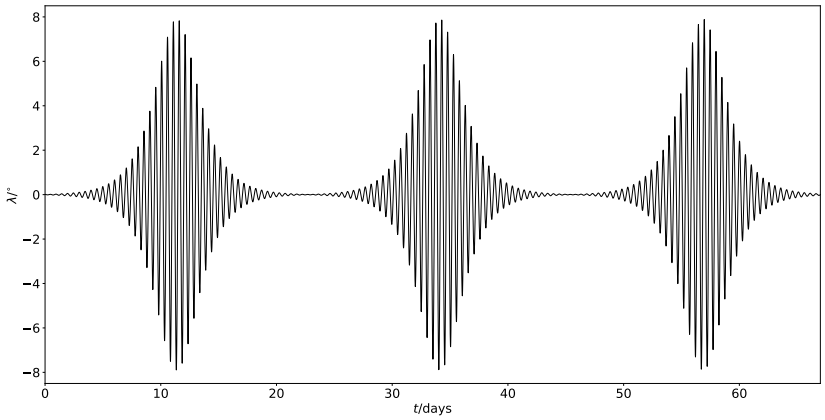

(c) Latitude over time.

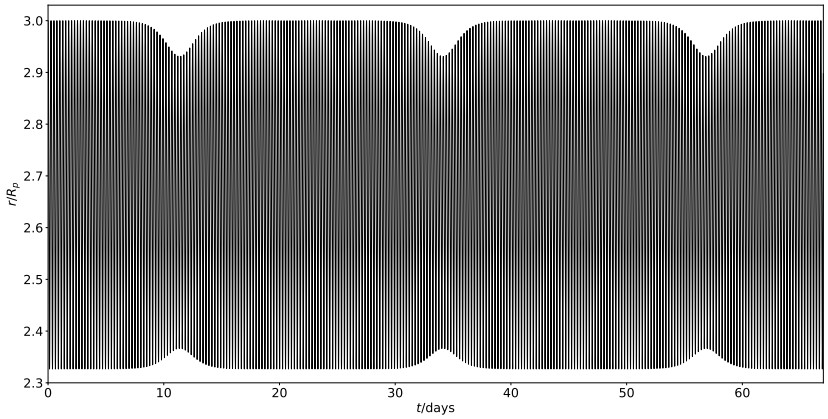

(d) Radial range over time.

Figure 3.2: Trajectory of grain around Saturn, with charge-to-mass ratio of $L_* = -2.05$, and initial launch position of $r_L = 3\,R_p$. This grain experiences a resonance between its radial and vertical frequencies, $|\kappa_c| = 2\Omega_b$, described in §§3.5.2, 3.5.3 and 3.6.2.

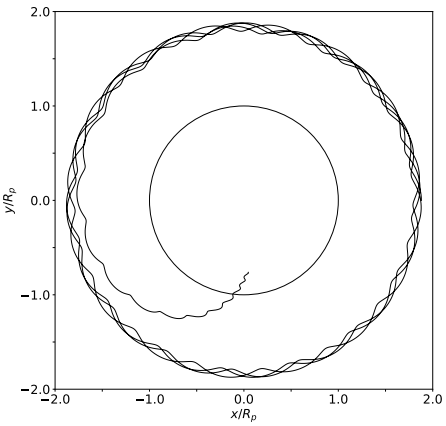

(a) Plan view, with Jupiter denoted by circle.

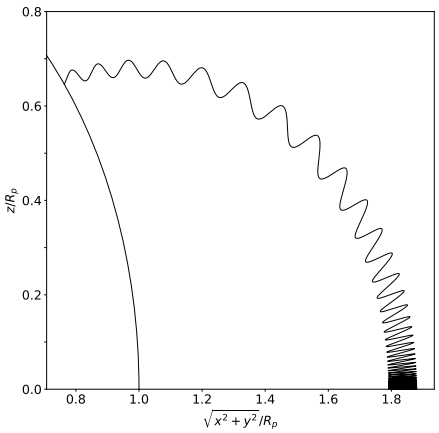

(b) Vertical displacement against cylindrical radial distance, with Jupiter drawn as arc.

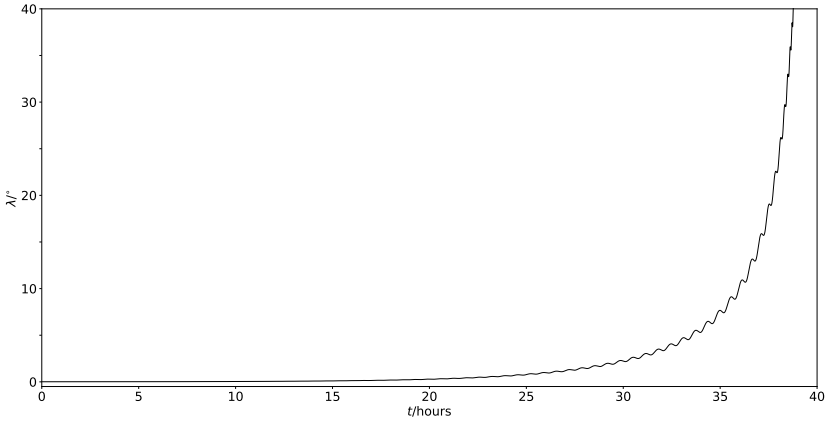

(c) Latitude over time.

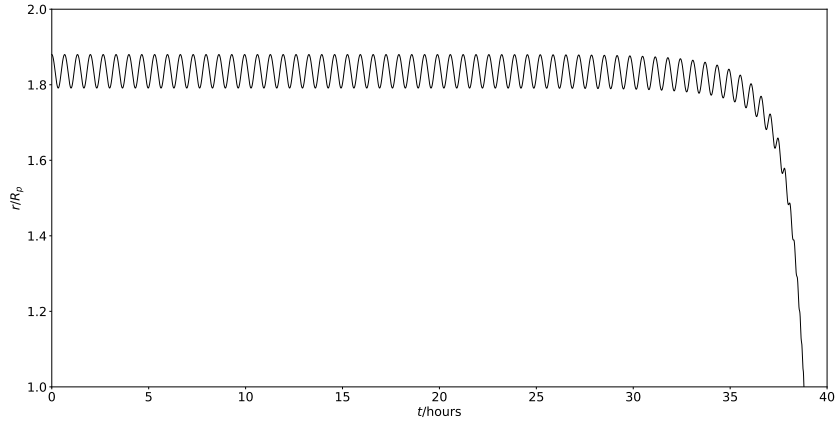

(d) Radial range over time.

Figure 3.3: Trajectory of vertically unstable grain around Jupiter, with charge-to-mass ratio of $L_* = 9.32$, and initial launch position of $r_L = 1.88\,R_p$. The grain's vertical oscillations grow until it collides with the planet.

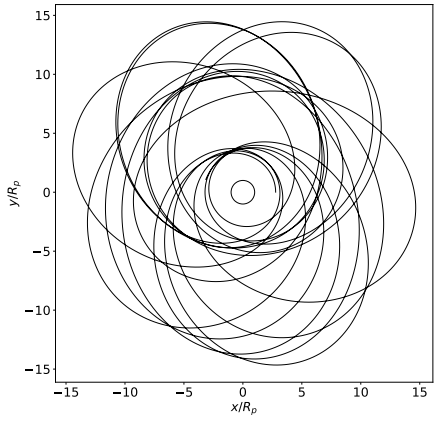

(a) Plan view, with Jupiter denoted by circle.

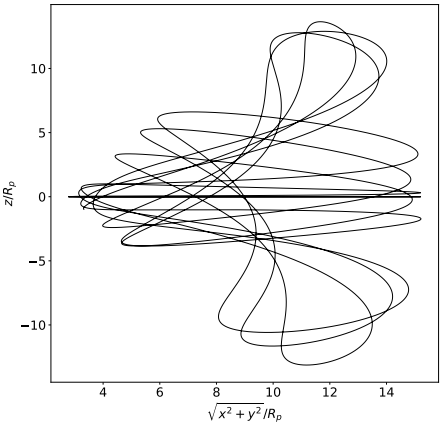

(b) Vertical displacement against cylindrical radial distance.

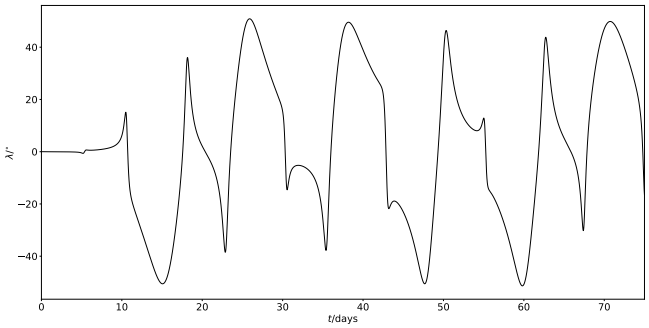

(c) Latitude over time.

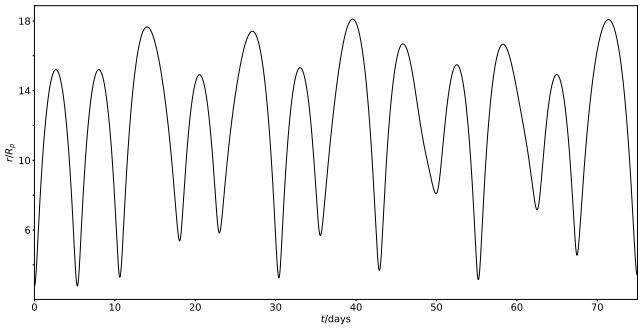

(d) Radial range over time.

Figure 3.4: Trajectory of stable grain around Jupiter, with charge-to-mass ratio of $L_* = 0.42$, and initial launch position of $r_L = 2.78\,R_p$. Large radial oscillations excite large vertical oscillations after about 10 days.

3.2.2 Stability Maps of Saturn and Jupiter

In order to further test the numerical code (§2.4) and cover the parameter space in a systematic way following Jontof-Hutter (2012), 8000 simulations were run, for positive and negative charges respectively, over a grid of 80 values of L_* (Eq. 1.3) and 100 values of r_L (launch position), sampling a range of charge-to-mass ratios from gravity-dominated to electromagnetically-dominated ($L_* = 0.01$ - 100 on a $\log_{10}$-scale), and sampling launch positions from the planetary surface to beyond the main ring system ($r_L = 1$ - $3\,R_p$ on a linear scale). The dust grains were initialised with the circular Kepler velocity of $v_{\rm K} = \sqrt{\frac{GM_p}{r}}$, appropriate for icy regolith removed from the parent ring bodies, and their trajectories followed for 0.1 years, as Jontof-Hutter (2012) determined that all relevant dynamical timescales are < 0.1 years, and that the appearance of the stability maps did not change appreciably over longer integration times. The results of these $16,000$ simulations for both Saturn and Jupiter are shown in Figure 3.5. The launch positions of the grains were chosen to span the full extent of the main rings, and sample positions both inside and outside synchronous orbit, $R_{\rm syn}$, the location where a grain orbiting at its Keplerian velocity matches the rate at which the planet is spinning.

There are four orbital outcomes awaiting the dust grain; for reference, the designated colour key in Figure 3.5 is included in parentheses:

- Stable (yellow).
  The grain remains in orbit close to the ring-plane. An example of this is shown in Figure 3.1.

- Stable with large vertical excursions (light grey).
  The grain remains in orbit and reaches latitudes exceeding λ_m. Examples of this are shown in Figures 3.2 and 3.4.

- Radially unstable (black).
  The grain either collides with the planet ($r \leq R_p$) or escapes the system ($r > 30\,R_p$).

- Vertically unstable (dark grey).
  The grain strikes the planet above a latitude threshold of $\lambda_m = 5°$. An example of this is shown in Figure 3.3.

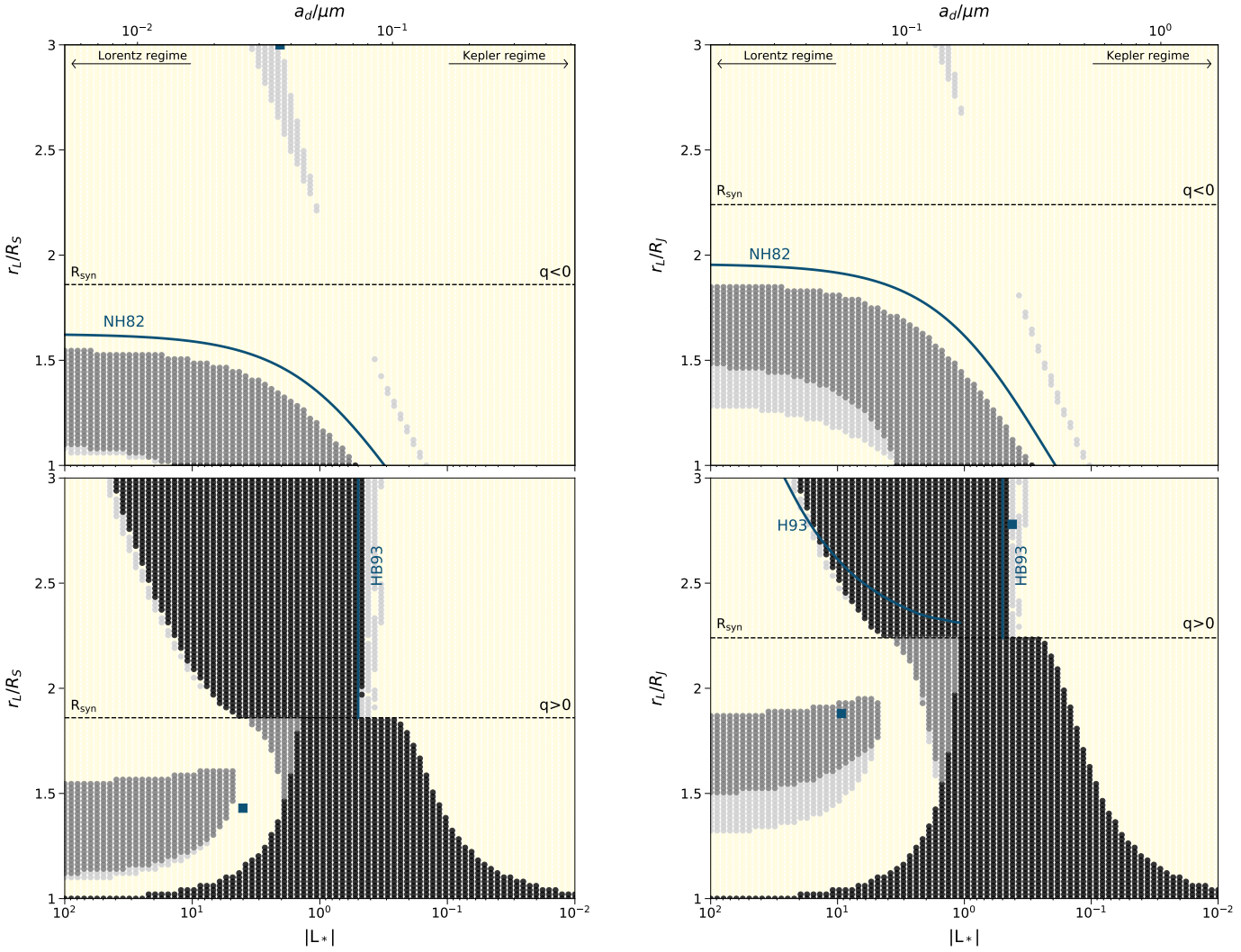

(a) Saturn.

(b) Jupiter.

Figure 3.5: Stability maps for Saturn and Jupiter, with the $\vec{B}$ field modelled as an aligned centred dipole. r_L is given in units of the respective planetary radii around which the grains are launched. The colour key (yellow, light grey, dark grey, black) is explained in the main text of this section. The blue squares denote trajectories shown in Figures 3.1 - 3.4. The earlier work of Northrop & Hill (1982), Horányi et al. (1993a) and Hamilton (1993), giving analytical stability boundaries, are given by the blue curves labelled NH82, H93 and HB93 respectively. The top horizontal axes indicate grain sizes representative of a charging potential of ± 5 V and grain density $\rho_d = 1\,\mathrm{g\,cm^{-3}}$, refer to equations 1.4 and 1.5.

The stability boundaries derived by Northrop & Hill (1982), Horányi et al. (1993a), and Hamilton & Burns (1993) are overplotted on the simulation results in Figure 3.5, and indicate that further analysis is necessary to understand the rich and varied behaviour across the parameter space, which is provided by the work of Jontof-Hutter & Hamilton (2012a), and described in more detail in §§3.5.2, 3.5.3 and 3.6.2 .

The curves labelled NH82 were obtained by converting Northrop & Hill (1982)'s equation (10) for the marginal stability radius, ρ_c, into the parameters of this work:

$$\rho_c^3 = \frac{2}{3} \frac{GM_p}{\left(\Omega_p - \frac{\Omega_p}{3L_*}\right)}. \tag{3.1}$$

The $L_* = \frac{1}{2}$ radial stability boundary labelled HB93 is obtained by considering when the escape velocity of Eq. 1.2, described in Hamilton & Burns (1993), is real-valued. Horányi et al. (1993a) modelled the largest grain sizes that will remain tied to magnetic field lines as a function of distance from Jupiter, and data from their Figure 2 is digitised and presented as curve H93 on Figure 3.5.

In order to understand the various orbital outcomes observed in Figure 3.5, an analysis following Jontof-Hutter (2012) is performed, and necessitates an understanding of the Hamiltonian of the system, presented in §3.3. After the analysis in §§3.5.2, 3.5.3 and 3.6.2, a discussion of the similarities/differences between the stable/unstable regions of Saturn and Jupiter follows. The stability boundaries are summarised in Figure 3.20, and are overplotted on top of the numerical results of Figure 3.5 in Figure 3.21 following a description of the theory in the next sections.

3.3 Hamiltonian and Potential

The Hamiltonian for a dust grain of mass m_d and charge q_d in orbit around a rotating magnetic planet of mass M_p and radius R_p can be expressed (e.g. Iñarrea et al. 2004) as

$$H = \frac{1}{2m_d}\left(\vec{p} - q_d\vec{A}\right)^2 + U(\vec{r}), \tag{3.2}$$

where $\vec{r} = (x, y, z)$ and $\vec{p}$ is the conjugate momentum of $\vec{r}$. The scalar potential $U(\vec{r})$ contains terms describing the gravitational and electric interactions, while the vector potential $\vec{A}$ describes the magnetic forces.

For a magnetic dipole with strength $|\vec{m}| = g_1^0 R_p^3$ aligned with the spin axis of the planet, the vector field is:

$$\vec{A} = \frac{\vec{m} \times \vec{r}}{r^3}, \tag{3.3}$$

and as $\vec{B} = \vec{\nabla} \times \vec{A}$:

$$\vec{B} = \frac{3(\vec{m} \cdot \vec{r})\vec{r}}{r^5} - \frac{\vec{m}}{r^3}. \tag{3.4}$$

Under the assumption that the planet is surrounded by a conducting plasma, which rigidly rotates with the planet at Ω_p, there is a corotational electric field (e.g. Birmingham & Northrop 1979, refer to §1.3.1), Eq. 1.37 repeated here for reference:

$$\vec{E} = -(\vec{\Omega}_p \times \vec{r}) \times \vec{B}.$$

If $\vec{\Omega}_p$ and $\vec{m}$ are aligned along z, then $\vec{E} = -|\vec{m}|\Omega_p(\frac{x}{r^3}, \frac{y}{r^3}, 0)$ using Eq. 1.37. Further restricting attention to motion in the equatorial plane, so that $r^2 = x^2 + y^2 := \rho^2$ (cylindrical radius), the scalar electric potential can be found using $q_d\vec{E} = -\vec{\nabla}\Psi$:

$$\begin{aligned}
\frac{\partial}{\partial x}\left(\frac{x^2+y^2}{r^3}\right) &= \frac{\partial}{\partial x}\left(\frac{1}{\sqrt{x^2+y^2}}\right) = -\frac{x}{r^3}, \\
\frac{\partial}{\partial y}\left(\frac{x^2+y^2}{r^3}\right) &= \frac{\partial}{\partial y}\left(\frac{1}{\sqrt{x^2+y^2}}\right) = -\frac{y}{r^3}, \\
\frac{\partial}{\partial z}\left(\frac{x^2+y^2}{r^3}\right) &= 0,
\end{aligned}$$

so that $\Psi = q_d|\vec{m}|\Omega_p\left(\frac{x^2+y^2}{r^3}\right) = q_d|\vec{m}|\Omega_p\psi$. Using the expressions for the magnetic dipole vector potential of Eq. 3.3 and dimensionless electric potential, $|\vec{A}| = A_\phi = \frac{|\vec{m}|\rho}{r^3}$ and $\psi = \frac{\rho^2}{r^3}$, in cylindrical coordinates (ρ, ϕ, z), the Hamiltonian of Eq. 3.2 can be expressed as

$$H = \frac{1}{2m_d}(p_\rho^2 + p_z^2) + \frac{1}{2m_d\rho^2}(p_\phi - q_d\rho A_\phi)^2 + U(r), \tag{3.5}$$

where the canonical conjugate momentum is

$$\frac{p_\phi}{m_d} = \rho^2(\dot{\phi} + \Omega_g), \tag{3.6}$$

substituting in for the gyrofrequency,

$$\Omega_g = \frac{q_d B}{m_d} = \frac{q_d|\vec{m}|}{m_d r^3}. \tag{3.7}$$

The potential, $U(r)$ in Eq. 3.5, contains terms relating to the gravitational and corotational electric field of the planet:

$$U(r) = -\frac{GM_p m_d}{r} + \frac{q_d \vec{m}\Omega_p\rho^2}{r^3}. \tag{3.8}$$

Equation 3.5 can be expressed as

$$H = \frac{p_\rho^2 + p_z^2}{2m_d} + U(\rho, z), \tag{3.9}$$

where the potential in terms of the cylindrical radius and vertical displacement is

$$U(\rho, z) = \frac{1}{2m_d\rho^2}\left(p_\phi - q_d|\vec{m}|\frac{\rho^2}{r^3}\right)^2 - \frac{GM_p m_d}{r} + \frac{q_d|\vec{m}|\Omega_p\rho^2}{r^3}. \tag{3.10}$$

Equations 3.9 and 3.10 are directly equivalent to expressions 3 and 4 in Howard et al. (1999), dividing through by m_d:

$$\begin{aligned}\mathcal{H} = \frac{H}{m_d} &= \frac{\dot{\rho}^2 + \dot{z}^2}{2} + \frac{1}{2\rho^2}\left(\frac{p_\phi}{m_d} - \frac{q|\vec{m}|\rho^2}{m_d r^3}\right)^2 - \frac{GM_p}{r} + \frac{q|\vec{m}|\Omega_p\rho^2}{m_d r^3} \\ \implies \mathcal{H} &= \frac{\dot{\rho}^2 + \dot{z}^2}{2} + \frac{1}{2\rho^2}\left(\frac{p_\phi}{m_d} - \Omega_g\rho^2\right)^2 - \frac{GM_p}{r} + \Omega_g\Omega_p\rho^2.\end{aligned} \tag{3.11}$$

Then substituting for L_* using the expression of 1.3, Eq. 3.11 can be written as

$$\mathcal{H} = \frac{\dot{\rho}^2 + \dot{z}^2}{2} + \mathcal{U}^e, \tag{3.12}$$

where

$$\mathcal{U}^e = \frac{1}{2\rho^2}\left(\frac{p_\phi}{m_d} - L_* \frac{GM_p\rho^2}{\Omega_p r^3}\right)^2 + \frac{GM_p}{r}\left(L_*\frac{\rho^2}{r^2} - 1\right), \tag{3.13}$$

as stated in Jontof-Hutter (2012)'s equations (3.3) and (3.4).

Although some orbits are locally unstable, the grain could enter a region of parameter space where its orbit is globally stable. With a global analysis in mind, the potential of Eq. 3.13 can be manipulated into a more useful form, as given in §3.5.1.

3.4 Azimuthal Motion

3.4.1 Guiding Centre Approximation

As introduced in §3.1, Alfvén (1940, 1950) developed a first order perturbation theory for the motion of a charged particle in a magnetic field. This treats the motion as a superposition of a relatively fast circular epicycle superposed around an equilibrium point, the guiding centre, which itself drifts. This is illustrated in Figure 3.6. Highly charged grains are almost 'tied' to magnetic field lines, that is, they gyrate in tight fast orbits around the field lines which orbit at Ω_p (e.g. Mendis et al. 1982).

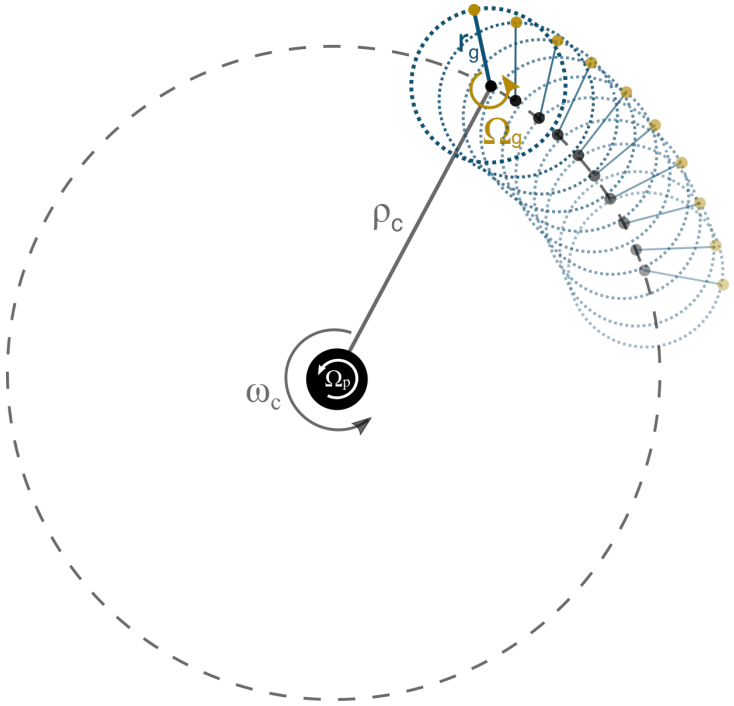

Figure 3.6: The guiding centre model. The charged grain (yellow point) gyrates in an epicycle of size r_g at frequency Ω_g around the guiding centre (small black point), which is located at a distance of ρ_c from the central planet (large black point) and drifts with frequency ω_c. The planet itself rotates at Ω_p, and the magnetic field lines are assumed to rotate rigidly at this rate. Snapshots for some past instances are indicated by progressively fainter drawings.

The planet's magnetic field defines a direction. It is constructive to consider the motion of the grain parallel and perpendicular to $\vec{B}$, which is :

$$\vec{F}_{\parallel} = m_d \frac{d\vec{v}_{\parallel}}{dt} \tag{3.14a}$$

$$q_d(\vec{v}_{\perp} \times \vec{B}) + \vec{F}_{\perp} = m_d \frac{d\vec{v}_{\perp}}{dt}, \tag{3.14b}$$

where $\vec{F}$ is any external force field which interacts with the grain, with longitudinal component $\vec{F}_{\parallel} = \frac{\vec{F}\cdot\vec{B}}{B}$ and transverse component $\vec{F}_{\perp} = \frac{\vec{F}\times\vec{B}}{B}$. The overall motion of the grain is composed of a constant velocity in the $\parallel$ direction and a circular motion in the $\perp$ direction, resulting in a spiral in the non-rotating frame. In Figure 3.6, a relatively slow Ω_g has been sketched for clarity and therefore a loose spiral would be traced out by the grain.

Equation 3.14b can be further separated into gyratory motion about the field line (subscript g) and motion relative to the field line about a guiding centre (subscript c), as $\vec{v}_{\perp} = \vec{v}_g + \vec{v}_c$, so that the Lorentz accelerations perpendicular to $\vec{B}$ can be written as

$$m_d \frac{d\vec{v}_g}{dt} = q_d(\vec{v}_g \times \vec{B}), \tag{3.15a}$$

$$m_d \frac{d\vec{v}_c}{dt} = q_d(\vec{v}_c \times \vec{B}) + \vec{F}_{\perp}. \tag{3.15b}$$

Since the magnetic dipole will be aligned with z for the sake of analysis (pointing out of the page in Figure 3.6), the $\perp$ direction is synonymous with azimuthal gyromotion, $v_{\perp} \rightarrow v_g$. Equating the magnitude of the Lorentz force to the centripetal force in Eq. 3.15a results in a expression for $v_g = \frac{q_d r_g B}{m_d}$ and an expression for the gyrofrequency:

$$\Omega_g = \frac{q_d B}{m_d}. \tag{3.16}$$

The perturbation theory of Alfvén (1940, 1950) holds under the assumption that the magnetic field variations in space, ∂x_j, and time, dt, are small within a gyroradius and a gyroperiod, that

is

$$r_g \ll \frac{\partial B_j}{\frac{\partial B_j}{\partial x_k}}, \tag{3.17a}$$

$$\frac{1}{\Omega_g} \ll \frac{\partial B_j}{\frac{dB_j}{dt}}. \tag{3.17b}$$

3.4.2 Drifts

Equation 3.15a describes the Larmor motion of the epicycle, while Eq. 3.15b describes the motion of the guiding centre, which can be described as

$$\vec{v}_c = \frac{\vec{F}_\perp \times \vec{B}}{q_d B^2}, \tag{3.18}$$

assuming that the drift velocity is constant in time.

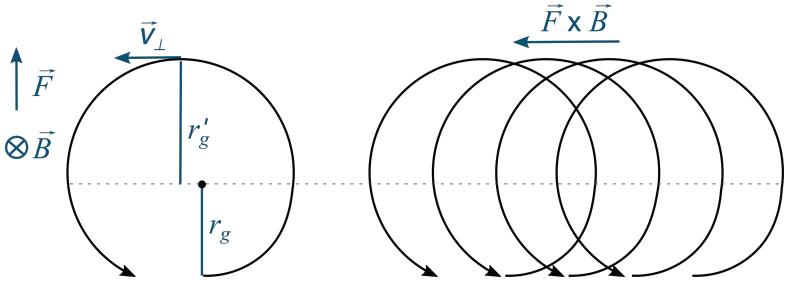

Figure 3.7: The guiding centre, indicated by the black point, drifts due to the variation in gyroradius over the course of a gyration: $r_g \rightarrow r_g{}'$. The magnetic field, $\vec{B}$, points into the page. The regions of the gyration labelled r_g (below the dashed line) have reduced gyroradius (and slower velocities) compared to those labelled $r_g{}'$.

The presence of an additional force, $\vec{F}_\perp$, causes the grain to undergo variations in velocity as it executes gyrations. At some points in the grain's orbit, $\vec{F}_\perp$ will act in the same direction as the Lorentz force, causing a larger gyroradius and acceleration, whilst at other points in the gyro-orbit $\vec{F}_\perp$ will oppose the Lorentz force, causing a smaller gyroradius and deceleration. Once the periodic variation in gyroradius is averaged over, a net drift remains because the gyro-orbit

does not quite close. This is illustrated in Figure 3.7, showing how the velocity vector has a leftward component, $\vec{F} \times \vec{B}$, during the half of the gyro-orbit where velocity is fastest (labelled $r_g{}'$).

For a charged grain in a planetary gravitational and magnetic field, the sources of $\vec{F}_\perp$ to consider are the gravitational attraction of the planet, $\vec{F}_\perp = m_d\vec{g}$, and the corotational electric field of Eq. 1.37, $\vec{F}_\perp = q_d\vec{E}$:

$$\vec{v}_G = \frac{m_d\vec{g} \times \vec{B}}{q_d B^2}, \tag{3.19}$$

$$\vec{v}_E = \frac{\vec{E} \times \vec{B}}{B^2}. \tag{3.20}$$

In the case of Saturn and Jupiter, $\vec{E}$ points radially outward, and explains the observations of dust streams (§1.2.2).

Analogously, a variation in the strength of the magnetic field causes a drift in a direction perpendicular to both the field and the direction in which the field increases (Lehnert 1964):

$$\vec{v}_\nabla = \frac{1}{2B^2}\frac{v_\perp^2}{\Omega_g}(\vec{B} \times \vec{\nabla}B), \tag{3.21}$$

as regions of stronger magnetic field strength cause the grain to exhibit smaller gyro-orbits and vice versa, and causing the gyro-orbit to not quite close, as illustrated in Figure 3.7.

In addition, vertical motion along the curved magnetic field lines results in centrifugal forces (Jontof-Hutter 2012) and causes a drift perpendicular to both the centrifugal force and the magnetic field. This effect is weak close to the equatorial plane and will not be considered here in detail. The drifts of Equations 3.19, 3.20 and 3.21 are illustrated in Figure 3.8.

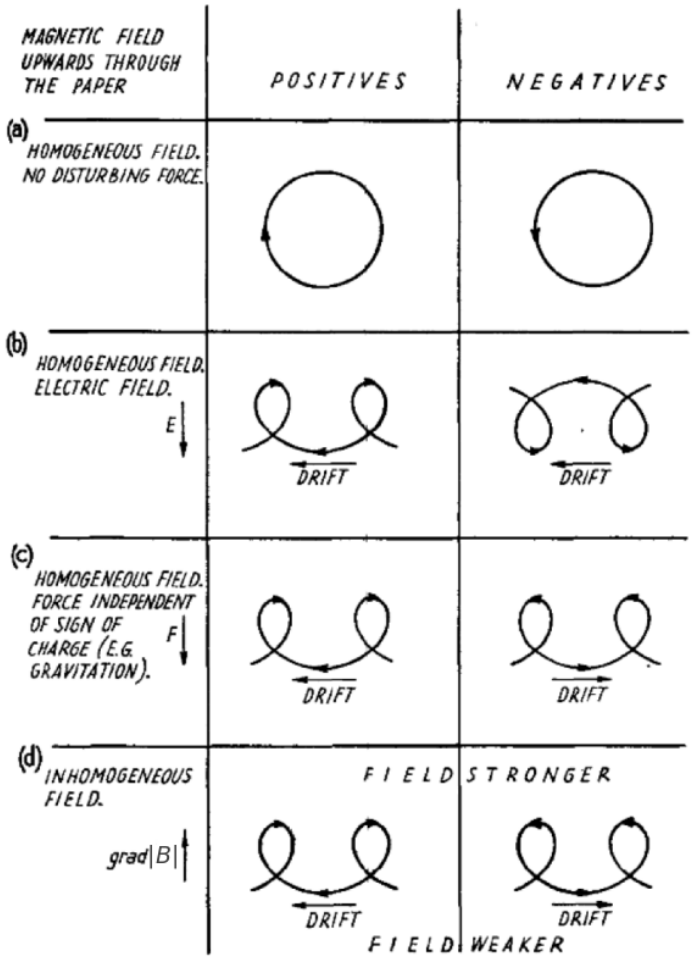

Figure 3.8: Various types of drifts for positively and negatively charged grains: (a) in the absence of a perturbing force, the grain exhibits gyromotion alone – the Ω_g motion described in Figure 3.6; (b) $\vec{E} \times \vec{B}$ drift of Eq. 3.20; (c) $\vec{g} \times \vec{B}$ drift of Eq. 3.19; (d) $\vec{\nabla} B$ drift of Eq. 3.21, from Alfvén (1950) with minor alteration of symbol $H \rightarrow B$.

3.4.3 Orbital Velocity of the Guiding Centre

The guiding centre's orbital frequency, ω_c, is the result of the net effect of the drifts described in §3.4.2. The equilibrium point is the guiding centre of epicyclic motion and an expression can be derived from considering the stationary points of the potential. Beginning with the potential of Eq. 3.13, substituting for $\frac{p_\phi}{m_d} = \rho_c^2(\omega_c + \Omega_{gc})$, the canonical conjugate momenta for grains at the guiding centre, and evaluating in the equatorial plane ($r \to \rho$), gives the potential in a more useful form:

$$\mathcal{U}^e = \frac{1}{2}\frac{\rho_c^4\omega_c^2}{\rho^2} + \frac{\rho_c^4\omega_c^3 L_*}{\Omega_p\rho^2} - \frac{\rho_c^2\omega_c G M_p L_*}{\Omega_p\rho^3} + \frac{\rho_c^4\omega_c^4 L_*^2}{2\rho^2\Omega_p^2} - \frac{\omega_c^2\rho_c^2 L_*^2 G M_p}{\rho^3\Omega_p^2} + \frac{G^2 M_p^2 L_*^2}{2\Omega_p^2\rho^4} + \frac{G M_p L_*}{\rho} - \frac{G M_p}{\rho}. \tag{3.22}$$

The derivative of the potential, Eq. 3.22, is

$$\frac{\partial\mathcal{U}^e}{\partial\rho} = -\frac{\rho_c^2\omega_c^2}{\rho^3}\left(\rho_c^2 + 2\frac{\rho_c^2\omega_c L_*}{\Omega_p} + \frac{\rho_c^2\omega_c^2 L_*^2}{\Omega_p^2}\right) - \frac{G M_p}{\rho^2}\left(L_* - 1 - 3\frac{\rho_c^2\omega_c L_*}{\rho^2\Omega_p} - 3\frac{\rho_c^2\omega_c^2 L_*^2}{\rho^2\Omega_p^2} + 2\frac{G M_p L_*^2}{\Omega_p^2\rho^3}\right), \tag{3.23}$$

and making substitutions of $\frac{\partial\mathcal{U}^e}{\partial\rho}\big|_{\rho=\rho_c,z=0} = 0$ and $\omega_c = \sqrt{\frac{GM_p}{\rho_c^3}}$, so that at equilibrium,

$$\rho_c\omega_c^2 + \frac{G M_p L_*}{\rho_c^2}\left(1 - \frac{\omega_c}{\Omega_p}\right) - \frac{G M_p}{\rho_c^2} = 0, \tag{3.24}$$

which is in agreement with Jontof-Hutter & Hamilton (2012a).

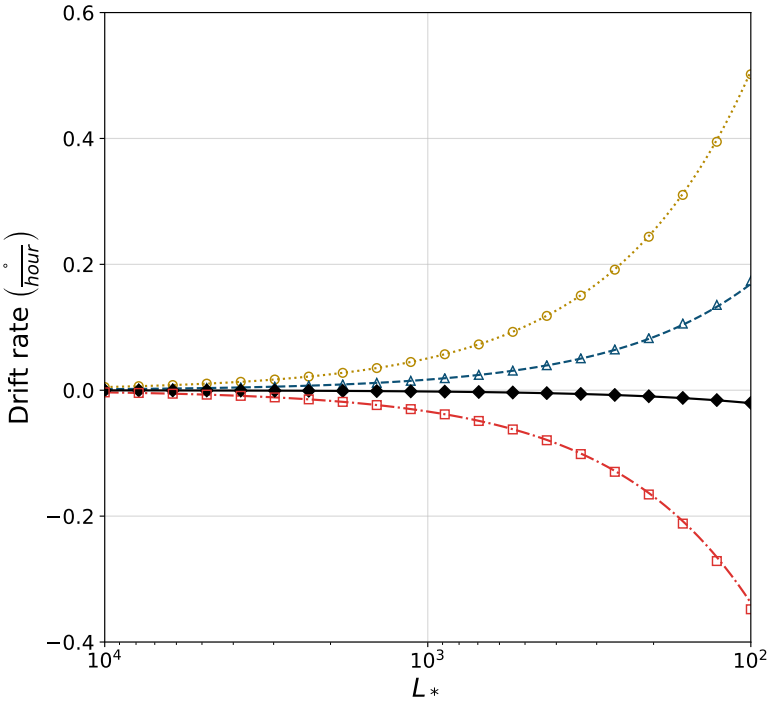

Figure 3.9: Drift rates for highly charged grains launched inside, and close to, synchronous orbit ($r_L = 0.98\,R_{\text{syn}}$) around Saturn, expressed in the corotating frame, reproducing Jontof-Hutter (2012)'s Figure 3.12. The analytical solutions for azimuthal motion are plotted as curves: the lowermost red dot-dashed shows $\vec{g} \times \vec{B}$ drift, Eq. 3.19; the uppermost yellow dotted curve shows $\vec{\nabla} B$ drift, Eq. 3.21; the dashed blue curve is a superposition of the $\vec{\nabla} B$ and gravity drifts; and the solid black curve shows the guiding centre's motion in a gravitational and rotating magnetic field, ω_c, Eq. 3.24. Numerical simulations are indicated by markers, with open symbols indicating no planetary rotation. Circles indicate that only $\vec{B}$ terms were included, squares that only $\vec{g}$ field terms were included, triangles that both $\vec{g}$ and $\vec{B}$ terms were included. The filled diamonds indicate simulation runs performed with gravitational and magnetic field terms for a rotating planet.

Twenty simulations were run to check numerical results against the drift equations 3.19, 3.20, 3.21, and 3.24. Figure 3.9 shows good agreement between the numerical and analytical results, and confirms Jontof-Hutter (2012)'s results. The drift rates in Figure 3.9 are relative to the

magnetic field, this can be seen in how the very highly charged grains' drift rates in Figure 3.9 tend to zero, as those grains are 'tied' to the field lines. The expressions given by Equations 3.21 and 3.19 are *relative* to the magnetic field lines, whereas the simulations were performed in an inertial frame centred on the planet, and therefore a correction of $(-\Omega_p t)$ was necessary to transform the azimuthal angular displacement of the grains to the magnetic field's corotating frame. The $-\Omega_p t$ correction was unnecessary for the simulations with only $\vec{\nabla} B$ and $\vec{g} \times \vec{B}$ drifts, as those contain no rotating field terms. Note that Figure 3.9 does not include an $\vec{E} \times \vec{B}$ drift of Eq. 3.20 as there is no electric field in the corotating frame (§1.3.1).

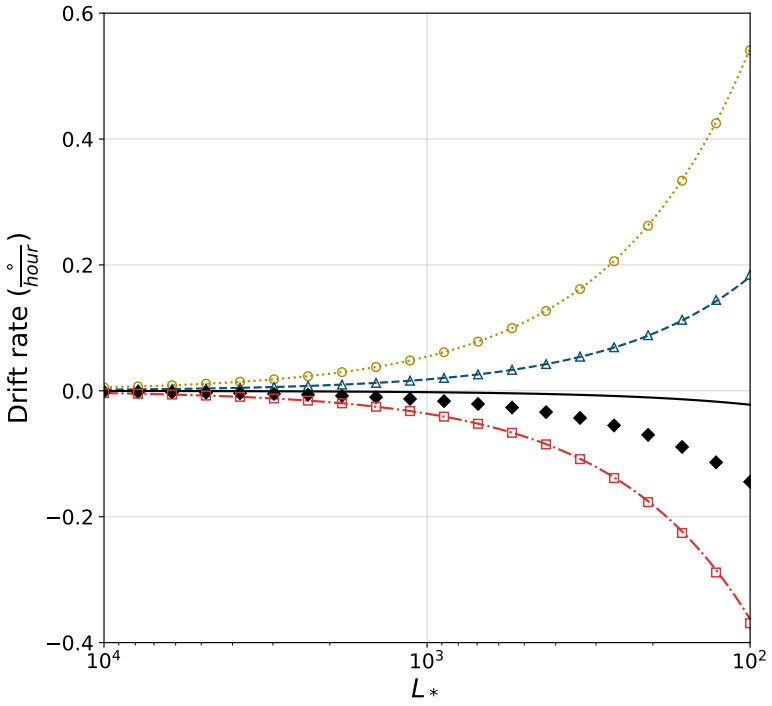

Figure 3.10: As for Figure 3.9, but for grains launched further away from synchronous orbit with $r_L = 0.7\, R_{\text{syn}}$.

As it will be described in §3.5.1, the gyroradii are small near synchronous orbit: as $r_L \to R_{\text{syn}}, n_L \to \Omega_p \implies r_g \to 0$, Eq. 3.26, and therefore the epicyclic approximation of §3.4.1 holds. However, further from R_{syn} the conditions of 3.17 no longer hold, as the gyro-orbits

of the grains are larger than the characteristic scales for variations in the magnetic field (3.17). This leads to poorer agreement between ω_c curve of Eq. 3.30 and the simulated results, as demonstrated in Figure 3.10.

3.5 Radial Motion

3.5.1 Gyroradius

Following Jontof-Hutter (2012)'s method, the potential of Eq. 3.13 can be written as a polynomial by straightforward algebraic manipulations, substituting in for the gyrofrequency evaluated at the launch position, $\Omega_{gL} = \frac{L_* n_L^2}{\Omega_p}$, and the Keplerian orbital frequency at the launch position, $n_L^2 = \frac{GM_p}{r_L^3}$:

$$\mathcal{U}^e(r, L_*) = \frac{GM_p}{r_L}\left(A\frac{r_L^4}{r^4} + B\frac{r_L^3}{r^3} + C\frac{r_L^2}{r^2} + D\frac{r_L}{r}\right). \tag{3.25}$$

The dimensionless coefficients of Eq. 3.25 are

$$A = \frac{n_L^2 L_*^2}{2\Omega_p^2}, \quad B = -\frac{n_L L_*}{\Omega_p}\left(\frac{n_L L_*}{\Omega_p} + 1\right), \quad C = \frac{1}{2}\left(\frac{n_L L_*}{\Omega_p} + 1\right)^2, \quad D = L_* - 1.$$

Expressed in this manner, $\mathcal{U}^e$ is in a more useful form for stability analysis, refer to §§3.5.2, 3.5.3 and 3.6.2.

The size of the epicycles can be approximated by solving, to first-order, the distance to the minimum $\frac{\partial U}{\partial r}\Big|_{\rho=\rho_c, z=0} = 0$. Differentiating Eq. 3.25 with respect to r, taking $r \to \rho_c$, dropping higher order terms since the gyroradius is much smaller than the launch radius, $r_g \ll r_L$, substituting for Ω_{gL} (using Equations 1.3 and 3.16) and eliminating $L_* = \frac{\Omega_p \Omega_{gL}}{n_L^2}$ results in an expression for the gyroradius:

$$r_g = \frac{r_L(\Omega_p - n_L)\Omega_{gL}}{\Omega_{gL}^2 - \Omega_{gL}(3\Omega_p + n_L) + n_L^2}, \tag{3.26}$$

which is a signed quantity, and only depends on parameters known at launch, denoted by subscript L (Jontof-Hutter 2012). Note the gyrofrequency of Eq. 3.16 evaluated at the launch

distance r_L can be expressed in terms of the Kepler orbital frequency, n_L:

$$\Omega_{gL} = \frac{n_L^2 L_*}{\Omega_p}. \tag{3.27}$$

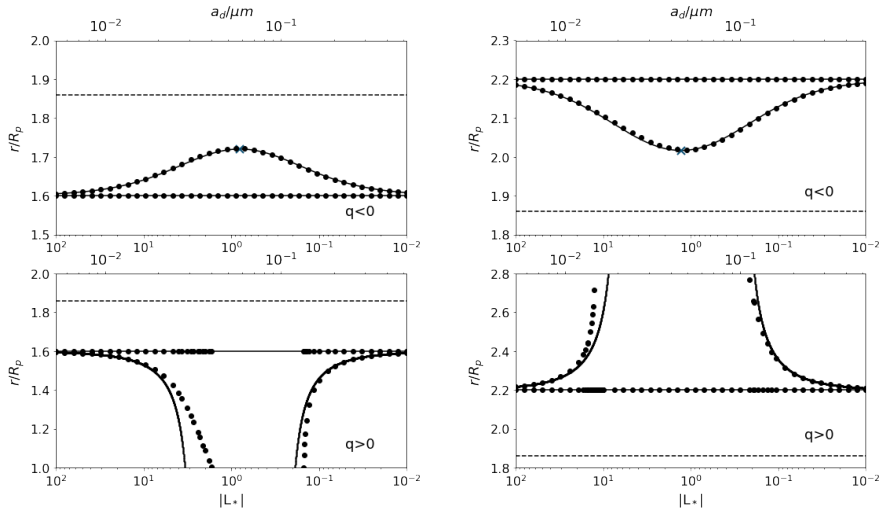

(a) Negative (top) and positive (bottom) grains launched at $r_L = 1.6\,R_S$.

(b) Negative (top) and positive (bottom) grains launched at $r_L = 2.2\,R_S$.

Figure 3.11: Total radial range of grains launched at r_L, with Keplerian velocity $v_K = \sqrt{\frac{GM_p}{r_L}}$ around Saturn; the left hand plot shows results for grains launched inside R_{syn}, the right hand plot for outside R_{syn}. Analytical results, Eq. 3.26, are shown as solid curves, numerical simulation results are given by points. The blue cross indicates the location of the maximum radial excursion given by Eq. 3.28. Synchronous orbit is denoted by dashed line.

The assumptions under which Eq. 3.26 was derived hold in the Lorentz and Kepler limits, where the gyroradius is small, but not for intermediate L_*. The validity of the epicyclic approximation (3.17) does not hold far away from R_{syn}. The work of Mendis et al. (1982) and Mitchell et al. (2003) found that positive grains with intermediate-sized charge-to-mass ratios exhibited large non-circular epicycles. Therefore, it is anticipated that the first-order expression of Eq. 3.26 will not recover the true behaviour of such grains, and this is explored further in §3.5.3. This is illustrated in Figure 3.11, plotting the radial range of motion $2r_g$ over a range of charge-to-mass ratios both inside and outside synchronous orbit.

The turning points of Eq. 3.26 can found by solving $\frac{dr_g}{dL_*} = 0$, and are indicated in Figure 3.11,

$$\text{For } L* < 0: \quad L_* = -\frac{\Omega_p}{n_L}, r_g^- = \frac{r_L}{3}\left(\frac{n_L - \Omega_p}{n_L + \Omega_p}\right) \tag{3.28}$$

$$\text{For } L* > 0: \quad L_* = +\frac{\Omega_p}{n_L}, r_g^+ = \frac{r_L(\Omega_p - n_L)}{n_L - 3\Omega_p}. \tag{3.29}$$

Given the ellipticity of epicycles for positive grains, although Eq. 3.28 does a good job of describing a negatively-charged grain's maximum excursion, Eq. 3.29 does not describe a positively-charged grain's radial range well.

3.5.2 Local Radial Stability

For a grain to be radially stable, it must exhibit epicyclic motion about the guiding centre (§3.4.1). That is, it must gyrate about an equilibrium point (guiding centre, §3.4) determined by taking the derivative of the potential: $\frac{\partial U}{\partial \rho} = 0$. The epicyclic frequency, κ_c, is that at which the grain oscillates radially.

The grains under study are those launched from parent main ring bodies, and therefore the equatorial equilibrium points are considered. The stability is determined by considering the nature of the equilibria: if $\frac{\partial^2 U}{\partial \rho \partial z}\Big|_{\rho=\rho_c, z=0} = 0, \quad r \to \rho$, then stability against radial or vertical perturbations depends on the signs of $\frac{\partial^2 U}{\partial \rho^2}$ and $\frac{\partial^2 U}{\partial z^2}$, respectively (Northrop & Hill 1982). As the parent ring bodies themselves are unaffected by electromagnetic forces and hence the grains will be launched with an initial Keplerian velocity, it is important to distinguish between physical quantities evaluated at the Kepler launch position and those at the guiding centre, following Jontof-Hutter (2012): subscript c denotes the guiding centre, and subscript L denotes the launch position. As in the previous sections, the magnetic field of the planet is treated as an aligned centred dipole. Cases where the oscillations about the equilibria remain small are locally stable, the case which will be presented in this section, but there are also cases where the grain experiences large radial excursions (§3.5.1), and for those a global stability analysis is necessary (§3.5.3).

Stability requires the existence of an equilibrium point. Local stability of the guiding centre is determined using $\frac{\partial^2 U}{\partial \rho^2}\Big|_{\rho=\rho_c, z=0} = 0$. Equation 3.24 in §3.4.3 can be solved straightforwardly:

$$\omega_{c\pm} = \frac{1}{2\rho_c}\left(\frac{GM_pL_*}{\rho_c^2\Omega_p} \pm \sqrt{\left(\frac{GM_pL_*}{\Omega_p\rho_c^2}\right)^2 - \frac{4GM_p}{\rho_c}(L_*-1)}\right). \tag{3.30}$$

The number of solutions is determined in the usual manner; when the discriminant of the quadratic in ω_c given by Eq. 3.24 is positive there are two real roots:

$$\left(\frac{GM_pL_*}{\Omega_p\rho_c^2}\right)^2 - \frac{4GM_p}{\rho_c}(L_*-1) > 0. \tag{3.31}$$

A condition which satisfies the inequality of 3.31 is $L_* < 1$. Therefore there are no local radially unstable orbits for negatively charged grains. To consider the stability criteria for positive grains, if $L_* > 1$ then there are only two real roots (that is, two equilibrium points) if the condition of 3.31 holds, namely,

$$\left(\frac{\rho_c}{R_{\text{syn}}}\right)^3 < \frac{L_*^2}{4(L_*-1)}, \tag{3.32}$$

where $\Omega_p = \sqrt{\frac{GM_p}{R_{\text{syn}}^3}}$.

Inside synchronous orbit, R_{syn}, the left hand side of Eq. 3.32 < 1 and so two equilibria always exist. As ρ_c increases to greater distance from the planet away from R_{syn}, there are fewer L_* values for which the inequality of 3.32 holds and so the region of local instability extends upward from R_{syn} to include an larger range of charge-to-mass values, Figure 3.5.

For a local radial stability analysis, large oscillations are neglected and only small amplitude motion near the guiding centre are considered,

$$\ddot{\rho} + \frac{\partial^2 U}{\partial \rho^2}\rho = 0. \tag{3.33}$$

Small radial motions are stable when the second derivative is positive: $\left.\frac{\partial^2 U}{\partial \rho^2}\right|_{\rho=\rho_c,z=0} = \kappa_c^2 > 0$. An expression for the epicyclic frequency,

$$\kappa_c^2 = \omega_c^2 - 4\omega_c\Omega_{gc} + \Omega_{gc}^2, \tag{3.34}$$

is given in Mendis et al. (1982), noting that they use the opposite sign convention for the gyrofrequency, which is evaluated at the guiding centre, similarly to Eq. 3.27:

$$\Omega_{gc} = \frac{n_c^2 L_*}{\Omega_p} = \frac{q_d B}{m_d}. \tag{3.35}$$

In the Kepler limit, $\kappa_c \to n_c$, the expected behaviour of the grain's frequencies converging to the gravitational limit and the epicyclic ellipse has a minor to major axis ratio of $\frac{1}{2}$ (Mendis et al. 1982). In the Lorentz limit, $\kappa_c \to \Omega_{g_c}$ and $\omega_c \to \Omega_p$, and the general elliptical epicycle reduces to a circle, the well-known behaviour of gyrating ions and electrons about a magnetic field line. In both these limiting cases, the radial excursions are small and, because $\kappa_c^2 > 0$, radially stable.

A local stability analysis is also applicable where a grain's gyrations are small near synchronous orbit. This occurs because electromagnetic forces are small, due to the relative velocity of the grain to the magnetic field being small near R_{syn}. Substituting $\omega_c = n_c = \Omega_p$ into Eq. 3.35 gives

$$\kappa_c^2 = \Omega_p^2(1 - 4L_* + L_*^2) \quad \text{for } \rho_c = R_{\text{syn}}. \tag{3.36}$$

Setting expression 3.36 equal to zero and solving the quadratic shows that grains with $2 - \sqrt{3} < L_* < 2 + \sqrt{3}$ close to R_{syn} are locally unstable.

3.5.3 Global Radial Stability

As discussed by Mendis et al. (1982), positive grains with an intermediate charge-to-mass ratio exhibit large radial excursions. This can be seen in Figure 3.11. Therefore, there are regions in the (L_*, r_L) parameter space, in-between the Lorentz and Kepler limiting cases, for which the small radial amplitude oscillations of Eq. 3.33 does not hold and hence a local radial stability analysis (§3.5.2) is not valid.

In order to perform a more comprehensive stability analysis, it is necessary to return to the quartic potential expression of 3.25 to determine globally stable equilibria. There are two possible unstable outcomes: either the dust grain escapes the system (part a) of this section) or collides with the planet (part b) of this section). The A coefficient term of Eq. 3.25, which goes as $\frac{r_L^4}{r^4}$, dominates as the distance to the planet decreases (the grain is, of course, launched outside of

the planet making $\frac{r_L}{r} > 1$). Close to the planet, $U(r \to 0, L_*) \to +\infty$, and for distant grains, $U(r \to \infty, L_*) \to 0$. Therefore, the potential can have at most two local minima and one local maximum (recalling its quartic form), and this overall shape of the potential curve is useful to bear in mind when considering the stability of orbits and which state is energetically favourable. Orbital stability is determined by whether or not there exists a potential barrier preventing the grain from either colliding with the planet or from escaping the system.

Escape or collision with the planet is the unstable outcome when the launch location is outside or inside of synchronous orbit respectively, as this determines the direction in which the Lorentz force acts (positive grains' radial ranges are displaced away from R_{syn}, while negative grains' radial ranges are relatively small and cannot reach R_{syn}, Figure 3.11). The potential prohibits grains launched with Kepler initial conditions from crossing synchronous orbit. Each of the radially unstable outcomes will be considered in turn.

a) Global Radial Instability: Escape the System

A system seeks the lowest energy state. Substituting in $r = r_L$ in Eq. 3.25 gives the launch potential:

$$U(r_L, L_*) = \frac{GM_p}{r_L}\left(L_* - \frac{1}{2}\right). \tag{3.37}$$

If the launch potential is greater than the potential as it approaches infinity then it is energetically favourable for the grain to escape; the instability criterion is $U(r_L, L_*) > U(r \to \infty, L_*)$. By Eq. 3.37, with $L_* > \frac{1}{2}$ the grain is able to escape. This agrees with what was described in §1.2.2, considering when the escape velocity, Eq. 1.2, is real-valued. That is to say, all the escaping grains are positively-charged.

For moderately-charged grains outside synchronous orbit, the potential given by Eq. 3.25 decreases monotonically (due to the dominant B coefficient term, which is negative) for $L_* \gtrsim \frac{1}{2}$, and therefore $L_* = \frac{1}{2}$ is a globally stable boundary, as for any higher charge-to-mass ratio it is not energetically favourable for the grain to escape.

Things are slightly more complicated for more highly-charged grains (larger L_*, smaller grains) as the potential $U(r, L_*)$ has local extrema which can be larger in magnitude than the height of

the launch potential. Stability is determined by the relative height of the local maximum. For $L_* \sim 1$, there is no maximum, but as L_* increases, the potential does exhibit such a curve, refer to Figure 3.12.

Whether escape actually occurs depends on the shape of the potential; if there exists a potential maximum outside of the planet which is larger than the launch potential, then the grain will remain in stable orbit because it is prevented from leaving the system, as shown by the blue dotted curve of Figure 3.12. An example of an escaping grain, where the launch potential exceeds the grain's potential at its orbital distance, is shown in the green dashed curve of Figure 3.12. The orange solid curve of Figure 3.12 illustrates a critical case, where the grain's potential at its orbital distance equals the launch potential, Eq. 3.37, and provides the stability boundary.

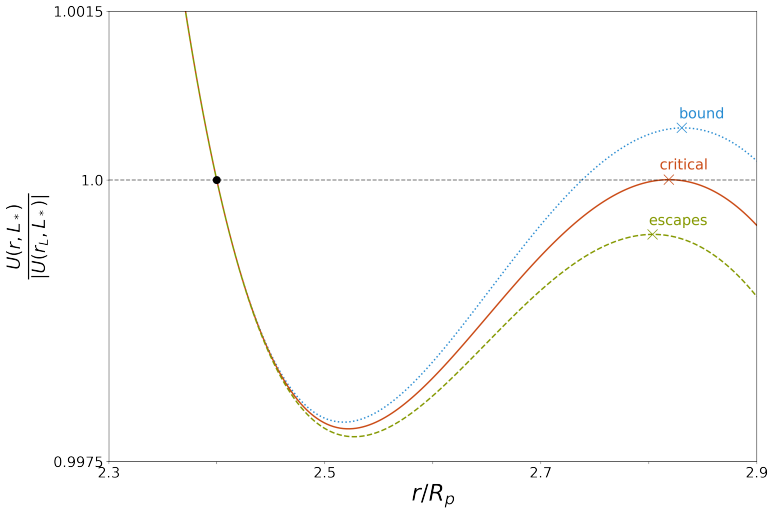

Figure 3.12: Three example potential wells for a launch position outside of synchronous orbit, $r_L = 2.4\,R_p$ (indicated by black point). The grains' potentials are scaled by the launch potential. The location of the stationary point, $U(r_{\text{stat}}, L_*)$, for each potential is indicated by the coloured crosses. The green dashed curve ($L_* = 7.58$) illustrates an escaping grain with $U(r_{\text{stat}}, L_*) < U(r_L, L_*)$; the orange solid curve ($L_* = 7.65$) shows the critical case of $U(r_{\text{stat}}, L_*) = U(r_L, L_*)$; the blue dotted curve ($L_* = 7.72$) shows a stable bound orbit with $U(r_{\text{stat}}, L_*) > U(r_L, L_*)$.

Following Jontof-Hutter (2012)'s procedure, and forcing the potential to have a root at $r = r_L$ by taking

$$U(r, L_*) - U(r_L, L_*) = 0, \tag{3.38}$$

it is possible to determine the (r_L, L_*) values for which $U(r, L_*) = U(r_L, L_*)$. The remaining roots can be found from the cubic expression

$$\frac{U(r, L_*) - U(r_L, L_*)}{(r - r_L)}. \tag{3.39}$$

The critical quartic of $U(r, L_*)$, an example given by the orange solid curve in Figure 3.12, where the turning point is a local maximum and equals $U(r_L, L_*)$, is found in a semi-analytical fashion.

The bisection method is used to search for where the peaks of the cubic functions, given by expression 3.39, are zero, refer to Figure 3.13. For a given launch location, r_L, the bisection method divides up the L_* parameter space, looking for where the peak of expression 3.39 changes sign within a small enough tolerance, so that the root can be approximated. The local peaks are themselves obtained numerically, using a method which searches for rising or falling values either side of the r value in question. This process is repeated for all launch locations so that a curve delineating the stability boundary of radial escape in (r_L, L_*) space can be determined.

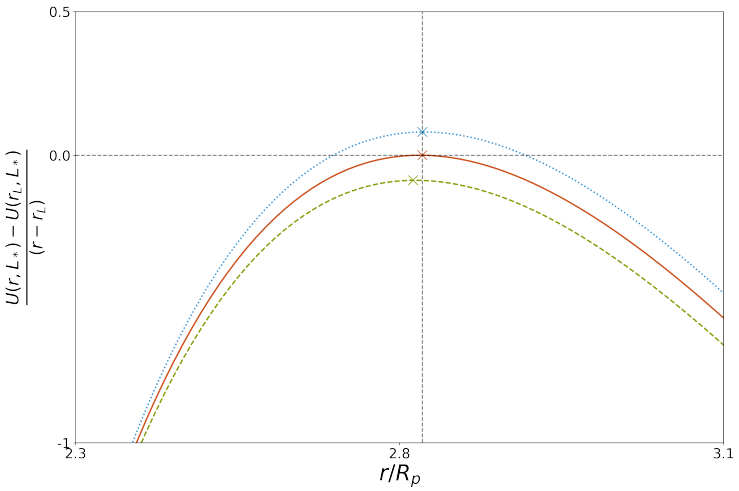

Figure 3.13: Some illustrative curves describing the method used to determine the critical quartic (described in the main text) for a grain launched outside synchronous orbit at $r_L = 2.4\,R_p$; the colour/line-style key is the same as in Figure 3.12 and refers to $L_* = 7.58, 7.65, 7.72$, although the method tries other L_* values in refining its search. The critical $L_* = 7.65$ (solid orange curve) has a stationary point (denoted by cross) located at the launch potential, indicated by the dashed lines, $U(r_{\text{stat}}, L_*) = U(r_L, L_*)$ at $r_{\text{stat}} = 2.82\,R_p$.

b) Global Radial Instability: Collide With Planet

The other radially unstable possibility is that the grain crashes into the planet. Although the potential, given by Eq. 3.13, varies with latitude, for simplicity only motion close to the equatorial plane is considered. A similar approach to §3.5.3a) is used, essentially using energy considerations to determine which parameters create a state that causes grains to move inward of $r = R_p$.

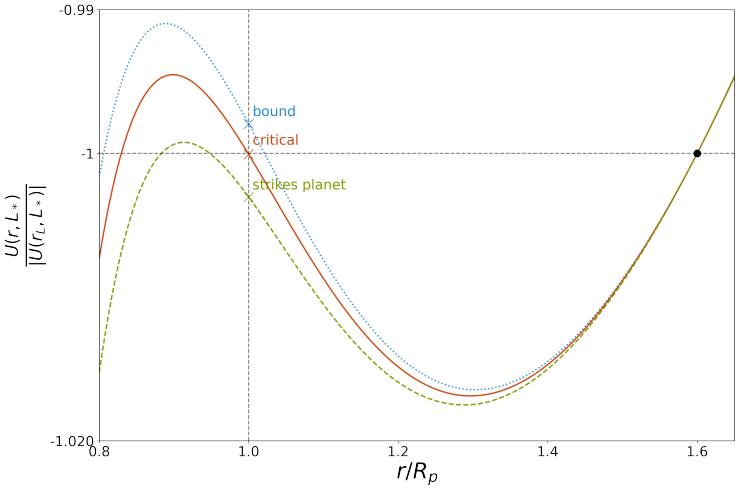

Figure 3.14: Potential wells for grains launched inside of synchronous orbit ($r_L = 1.6\,R_p$ indicated by black point), with notional peaks occurring inside the planet. The value of the potential at the planetary surface is indicated by the corresponding coloured cross. The blue dotted curve ($L_* = 0.0983$) shows a stable orbit, for which $U(R_p, L_*) > U(r_L, L_*)$. The green dashed curve ($L_* = 0.0995$) shows an unstable orbit, where it is energetically favourable for the grain to fall onto the planet, $U(R_p, L_*) < U(r_L, L_*)$. The orange solid curve ($L_* = 0.0988$) shows the critical stability boundary, where $U(R_p, L_*) = U(r_L, L_*)$

Recalling that grains with $L_* < \frac{1}{2}$ remain in orbit, the radial instability analysis needs to consider positively charged grains. The potential of Eq. 3.25 for positively-charged grains decreases in strength as r decreases inward away from r_L. This is due to the $\left(\frac{r_L}{r}\right)$ term in Eq. 3.25 being greater than unity, so that the negative cubic B coefficient term causes the potential to decline as $r \to R_p$. The potential does not increase in this radial range $[R_p, r_L]$ and therefore there is at most one local potential maximum inside of the launch location. Thus, there are two scenarios in which a potential barrier exists that prevents the grain from crashing into the planet. The first is illustrated by Figure 3.14, with $U(R_p, L_*) \geq U(r_L, L_*)$, this is where the grain can remain in stable orbit in an energy state that is lower than that at the planet's surface. The second scenario

is illustrated by Figure 3.15 , with $U(r_{\text{stat}}, L_*) \geq U(r_L, L_*)$, this is where there exists a local maximum exterior to the planet inside of the launch location which is greater than the launch potential.

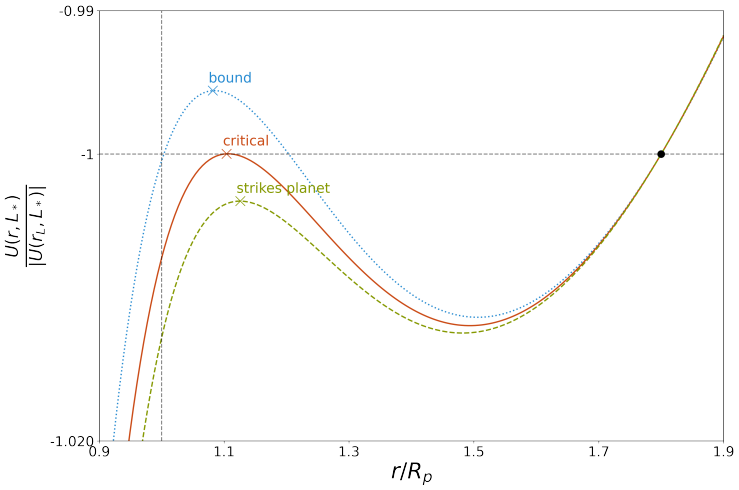

Figure 3.15: Potential wells for grains launched inside of synchronous orbit ($r_L = 1.8\,R_p$ indicated by black point), with peaks occurring outside the planet. The value of the potential peak is indicated by the corresponding coloured point marking the stationary point at r_{stat}. The blue dotted curve ($L_* = 0.1255$) shows a stable orbit, for which $U(r_{\text{stat}}, L_*) > U(r_L, L_*)$. The green dashed curve ($L_* = 0.1275$) shows an unstable orbit, where it energetically favourable for the grain to fall onto the planet, $U(r_{\text{stat}}, L_*) < U(r_L, L_*)$. The orange solid curve ($L_* = 0.1266$) shows the critical stability boundary, where $U(r_{\text{stat}}, L_*) = U(r_L, L_*)$.

For the first case (an example illustrated by Figure 3.14), for which the stability criterion is $U(R_p, L_*) = U(r_L, L_*)$, given by the solid orange curve, it is possible to write a quadratic expression in L_* by substituting $r = R_p, r_L$ into Eq. 3.25 and setting those expressions equal:

$$\frac{n_L^2 r_L^2}{2\Omega_p^2 R_p^2}\left(\frac{r_L}{R_p} - 1\right) L_*^2 + \left(1 - \frac{n_L r_L^2}{\Omega_p R_p^2}\right) L_* + \frac{1}{2}\left(\frac{r_L}{R_p} - 1\right) = 0. \tag{3.40}$$

Given that Eq. 3.40 is quadratic and there are certain charge-to-mass ratios for which the discriminant is greater than 0, there are two stability boundaries which can be obtained analytically:

$$L_{\pm} = \frac{\Omega_p \left(R_p \left(R_p^2 \Omega_p - n_L r_L^2 \right) \pm \sqrt{R_p^3 \left(R_p \Omega_p - n_L r_L \right) \left(R_p^2 \Omega_p + R_p n_L r_L - 2 n_L r_L^2 \right)} \right)}{n_L^2 r_L^2 \left(R_p - r_L \right)}. \tag{3.41}$$

It should be noted that the stability boundaries given by Eq. 3.41 have only taken into account the cases where the potential peak occurs within the planet. Figure 3.15 illustrates cases where the potential peak occurs between the planet and launch location. In such cases, radial instability can occur where $U(r_{\text{stat}}, L_*) < U(r_L, L_*)$, as indicated by the green dashed curve in Figure 3.15. This additional condition for instability can be solved in a similar fashion to that described for escape in §3.5.3a).

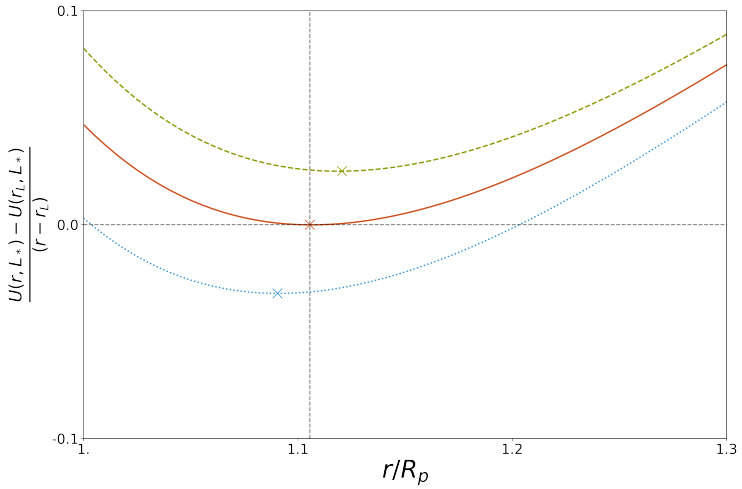

Figure 3.16: Some illustrative curves describing the method used to determine the critical quartic (described in the main text of this section) for a grain launched inside synchronous orbit at $r_L = 1.8\,R_p$; the colour/line-style key is the same as in Figure 3.15 and refers to $L_* = 0.1255, 0.1266, 0.1275$, although the method tries other L_* values in refining its search. The critical $L_* = 0.1266$ (solid orange curve) has a stationary point (denoted by cross) located at the launch potential, indicated by the dashed horizontal line $U(r_{\text{stat}}, L_*) = U(r_L, L_*)$ at $r_{\text{stat}} = 1.11\,R_p$.

As before, define a quartic expression for the potential which has a root at $r = r_L$ by design using expression 3.38. By factoring out $(r - r_L)$, the remaining roots can be located using the cubic function 3.39. The critical quartic of $U(r, L_*)$, an example given by the orange curve in Figure 3.15, occurs where the stationary point is a local maximum and equals $U(r_L, L_*)$. This critical quartic is found in a semi-analytic manner, by using the bisection method to search for where the minima of the cubic functions (3.39) are zero, refer to Figure 3.16. For a given launch

location, r_L, the bisection method divides up the L_* parameter space, looking for where the minimum of the cubic 3.39 changes sign within a small enough tolerance of zero.

The local minima are themselves obtained numerically, using a method which searches for rising or falling values either side of the r value in question. This process is repeated for all launch locations so that a curve delineating the stability boundary of radial escape in (r_L, L_*) space can be determined. However, Jontof-Hutter (2012) note that corrections to the expressions of 3.41 are actually only necessary near $R_{\rm syn}$, close to where the potential maximum is located at the planetary surface, $U(R_p, L_*) = U(r_L, L_*)$, intermediate between the two cases illustrated by Figures 3.14 and 3.15. This correction is shown by the black dotted curve of Figure 3.20 for $q_d > 0$.

3.6 Vertical Motion

3.6.1 Mirror Motion

The configuration of a centred aligned magnetic dipole is azimuthally symmetric and varies in field strength from weakest at the equatorial plane to strongest at the poles. Cylindrical coordinates (r, ϕ, z) are a natural choice as the symmetry can be exploited: $\frac{\partial B_\phi}{\partial \phi} = 0$, when z points along the axis of symmetry. Taking the divergence (Gauss's law),

$$\frac{1}{r}\frac{\partial}{\partial r}(rB_r) + \frac{\partial B_z}{\partial z} = 0. \tag{3.42}$$

Integrating Eq. 3.42 enables the radial component of the magnetic field to be obtained:

$$B_r = -\frac{1}{2} r \frac{\partial B_z}{\partial z}, \tag{3.43}$$

valid so long as B_z is not a function of r (not the case everywhere, but a reasonable approximation in some small regions).

The z component of the Lorentz force for a grain gyrating with a gyroradius r_g around a field line is $-q_d v_\phi B_r$. Substituting for B_r using Eq. 3.43, and noting that the ϕ-velocity for $\pm$ charged grains is in the $\mp$ ϕ-direction so that $v_\phi = \mp v_\perp$ gives

$$F_{Lz} = \mp \frac{q_d}{2} v_\perp r_g \frac{\partial B_z}{\partial z}. \tag{3.44}$$

Then substituting for the gyroradius, $r_g = \frac{m_d v_\perp}{q_d B}$:

$$F_{Lz} = \mp \frac{\frac{1}{2} m_d v_\perp^2}{B} \frac{\partial B_z}{\partial z}, \tag{3.45}$$

and using $v_\perp = r_g \Omega_g$ and $\Omega_g = \frac{q_d B}{m_d}$ gives

$$F_{Lz} = \mp \frac{q_d}{2} r_g^2 \Omega_g \frac{\partial B_z}{\partial z}. \tag{3.46}$$

The magnetic moment, μ, of the gyrating grain is the current multiplied by the area encircled; by introducing factors of π, the constant term of expression 3.46 can be written in a more elucidating manner,

$$\pm\, q_d \frac{\Omega_g}{2\pi} \pi r_g^2 =: \mu. \tag{3.47}$$

From Eq. 3.46, the z component of the motion of the charged grain, Eq. 3.14a, can be expressed

$$F_{Lz} = m_d \frac{dv_\parallel}{dt} = -\mu \frac{\partial B_z}{\partial z}, \tag{3.48}$$

taking the same definition of $\parallel$ along the B field, which is assumed to be a centred aligned dipole so that in the equatorial plane it points along z. The rate of change of the kinetic energy associated with the longitudinal motion is

$$\frac{d}{dt}\left(\frac{1}{2} m_d v_\parallel^2\right) = m_d \frac{dv_\parallel}{dt} v_\parallel = -\mu \frac{dB}{dt}, \tag{3.49}$$

by using the chain rule and Eq. 3.48.

The kinetic energy of a charged grain cannot change in a static magnetic field (or equivalently in an azimuthally symmetric field rotating about its axis), that is, the sum of the kinetic energies associated with the longitudinal and transverse motions remains constant:

$$\frac{d}{dt}(\frac{1}{2}m_d v_{\parallel}^2) + \frac{d}{dt}(\frac{1}{2}m_d v_{\perp}^2) = 0. \tag{3.50}$$

Manipulating expressions 3.45, 3.48 and 3.49, leads to

$$-\mu\frac{dB}{dt} + \frac{d}{dt}(\mu B) = 0, \tag{3.51}$$

and therefore

$$\frac{d\mu}{dt} = 0. \tag{3.52}$$

The magnetic moment is conserved during the motion of the guiding centre, and is known as the *first adiabatic invariant*. This conservation result of Eq. 3.52 was used as a test for the numerical integrators (§2.4). From Equations 3.45 and 3.48, $\mu = \frac{\frac{1}{2}m_d v_{\perp}^2}{B}$, so that in order for μ to be constant when the grain moves into regions of stronger B, the transverse kinetic energy has to increase. However, the transverse kinetic energy can never exceed the total kinetic energy and therefore when the grain travels into a region of sufficiently strong B such that the kinetic energy is totally associated with its transverse motion, the grain cannot continue in the same direction and is reflected back. Hence the term *magnetic mirror*. When encountering stronger fields towards the poles of the planet, charged grains are reflected back towards the equatorial plane, this can initiate an oscillation between the poles, with a characteristic bounce period, which is discussed in §3.6.2.

3.6.2 Local Vertical Stability

For a grain to be vertically stable, it must exhibit bounce motion without colliding with the planet (§3.6.1). That is, it must move about an equilibrium point determined by taking the derivative of the potential: $\frac{\partial U}{\partial z} = 0$. Northrop & Hill (1982) first studied the vertical stability of grains, and their work was developed by Jontof-Hutter (2012). Equation (9) of Northrop & Hill (1982) describes the square of the bounce frequency,

$$\Omega_b^2 = \left.\frac{\partial^2 U}{\partial z^2}\right|_{\rho=\rho_c, z=0} = 3\omega_c^2 - 2n_c^2, \tag{3.53}$$

where the substitutions $n_c^2 = \frac{GM_p}{\rho^3}, v = \rho\omega_c$ have been used to convert to the notation of this thesis. In an similar analysis to the radial stability sections, §§3.5.2, 3.5.3, by considering the sign of the second derivative of the potential, when Eq. 3.53 is positive then the grain is stable against vertical perturbations. Global vertical stability analysis, involving larger oscillations and non-circular gyro-orbits is beyond the scope of this work.

When $\Omega_b^2 < 0$, the grain is unstable. The first term of Eq. 3.53 is centrifugal, the second term is gravitational. The gravitational term is negative and therefore acts to destabilise the grain. This can be understood intuitively by considering the curvature of the dipole magnetic field lines of the planet, explained in Figure 3.17.

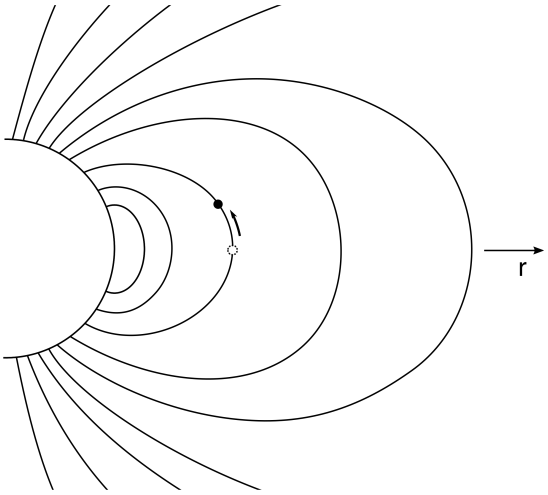

Figure 3.17: A grain moving away from the equatorial plane along a magnetic field line moves closer to the planet due to its curvature, and therefore the grain experiences a stronger gravitational force due to the inverse square law. Since the gravitational term in Eq. 3.53 is negative, this shifts Ω_b^2 towards negativity and hence instability.

Northrop & Hill (1982) derive an expression for the marginal stability radius (by setting $\Omega_b^2 = 0$) for negative grains,

$$\begin{aligned} \rho_{crit}^3 &= \frac{2}{3}\frac{GM_p}{\left(\Omega_p - \frac{GM_p}{3}\frac{mc}{q\mu}\right)^2} \\ &= \frac{2}{3}\frac{GM_p}{\left(\Omega_p - \frac{\Omega_p}{3L_*}\right)^2}, \end{aligned} \tag{3.54}$$

where the first line of Eq. 3.54 uses the notation and units of Northrop & Hill (1982), so there is an additional factor of c. The work of Northrop & Hill (1982) enables an understanding of vertical instability for high charge-to-mass ratios in the absence of magnetic mirror forces, whilst the work of Jontof-Hutter (2012) develops an understanding for all charge-to-mass ratios with additional terms accounting for more complicated forces, these scenarios are discussed in turn.

a) Vertical Instability: Highly Charged Grains

In the Lorentz limit, $\omega_c \to \Omega_p$ so that Eq. 3.53 becomes, using the Kepler frequency formula, $3\frac{GM_p}{R_{\text{syn}}^3} = 2\frac{GM_p}{\rho_{\text{crit}}^3}$ for the case of marginal stability, and can be expressed as

$$\frac{\rho_{\text{crit}}}{R_{\text{syn}}} = (2/3)^{\frac{1}{3}}, \tag{3.55}$$

which predicts a vertical instability boundary for Saturn at about $1.625\,R_{\text{S}}$ (§1.2.3).

An important distinction to note is that in Northrop & Hill (1982)'s model, a grain is launched on a circular orbit at ω_c (so no gyromotion around field lines). However, in this work, with grains launched at Kepler velocities, there is gyromotion to consider because there is motion relative to the guiding centre. As discussed in §§1.2.3 and 3.6.1, this gyromotion leads to a magnetic mirror force, which causes the grain to 'bounce' away from regions of high magnetic field strength.

b) Vertical Instability: Any Charge

Jontof-Hutter & Hamilton (2012a) derive an expression for the bounce frequency, by averaging the restoring acceleration over a gyro-orbit, $\Omega_b^2 = \frac{\langle z \frac{\partial^2 U}{\partial z^2} \rangle}{\langle z \rangle}$, and adding a magnetic mirroring term following Lew (1961) and Thomsen & Van Allen (1980):

$$\Omega_b^2 = 3\omega_c^2 - 2n_c^2 + \frac{r_g^2}{\rho_c^2}\left(\frac{9}{2}\Omega_{gc}(\Omega_{gc} - \omega_c + \Omega_p) - \frac{3}{2}n_c^2\right). \tag{3.56}$$

Certain assumptions have been made in Eq. 3.56, namely that that the temporal and spatial scales of the epicycles (gyro-orbits) are relatively small, $r_g \ll r_L$ and $\kappa_c \gg \Omega_b$. Given Figure

3.11, there is expected to be poor agreement for positively charged grains, which collide with the planet or escape the system (radially unstable) for intermediate L_*, where the Lorentz force and gravity are comparable in strength.

In order to plot out the stability boundary in (L_*, r_L) space, it is necessary to solve the equation $\Omega_b^2 = 0$. This is a numerical root-finding exercise, and due to Eq. 3.56 being expressed implicitly in terms of L_* it is more straightforward to use the secant method over the Newton-Raphson method, as it does not require a derivative. The secant method is able to locate all roots, provided the initial guesses cover an appropriate range of the parameter space. Some example plots showing the root-finding for Eq. 3.56 are given in Figure 3.18.

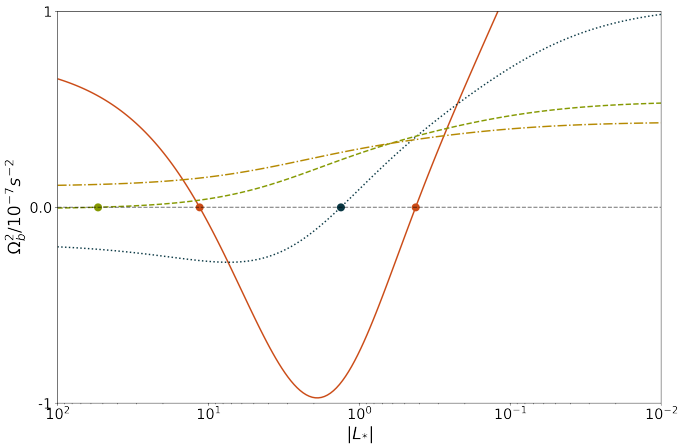

Figure 3.18: Ω_b^2 for various launch locations around Saturn plotted against $-L_*$, with roots indicated by points. Close to the planet there is a small region of double roots, as shown by the $r_L = 1.03\,R_p$ solid orange curve, and moving further out there are single roots, as shown by the $r_L = 1.2\,R_p$ dotted blue curve. Beyond approximately $1.55\,R_p$ there are no roots, indicating the transition from vertical instability to stability (Northrop & Hill 1982), and illustrated by the $r_L = 1.55\,R_p$ dashed green and $r_L = 1.65\,R_p$ dot-dashed yellow curves.

This procedure of locating roots for a given r_L, is then repeated for all relevant launch locations so that a stability boundary can traced out in (L_*, r_L) space. The double root example shown in Figure 3.18 for Eq. 3.56, which was derived by Jontof-Hutter (2012), indicates there is a second solution that the curve described by Northrop & Hill (1982) and given in Eq. 3.54 does not find.

3.7 Timescales

The guiding centre approximation (§3.4.1) with the method outlined in Jontof-Hutter (2012), described in the preceding sections, provides expressions for the radial, vertical and azimuthal motions in the inertial frame. More highly charged grains exhibit motion on these three characteristic timescales, $\kappa_c, \Omega_b, \omega_c$, as the grain gyrates about the orbiting guiding centre and is mirrored up and down field lines, which is shown by the divergence of the three curves in Figure 3.19 as $|L_*|$ increases.

Figure 3.19a agrees well with Jontof-Hutter (2012), noting that the azimuthal and radial curves were mislabelled in that work. In the Keplerian limit, where gravity dominates, the three frequencies all converge to the Kepler orbital frequency: $\kappa_c, \Omega_b, \omega_c \to n_c$, as shown by the dot-dashed grey line in Figure 3.19. In the Lorentz limit, $\kappa_c \to \Omega_{gc}$, $\omega_c \to \Omega_p$.

Figure 3.19b shows that slightly further out from synchronous orbit, the guiding centre approximation does not provide such a good approximation as the gyroradii grow in size (Figure 3.11), indicated by the minor discrepancy between numerical and theoretical results.

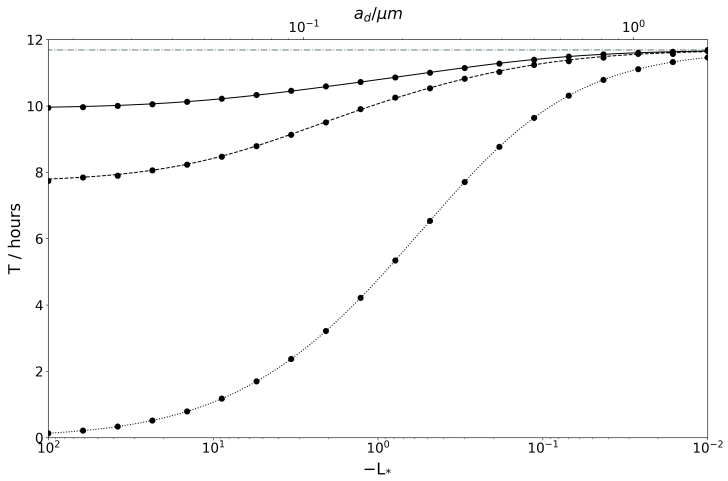

(a) Jupiter

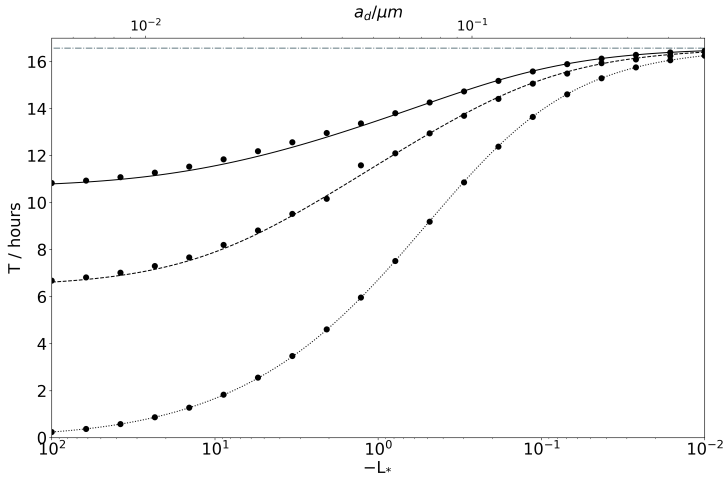

(b) Saturn

Figure 3.19: Time periods for negatively-charged grains launched around **(a)** Jupiter near to synchronous orbit ($1.12\,R_{\rm syn}$) at $r_L = 2.5\,R_{\rm J}$ and **(b)** Saturn quite near to synchronous orbit ($1.34\,R_{\rm syn}$) at $r_L = 2.5\,R_{\rm S}$, extending the work of Fig. 3.11 of Jontof-Hutter (2012). The dash-dotted grey curve shows the Keplerian time period at that orbital distance. The black curves show the theoretical solutions: the dotted curve shows the radial period $\frac{2\pi}{\kappa_c}$ of Eq. 3.34; the dashed curve shows the vertical period, $\frac{2\pi}{\Omega_b}$ of Eq. 3.56; the solid curve shows the azimuthal period $\frac{2\pi}{\omega_c}$ of Eq. 3.30. The filled circles show numerically integrated results.

3.8 Summary and Discussion of Stability Boundaries

The previous sections have outlined the methods used to determine the solutions for the stability boundaries, in an analytical/semi-analytical fashion, derived from the literature. These are summarised in Figure 3.20 and outlined below:

- Local radial stability $L_* = 2 \pm \sqrt{3}$, Eq. 3.36 of §3.5.2, following Jontof-Hutter (2012)
- Global radial stability: escape the system, §3.5.3a), following Hamilton & Burns (1993), Horányi et al. (1993b) and Jontof-Hutter (2012)
- Global radial stability: collide with the planet, §3.5.3b), following Jontof-Hutter (2012)
- Local vertical stability (§3.6.2), following Northrop & Hill (1982) and Jontof-Hutter (2012)

In addition to the stability boundary curves, the resonant feature $|\kappa_c| = 2\Omega_b$ is plotted in Figure 3.20 for negative charges. For these grains their radial and vertical motions are coupled, energy is transferred from radial modes to vertical modes repeatedly, resulting in large vertical excursions (denoted by pale grey datapoints in Figure 3.21); an example of an individual grain experiencing this is shown in Figure 3.2.

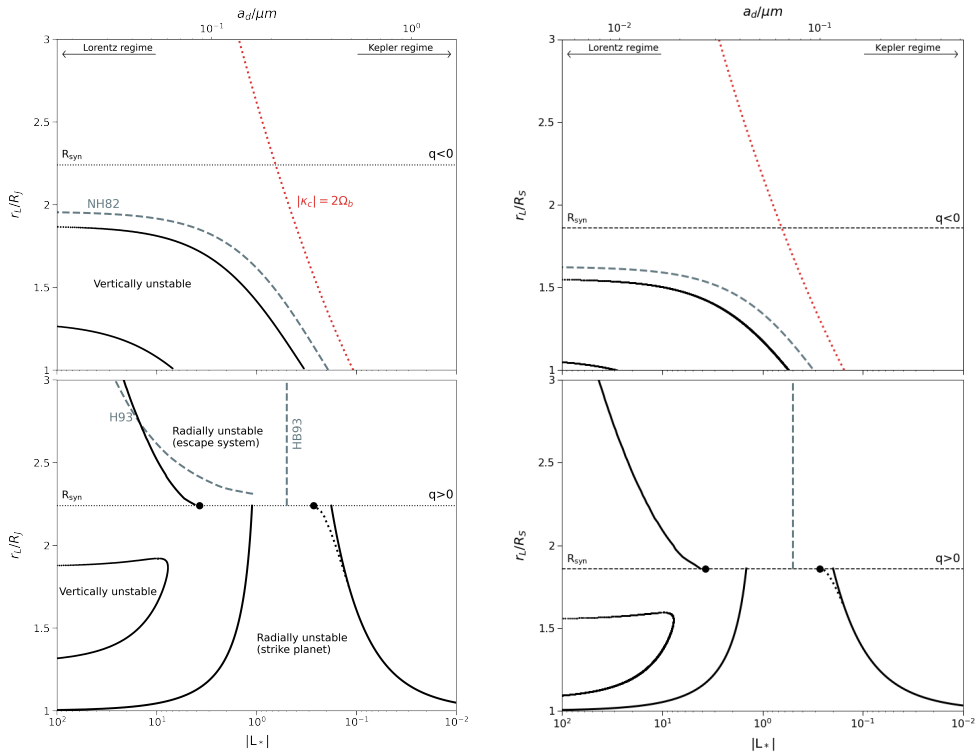

(a) Jupiter **(b)** Saturn

Figure 3.20: Analytical and semi-analytical solutions for stability boundaries derived in this chapter. Results for positively charged grains (bottom) and negatively charged grains (top) are shown for Jupiter on the left hand side and for Saturn on the right hand side. The curves enclose unstable regions; stable regions lie outside those. The grey dashed curves indicate older results from Northrop & Hill (1982), Hamilton & Burns (1993) and Horányi et al. (1993b). Black curves are results obtained by following the theory of Jontof-Hutter (2012): the vertically unstable region is obtained from a local vertical stability analysis (§3.6.2), and the radially unstable regions are obtained by considering both a local (§3.5.2) and global (§3.5.3) stability analysis. The solid/dotted black curves delineating the global radially unstable positive stability boundary for grains striking the planet show the quadratic solutions described on page 113, Eq. 3.41. The dotted curve ($q_d > 0$) indicates that the right-most curve requires a semi-analytical approach to obtain the stability boundary near R_{syn}, when the potential's stationary point is located at the planetary surface, a case intermediate between those illustrated in Figures 3.14 and 3.15, where $U(r_{\text{stat}}, L_*) = U(R_p, L_*)$. The feature labelled $|\kappa_c| = 2\Omega_b$ (red dotted curve) shows a resonance between radial epicyclic and vertical bounce frequencies, where energy transfer from radial to vertical modes results in stable large vertical excursions.

Generally, there is good agreement between the numerical results and the analytical/semi-analytical solutions as shown in Figure 3.21, verifying the work of Jontof-Hutter (2012). The radial stability theory match the numerical results very well, as shown in Figure 3.21 by the solid black curves tracing the black numerical datapoints' boundaries in the lower plots, $q_d > 0$. However, due to the assumption that grains remain close to the equatorial plane in the derivation of Eq. 3.40, the high latitude collisions with the planet are missed (dark grey datapoints in $q_d > 0$ subplots of Figure 3.21 around $L_* = +2, r_L = 2$). The stable region near synchronous orbit around $L_* = +0.2$, indicated by the yellow datapoints lying in the region between the dotted and solid curves for $q_d > 0$ in Figure 3.21, are grains which have launch potentials that are lower than the potential at the planet's surface, $U(r_L, L_*) < U(R_p, L_*)$, and which also have their potential peak being greater than their launch potential, $U(r_{\text{stat}}, L_*) > U(r_L, L_*)$, so that it is energetically favourable for them to remain in orbit as illustrated by the dotted blue curve in Figure 3.15. The global radial stability curves meet the local stability results of $L_* = 2 \pm \sqrt{3}$ at R_{syn}, described by the roots of Eq. 3.36, for grains with small gyroradii close to synchronous orbit. A local radial stability analysis holds where the gyroradius is small, that is, close to synchronous orbit (Eq. 3.26).

The vertical stability boundary for negative grains predicted by Northrop & Hill (1982) and described by the dashed grey curve in the upper plot of Figure 3.20 misses the second solution close to the planet. The theory of Jontof-Hutter (2012) does find a second solution (solid black curves in Figure 3.20 for $q_d < 0$, upper plots), although that inner stability boundary for moderate L_* does not describe the numerical results very well (shown in Figure 3.21). This is for the same reason that the gyroradii of Figure 3.11 show poor agreement between theoretical and numerical results for moderate L_*: the epicyclic theory of the Guiding Centre approximation (§3.4.1) breaks down when the epicycles become large and non-circular due to the grain experiencing large variations in magnetic field strength as it orbits, so that the assumptions for that approximation do not hold (3.17). For the same reason, of the epicyclic model breaking down, the vertical stability boundary for positive grains also departs from the numerical results where $L_* < 10$ (Figure 3.21, lower plots with $q_d > 0$).

The vertical stability boundary bends towards the planet with decreasing $|L_*|$ for negative grains and away from the planet for positive grains (Figure 3.20). This can be explained by considering the $3\omega_c^2 - 2n_c^2$ term of Equations 3.53 and 3.56. For negative grains within R_{syn} (where $n_c >$

ω_c, recalling the Kepler frequency being inversely proportional to the radial distance to the $\frac{3}{2}$ power), the guiding centre frequency increases as the outward Lorentz force weakens with decreasing $|L_*|$. This can be understood by considering that the guiding centre is therefore displaced outward to a lesser extent, so that $|\omega_c|$ is not reduced as much. The root, where $3\omega_c^2 - 2n_c^2$ changes sign, requires a larger n_c for smaller $|L_*|$, that is, a smaller launch position. Conversely, for positive grains inside synchronous orbit (where $n_c > \omega_c$, recalling the Kepler frequency being inversely proportional to the radial distance to the $\frac{3}{2}$ power), the guiding centre frequency decreases as the inward Lorentz force weakens with decreasing $|L_*|$. This can be understood by considering that the guiding centre is therefore displaced inward to a lesser extent, so that $|\omega_c|$ is not increased as much. Therefore, the root, where $3\omega_c^2 - 2n_c^2$ changes sign, requires a smaller n_c for smaller $|L_*|$, that is, a larger launch position.

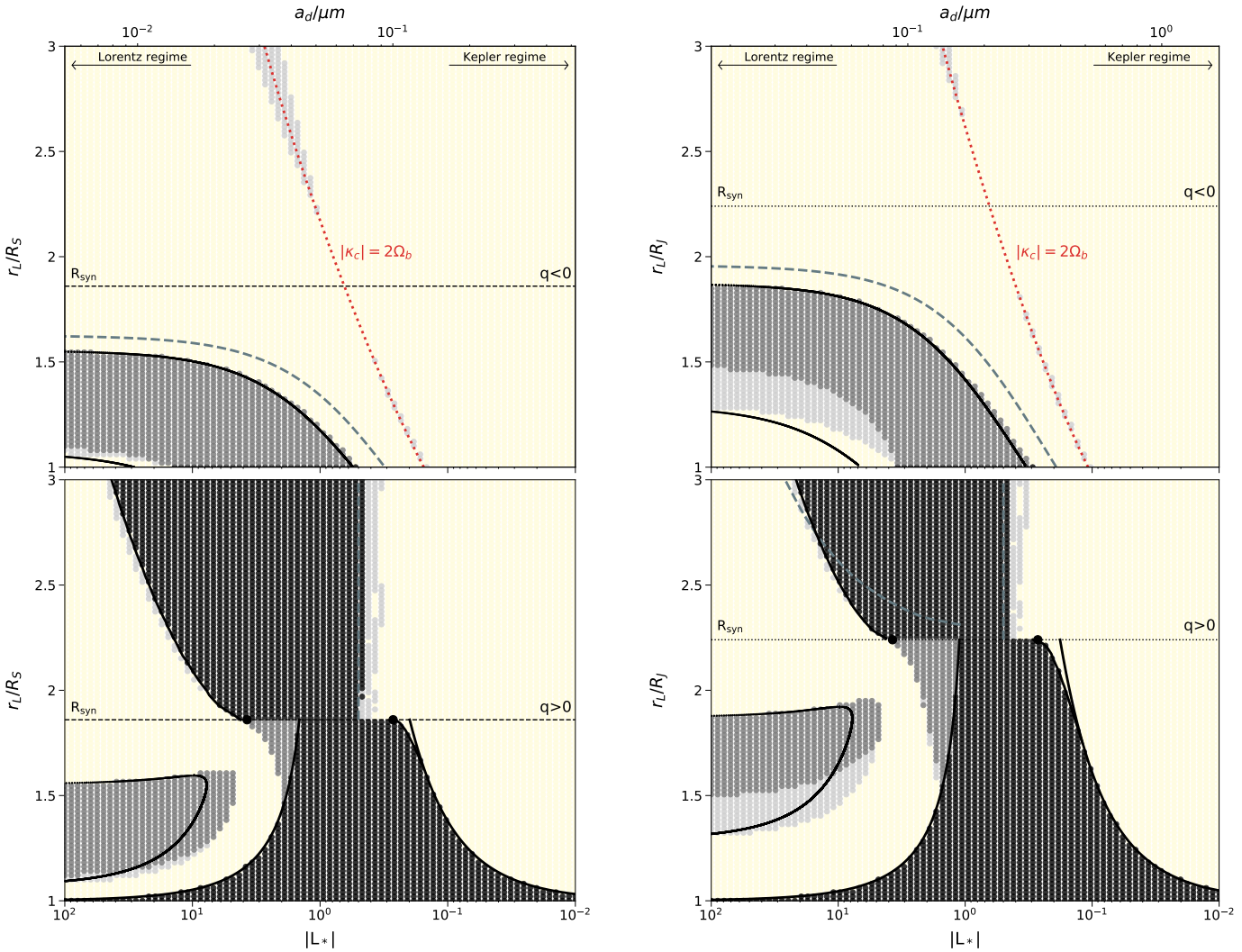

(a) Saturn.

(b) Jupiter.

Figure 3.21: As Figure 3.5, but with the inclusion of theoretical stability boundary curves as derived by Jontof-Hutter (2012). Stability maps for positively (bottom) and negatively (top) charged grains orbiting Saturn (left) and Jupiter (right), with the $\vec{B}$ field modelled as an aligned centred dipole. The colour key (yellow, light grey, dark grey, black) is explained in §3.2.2, but repeated here for reference: yellow = stable, light grey = stable with large vertical oscillations, dark grey = vertically unstable, black = radially unstable. A resonant feature is described by the dotted red curve. The earlier stability boundaries of Northrop & Hill (1982), Horányi et al. (1993a) and Hamilton (1993) are plotted on Figure 3.5. Grain radii are labelled on the upper axis assuming a grain density of water-ice and $\phi_d = \pm 5$ V, Eqs. 1.5 and 1.4.

Comparing Jupiter and Saturn, in Figure 3.21, it can be seen that Saturn's vertical instability region is translated inward, due to its lower synchronous orbit ($R_{\text{syn}} = 1.86\,R_{\text{S}}$ compared to $R_{\text{syn}} = 2.24\,R_{\text{J}}$). Most of the grains experiencing large vertical excursions collide with Saturn, unlike the case at Jupiter where there is a substantial stable population shown by the light grey datapoints in Figure 3.21. This is due to the curvature of Saturn's surface being that much closer to the region of large vertical oscillations. Both Saturn and Jupiter display grains with $L_* \lesssim \frac{1}{2}$ which exhibit large radial displacements but do not have sufficient energy to escape (Eq. 3.37), instead the radial motion excites vertical motions as indicated by the pale grey datapoints outside synchronous orbit in Figure 3.21 (lower plot, $q_d > 0$) denoting stable orbits with large vertical excursions; an example of such a trajectory is shown in Figure 3.4.

Having explored and verified the numerical and (semi-) analytical expressions for the motions of constant-charge grains orbiting in dipole aligned planetary magnetic and gravitational fields (Jontof-Hutter & Hamilton 2012a), attention will next be paid to the effects of time-variable charging, including planetary shadowing effects, and more complex fields involving the J_2 oblate gravity term, and the higher order g_n^m coefficients describing Saturn's northward-offset magnetic dipole.

4

Time-Variable Charging of Dust

Before proceeding to the description of the algorithms used to control the charging of the grains, it is necessary to include background theory on the charging environment in planetary rings. The planetary ring environment in which dust grains are immersed is dynamic, and the charge of a dust grain fluctuates based on the currents it encounters. The grain's charge is a dominant factor in influencing its motion in planetary magnetospheres, therefore how the charge varies over time is highly significant. Considering all temporally- and spatially-varying currents incident on the grain as well its back-influence on the environment is a complex endeavour, and progress will be attempted by building up the charging model through piecing together parts under simplifying but realistic assumptions, described in the following sections.

There are four main charging currents to consider: the electron and ion currents of the plasma, the photoelectron current due to solar radiation, and the secondary electron emission current due to ionisation of the grain and ejection of electrons. Each of these currents dominate in certain regimes, so that for the problem in question, there may be certain currents that are negligible. There are several review articles detailing these processes and aspects of dust in plasmas, with Horányi (1996) and Graps et al. (2008) being particularly relevant for planetary magnetospheres and for planetary rings environments. A distinction between dust in plasmas and dusty plasmas

should be noted (§1.3.2). For an intergrain distance of λ_{mfp} (the grain's collisional mean free path), a grain size of a_d and a plasma Debye length of λ_{D}, the 'dust-in-plasma' regime when $a_d \ll \lambda_{\text{D}} < \lambda_{\text{mfp}}$ (1.40) is a plasma containing isolated screened grains and a particle dynamics approach can be used, as is the case here. For *dusty plasmas*, reviewed by Goertz (1989), Northrop (1992), and Mendis & Rosenberg (1994), the collective effects of charged dust become relevant (Verheest 2000): when $a_d \ll \lambda_{\text{mfp}} < \lambda_{\text{D}}$.

The first currents considered here are the plasma currents (§4.1.1), and an initial starting point is to reproduce the work of Cui & Goree (1994), which considers dust in plasma (§4.1.5). A continuous charging model is described (§4.1.2) before the need for a discrete charging model is explained (§4.1.3), as this provides useful confirmation that the discrete charging algorithms (§§4.1.4 and 4.2) are behaving accurately, as the continuous and discrete models should converge over time.

4.1 An Approach to Modelling Time-Variable Charging

In order to work towards a time-variable charging model, the work of Cui & Goree (1994) was followed as a particular instance to introduce and illustrate various principles relevant to variable charging in planetary magnetospheres, including continuous (§4.1.2) versus discrete charging (§4.1.3). They do not include photo– and secondary–electron emission, only plasma currents (§4.1.1), although these will be considered in §4.2, when an approach to stochastic charging that can be integrated alongside the equations of motion (Chapter 2) is described and tested. Cui & Goree (1994) model dust in plasma by assigning probabilities to the amount of time between charging events (§4.1.4a)) and the sequence of electrons and ions collected by grains (§4.1.4b)). Simulation results are presented in §4.1.5.

4.1.1 Plasma Currents

Initially the plasma currents incident on the grain are treated as continuous in time, despite the discrete nature of the charge carriers, in order to provide estimates of equilibrium physical quantities with which to check the discrete model (§§4.1.4 and 4.2). The dust grain with a surface potential ϕ_d (relative to the plasma potential) is assumed to be spherical with radius a_d,

immersed in a uniform and steady-state plasma with Debye length $\lambda_{\rm D}$. Orbital motion limited theory (OML), dating back to the work of Mott-Smith & Langmuir (1926), under the assumption of Eq. 1.40, is used to describe the currents collected by the grain:

$$\left.\begin{aligned} I_e &= I_e^0 \exp\left(\tfrac{e\phi_d}{k_{\rm B}T_e}\right) \\ I_i &= I_i^0 \left(1 - \tfrac{Z_i e\phi_d}{k_{\rm B}T_i}\right) \end{aligned}\right\} \quad \phi_d < 0, \\ \left.\begin{aligned} I_e &= I_e^0 \left(1 + \tfrac{e\phi_d}{k_{\rm B}T_e}\right) \\ I_i &= I_i^0 \exp\left(-\tfrac{Z_i e\phi_d}{k_{\rm B}T_i}\right) \end{aligned}\right\} \quad \phi_d \geq 0. \tag{4.1}$$

Here, the positive charge ions and electrons, denoted with a subscript i and e respectively, follow a Maxwellian distribution characterized by plasma temperatures T_i, T_e. Henceforth, *ions* refer to positively charged ions. The charge of the ions is $q_i = Z_i e$ (where $e = +1.602176634 \times 10^{-19}$ C, so that $q_e = -e$). Since the drift velocity between the plasma and dust grains is much smaller than the thermal velocities (discussed further in §4.1.2b)), the coefficients take the form of

$$I_\alpha^0 = 4\pi a_d^2 n_\alpha q_\alpha \sqrt{\frac{k_{\rm B}T_\alpha}{2\pi m_\alpha}}, \tag{4.2}$$

where $q_\alpha, n_\alpha, m_\alpha$ denote the charge, number density, mass of the plasma species $\alpha = \{e, i\}$ respectively (Horányi 1996). Equations 4.1 and 4.2 can be written in a more succinct form following Graps et al. (2008, §2.1), but the separate expressions, depending on the sign of ϕ_d, have been included here for clarity.

4.1.2 Continuous Charging Model

a) A Grain at Rest in a Plasma

Before embarking on a description of stochastic charging algorithms (§§4.1.4 and 4.2), that will be argued to be more realistic, it is necessary to explain the continuous charging model, which will provide a useful verification for the discrete stochastic model. A grain immersed in a plasma will charge up by collecting electrons and ions, according to the differential equation

$$\frac{dq_d}{dt} = \sum_{\alpha=e,i} I_\alpha, \tag{4.3}$$

which can be solved for $q_d(t)$ by substituting in for I_α using Equations 4.1 and 4.2, which relate the currents to the surface potential, ϕ_d. The grain's charge is related to its surface potential through

$$q_d = 4\pi\epsilon_0 a_d \phi_d. \tag{4.4}$$

Therefore, it can be seen that the differential equation of 4.3 takes the form of some non-linear function of q_d, and, for small $q_\alpha\phi_d/k_\mathrm{B}T_\alpha$, is linear.

The equilibrium potential ϕ_eq, which occurs when the electron and ion currents incident on the grain have equal magnitude, is obtained by setting Eq. 4.3 equal to zero, assuming plasma quasi-neutrality ($n_e \approx n_i$), and using the $\phi_d < 0$ expressions of Eq. 4.1, as the electrons are ~ 43 times more mobile than protons when $\phi_d = 0$ initially (Graps et al. 2008) and hence collide more frequently with the grains:

$$\sqrt{\frac{T_i}{T_e}}\left(1 - \frac{e\phi_\mathrm{eq}}{k_\mathrm{B}T_i}\right)\exp\left(-\frac{e\phi_\mathrm{eq}}{k_\mathrm{B}T_e}\right) - \sqrt{\frac{m_i}{m_e}} = 0. \tag{4.5}$$

The root of the transcendental equation 4.5 can be found numerically; this was done using the Newton-Raphson method, where Eq. 4.5 was written as $f(X) = 0$ and the required derivative was found using the substitution of $X = \frac{e\phi_\mathrm{eq}}{k_\mathrm{B}T_i}$. This yields

$$\phi_\mathrm{eq} = \frac{k_\mathrm{B}T_e}{e}\frac{T_i}{T_e}X = K_\phi\frac{k_\mathrm{B}}{e}T_e \tag{4.6}$$

with the constant K_ϕ introduced to match Cui & Goree (1994)'s units. Results are given in Table 4.1, and compared to Cui & Goree (1994). Highlighting the case where $T_i = T_e$, $Z_i = 1$, an equilibrium potential of $-2.5\frac{k_\mathrm{B}T_e}{e}$ is obtained, as first calculated by Spitzer (1941).

m_i (amu)	T_i/T_e	K_ϕ ($\mathrm{V\,eV^{-1}}$)		K_q ($\mu\mathrm{m^{-1}\,eV^{-1}}$)		K_{τ_c} ($\mathrm{s\,\mu m\,cm^{-3}\,eV^{-\frac{1}{2}}}$)	
		Present work	Cui & Goree (1994)	Present work	Cui & Goree (1994)	Present work	Cui & Goree (1994)
1	0.05	-1.698	-1.698	-1179	-1179	7.66×10^{2}	7.66×10^{2}
1	1	-2.501	-2.501	-1737	-1737	1.51×10^{3}	1.51×10^{3}
40	0.05	-2.989	-2.989	-2076	-2073	2.06×10^{3}	2.05×10^{3}
40	1	-3.991	-3.952	-2772	-2631	4.11×10^{3}	3.29×10^{3}

Table 4.1: Coefficients of Equations 4.6 - 4.8 solved numerically for Hydrogen ($m_i = 1$ amu) and Argon ($m_i = 40$ amu) and compared to Cui & Goree (1994).

The equilibrium charge number $N_{\mathrm{eq}} = \frac{q_{\mathrm{eq}}}{e}$ can be found by substituting Eq. 4.6 into Eq. 4.4:

$$N_{\mathrm{eq}} = \frac{4\pi\epsilon_0 K_\phi}{e}\frac{k_{\mathrm{B}}T_e}{e}\left(\frac{a_d\times10^{-6}}{\mu\mathrm{m}}\right) = K_q\left(\frac{a_d}{\mu\mathrm{m}}\right)\frac{k_{\mathrm{B}}T_e}{e}, \tag{4.7}$$

where the grain's radius is expressed in micrometres and a factor of e is absorbed into the energy to match Cui & Goree (1994)'s choice of units (see Table 4.1).

Another useful quantity to find is the timescale τ_c during which a grain charges up in a plasma. Cui & Goree (1994) define τ_c as the time taken for an initially uncharged grain to approach its equilibrium charge within one e-fold, that is, the time taken for the grain to charge up to $\left(1-\frac{1}{\mathrm{e}}\right)\approx 63\%$ of its equilibrium value, illustrated in Figure 4.1. Cui & Goree (1994) introduce a coefficient K_{τ_c} so that

$$\tau_c = K_{\tau_c}\frac{\sqrt{k_{\mathrm{B}}T_e}}{a_d n_\alpha}, \tag{4.8}$$

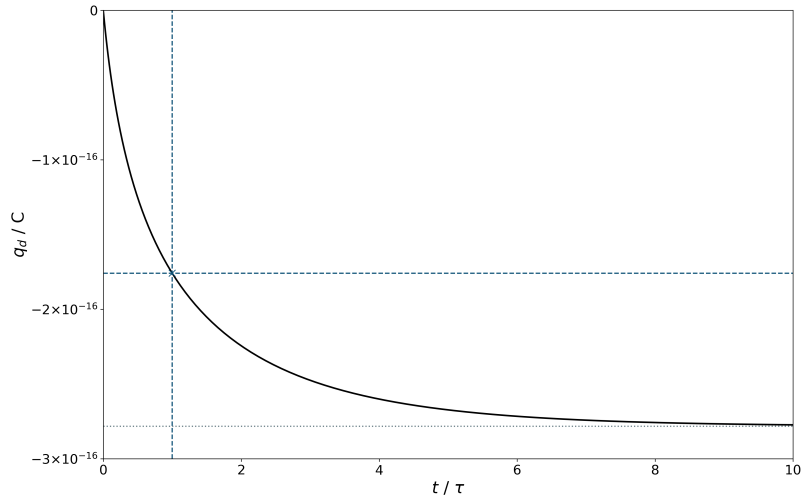

Figure 4.1: Continuous charging of a grain in a Hydrogen plasma with $T_i = T_e$ (second row of Table 4.1). The equilibrium charge is indicated by the dotted grey horizontal line. The e-folding charge value is indicated by the horizontal dashed blue line, which shows $(1 - \frac{1}{\mathrm{e}})q_{\mathrm{eq}}$ and the vertical blue dashed line indicates the charging timescale, τ_c.

indicating that charging rates are faster for higher plasma densities and larger grains, as makes physical sense given that larger grains provide a larger collecting area. The value of τ_c was estimated by locating the point of intersection of the exponentially decaying $q_d(t)$, obtained by numerically integrating Eq. 4.3, with the horizontal line $q_d = (1 - \frac{1}{\mathrm{e}})q_{\mathrm{eq}}$, as described in Figure 4.1. Electrons are collected more quickly, due to their higher mobility, resulting in an exponentially growing negative potential; as the negative charges collect, Coulomb repulsion results in the electron and ion currents saturating (Figure 4.2).

Substituting that graphically-determined charging timescale, τ_c, into Eq. 4.8 and re-arranging for K_{τ_c} (multiplying by a factor of $e^{\frac{1}{2}}$ to convert energy units) yields the rightmost column of Table 4.1. In order to verify the continuous charging model, as there were some discrepancies with Cui & Goree (1994), as shown by the Argon results in Table 4.1, the model was used to reproduce Shohet (2017)'s example for an Argon plasma. There is good agreement with Shohet (2017), Figure 4.2, with equilibrium reached within a few tenths of a millisecond: $\phi_{\mathrm{eq}} \approx -6\,\mathrm{V}$, $q_{\mathrm{eq}} = -3.4 \times 10^{-16}\,\mathrm{C}$.

As described in §1.2.3, the *CDA* instrument onboard *Cassini* observed grains on the scale of

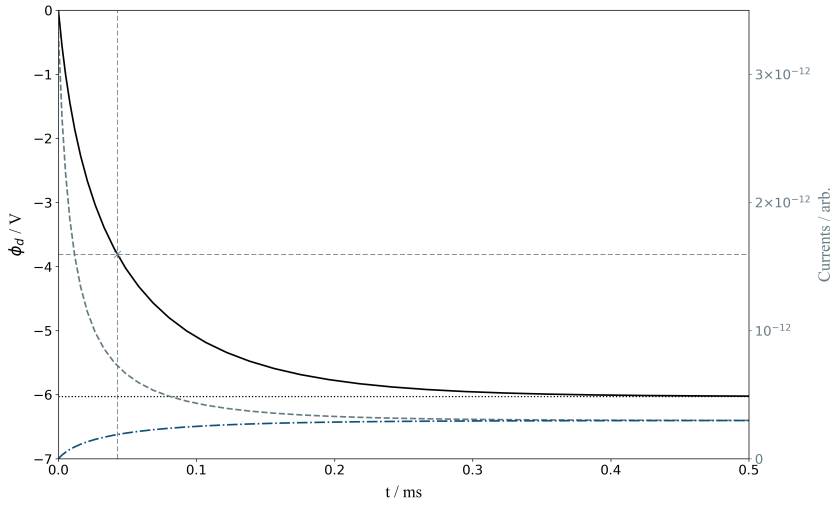

Figure 4.2: Continuous charging of a grain in an Argon plasma ($m_i = 40$ amu) with $T_e = 100T_i = 2.5$ eV, $n_i = n_e = 10^{14}\,\mathrm{m}^{-3}$ and dust grain of radius $a_d = 0.5\,\mu\mathrm{m}$. The grain potential is shown by the solid black exponential curve. The dash-dotted blue and dashed grey curves show I_i, I_e, the plasma ion and electron currents respectively. The equilibrium potential is indicated by the dotted black horizontal line. The e-folding potential value is indicated by the horizontal dashed grey line, which shows $(1 - \frac{1}{\mathrm{e}})q_{\mathrm{eq}}$ and the vertical grey dashed line indicates the corresponding time at which that occurs, τ_c. A scaling factor of 0.25 has been introduced for the currents to avoid crossing the potential curve, hence the arbitrary units on the right hand vertical axis. The equilibrium charge value is $-3.4 \times 10^{-16}\,\mathrm{C}$.

nanometres. For such small grains, the discrete nature of the electrons and ions present in the plasma and solar photoemission becomes important to consider as the grain carries only a small number of charges so any individual charging event changes the grain's potential significantly. Burns et al. (2001) quantify the number of excess charges on an isolated grain:

$$N_{\mathrm{ex}} \approx 700 \left(\frac{\phi_d}{\mathrm{V}}\right)\left(\frac{a_d}{\mu\mathrm{m}}\right). \tag{4.9}$$

For the example given in Figure 4.2 for a $0.5\,\mu\mathrm{m}$ grain, Eq. 4.9 estimates $2100e$, which is in agreement with the result from the continuous charging model, which gives $3.4 \times 10^{-16}\,\mathrm{C}/e \approx 2100$. However, for grains on nanoscales, the numbers are 1000 times smaller, for a given potential, and therefore a discrete model must be developed (§4.1.3).

The work of Cui & Goree (1994) was included in the review by Goree (1994), with equilibrium charge number and charging times plotted as a function of grain size for combinations of plasma temperature ratios and ion masses. Their results were compared to the implementation of the continuous charging model, with good agreement found for both Argon and Hydrogen plasmas (Figure 4.3).

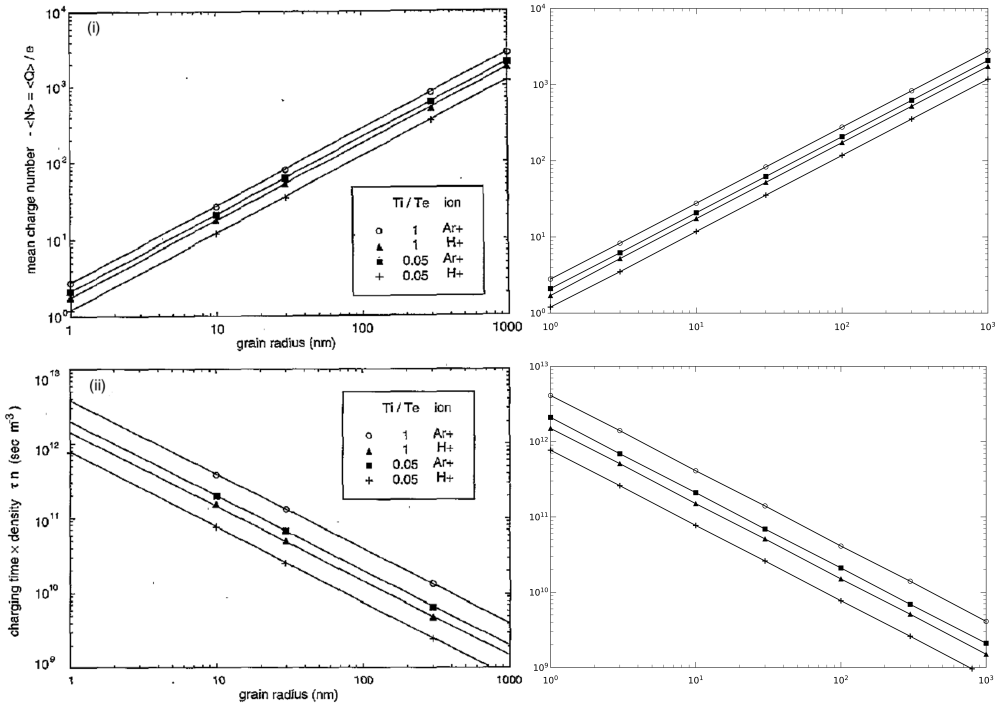

Figure 4.3: Comparing results calculated in this present work (right) with results of Goree (1994, left) . The top row, labelled (i), shows the mean charge number, and the bottom row, labelled (ii), shows the charging time, as a function of grain radius for the combinations of temperature ratios and ion masses described in Table 4.1 and labelled in the legend. Marker symbols have been chosen to match Fig. 1 of Goree (1994).

b) A Grain in Motion Relative to the Plasma

Including the relative motion of the grain through the plasma complicates the current expressions (Eq. 4.1), which were derived assuming a Maxwellian velocity distribution, that is, there were no direction-dependent properties included. However, in the reference frame of the orbiting dust grain, the plasma appears to have a net streaming velocity (Whipple 1981). This anisotropy is more pronounced for the ions, whose thermal speeds are lower than those of the electrons – most

of the ions are collected on the front of the grain. Kanal (1962) derived an expression for the plasma currents incident on a moving sphere, refer to Whipple (1981, Eq. 4.1), which is also described in the works of e.g. Havnes et al. (1992a); Horányi (1996); Graps et al. (2008).

The terms in such current expressions for a moving grain in a plasma depend on the Mach number (Graps et al. 2008), which is the ratio of the dust-to-plasma relative velocity to the plasma ion/electron thermal speed: $\mathcal{M} = v_{\text{rel}}/\sqrt{2k_{\text{B}}T_\alpha/m_\alpha}$. In the limit $\mathcal{M} \to 0$, the plasma current expressions become identical to Eq. 4.1. This is a reasonable approximation for dust grains in planetary magnetospheres, as argued by Jontof-Hutter (2012). Any difference in velocity between a Kepler-launched grain in the main rings and the velocity of the plasma (rotating at $R_{\text{syn}}\Omega_p$) is $v_{\text{rel}} \lesssim 10\,\text{km}\,\text{s}^{-1}$. The plasma temperatures required to exceed $10\,\text{km}\,\text{s}^{-1}$ are $T_e \gtrsim 3\,\text{K}$, $T_i \gtrsim 6000\,\text{K}$, by $\sqrt{2k_{\text{B}}T_\alpha/m_\alpha}$. By comparison, the plasma of the main rings is $\sim 1 - 10\,\text{eV}$ (Krupp et al. 2018), corresponding to a temperature of $\sim 10^4 - 10^5\,\text{K}$, thereby exceeding that of the grain's motion relative to the plasma. Jontof-Hutter (2012) examines the limiting case of a grain with velocity much larger than the sound speed, and also find that the current expressions reduce to Eq. 4.1. However, they caution the reader, noting the assumptions that were used to derive the current expressions for the moving grains in plasma may not be applicable for sub-micron grains with small numbers of individual charges. Jontof-Hutter (2012) did not consider the stochastic nature of dust charging for such small grains and this has significant consequences that are explored in §§4.1.3, 4.1.4 and 4.2.

4.1.3 Discrete Charging Model

In studying the random perturbations of the planetary magnetic field on the dust dynamics, Spahn et al. (2003) argue that stochastic charging variations can dominate the dynamics of sub-micron grains. The importance of the discretisation of the charging process is highlighted by an example in Hsu et al. (2011): an isolated grain carries $\sim 0.7\left(\frac{\phi_d}{\text{V}}\right)\left(\frac{a_d}{\text{nm}}\right)$ charges, by Eq. 4.9, and therefore a $5\,\text{nm}$ grain with a $-2\,\text{V}$ potential has only 7 additional electrons, and a single electron represents a $\sim 14\%$ change in the Lorentz force. Therefore, a more realistic charging model needs to take account of the discrete nature of charge carriers in plasma and the stochasticity of their absorption by small dust grains. That is, it is necessary to take into account the probabilities of these events occurring. Cui & Goree (1994) modelled the random nature of both the time interval between absorption events and the absorbed plasma particle type (i.e.

whether it is an electron or ion that is collected by the grain). In §4.2 a novel approach to discrete stochastic charging, building upon the work of Hsu et al. (2011), is implemented and compared to the work of Cui & Goree (1994).

Although there is a random element to the charging events, as the grain is immersed in a mixture of electrons and ions that are at varying distances (and hence varying absorption times), they are not uniformly random – through Coulomb attraction the grain is more likely to collect the opposite charge. The events follow probability distributions which depend on the grain's surface potential. Cui & Goree (1994) encapsulate the effect of the changing grain potential on the probability of absorbing an electron or ion through defining:

$$p_\alpha = \frac{I_\alpha(\phi_d)}{q_\alpha}, \tag{4.10}$$

which are probabilities per unit time of absorbing a plasma particle of species α (that is, electrons or ions). More ions are attracted and more electrons are repelled as the grain potential becomes increasingly negative. Equation 4.10 has this sought-after behaviour of p_i increasing and p_e decreasing with increasing $|\phi_d|$ for $\phi_d < 0$, and p_i decreasing and p_e increasing with increasing $|\phi_d|$ for $\phi_d > 0$, as can be seen from Equations 4.1 and 4.2. Thus, the OML currents of the continuous charging model are converted into probabilities for the discrete charging model. The time at which the plasma particle arrives at the grain is randomised and consistent with the probabilities per unit time defined in Eq. 4.10. The nature of the plasma particle, whether it is an ion or electron, is determined by the second step of the algorithm described in §4.1.4b).

4.1.4 Stochastic Charging Algorithm: Randomising Timestep and Particle Type

The physical model outlined above was implemented as described in Figure 4.4, following Cui & Goree (1994). The grain is initialised with zero charge. The model evolves in time by repeating two computation steps until the maximum integration time is reached, which is defined to ensure that a suitably large number of charging timescales has been spanned. Referring to Figure 4.4, these two steps (enclosed in separate dashed boxes), are more fully explained in the following §§4.1.4a) and b).

a) Time Update

The time interval Δt_n during which a plasma particle is absorbed by the grain for the n^{th} timestep is random, with probabilities that depend on the grain's surface potential. The total probability per unit time of absorbing a plasma particle is

$$p_{\text{tot}} = \sum_{\alpha} p_{\alpha}, \tag{4.11}$$

the sum of the individual probabilities per unit time, given by Eq. 4.10, which depends on the currents and hence the grain's surface potential by Eq. 4.1. Numerous authors assume that quantised grain charging corresponds to a Poisson process (Morfill et al. 1980; Khrapak et al. 1999; Hsu et al. 2011; Dzhanoev et al. 2016). If the number of events in a certain time period is Poissonian (events occurring independently at a constant rate over time), then the time interval between events follows an exponential distribution.

The result that an exponential probability density function can be used to model the waiting times between any two successive Poisson events can be derived in the following manner. Let X_n denote the time interval between the $(n-1)^{th}$ and n^{th} charging events. The first charging event occurs after a time Δt_1, if and only if no events of the Poisson process (with average rate λ) occur in the preceding interval $[0, t_1]$, that is

$$P(X_1 > \Delta t_1) = P(N(\Delta t_1) = 0) = \exp(-\lambda \Delta t_1), \tag{4.12}$$

where the number of events in any time interval Δt has a Poisson distribution:

$$P(N(\Delta t) = k) = \exp(-\lambda \Delta t) \frac{(\lambda \Delta t)^k}{k!}, \; k = 0, 1, \ldots. \tag{4.13}$$

The distribution X_n also takes the exponential form of Eq. 4.12, under the assumptions that (i) the number of events by time t_{n-1} is independent of the number of events occurring between t_{n-1} and t_n, that is the number of charging events that occur in disjoint time intervals are independent; and (ii) the probability distribution of $N(\Delta t_{n-1} + \Delta t_n) - N(\Delta t_{n-1})$ is the same for all Δt_n, that is the distribution of charging events that occur in a given time interval does not depend on its location (Ross 2014).

Using Eq. 4.12 for any general time,

$$P(X_n > \Delta t_n) = \exp(-\lambda \Delta t_n), \tag{4.14}$$

the cumulative probability distribution function can be written

$$P(X_n \leq \Delta t_n) = 1 - P(X_n > \Delta t_n) = 1 - \exp(-\lambda \Delta t_n). \tag{4.15}$$

The plasma particles arrive at a rate of p_{tot} given by Eq. 4.11, which is constant for a given grain surface potential, i.e. a given time interval. So during a time interval Δt_n, the probability for a grain to collect a plasma particle is

$$P = 1 - \exp(-p_{\text{tot}} \Delta t_n). \tag{4.16}$$

A random number R_1 is generated from the uniform distribution $U(0, 1]$ and equated with the probability of Eq. 4.16, then re-arranging for the time interval of that step gives

$$\Delta t_n = -\frac{\ln(1 - R_1)}{p_{\text{tot}}}. \tag{4.17}$$

Figure 4.4 shows how this step fits into the charging algorithm.

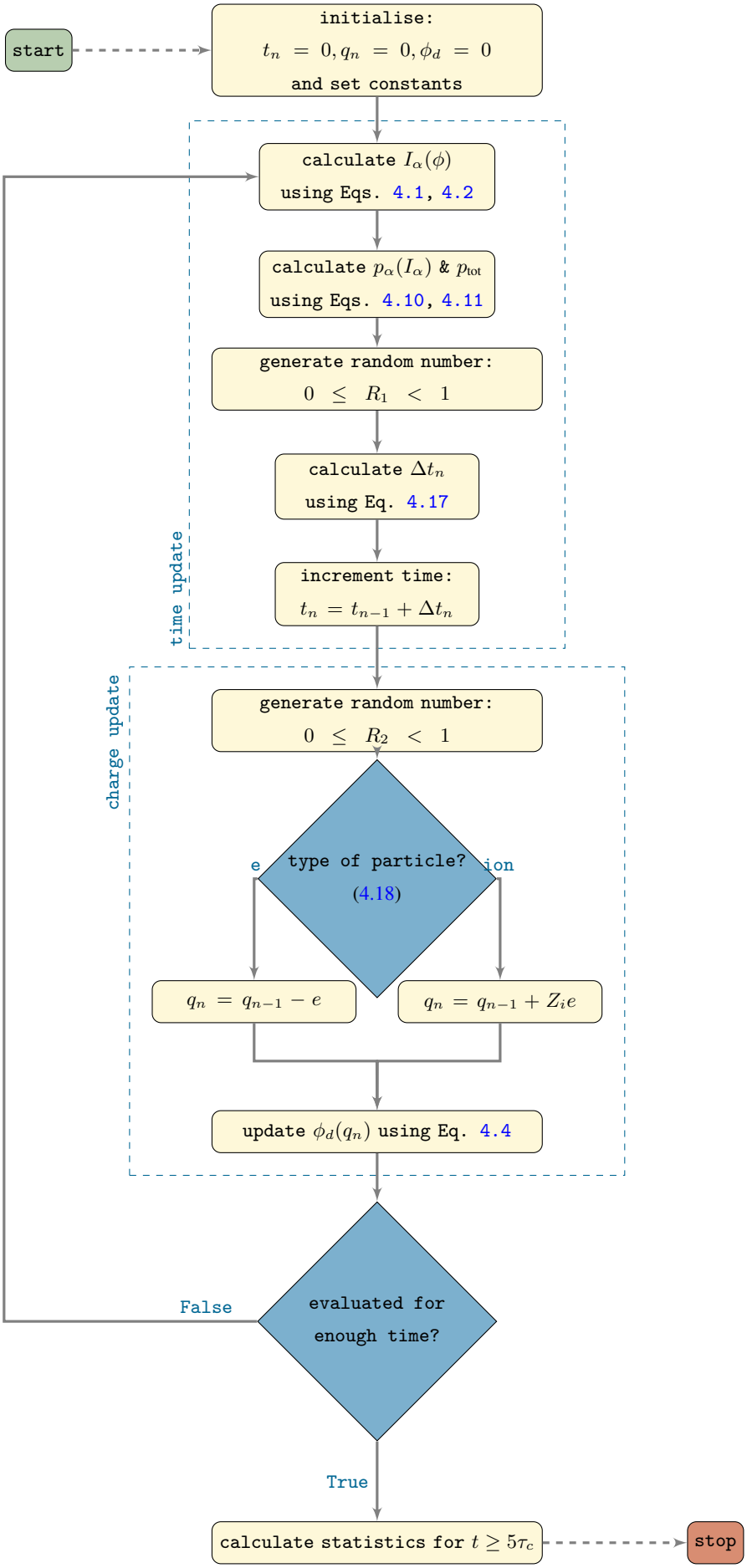

Figure 4.4: Flowchart describing the implementation of Cui & Goree (1994)'s discrete plasma charging model, adapted from their paper.

b) Charge Update

The probability that the n^{th} particle is species α is obtained by dividing Eq. 4.10 by Eq. 4.11: $\frac{p_\alpha}{p_{\text{tot}}}$. A second random number R_2 is generated to compare to that probability to determine whether the next plasma particle is an electron or an ion. This is then used to increment the total charge of the grain:

$$\begin{aligned} q_n &= q_{n-1} - e \quad \text{if} R_2 < \frac{p_e}{p_{\text{tot}}}, \\ q_n &= q_{n-1} + Z_i e \quad \text{if} R_2 > \frac{p_e}{p_{\text{tot}}}. \end{aligned} \tag{4.18}$$

Once the charge is updated, the grain's surface potential must be advanced, and then the loop continues as p_α depends on ϕ_d, Figure 4.4.

4.1.5 Simulation Results

Simulations were carried out using the method outlined in §4.1.4. The discrete model's charge values oscillate about the curve predicted by the continuous charging model, and both tend towards the equilibrium value calculated numerically, described by Eq. 4.7.

A comparison between a 10 nm and 100 nm grain is given in Figures 4.5 and 4.6. Both have an initial transient period where the charge on the grain grows rapidly negative. This is because initially the grain is positively charged relative to its equilibrium value and therefore is more likely to accumulate negative charges, and the electron flux is greater ($m_e < m_i$, electrons are more mobile). A comparison of the charging timescale, labelled on the upper horizontal axes of Figures 4.5 and 4.6, shows that for a given set of plasma parameters, the larger grain charges up more rapidly than the smaller grain, as described by Eq. 4.8. It is also apparent that the larger grain has smaller fractional charge fluctuations, as the fluctuations in Figure 4.6 appear smoother compared to Figure 4.5.

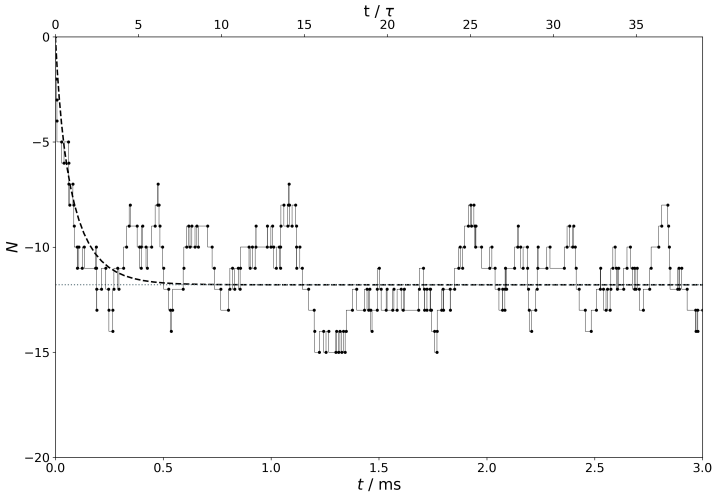

Figure 4.5: Time series of the charge number, $N = q_d/e$, for a grain of radius $10\,\mathrm{nm}$ with plasma parameters: $m_i = 1$ amu, $Z_i = 1$, $n = 10^{15}$ m^{-3}, $T_e = 1\,\mathrm{eV}$, $\frac{T_i}{T_e} = 0.05$. The smooth dashed black curve is the continuous charging model, described in §4.1.2, the stepped series is the discrete charging model of §4.1.4, and the dotted grey horizontal line indicates the equilibrium charge number, $N_{\mathrm{eq}} \approx 12$, corresponding to $\phi_{\mathrm{eq}} \approx -1.7\,\mathrm{V}$. The charging time is $\sim 77\,\mu\mathrm{s}$.

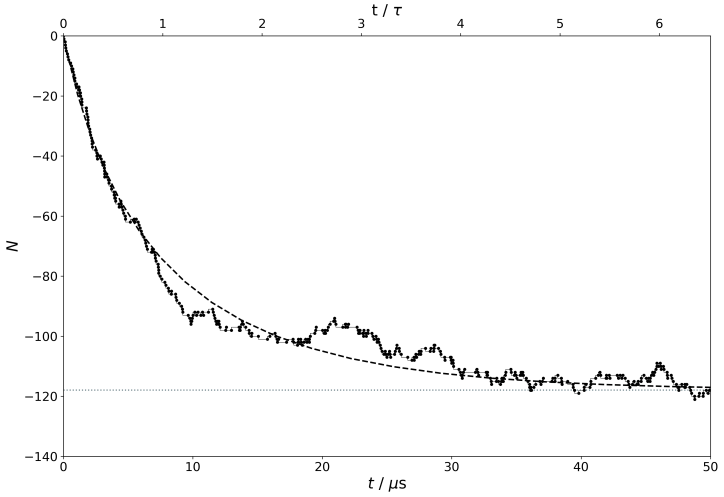

Figure 4.6: Time series of the charge number, $N = q_d/e$, for a grain of radius $100\,\mathrm{nm}$ with plasma parameters as in Figure 4.5, with the same linestyles for the respective continuous charging model, the discrete charging model and equilibrium value. $N_{\mathrm{eq}} \approx 118$, corresponding to $\phi_{\mathrm{eq}} \approx -1.7$ V, and the charging time is $\sim 7.7\,\mu\mathrm{s}$.

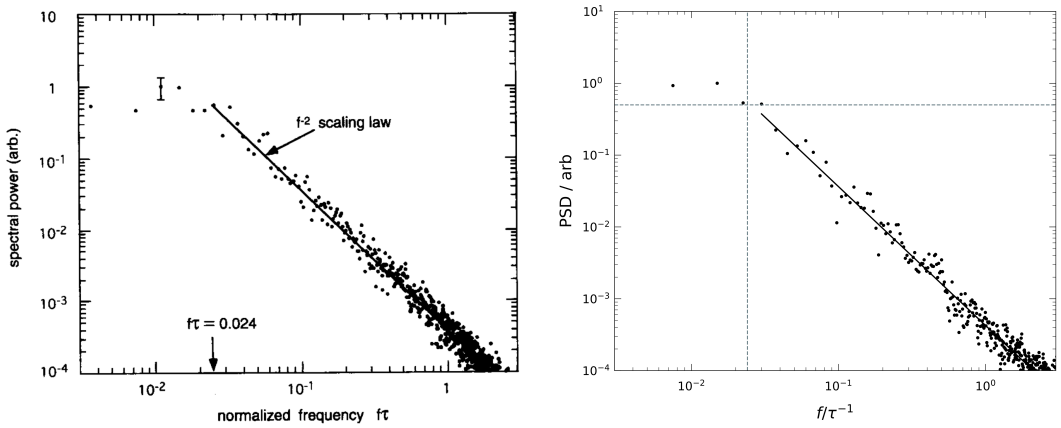

Figure 4.7: Power spectrum of charge fluctuations, with the same plasma and grain parameters as those used in Figure 4.6. Present work shown on the right, with reference values of $f\tau_c = 0.024$ and spectral power $= 0.5$ drawn as grey dashed lines, and compared to Cui & Goree (1994) with the power law f^{-2} shown by a solid black line. Frequencies have been scaled by the inverse of the charging time.

The nature of the charge fluctuations can be studied using the standard method of computing the power spectral density (PSD) for the time series $q_d(t)$, in order to ascertain which frequencies contain the signal's power and to see whether charge fluctuations tend to be dominated by high or low frequencies. The PSD was calculated using Welch's method: the time series is split into overlapping segments, a window is applied to the segments, then the discrete Fourier transform is used to compute the modified periodogram for each segment, which are then averaged (Welch 1967), using the SciPy implementation (Virtanen et al. 2020). The plasma and grain parameters of Figure 4.7 are the same as those used in Figure 4.6 with the solution evolved for longer in order to study the charge fluctuations over $100\tau_c$. The initial transient decay period shown in Figure 4.6 is not included in the analysis, so that $5\tau_c < t < 105\tau_c$. In order to allow a direct comparison with Cui & Goree (1994, Fig. 6), the frequencies of Figure 4.7 are normalised by the inverse of the charging time. The power spectrum result of Cui & Goree (1994) is verified, with Figure 4.7 showing that the charge fluctuations are dominated by low frequencies and that at higher frequencies the power drops off as approximately the inverse second power of frequency.

Cui & Goree (1994) also study the charge distribution function for grains, in order to quantify at a given time the fraction of grains holding a certain charge (assuming they are isolated, Eq. 1.40). This is something that could be useful for ring rain (§1.2.3) study, to see how long water-ice versus silicate dust spends at a certain charge level, although the manner in which to model

the differing compositions is beyond the scope of this work.

The algorithm described in this section (Figure 4.4) determines how long a time interval is between successive stochastic charging events. However, flipping the problem by asking how many charging events occur within a given time interval allows the charging updates to be implemented alongside the equations of motion in the adaptive integration method (§2.2).

4.2 Charging Algorithm Using Poisson Processes

An approach based on but different to that described in §4.1 for the discrete charging of a grain is motivated by the need to simultaneously solve the charging equation alongside the orbital equations of motion. The adaptive integrator (§2.2) outputs the orbital motion solution for the grain at each timestep. As described in §4.1.3, the grain's charge varies stochastically with time and therefore in each timestep the number of electrons/ions collected by the grain must be estimated. Instead of modelling the inter-arrival times of plasma particles using an exponential distribution, the Poisson distribution can be used to model the number of charged particles being collected by the grain in a given timestep. The type of particle is handled by the algorithm as described below, involving Poisson and binomial probability distributions and weighting the various currents appropriately.

A novel stochastic charging algorithm based on the work of Hsu et al. (2011) was developed, which models the photoelectron current, I_ν, given below in Eq. 4.19, in addition to the plasma currents considered in Cui & Goree (1994)'s model (§4.1.4). The photoelectron current depends on the grain's material properties, with an efficiency coefficient κ_ν, which enters the factor $f = 2.5 \times 10^{14} \kappa_\nu \left(\frac{AU}{r}\right)^2 \mathrm{m}^{-2}\,\mathrm{s}^{-1}$, effective area πa_d^2, and potential ϕ_d:

$$I_\nu = \begin{cases} \pi a_d^2 e f & \text{if } \phi_d < 0, \\ \pi a_d^2 e f \exp\left(-\frac{e\phi_d}{k_\mathrm{B} T_\nu}\right) & \text{if } \phi_d \geq 0, \end{cases} \tag{4.19}$$

where the mean energy of the photoelectrons $\sim 2.7 k_\mathrm{B} T_\nu$ (e.g. Horányi 1996).

There is another current that needs to be considered, before preceding to a description of the stochastic charging algorithm. Plasma particles incident upon the dust grain can be energetic

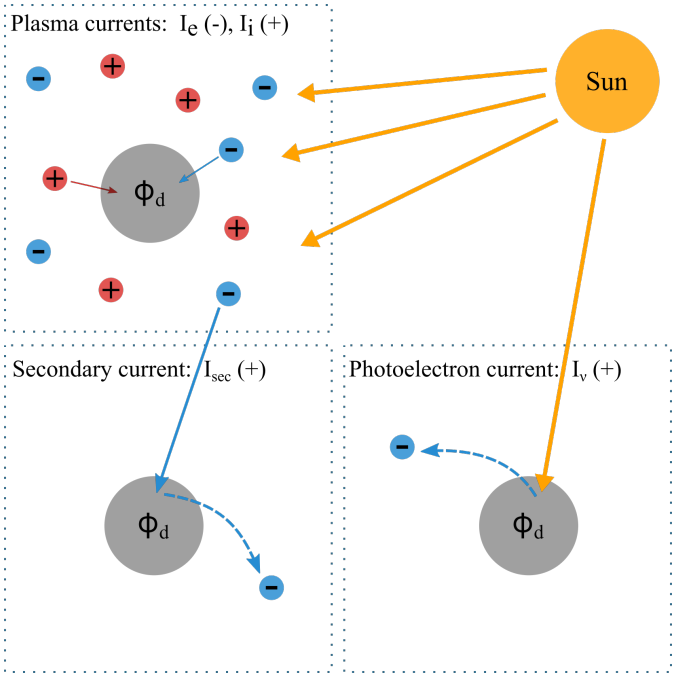

Figure 4.8: Schematic sketch of dust charging currents in Saturn's environment, based on Hsu (2010, Fig. 1.7).

enough to ionise the material and produce the emission of secondary electrons. Like the photoelectron current, Eq. 4.19, and ion current, I_i of Eq. 4.1, this flux of escaping electrons represents a positive grain-charging current, $I_{\rm sec}$. These various currents are summarised in Figure 4.8. The secondary electron emission depends on the primary incident particle's energy as well as the material and surface properties of the dust (Dionne 1975). Low energy incident particles have a low yield, as to be expected since these will be unable to sufficiently excite secondary electrons, but high energy particles too have a low yield, as they can pass through the grain losing little energy. Between these two extrema, there is a characteristic primary incident particle energy that results in a maximum yield of secondary electrons (Dionne 1975). Meyer-Vernet (1982); Horányi (1996); Hsu et al. (2011), amongst others, provide expressions for the secondary emitted electron flux, with Chow et al. (1993) accounting for the increase in secondary emission yield with decreasing grain size.

Inside of $\sim 5\,R_{\rm S}$, charge equilibrium is reached principally by the balance between plasma currents, Eq. 4.1, and it is only further out, as the electron temperature increases with distance from Saturn, that the secondary electron current becomes the major positive current, superseding

I_i and I_ν (Hsu et al. 2011). Indeed, Jontof-Hutter (2012, Fig. 5.1) plot charging contributions for a $10\,\mathrm{nm}$ grain in Jupiter's main ring and find that I_{sec} is orders of magnitude smaller than I_i, I_ν at lower temperatures ($T_e \lesssim 1\,\mathrm{eV}$), which is a reasonable analogy to Saturn having a tenuous plasma density of $n \sim 1\,\mathrm{cm}^{-3}$ in the vicinity of the main rings (Johnson et al. 2006). Therefore, for the purposes of the study of the dust dynamics in the main rings, the secondary electron emission current will be omitted.

Returning to the problem of stochastically generating the number of charging events within a timestep, Hsu et al. (2011) introduce a Poisson process approach, which is further developed in the work of Hsu et al. (2018a). They developed their procedure independently of Cui & Goree (1994) but reach a similar approach. Their method can be summarised as (i) Generate a random number to determine how many events occur during the timestep using a Poisson probability distribution, and (ii) Decide the type of charging events that occurs according to the relative strengths of the various currents.

For the plasma and photoemission currents, the expected number of charging events occurring between a time t_n and $t_n + h$ (i.e. the rate) for a current of type α is

$$\lambda_\alpha = \int_{t_n}^{t_n+h} \frac{I_\alpha}{e} dt \quad \text{for} \;\; \alpha = i, e, \nu, \tag{4.20}$$

where the currents are given by Eqs. 4.1 and 4.19. A random number is generated from a uniform distribution, $R_{\mathrm{P}}^\alpha \sim U(0,1]$, and compared to the Poisson distribution for each current type,

$$P(\lambda_\alpha, k_\alpha) = \exp(-\lambda_\alpha)\frac{\lambda_\alpha^{k_\alpha}}{k_\alpha!}, \text{for } k_\alpha = 0, 1, \ldots \tag{4.21}$$

given a number of charging events $k_\alpha = 0, 1, \ldots$ (cf. Eq. 4.13). So, for example, if $\lambda_\alpha = 0.4$ for a given current type (assuming a single current for simplicity) and the random number happens to be $R_{\mathrm{P}}^\alpha = 0.965$, then comparing to the corresponding probabilities:

$$\begin{aligned} &P(\lambda_\alpha = 0.4, k_\alpha = 0) = 0.670\ldots, \\ &P(\lambda_\alpha = 0.4, k_\alpha = 1) = 0.268\ldots, \\ &P(\lambda_\alpha = 0.4, k_\alpha = 2) = 0.0536\ldots, \\ &P(\lambda_\alpha = 0.4, k_\alpha = 3) = 0.00715\ldots, \\ &\quad\ldots \end{aligned} \tag{4.22}$$

which are illustrated in Figure 4.9, it can be seen that the $k_\alpha = 2$ event is chosen as R_{P}^{α} falls within that bin; that is, two charges happen to be collected by the grain during that timestep. The nature of the charges, whether electron or ion, depends on the current type in question; the way that the code developed here handles multiple current types is explained in greater detail by Figures 4.15 and 4.16 in §4.2.1b).

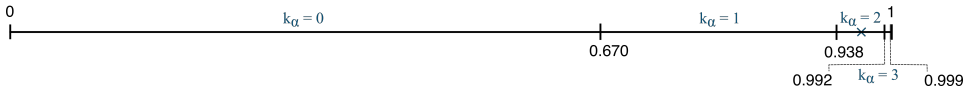

Figure 4.9: Poisson probabilities of 4.22 for $\lambda_\alpha = 0.4$ for $k_\alpha = 0, 1, 2, 3$. A cross marks $R_{\mathrm{P}}^{\alpha} = 0.965$, described in the main text.

Hsu et al. (2011) sets an upper bound on the expected number of charging events in a given time interval, $\lambda_\alpha \sim 0.4$ so that the probability of having more than one charging event per step is $1 - P(k_\alpha = 0, 1) = 1 - \mathrm{e}^{-0.4}(1 + 0.4) \approx 6.2\%$. That is, they choose their timestep sizes so that no more than a single charging event takes place during each step in most cases. The exact time of the charging event is unknown (beyond the resolution of the step size chosen by the orbital integrator), and therefore allowing more than one charging event per step would enhance this inaccuracy because it would permit several charging events to occur simultaneously at the start of a (single larger) step. The charging timescale should determine the modelling timestep used in the numerical integration.

The method of Hsu et al. (2011) either permits the occasional multiple charging event to occur in a single step or discards steps with $\lambda_\alpha > 0.4$, which has the potential to skew the probability distribution towards prohibiting rare multiple events. In this thesis, a timestep-splitting approach is taken to *ensure* that no more than a single charging event occurs within a single (sub)step, by recursively splitting the step until that condition is fulfilled. This novel stochastic charging method automates the process of simultaneously updating the equations of motion (Eq. 2.1) and charging equation (Eq. 4.3) by utilising a binary tree traversal algorithm (§4.2.1).

4.2.1 Binary Tree Traversal for Charge Distribution

If the adaptive integrator for the equations of motion (§2.2) returns a timestep during which the total number of charging events for all the currents is greater than one, $\sum_\alpha k_\alpha > 1$, then the timestep is divided in half and the charging events are distributed across the step according to binomial probability distributions, weighted according to the respective strengths of the contributing currents, which will be explained further in the following examples, refer to Figures 4.15 and 4.16. This is different to the approach of Hsu et al. (2011), which either allows (without adjustment) or discounts the occurrence, albeit rare, of multiple charging events within a single step. The precise method of the tree-traversing algorithm for multiple currents is outlined in §4.2.1b), but it is enlightening to describe a specific single current case (§4.2.1a)) before generalising.

a) Single Current

The decision of how to distribute the multiple charging events for a single current, generated by the Poisson distribution (shown by example in Figure 4.9), in time across the step is a matter of finding the random variable X_α, denoting the number of electrons/ions collected by the grain for the first half-step, as in general (for each current type) the number of charging events in the second half-step must be the difference between the number of charging events for the full step and the first half-step: $k_\alpha - X_\alpha$. The number of charging events for the first half-step, x_α, is obtained from the binomial distribution, as it can be modelled as the probability of obtaining X_α events in the first half-step out of k_α Bernoulli trials. Therefore, the probability of choosing the number of charging events to occur in the first half-step can written as

$$P(X_\alpha = x_\alpha) = \frac{k_\alpha!}{x_\alpha!(k_\alpha - x_\alpha)!}\left(\frac{1}{2}\right)^{k_\alpha} \text{ for } x_\alpha = 0, 1, \ldots, k_\alpha, \tag{4.23}$$

given the total number of charging events in the whole step, k_α; noting the assumption that any electron/ion is equally likely to encounter the dust grain in the first or second sub-step, hence a probability of $\frac{1}{2}$ in the binomial probability (4.23).

Consider the simple case of a single current I_α, once a random number, $R_1^\alpha \sim U(0, 1]$ has been generated and compared to the Poisson distribution, which causes two electrons/ions to collect

on the grain, $k_\alpha = 2$, as illustrated in Figure 4.9. Since only one or zero charging events are permitted per timestep, the step is split in half, and the order in which the two events occur over time is generated using a binomial distribution with a second random number, $R_\mathrm{B} \sim U(0,1]$ in a similar fashion, described in Figure 4.10. If R_B = 0.7641, for example, then both charging events occur in the first half-step, which will need to be further split again (and the zero events in the second half-step stored).

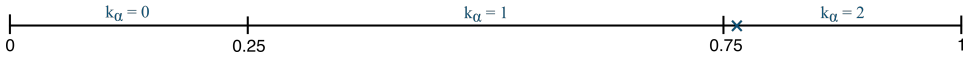

Figure 4.10: Binomial probabilities of Eq. 4.23 for $k_\alpha = 2$. A cross marks $R_\mathrm{B} = 0.7641$, described in main text.

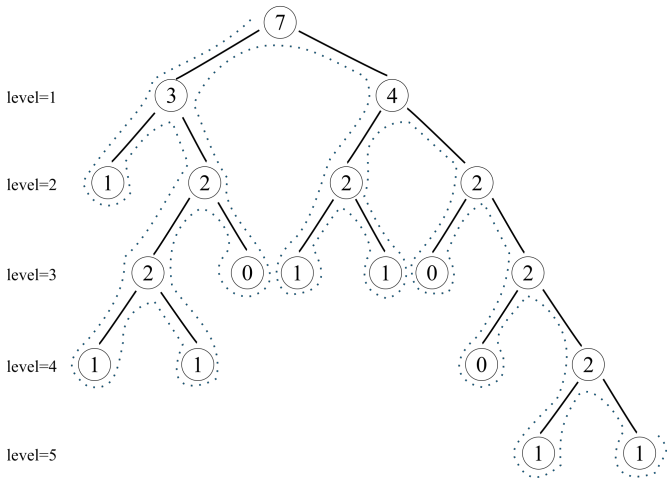

Figure 4.11: A binary tree example, showing how 7 charging events in the initial stepsize could be randomly distributed between substeps. Each numbered circle represents a node, a structure containing the number of charging events at that level. The root is the top node in the tree. Each node must have either 0 or 2 children (nodes which are directly connected below the node in question) as the substep either contains $k_\alpha = \{0, 1\}$ or must be split again. The number of events in the right branch is the difference between the number of events in the parent and the left branch. The order of the steps for pre-order traversal, indicated by the dotted blue line, is 1) visit node 2) go to left branch 3) go to right branch, so that in this example it is 7312211042112020211, with the code returning the leaf nodes and corresponding levels: $[(k_\alpha = 1, l = 2), (1,4), (1,4), (0,3), (1,3), (1,3), (0,3), (0,4), (1,5), (1,5)]$.

The recursive nature of the problem of assigning charging events between substeps lends itself well to using binary trees, hierarchical data structures consisting of nodes and edges, which are described by Figure 4.11. The root node contains the initial timestep's charging event number, $k_\alpha > 1$, then the left and right branches are populated at each level as the (sub)steps are split

in half recursively and charging events assigned to each based on binomial probabilities (4.23), until the base case of $k_\alpha = \{0, 1\}$ is achieved, thereby terminating the tree structure at leaf nodes.

The arrow of time means that the code must execute a *pre-order tree traversal* (a variant of depth first traversal), so that the nodes are visited in the correct order and the timestep is incremented from leftmost leaf node to rightmost leaf node. The code abstracts the binary tree away and uses a tree walker function to track the level of the node and randomly generate the children of the current node it is located at, thereby adding a *left branch* and *right branch* frame object to the top of the call stack; then when the leaf node is reached, each walker function call is returned and a frame object is popped off the call stack.

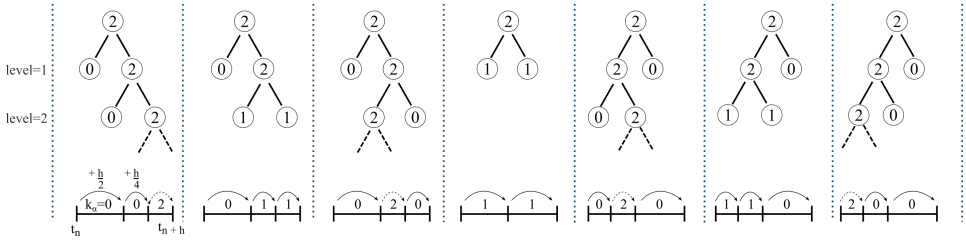

Figure 4.12: The time-step splitting lends itself well to recursion and a binary tree structure, as illustrated for the single current $k_\alpha = 2$ case. All possible charging event outcomes down to a level 2 are shown. Dashed lines denote where $k_\alpha > 1$ beyond the level 2 included here and where further splitting is required. The corresponding timestep splitting is shown below each binary tree outcome. Arrows indicate how the step is traversed, by adding $\frac{h}{2^l}$ for each base case, with dashed arrows indicating where the timestep would need to be further refined in order to distribute the charges.

The depth of the leaf node l enables the timestep to be traversed in increments of $\frac{h}{2^l}$. Figure 4.12 illustrates this, showing all possible outcomes for a simple example. A more complex single current case is given in Figure 4.13.

The code was tested to ensure that all edge cases were accounted for, by running batches of 10^6 simulations and counting up each binary tree outcome for an extensive range of k_α and maximum tree depth. The resulting distributions agreed with theoretical predictions (obtained by standard probability theory), Figure 4.14.

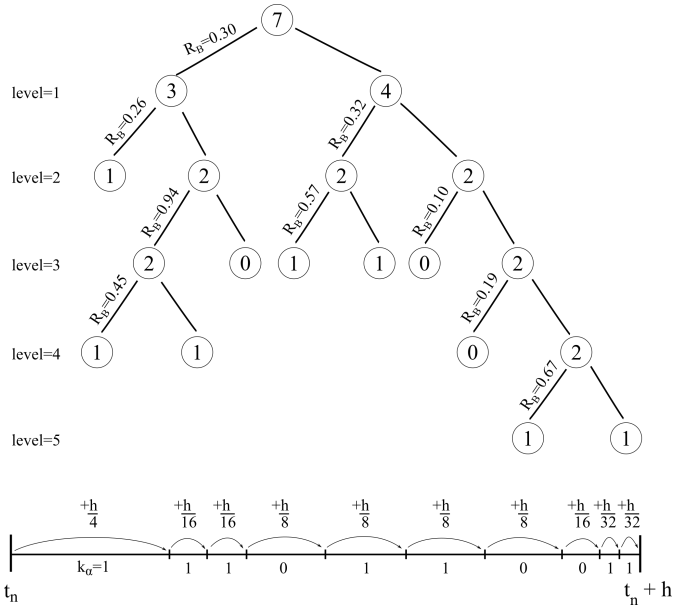

Figure 4.13: A single current binary tree example for a $k_\alpha = 7$ event generated by a Poisson distribution, with each decision of how to split the charging events obtained by the binomial probabilities, R_B. The corresponding timestep traversal is drawn underneath, each substep being incremented by $\frac{h}{2^l}$ for the base case levels.

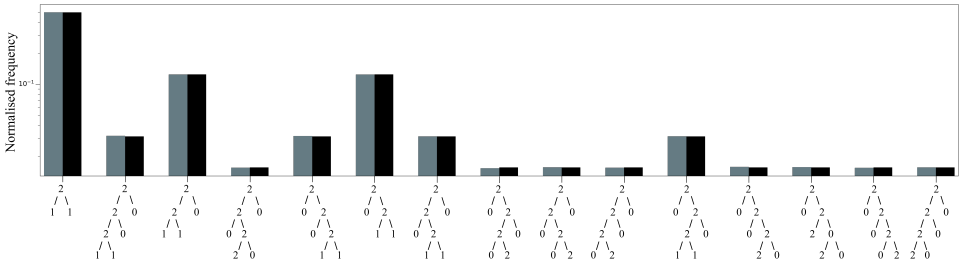

Figure 4.14: Unit testing the binomial probability code for a single current, $k_\alpha = 2$, down to tree level $= 3$. The predicted frequencies are plotted as darker (right) bars, the simulated frequencies for 10^6 runs are plotted as lighter (left) bars for each binary tree output, which are labelled on the horizontal axis.

b) Multiple Currents

The approach can be generalised for multiple current types to account for the photoelectron current and plasma electron and ion currents simultaneously. The expected number of charging events, λ_α, is calculated for each current respectively using Eq. 4.20. Together with the Poisson distribution (4.21) and a uniform random number for each current, $R_{\mathrm{P}}^{\alpha} \sim [0, 1)$, this generates the number of charging events in a given timestep for each current, k_α. If $\sum_\alpha k_\alpha > 1$, then the step must be split and the events distributed in smaller substeps using a similar approach to that used for a single current. However, given that there are multiple currents to consider, the binomial probability distributions for each type of current $\alpha = i, e, \nu$, given by 4.23, must be weighted according to the fraction of events that each contributes,

$$W_\alpha = \frac{k_\alpha}{\sum_\alpha k_\alpha}. \tag{4.24}$$

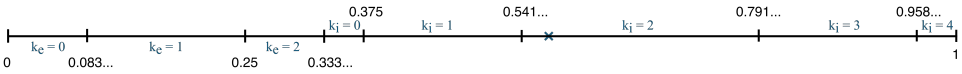

Figure 4.15: Weighted binomial probabilities for $k_e = 2, k_i = 4, k_\nu = 0$. The plasma electron current has a weight of $W_e = \frac{2}{6}$, the plasma ion current $W_i = \frac{4}{6}$, and $W_\nu = 0$. For instance, the $k_e = 0$ probability spans the range 0 to $\frac{2}{6} \times \frac{2!}{0!2!}\left(\frac{1}{2}\right)^2 = \frac{1}{12} \approx 0.083\ldots$, and the $k_i = 0$ probability spans the range $\frac{2}{6}$ to $\frac{2}{6} + \frac{4}{6} \times \frac{4!}{0!4!}\left(\frac{1}{2}\right)^4 = \frac{3}{8} = 0.375$. A cross marks $R_{\mathrm{B}} = 0.57$, which would mean that two plasma ion charging events occur in the first half-step.

Figure 4.15 shows such a weighted binomial probability distribution for multiple currents. Once the number and type of charging events in the first half-step has been determined, the remaining events must occur in the second half-step, which will have its own weighted binomial probability distribution, then both half-steps check the condition for further splitting, $\sum_\alpha k_\alpha > 1$, and further timestep splitting is applied if necessary. This process is repeated until the base case of $k_\alpha = \{0, 1\}$ is achieved. A resulting binary tree structure for multiple current types with the Poisson-generated events $k_e = 2, k_i = 4, k_\nu = 0$ (the same case as illustrated in Figure 4.15) is shown in Figure 4.16.

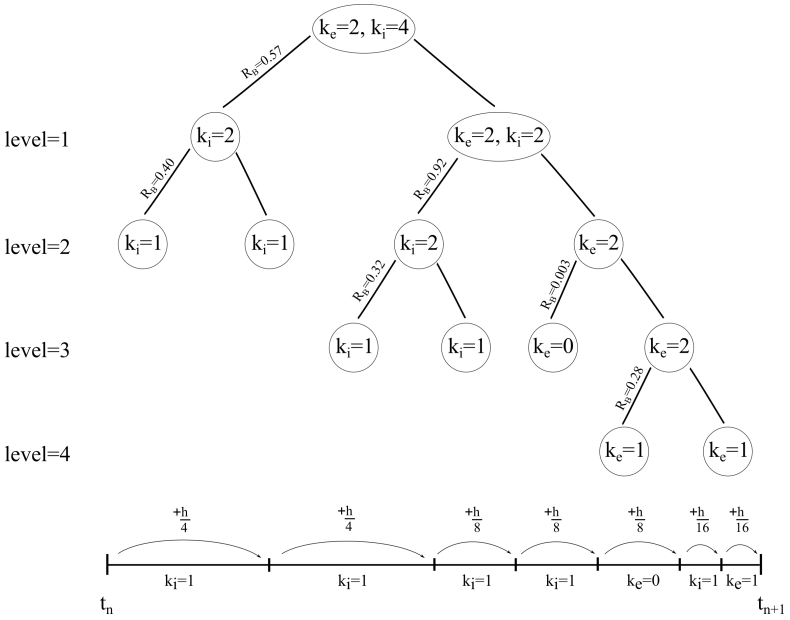

Figure 4.16: As Figure 4.13, but for multiple currents showing $k_e = 2, k_i = 4, k_\nu = 0$.

As in §4.2.1a), the code was tested to ensure that all edge cases were accounted for, by running batches of 10^6 simulations and counting up each binary tree outcome for a range of k_α and a specified maximum tree depth. The resulting distributions agreed with theoretical predictions, refer to Figure 4.17.

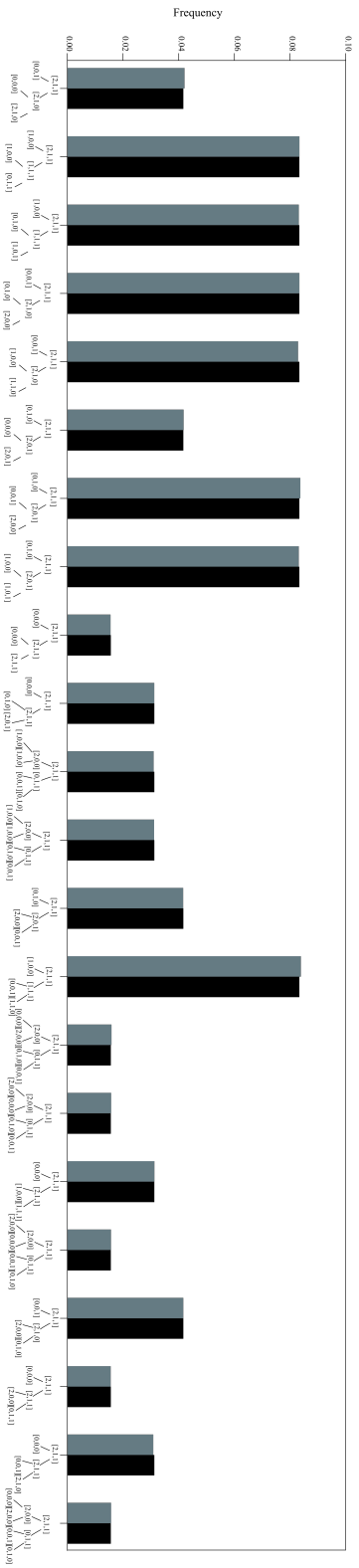

Figure 4.17: Unit testing the binomial probability code for multiple currents, $k_e = 2, k_i = 1, k_\nu = 1$, down to tree level $l = 2$. The predicted frequencies are plotted as darker (right) bars, the simulated frequencies for 10^6 runs are plotted as lighter (left) bars for each binary tree output, which are labelled on the horizontal axis. The shorthand, e.g., $[2, 1, 1]$ has been used in place of $k_e = 2, k_i = 1, k_\nu = 1$.

4.2.2 Applying the Binary Tree Traversal Algorithm

Having tested the novel stochastic grain charging algorithm, the code was applied to the problem of dust in plasma as posed by Cui & Goree (1994), described in §4.1.5. The I_e and I_i plasma currents, Eqs. 4.1 and 4.2, were used in the binary tree traversal method described in §4.2.1b). Figures 4.18a and 4.18b show the algorithm reproduces the expected results.

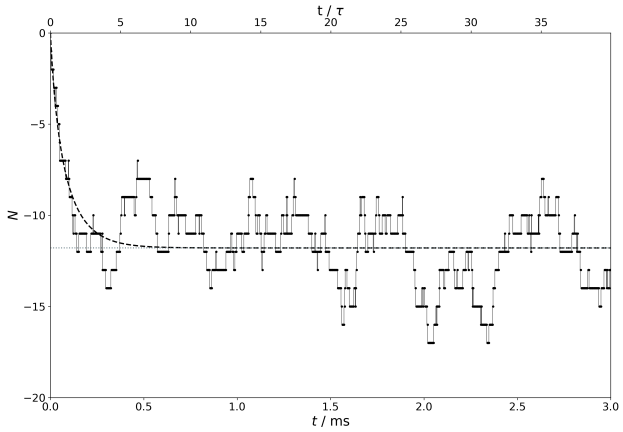

(a) $a_d = 10\,\mathrm{nm}$, refer to Figure 4.5 for simulation parameters.

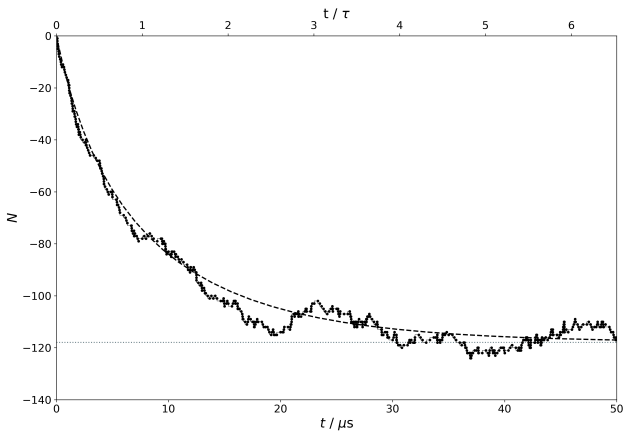

(b) $a_d = 100\,\mathrm{nm}$, refer to Figure 4.6 for simulation parameters.

Figure 4.18: Time series of the charge number, $N = q_d/e$, for two different grain sizes: $10\,\mathrm{nm}$ (top) and $100\,\mathrm{nm}$ (bottom) with plasma parameters and linestyles as described in §4.1.5.

The charging algorithm was integrated for $1000\,T_{\rm K}$ to check its long-term behaviour and include the effects of the photoelectron emission current, Eq. 4.19, in addition to the plasma currents, Eq. 4.1. At Saturn, the photo-emission factor is $f \approx 2.7 \times 10^{12}\,\mathrm{m^{-2}\,s^{-1}}$ (Horányi 1996). The simulation was run with hydrogen plasma parameters used by Hsu et al. (2011) and Hsu et al. (2018a): $n = 0.3\,\mathrm{cm^{-3}}$, $T_e = 5\,\mathrm{eV}$, $T_i = T_e$, $T_\nu = 2.5\,\mathrm{eV}$, for an initially uncharged grain launched around Saturn at $r_L = 1.48\,R_{\rm S}$ with radius, $a_d = 10\,\mathrm{nm}$ and a dielectric constant for water of $\kappa_\nu = 0.1$. The algorithm appears well-behaved as the charge does not grow to unphysical values (Figure 4.19). The steps of the charging algorithm and how it is implemented alongside the orbital code are summarised in Figure 4.20.

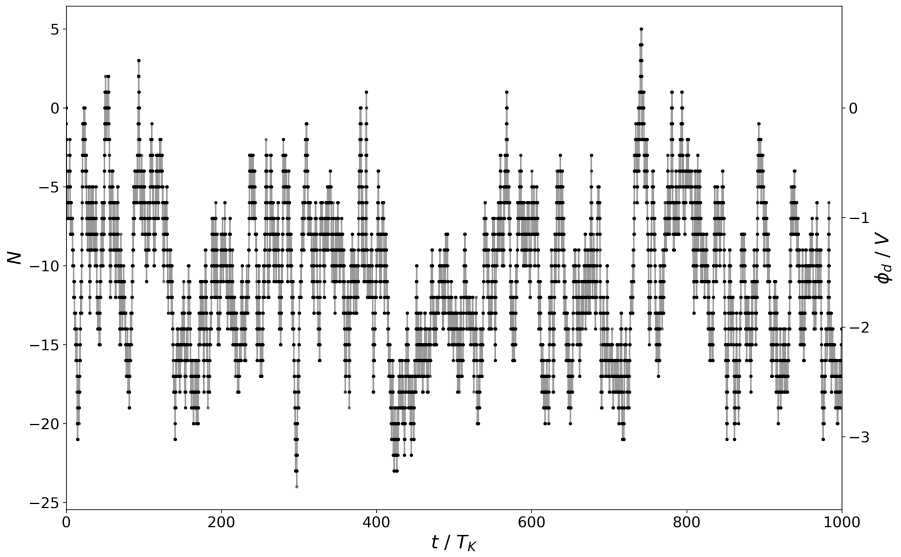

Figure 4.19: Time series of the charge number, $N = q_d/e$, and grain potential, ϕ_d, for a grain of radius $10\,\mathrm{nm}$ with plasma parameters following Hsu et al. (2018a), as described in the main text. The grain's potential is labelled on the right hand vertical axis using Eq. 4.4.

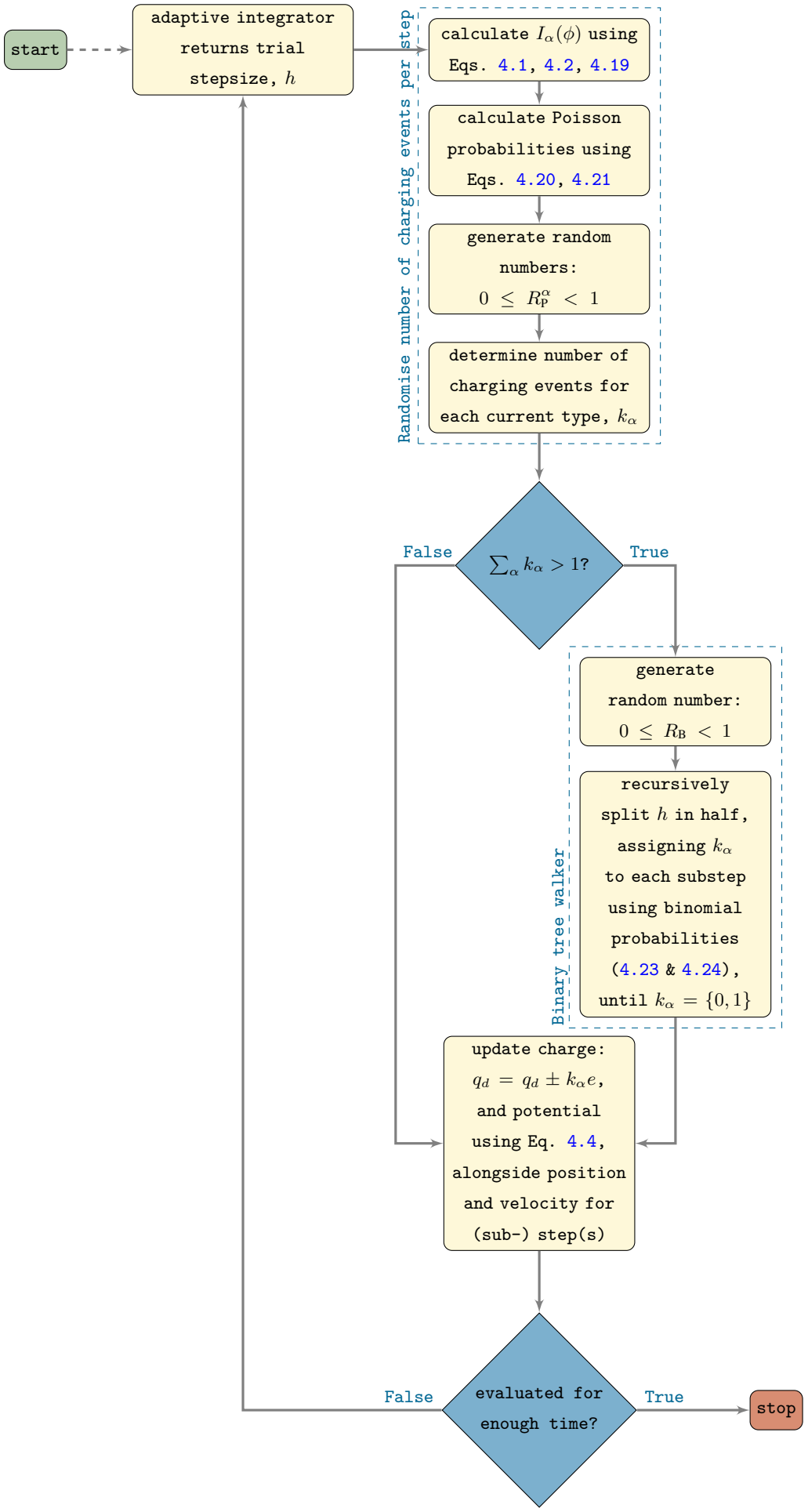

Figure 4.20: Simplified flowchart describing implementation of discrete stochastic charging algorithm alongside orbital code.

4.3 Planetary Shadow

The implementation of the photoelectron current necessitates the inclusion of the planetary shadow. As a grain passes behind the planet, relative to the Sun, it enters a shadow region where the photoelectron current is switched off, then as it passes back into sunlight, the photoelectron current switches back on; resulting in periodic changes in the surface potential of dust as it orbits around the planet. The equilibrium surface potential of a grain in sunlight is less negative than in shadow, as the solar photons eject electrons from the dust surface (Figure 4.8).

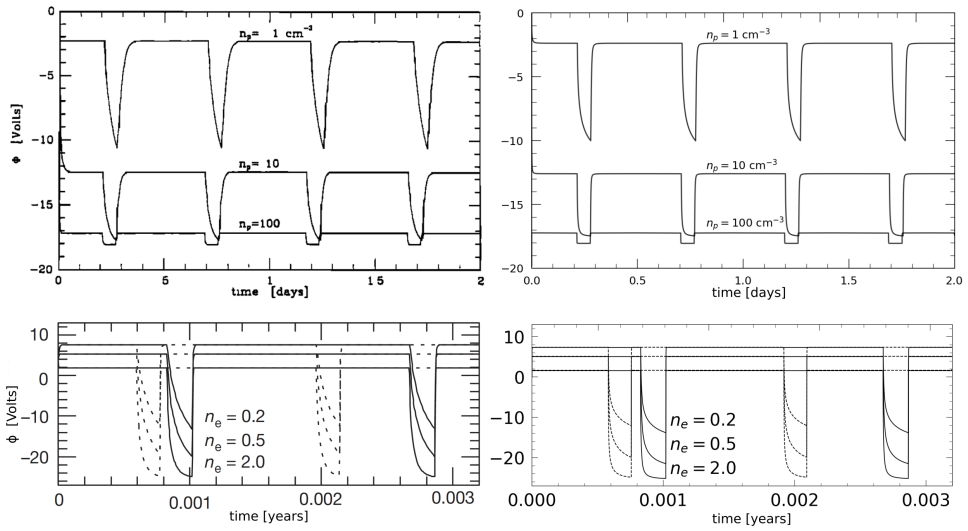

Figure 4.21: Reproducing continuous charging results, including I_e, I_i, I_ν, and planetary shadow, for micron-sized dust in Jupiter's gossamer rings. Top row: Horányi & Burns (1991, Fig. 5), bottom row: Hamilton & Krüger (2008, Fig. 3a). The original literature is shown on the left hand side.

The shadow's modulating effect on the photoelectron current changes the semi-major axes and eccentricities of grains (Horányi & Burns 1991). Figure 4.21 reproduces some previous literature results for variable-charged dust in Jupiter's gossamer rings. The slight differences between the shapes of the curves may be due to slight differences in the input parameters, as the full simulation parameters were not detailed. Hamilton & Krüger (2008) show that the transit of dust through the planet's shadow creates the Thebe extension, faint material in the rings outside the moon's orbit that had previously eluded understanding. Like Horányi & Burns (1991), they find that shadowing can cause significant changes to the sizes and shapes of dust orbits, that accumulate in phase over months; Figure 4.22 shows such a shadow resonance producing a

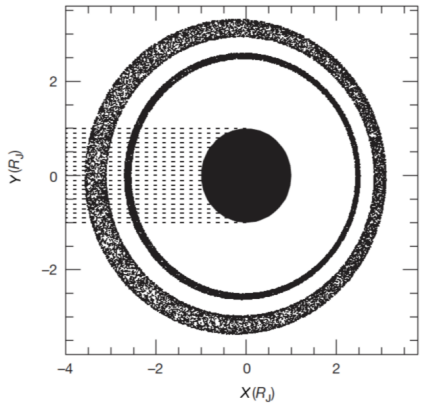

Figure 4.22: Numerical simulations by Hamilton & Krüger (2008, Fig. 3c) of $3.2\,\mu\mathrm{m}$ dust grains in an $n_e = 2\,\mathrm{cm}^{-3}$ plasma show the formation of asymmetric Thebe (outer) and Amalthea (inner) rings, as the grains pass through Jupiter's shadow (stippled region). The bottom left plot of Figure 4.21 shows the charging history for the same simulated grain.

non-axisymmetric ring that is offset away from the Sun.

The rate at which nanograins reach their equilibrium potential can be quite slow, as charging time is inversely proportional to grain size, Eq. 4.8. Therefore, during shadow transits, the grain may not have enough time to achieve charge equilibrium. The effect was studied by Horányi & Burns (1991), who noted that for micron-sized grains orbiting Jupiter in low plasma densities ($1\,\mathrm{cm}^{-3}$), grains did not achieve charge equilibrium, for the same reason of the transit time in shadow being longer than the characteristic charging time (top curve of upper subplot of Figure 4.21).

Like Figure 4.21, Figure 4.23 shows the consequences of this shadowing effect, by applying a continuous charging model including I_e, I_i and I_ν currents. As the grain enters the shadow for the first time ($t \approx 4\,\mathrm{h}$), the positive photoelectron current does not contribute to charging and so the grain surface potential becomes more negative (Figure 4.23a). The resulting larger charge-to-mass ratio leads to tighter gyrations (Figure 4.23b), then as the grain leaves the shadow ($t \approx 8\,\mathrm{h}$) and becomes more neutral, the gyrations become looser causing its radial distance to change as well as its velocity. Subsequently, the following transit time in shadow is shorter (around 2 hours at $t \approx 15 - 17\,\mathrm{h}$) so that the grain potential minimum at $t \approx 17\,\mathrm{h}$ is less negative than the first minimum ($t \approx 7\,\mathrm{h}$). The grain continues on its orbit slightly further away from the planet and enters the shadow briefly a third time before the $30\,\mathrm{h}$ integration time completes.

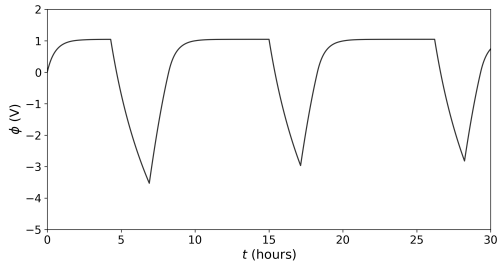

(a) Grain surface potential over time.

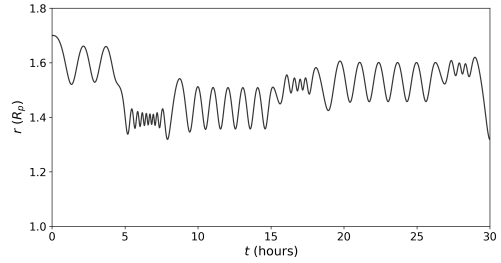

(b) Radial position over time.

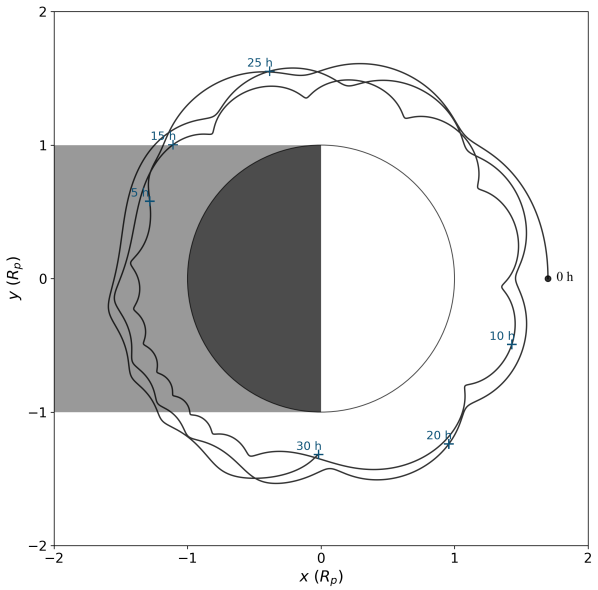

(c) Plan view of orbit, time indicated by 5 h markers .

Figure 4.23: Continuous charging model for a 10 nm grain orbiting Saturn at a distance of $1.7\,R_S$ in an $n = 1\,\mathrm{cm}^{-3}$, $T_e = T_i = 5\,\mathrm{eV}$ plasma. For simplicity, the planet's magnetic field is modelled as an aligned centred dipole, and the gravitational field only includes the spherical term. The photoelectron efficiency has been artificially boosted, setting $\kappa_\nu = 1$, to highlight the shadowing effect.

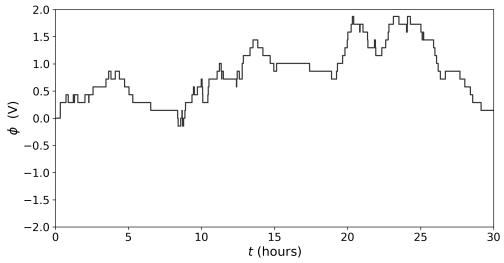

(a) Grain surface potential over time.

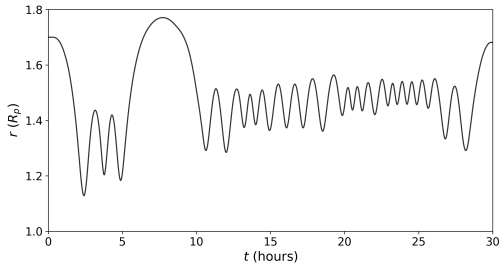

(b) Radial position over time.

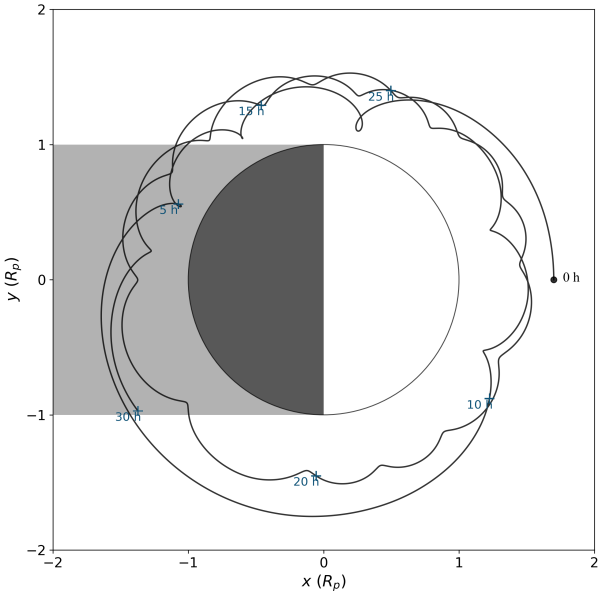

(c) Plan view of orbit, time indicated by 5 h markers.

Figure 4.24: As Figure 4.23, but using the discrete charging model described in §4.2.

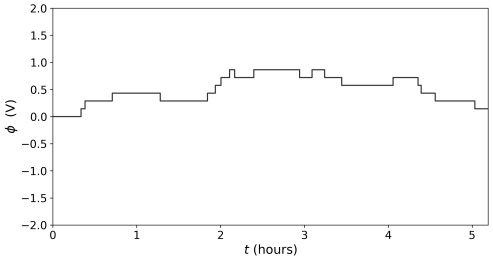

(a) Grain surface potential over time.

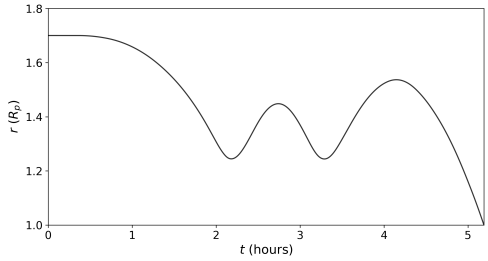

(b) Radial position over time.

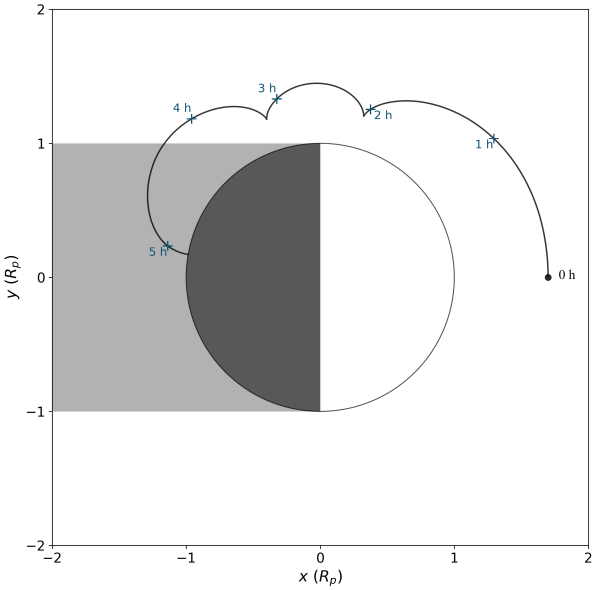

(c) Plan view of orbit, time indicated by 1 h markers.

Figure 4.25: As Figure 4.24, but using a different random seed.

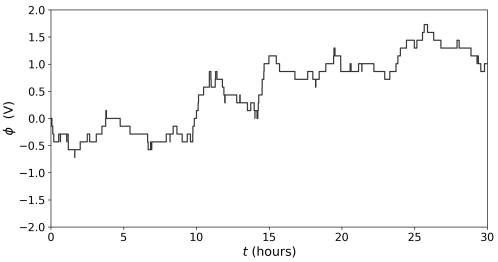

(a) Grain surface potential over time.

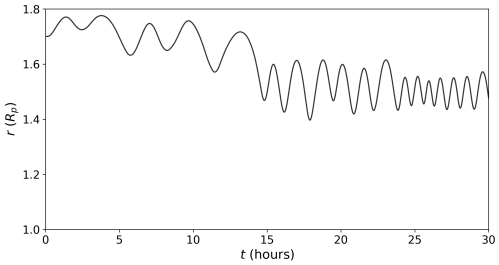

(b) Radial position over time.

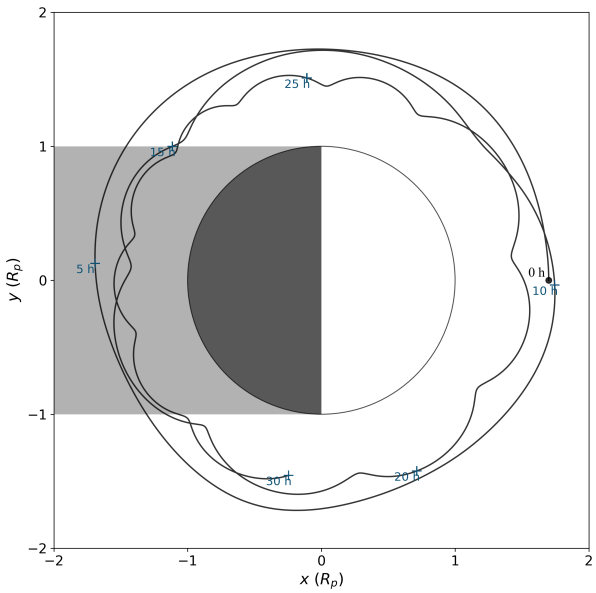

(c) Plan view of orbit, time indicated by 5 h markers.

Figure 4.26: As Figure 4.24, but using a different random seed.

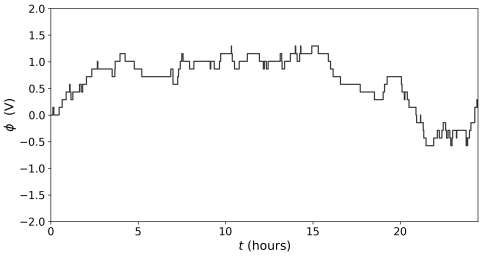

(a) Grain surface potential over time.

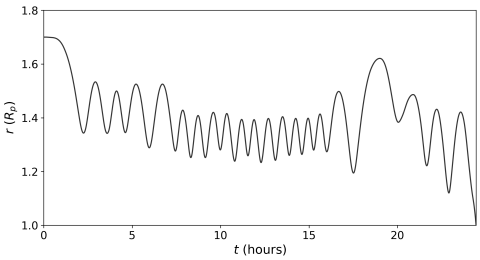

(b) Radial position over time.

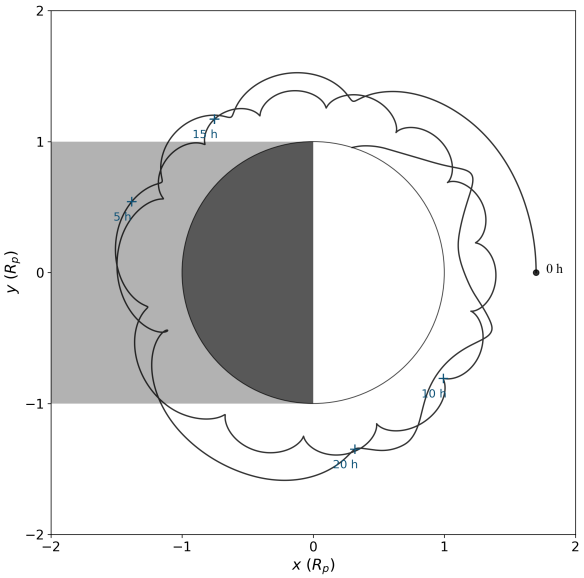

(c) Plan view of orbit, time shown by 5 h markers.

Figure 4.27: As Figure 4.24, but using a different random seed.

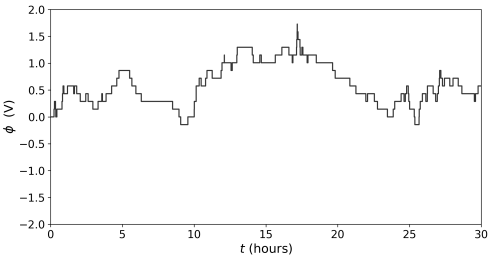

(a) Grain surface potential over time.

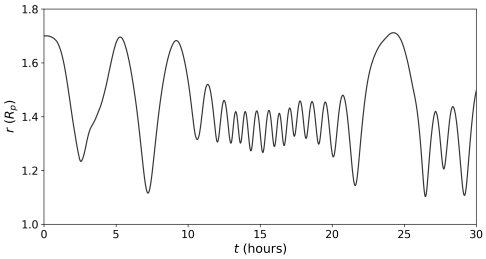

(b) Radial position over time.

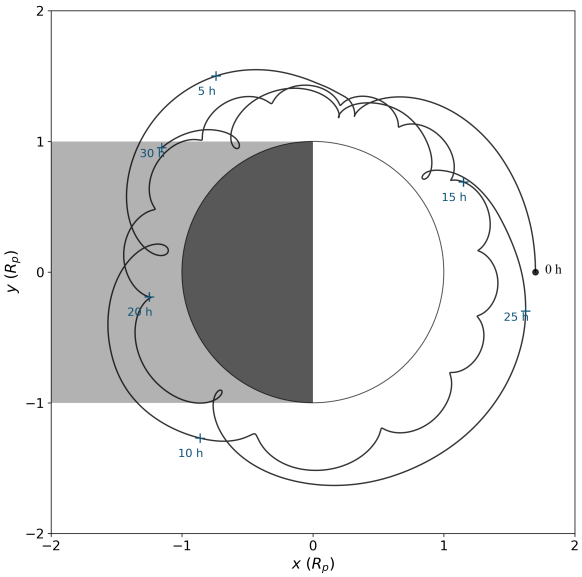

(c) Plan view of orbit, time shown by 5 h markers.

Figure 4.28: As Figure 4.24, but using a different random seed.

The importance of the stochastic variation in charge for orbital evolution is demonstrated in comparing the continuous charging model, Figure 4.23, to some discrete charging simulations: Figures 4.24 – 4.28 show very different orbital outcomes to the continuous charging results and also demonstrate how changing the random seed, that is, changing the number of charging events during the initial timestep for the grain, leads to orbital differences even when all other model parameters are kept the same. Figures 4.25 and 4.27 show how discharging from a positive potential, caused by entering the planetary shadow, can alter the gyroradius leading to an unstable orbit. Figures 4.24, 4.26 and 4.28 show orbits that remain stable over the $30\,\mathrm{hr}$ integration time, with different charging histories that result from stochastic kicks leading to different trajectories.

An interesting observation to make at this stage, before preceding to a more detailed re-visiting of ring rain in Chapter 5, that was introduced in §1.2.3, is that a grain can fall onto the planet's nightside (Figure 4.25) or dayside (Figure 4.27). The dominant loss mechanism for H_3^+ ions – dissociative recombination with electrons – is faster than a Saturn day and therefore an asymmetry in the longitudinal deposition of water-ice grains onto the ionosphere could add further insight into the explanation for the diurnal variation in peak electron density (Moore et al. 2018). O'Donoghue et al. (2016) report higher *auroral* H_3^+ density at local noon compared to midnight. Measurements of the mid-to-low latitude H_3^+ emission by the *Jupiter Infrared Auroral Mapper* on board *Juno* have proved inconclusive about day and night differences due to poor sampling (Migliorini et al. 2019).

The planetary shadow introduces an azimuthal asymmetry that needs to be considered in respect to both the final destination of grains and the initial launch location. The grain could be launched from any azimuthal angle, not only local noon (Figures 4.24 - 4.28). This could change the orbital outcome of grains, as any grains grains launched from within the planetary shadow would initially charge more negatively due to the absence of the photoelectron current. Such cases will be considered further in Chapter 5, where the orbital charge-varying dust model can be applied to studying the ring dust-planet connection, which was introduced in §1.2.3.

5

Dynamical Modelling of Ring Rain

Having described the most relevant physical processes for charged dust in the main rings of Saturn and motivated the need for their study through examples in Chapter 1; explained the numerical method for the study of test grains in Chapter 2; detailed the characteristic motions of charged dust in simplified planetary fields and verified previous literature results for constant charge-to-mass ratios in Chapter 3; and implemented a novel stochastic charging algorithm in Chapter 4, we return to the phenomenon of ring rain (§1.2.3) in this chapter. To turn our attention to the open questions still remaining and to see how the dynamical modelling developed in this work can contribute to our understanding of the ring dust - planet connection. Conclusions and further work are presented in Chapter 6.

5.1 Open Questions

The unanswered questions and unexplored avenues relating to ring rain are highlighted here and will serve to guide the focus of this chapter.

5.1.1 Silicate-to-Water-Ice Ratio and Latitudinal Water Deposition

There is more silicate material falling onto Saturn, compared to water-ice (§1.2.3). Hsu et al. (2018b) report an ice-to-silicate mass ratio as low as 2:1 , which is a much lower water fraction than that observed in the main rings: $\gtrsim 95\%$ (Zhang et al. 2017a,b). Such a large difference between the ring rain composition and the composition of bulk ring material could potentially be explained through a dynamical sorting mechanism, whereby only material from the least icy regions of the main rings (in the mid-C ring) finds its way onto the planet. However, Hsu et al. (2018b) state that their best-fitting simulations indicate only about half of the dust impacting the *CDA* originated from the C ring. Moreover, they find that the relative fraction of grains that arrived at *Cassini* from the B ring compared to those from the C ring remained almost constant. If it is assumed that grains rain onto planetary latitudes from radial positions in the rings that are magnetically conjugate (O'Donoghue et al. 2017), then the radial compositional variation in the main rings (in a broad sense, comparing the A, B, and C rings) should be reflected in the latitudinal variation in water-ice fraction (Figure 1.19). For example, dust from the C ring would rain onto Saturn in the region $L = 1.239 - 1.534$ (Figure 5.6) and so a lower water fraction in ring rain at those latitudes might be expected to reflect the higher non-icy composition of the mid-C ring. However, this does not appear to be the case as Hsu et al. (2018b) finds that the relative proportions of dust from each region of the rings remains fixed.

Since there does not appear to be a dynamical selection process in the main rings to explain the composition and latitudinal variations of ring rain, what are the alternatives? One suggestion relies on the time taken for water-ice to be removed from ring rain through photo-evaporation. This could explain the lower water-ice fraction at higher planetary latitudes as grains take a longer time to reach such latitudes and therefore would evaporate before reaching the planet, as the photo-evaporation lifetime of ice nanograins is only a few hours (Hsu 2020), and this is the case for some of the simulations presented in §5.4. Another point to consider is that the mechanism that produces the dust itself could preferentially generate silicate grains over water grains (Hsu et al. 2018b). Indeed, it seems plausible that the very same reason for latitudinal water-ice variation – its evaporation – could be involved: the hypervelocity impacts that generate dust, which Hsu et al. (2018b) assume is the primary source, could sublimate water-ice grains in the process, thereby removing them from ring rain.

Another speculative possibility to explain the higher silicate-to-water-ice ratio in ring rain, would

be that the initial velocity distribution of silicate-rich material originating from the plumes of Enceladus, Figure 1.24, material dredged up from the moon's ocean floor, is such that it dynamically sorts the grains onto unstable orbits falling onto the planet. This is a dynamical selection mechanism, but *outside* of the main rings, a process that Hsu et al. (2018b) argue is not occurring *within* the main rings. However, it is unlikely that many nanograins originating from Enceladus's orbit rain onto the planet, as the launch location is outside of R_{syn}, which leads to grains streaming outward (§1.2.2) on radially unstable orbits to escape the system (§3.5.2). However, Hsu et al. (2018b) report 10% of *CDA*-detected grains originate from the A and D rings, and Cassini Division so there is a proportion of grains, albeit small, that must be crossing synchronous orbit from outside.

5.1.2 Ring Structure and Electromagnetic Erosion

Another aspect of ring rain to consider, alongside the imprint it leaves upon the planetary atmosphere in the form of H_3^+ emission (§1.2.3), is the corresponding evacuation of dusty material from the rings and what that can reveal about their survival time. This electromagnetic erosion process has been used to describe the relationship between ring structure and H_3^+ emission (O'Donoghue et al. 2013, 2017), presented in Figure 1.18. The dust itself could originate from a number of sources, including meteoroid bombardment, and the subsequent ballistic transport of ejecta (Ip 1983; Durisen 1984; Lissauer 1984) is also associated with shaping the rings, including the inner edges of the A and B rings (e.g. Estrada et al. 2015); but for the purposes of this work the focus shall be on gravitoelectrodynamic processes.

As described in §1.2.3, an increase in H_3^+ emission is associated with more ice grains raining onto the planet, as a higher water influx reduces the electron density (through rapid recombination) and hence reduces the major loss channel of H_3^+. By assuming that the grains are highly charged and therefore travel from the rings along magnetic field lines onto the ionosphere, O'Donoghue et al. (2017) map the H_3^+ emission to its origins in the rings. They find a broad peak associated with the $1.525 - 1.625\,R_{\text{S}}$ instability region (near $43°\text{N}$) and the Cassini Division between the A and B rings. This outer edge of the B ring at $1.948\,R_{\text{S}}$ has been shown to be caused by resonance with Mimas (Goldreich & Tremaine 1978; Borderies et al. 1982), although that work did not include electromagnetic effects, which are of utmost importance for the dynamics of smaller grains and described below with regard to orbital stability (§3.6.2).

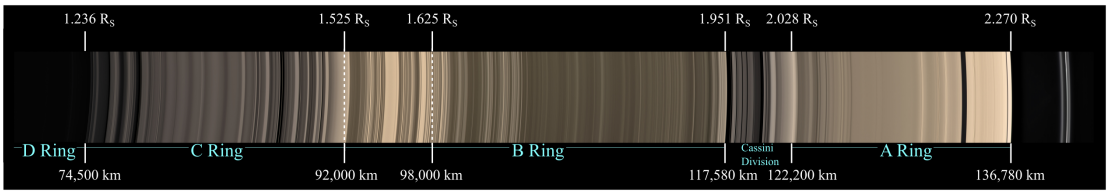

Figure 5.1: Natural colour mosaic of the unilluminated side of the main rings taken by *Cassini's NAC*, with key radial distances of the main rings labelled. The inner B ring's instability region ($1.525 - 1.625\,R_S$) is delineated by two dashed lines. Adapted version of Figure 1.6 (image credit: NASA/JPL/Space Science Institute (PIA08389)).

Figure 5.1 shows key features of the bulk structure of the rings. The dense B ring has two distinct sections, with the boundary between the more transparent inner region and more opaque outer region at $\sim 98,000\,\mathrm{km}$ ($\sim 1.625\,R_S$), this is clearly seen in the *UVIS* optical depth profile of Figure 1.8, where $\tau(r \approx 1.525 - 1.625\,R_S) \approx 1.5, \tau(r \approx 1.625 - 1.948\,R_S) \approx 4.5$. Inside of the B ring lies the C ring, where the opacity is much lower: $\tau(r < 1.525\,R_S) \approx 0.1$. Outside of the B ring, the opacity drops off dramatically in the Cassini Division ($r \approx 118,000 - 122,000\,\mathrm{km}$), beyond which lies the A ring: $\tau(r \approx 2.023 - 2.267\,R_S) \approx 1$.

The internal B ring boundary (at $r \sim 98,000\,\mathrm{km}$), where the opacity transitions from a more transparent inner ring section to a more opaque outer ring section was studied by Northrop & Hill (1982). This was discussed in §3.6.2, where the equation for the vertical stability boundary derived by Northrop & Hill (1982) was presented in Eq. 3.54 and shown to predict a value of $\sim 1.625\,R_S$, Eq. 3.55. Northrop & Hill (1982)'s analysis assumes the grains are highly charged so that the grain is constrained to slide along the magnetic field lines. They consider the gravitational and centrifugal forces acting on a grain displaced slightly away from the ring plane, Figure 1.17. The centrifugal force acts outward and therefore tries to slide the grain along its constraining field line to the furthest distance from the planet, shown in Figure 3.17 – the ring plane. Due to their respective radial dependences (gravity $\propto \frac{1}{r^2}$, centrifugal force $\propto r$), there is a distance at which inward-acting gravity overcomes the outward-acting centrifugal force, so that the grain runs up the field line onto the planet. Outside of the stability boundary, if perturbed normal to the ring plane, the grain oscillates back and forth and could be re-absorbed by the main ring particles (Northrop & Hill 1982).

This vertical instability can be seen in the stability map of Figure 3.21a for high L_* (grey dashed curve, $q_d < 0$). Due to Thomsen et al. (1982)'s suggestion that spokes (§1.2.1) are comprised

of negatively charged grains, Northrop & Hill (1982) restrict their focus to negatively charged grains only, although it should be noted that a similar boundary can also be seen for $q_d > 0$ (Figure 3.21a). The vertical stability boundaries are not a singular radial position but a curve that depends on the charge-to-mass ratio. In §3.6.2, the second solution to $\Omega_b^2 = 0$ derived by Jontof-Hutter & Hamilton (2012a) was presented, which describes a second curve much closer to the planet for grains with high $|L_*|$ and $q_d < 0$, that is also observed in Figure 3.21a.

The vertical instability boundary of Figure 3.21a actually lies closer to the planet than that predicted by Northrop & Hill (1982). This is because the numerical simulations use Keplerian initial conditions. The derivation of Northrop & Hill (1982) was for grains on *circular* orbits, that is, grains launched at the guiding centre orbital velocity (§3.4.1). Northrop & Hill (1983) relax this condition, and study grains launched at the Keplerian orbital velocity (grains that are launched from a large parent body in orbit around Saturn). For these cases, where the grain has a component of velocity around the guiding centre, there is gyromotion in addition to the guiding centre motion, and therefore an associated magnetic moment. This magnetic moment has a stabilising effect because the grain is reflected away from the planet towards the ring plane (§3.6.1), and so there is a radial range inside of the $1.625\,R_S$ stability boundary where the destabilising effect of gravity is countered, thereby bringing the marginal stability radius inward to $1.525\,R_S$ (Northrop & Hill 1983), which is observed in Figure 3.21a. The loss of material from the rings to the planet explains the lower observed opacity of the C ring ($r < 1.525\,R_S$).

Returning to ring features that are associated with observations of haze (Figure 1.16) and H_3^+ (Figure 1.18), which have been described in greater detail in §1.2.3, the question of how the stochastic charging of nanograins (§4.2) affects these ring stability boundaries can be studied, including the effects of planetary shadowing (§4.3), higher order gravitational and magnetic field terms (§1.3.1) and varied launch speeds (§5.4).

5.1.3 The Effect of Ring Rain on the Perceived Age of the Rings

The origin of Saturn's rings is still debated (e.g. Northrop & Connerney 1987; Connerney 2013; Crida et al. 2019). The rings could be primordial, material left over from the planetary nebula which has evolved but failed in its attempts at satellite building (Northrop & Connerney 1987), or they could be much younger, due to a more recent formation event such as the tidal stripping

of a satellite whose rocky core is lost to collision with Saturn (Canup 2010). Estimating mass loss through ring rain and other erosion processes is of paramount importance in establishing the age of the rings. The relatively low mass of Saturn's rings (introduced in §1.1.1), measured during the final orbits of *Cassini* to be equivalent to that of a 300 km wide icy satellite (Iess et al. 2019), holds implications for the age of the rings.

Firstly, given the pristine appearance of the main rings ($> 95\%$ water-ice, §1.1.1b)), and the observed flux of exogenous non-icy material in the form of meteoroids (Cuzzi & Estrada 1998), the rings are argued to be relatively young because there is insufficient ring material to dilute the pollutants that would be accrued over a longer time period and still maintain the observed rings' bright, youthful appearance. Secondly, given a ring mass loss mechanism, such as ring rain, where material is lost from the rings onto the planet, the rings are argued to have insufficient mass to remain in existence for longer than ~ 300 million years (O'Donoghue et al. 2018). Northrop & Connerney (1987) modelled the C ring as an initially dense ring like the B ring which is eroded, through the electromagnetic processes described above, to its present low opacity. Using calculations of the micrometeorite influx and electromagnetic erosion rates, they estimate a very young age for the rings: $4 - 67 \times 10^6$ yr. Based on more recent *CDA* observations of nanograins between the rings and planet, Hsu et al. (2018b) estimate the erosion time of the rings to be an order of magnitude longer: $\sim 1 - 4 \times 10^8$ yr, which is still an order of magnitude shorter than the age of the Solar System, and consistent with O'Donoghue et al. (2018)'s estimate for the age of the rings.

Crida et al. (2019) highlight the important distinction between the exposure age of the rings and the formation age of the rings. The latter is straightforwardly the amount of time elapsed since their formation until the present, whereas the exposure age of Saturn's rings is the time taken for the rings to pollute and darken via meteoroid bombardment to their present composition, assuming an initial pure water-ice progenitor. These ages need not be the same, as some mechanism can disconnect the two. Crida et al. (2019) suggest that ring rain is such a mechanism. The observed higher silicate-to-water-ice ratio in ring rain compared to that in the bulk ring material (§§1.2.3, 5.1.1) could be an indication that the rings are being 'cleaned'. Non-icy material could be preferentially removed by the ring rain mechanism so that the rings appear brighter and more youthful than they would otherwise, thereby concealing their older origin.

5.2 Literature Review of Ring Rain Dynamical Studies

Before proceeding to explore the ring dust - planet connection through simulations, there are three key papers to review (§§5.2.1 - 5.2.3) in addition to the work of Hsu et al. (2018b) described in §1.2.3, which use a similar dynamical approach to undertake their parametric studies of ring rain. These are described in detail in the following sections, in order to clarify gaps in the literature and identify unexplored avenues to venture down.

5.2.1 Constant $\frac{q_d}{m_d}$ and Keplerian Launch Velocities: Liu & Ip (2014)

This paper models positively and negatively charged nanograins with constant charge-to-mass ratios, through integrating a simple equation of motion including the planetary gravitational and rotating magnetic fields only. They note that the electrostatic potential of dust grains would be variable due to plasma charging and photoemission, but keep q_d/m_d constant due to the then poorly constrained plasma density and temperature distribution near the rings.

There is a slight error in Liu & Ip (2014), which propagates throughout, where they use the equation $\phi_d = \frac{4\pi q_d}{\epsilon_0 a_d}$ instead of Eq. 4.4. This means they erroneously write $\frac{q_d}{m_d} = 1.683 \times 10^{-4} \left(\frac{1\mu\text{m}}{a_d}\right)^2 \left(\frac{\phi_d}{\text{V}}\right)$ instead of $\frac{q_d}{m_d} = 2.7 \times 10^{-2} \left(\frac{1\mu\text{m}}{a_d}\right)^2 \left(\frac{\phi_d}{\text{V}}\right)$, refer to Eq. 1.5. Nevertheless, qualitatively their results are unchanged. They initially present results for only three representative charge-to-mass ratios, to show that negatively charged grains with sufficiently high q_d/m_d, launched at Keplerian velocity inside the Northrop & Hill (1983) stability boundary of $1.525\,R_S$ (§5.1.2), accelerate along magnetic field lines onto the planet – a result previously demonstrated by Jontof-Hutter & Hamilton (2012a) across a wider range of L_* (§3.6.2). Liu & Ip (2014) demonstrate that positively charged grains exhibit similar behaviour as their negative counterparts, apart from certain charge-to-mass ratios being radially unstable (colliding with the planet at low latitude), a result that was also previously shown by Jontof-Hutter & Hamilton (2012a), refer to the black region in Figure 3.21a (lower panel).

Liu & Ip (2014) then explore a wider class of orbits, launching positive and negative grains from radial positions spanning the inner edge of the C ring to the outer edge of the A ring. Their results align with the stability map results of Jontof-Hutter & Hamilton (2012a); namely, they find four classes of orbit: stable, radially unstable (collision with planet if launched within

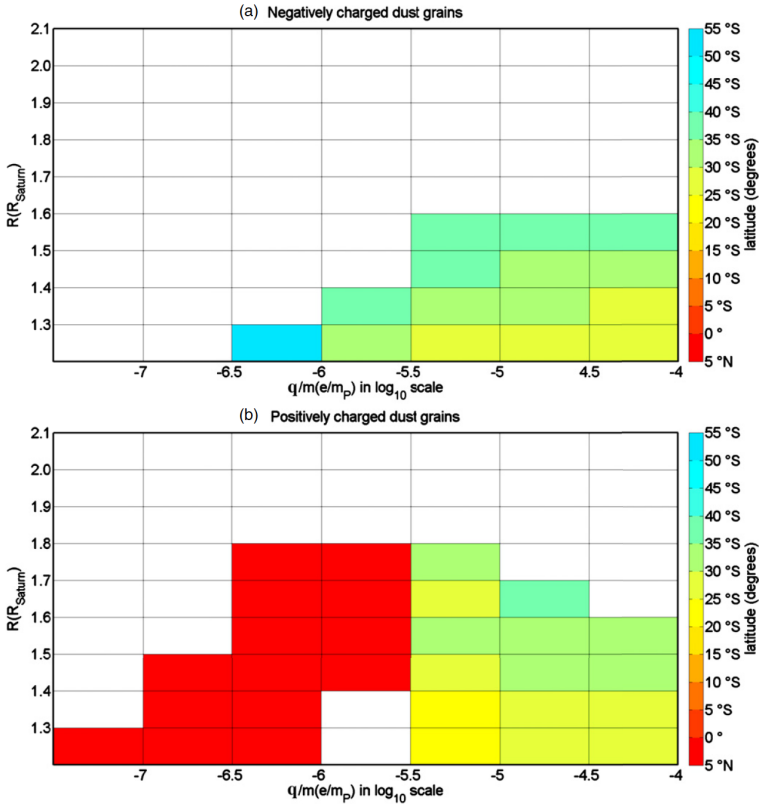

Figure 5.2: Comparing the latitudinal deposition angle (by colour) for grains across a range of charge-to-mass ratios and launch locations, for (a) negatively charged grains and (b) positively charged grains. Grains that do not collide with the planet are indicated by white. One caveat to note is their charge-to-mass ratios have a slight numerical error, explained in the main text. Image credit: Liu & Ip (2014, Fig. 5).

R_{syn} or escape the system if launched outside R_{syn}), and vertically unstable (colliding with the planet outside the equatorial region). Running 126 simulations, they plot the latitudinal impact position of grains against their launch positions (9 representative values) and charge-to-mass ratios (7 representative values), Figure 5.2.

Figure 5.2 is similar to the stability maps of Chapter 3 (Figures 3.5, 3.21), plotting launch position against charge-to-mass ratio, but with a less refined grid (126 simulations compared to $16,000$) and indicating the planetary collision latitude by colour instead of the orbital outcome classes (stable, radially unstable, vertically unstable). Liu & Ip (2014) find that positively charged grains dominate the equatorial zone influx below a certain charge-to-mass ratio, provided the launch position is inside R_{syn}, whereas outside R_{syn} there are grains within a certain

range of charge-to-mass ratios that move outward and escape the system, corresponding to the black regions of Figure 3.21. They find that *negatively* charged grains always contribute to mid-latitude influx, as shown by the (grey) vertically unstable region of the upper subplot ($q_d < 0$) of Figure 3.21a – there are no (black) radially unstable orbits in those results. Liu & Ip (2014) reason that grains with high enough charge-to-mass ratios launched inside $1.525\,R_S$ can explain the sharp discontinuity in mass distribution between the B and C rings. However, their model cannot explain the observed H_3^+ emission in the northern hemisphere, as their simulations result in only southern grain deposition. The low-velocity Keplerian initial conditions used in their parameter study, which is sufficient to explain dust generated by mutual collision of ring particles is developed further by Ip et al. (2016).

5.2.2 Constant $\frac{q_d}{m_d}$ and Vertical Launch Velocities: Ip et al. (2016)

Following on from the low initial velocity fixed-charge dust simulations of Liu & Ip (2014), Ip et al. (2016) model the trajectories of high-velocity ejecta produced by meteoroid bombardment. Ip et al. (2016) estimate the ejecta velocity to be $\sim 1.5 - 2.5\,\mathrm{km\,s^{-1}}$, based on a range of micrometeoroid impact velocities of $25 - 40\mathrm{km\,s^{-1}}$. They argue that velocities in the direction perpendicular to the ring plane, being least affected by collisional scattering or re-absorption with main ring material, leads to the grains having an initial vertical velocity component, Δv_z. Ip et al. (2016) use the same equation of motion for constant-charge grains as Liu & Ip (2014), with an northward-offset magnetic dipole. It should be noted that the same minor error in their numerical values of q_d/m_d (§5.2.1) is also present in Ip et al. (2016).

Ip et al. (2016) find that positively charged grains fall onto the planet at mid-latitudes in the same direction as their initial velocity boost (northern hemisphere for $v_z > 0$, southern hemisphere for $v_z < 0$) , provided they are launched within synchronous orbit and have a high enough charge-to-mass ratio, Figure 5.3. Negatively charged grains, however, only fall onto the southern hemisphere within the instability radius of $1.525\,R_S$ (Northrop & Hill 1983), otherwise oscillating about the ring plane. They argue that due to the low opacity of the C ring (spanning $1.237 - 1.525\,R_S$, Figure 5.1), the rate of influx of negatively charged grains is much lower than that of positively charged grains, which fall onto the planet from orbital distances spanning the much denser B ring ($1.525 - 1.86\,R_S$) as well as the C ring.

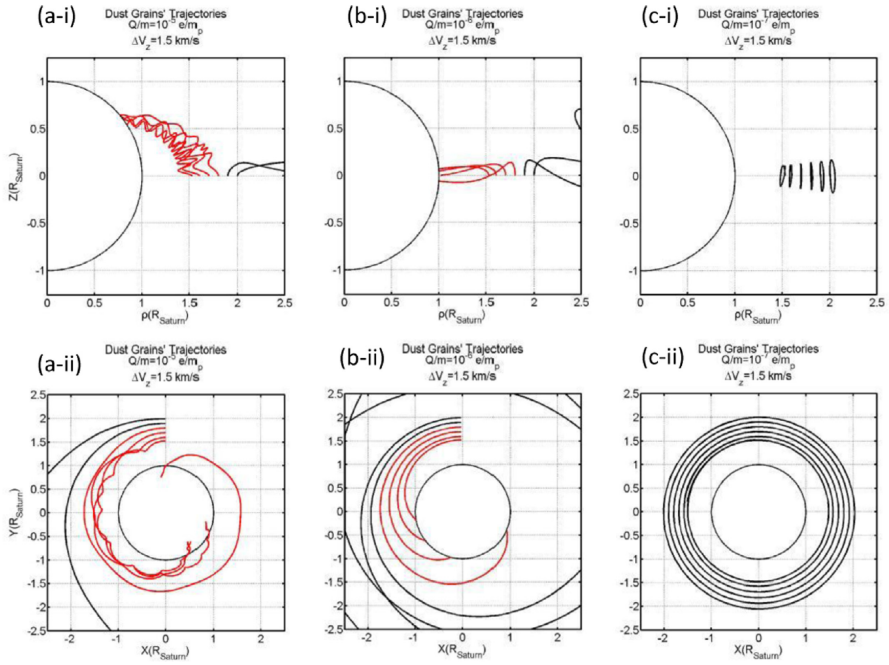

Figure 5.3: Trajectories of positively charged nanograins ejected with vertical upward velocity $\Delta v_z = +1.5\mathrm{kms}^{-1}$. The subplots labelled (i) are $\rho - z$ projections for three different charge-to-mass ratios shown left to right (with the caveat of their slight Q/m numerical error, explained in the main text). The subplots labelled (ii) are $x - y$ projections in the stationary frame of Saturn for the three different charge-to-mass ratios. Image credit: Ip et al. (2016, Fig. 2).

The observations of H_3^+ in the northern as well as southern hemispheres (O'Donoghue et al. 2013) could be explained by positive grains, interpreting the results of Ip et al. (2016), while the higher influx into the southern hemisphere of Saturn is due to its northward offset magnetic dipole (§1.3.1) – an azimuthal velocity crossed with a radial magnetic field term results in a vertical impulse, by the Lorentz force's right hand rule.

5.2.3 Variable $\frac{q_d}{m_d}$ and Ejecta Launch Velocities: Hsu et al. (2018a)

Hsu et al. (2018a) investigate the effect of varying charge on the trajectories of nanograins and their latitudinal deposition distribution, in contrast to the constant charge-to-mass ratios modelled by Liu & Ip (2014); Ip et al. (2016). Hsu et al. (2018a) note the importance of the grain charging history and the significant effect of even a single electronic charge on the subsequent grain trajectory (§4.2). Alongside the equation of motion used by Liu & Ip (2014);

Ip et al. (2016), including the J_2 gravity term and northward-offset aligned magnetic dipole model, Hsu et al. (2018a) simultaneously integrate the grain charging equation, Eq. 4.3, using a stochastic algorithm (Hsu et al. 2011) for the plasma and photoemission currents, assuming a constant plasma density and temperature. They choose a single launch position located inside of the inner edge of Northrop & Hill (1983)'s instability region, $r_L = 1.48\,R_S$, and launch 500 test grains, for a given plasma density ($n = \{0.1, 0.3, 0.7, 1.0\}\,\mathrm{cm}^{-3}$) and temperature ($T_e = 5\,\mathrm{eV}$), with a modest velocity boost in addition to the Keplerian velocity, chosen at random to uniformly cover all angles with a magnitude of $81\,\mathrm{ms}^{-1}$, slightly slower than the initial velocities chosen by Ip et al. (2016). The grain is assumed to be initially uncharged.

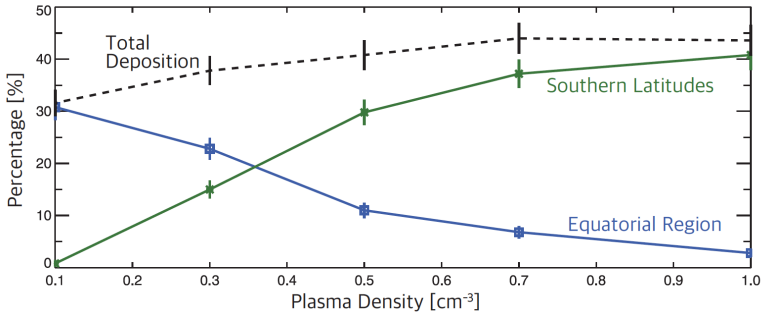

Figure 5.4: Comparing the number fraction of $10\,\mathrm{nm}$ grains falling into Saturn's equatorial region (blue) and southern latitudes (green) as a function of plasma density. The total deposition is shown by the black dashed line. Image credit: Hsu et al. (2018a), Fig. 2.

Hsu et al. (2018a) find grains that acquire fewer charges are deposited in equatorial regions, whilst grains acquiring more fall onto the planet's southern hemisphere and take longer to do so. Because the grain charging is modulated by the plasma density, they find that most of the grains fall onto the equatorial region when the plasma density is low, and by increasing the plasma density, Figure 5.4, more grains spiral along field lines to flow onto the planet at southern latitudes instead. They acknowledge the simplifying assumptions they have made, noting that the initial grain charge distribution, grain size distribution, plasma distribution alongside other factors will all play a role in the charging history, and will also determine the deposition of nanograins from the rings onto the planet.

5.2.4 Variable $\frac{q_d}{m_d}$, Ejecta Launch Velocities and Plasma Model: Hsu et al. (2018b)

The work of Hsu et al. (2018b), introduced in §1.2.3, characterised the influx of dust from the rings onto Saturn using measurements from the *CDA* and numerical simulations of test grains. Some of their key findings, the latitudinal variation in the deposition of water-ice and the silicate-to-water ratio of ring rain, were recapitulated in §5.1.1. The focus of this section is to describe their dynamical modelling approach and compare it to the previous literature (§§5.2.1-5.2.3).

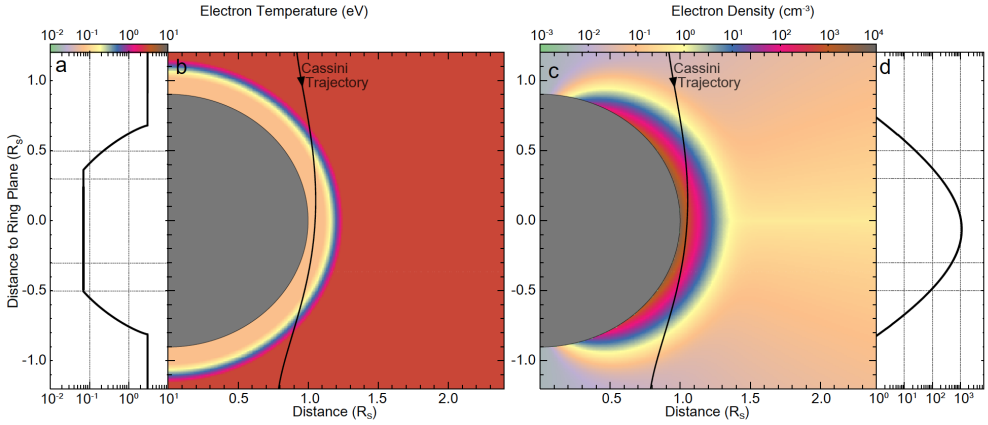

Figure 5.5: Plasma electron model used by Hsu et al. (2018b). Subplots b) and d) show the electron temperature and density as a function of radial distance, respectively. Subplots a) and c) show the electron temperature and density profiles along the labelled *Cassini* trajectory. Image credit: Hsu et al. (2018b), Fig. S1.

Hsu et al. (2018b) use a similar approach to Hsu et al. (2018a), that is, they simultaneously integrate the equations of motion and the charging equation to determine a test grain's position, velocity and charge, rather than keeping the grain charge constant as in the work of Liu & Ip (2014); Ip et al. (2016). The grain's charge is stochastically updated using the inhomogeneous Poisson process approach of Hsu et al. (2011), including the plasma and photoelectron emission currents. The orbital outcomes they consider include collision with Saturn or the ring plane, or escape from the system ($r > 2.5\,R_S$). In their equation of motion they include planetary gravitational (spherical and oblate terms) and (aligned offset dipole) magnetic fields, including the corotational electric field, and the drag force from Saturn's atmosphere. Rather than adopting the constant temperature and densities of Hsu et al. (2018a), Hsu et al. (2018b) implement a two-component plasma model for the planetary ionosphere and ring ionosphere, Figure 5.5. They

set the ring ionosphere to have a constant temperature of $3\,\mathrm{eV}$ and a plasma density decreasing with a scale height of $10°$ latitude from $0.3\,\mathrm{cm}^{-3}$ at the ring plane. They model Saturn's cold and dense ionosphere following Wahlund et al. (2018), and switch off both plasma and photoemission charging currents in the shadow of the dense A and B rings.

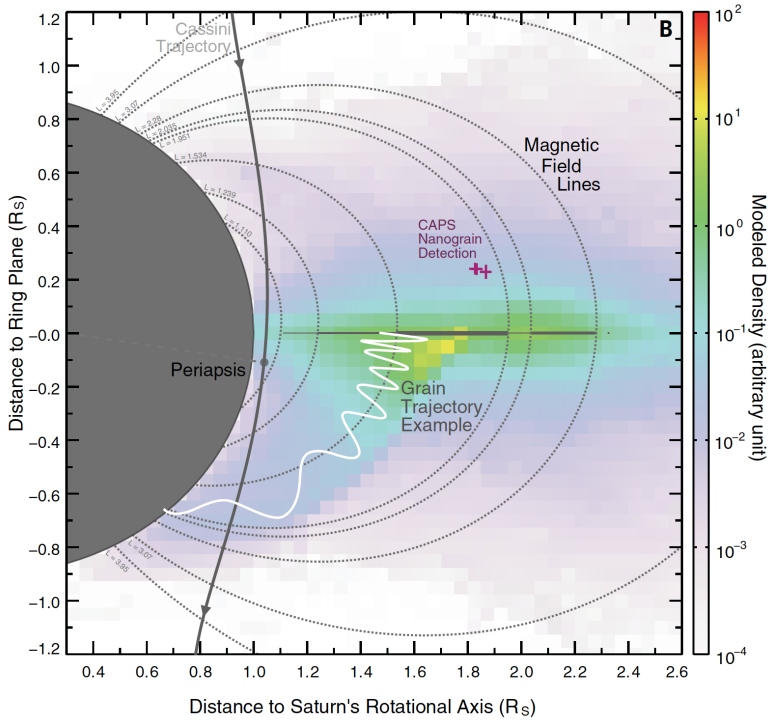

Figure 5.6: Hsu et al. (2018b)'s modelled grain number density in (r, z) space shown by colour, with a grid size of $0.05\,R_S$. Dotted curves indicate magnetic field lines connecting the rings to the planet, with the higher-latitude curves labelled L = 3.07, 3.95 indicating the orbits of Mimas and Enceladus respectively. The grey curve illustrates an example *Cassini Grand Finale* trajectory. An example grain trajectory is shown by the white curve. Image credit: Hsu et al. (2018b), Fig. 1B.

Hsu et al. (2018b) construct a library of test grain trajectories (e.g. Horányi & Cravens 1996; Juhász & Horányi 2002). This method involves dividing the (r, z) space in the vicinity of the planet and main rings into a grid and running a set of simulations that cover a range of initial conditions (launch location, velocity, charge and grain radius), numerically following each grain as the integration proceeds, and recording the number of hits that each $(\Delta r, \Delta z)$ grid cell receives. The grain number density of a particular $(\Delta r, \Delta z)$ grid cell is obtained by taking the sum of the total time spent by all grains in that cell, where a given grain's contribution is weighted according to its initial conditions. For example, a grain with a high initial charge that spends

an equal amount of time as a grain with a lower initial charge in a particular grid cell (with all other grain parameters equal), contributes less to the simulated grain density as the probability of generating a highly charged grain is lower (refer to Eq. 2 of Hsu et al. (2018b)'s supplementary material for details). Figure 5.6 shows their simulated dust number density, with a higher proportion of grains falling towards the southern hemisphere due to the northward dipole offset, as also found in the work of Hsu et al. (2018a).

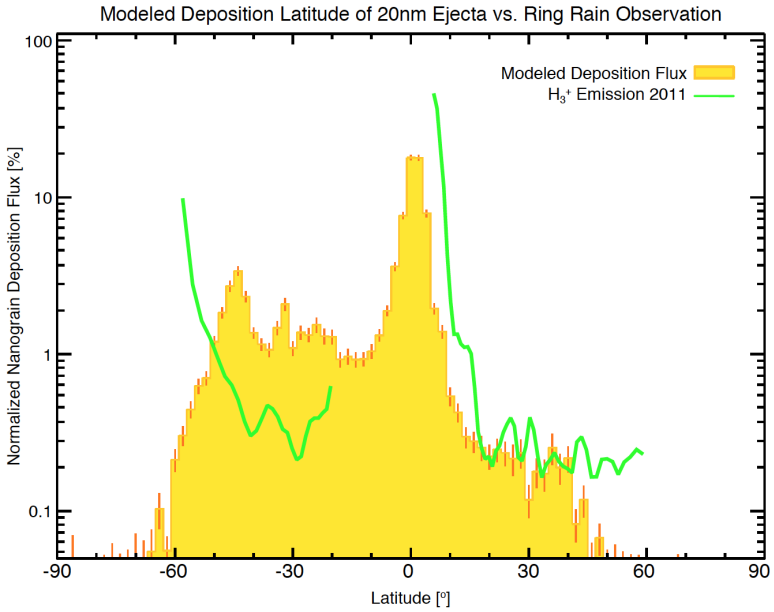

Figure 5.7: Latitudinal deposition of 20 nm modelled dust ejecta (yellow histogram) compared to H_3^+ observations (green curve O'Donoghue et al. (2013)). Image credit: Hsu et al. (2018b), Fig. S6.

Hsu et al. (2018b) relate their simulation results directly to ring rain, Figure 5.7. As their dust density results (Figure 5.6) indicate, more dust is deposited at southern latitudes ($\sim 30\%$ below $-15°$), compared to northern latitudes (only $\sim 3\%$ above $+15°$), with the majority of dust falling onto the equatorial region. Based on their best-fitting results for the dust measured by *Cassini's CDA* (§1.2.3), they choose to model 20 nm grains. Hsu et al. (2018b)'s simulations indicate that the ratio between grains from the B ring and those from the C ring is almost constant, with $\sim$ 40% originating from the B ring, $\sim$ 50% from the C ring, and $\sim$ 10% from the Cassini Division, A and D rings (§§1.2.3, 5.1.1), although they do not map their results directly to the main rings' structure.

Although Hsu et al. (2018b)'s choice of 20 nm grain size is based on their best-fit across a

grain size range of $5 - 40\,\mathrm{nm}$ for the *MA* impact rate measurements during Kepler ram orbits, it is likely that the nanodust covers a range of grain sizes across the nanoscale, including sizes smaller than the *CDA*'s calibrated range (Cassini Final Mission Report NASA/JPL 2019). Hsu et al. (2018b) assume the dust population originates from impact ejecta production, and the size distribution in the nanoscale is largely unknown (Hsu 2020). Therefore, a range of nanograin sizes is proposed in §6.2. Moreover, as both the charging timescale and charging currents, Eqs. 4.8, 4.1, 4.2, and 4.19, depend on the grain size and the plasma density, it is clear that a wide range of simulation parameters should be considered.

5.3 Ring Rain Simulation Method

Although progress has been made, the questions raised in §5.1.1-5.1.3 remain open, and the need for further dynamical studies of ring rain remains. Grains with constant charge-to-mass ratios released by low-velocity mutual collisions between ring particles (Liu & Ip 2014) and higher impact velocities (Ip et al. 2016) have been studied (§§5.2.1, 5.2.2). However, when studying the dynamics of nanograins in orbit around Saturn, a key parameter is the varying grain charge (§§5.2.3, 5.2.4), specifically its charging history based on the currents it encounters and any periodic modulating influences, such as the planetary shadow. Hsu et al. (2018a) note that variations in plasma density and temperature (e.g. Figure 5.4) will affect the dust charging times, Eq. 4.8, and alter the grain distribution raining from the rings onto the planet, with Hsu et al. (2018b) employing a more complex plasma model.

Modelling the plasma environment accurately then, is of key importance to the accuracy of the results. The *Cassini* mission provided a wealth of information regarding the plasma environment surrounding the rings, §1.1.2. Oxygen is the principal component of the main ring ionosphere based on *CAPS* measurements (Tokar et al. 2005; Young et al. 2005) and *INMS* measurements (Waite et al. 2005). The density and temperature of the plasma in the vicinity of the main rings is variable, Figure 1.11, according to the interactions of the O_2 ring atmosphere (produced by UV photon decomposition of ring ice) with the ring particles, and the ionisation rate which depends on the opening angle of the rings to sunlight and the local time (Johnson et al. 2006). The ring tilt angle will also influence the photoelectron current.

Wahlund et al. (2018) made in situ measurements, using *Cassini's RPWS* instrument, of Saturn's

cold, dense ionosphere, which was approximated in Hsu et al. (2018b)'s model, Figure 5.5. The rings cast a shadow on the planet, leading to reduced ionospheric plasma, so that Hsu et al. (2018b) switch off all currents, photoelectron *and* plasma, when test grains pass through shadowed regions. Wahlund et al. (2018) observe high levels of variability and fine structure in the ionosphere, and suggest ring rain as the cause, as variable amounts of infalling water could produce the observed sporadic electron depletions, although they note the difficulty of explaining the two orders of magnitudes difference between flybys by H_3^+ recombination alone.

The plasma environment is highly dynamic, with multiple sources and sinks (Johnson et al. 2006), and to fully consider the resulting complex temporal and spatial variability of the plasma environment in the vicinity of the main rings (§1.1.2), that changes with local time and season (Johnson et al. 2006; Wahlund et al. 2018) is beyond the scope of this work. Moreover, such complexity could cause results to be highly model dependent, which cautions that a complete plasma model should not be pursued at this stage but instead a sensitivity analysis using a parameter study approach (e.g. Hsu et al. 2018a) would be more appropriate.

As described in Chapters 2 and 4, the equation of motion of test grains under the influence of Saturn's gravitational, magnetic and corotational electric fields, including the J_2 and g_1^0, g_2^0, g_3^0 terms, alongside the current equation, including plasma and photoelectron currents (modulated by planetary shadow), were simultaneously updated according to a prescribed accuracy tolerance. The integrations were followed until the grain collided with the planet, escaped the main ring system ($r > 2.5\,R_S$), or collided with a main ring particle as it crossed the ring plane. The probability of a dust grain colliding with the ring plane, $\mathcal{A}$, can be parametrised following Cuzzi & Estrada (1998):

$$\mathcal{A} = \left[1 - \exp\left(-\frac{\tau}{\tau_s}\right)^p\right]^{\frac{1}{p}}, \tag{5.1}$$

with fitting parameters $\tau_s = 0.515$ and $p = 1.0335$, so that the higher the optical depth, τ, the less likely the grain will pass through.

5.4 Ring Rain Simulation Results

Grain launch locations were chosen inside, outside, and within the instability region, $1.525 - 1.626\,R_S$ (§5.1.2). Figures 5.8 - 5.12 illustrate orbital outcomes for grains launched from the outer B ring ($r_L = 1.7\,R_S$) with a vertically-directed velocity boost (as expected for impact ejecta, §5.2.2). Figures 5.8 and 5.9 show grains that experience low latitude oscillations before eventually crashing into the optically thick B ring, launched from outside and inside the planetary shadow respectively. The grains climb up magnetic field lines as they charge up but as they have a high probability of colliding with the optically thick outer B ring, Eq. 5.1, they do not survive crossing the ring plane. Physically, a grain composed of water-ice would not survive the $> 250\,\mathrm{h}$ integration time so a temporal cut-off at $\sim 10\,\mathrm{h}$ (Hsu 2020) should be used.

The simulation of Figure 5.10 has the same input parameters as Figure 5.9, but with the grain launched with a smaller vertical velocity boost. This grain eventually falls onto the nightside of Saturn at mid-latitude, but again, due to the long integration time, it would have photo-evaporated before impact. Figure 5.11 simulates the grain's trajectory using the same input parameters as Figure 5.10, but launched with an upward vertical velocity boost. The resulting orbit is very different, taking a fraction of the time to reach the planet and impacting in the equatorial region; a single plasma ion collected by the grain serves to destabilise it. Figure 5.12 launches the grain with the same input parameters as used in Figure 5.11 but from local noon, rather than midnight, and the grain also collides with Saturn but at mid-latitude. These preliminary results indicate that the dynamical lifetimes for dust falling into non-equatorial latitudes are significantly longer (Hsu et al. 2018b; Hsu 2020), which has consequences for the water-ice:silicate ratio, as described in §5.1.1. They also serve to highlight the chaotic nature of the nanograins' trajectories, being highly sensitive to initial conditions.

Figures 5.13 - 5.16 illustrate orbital outcomes for grains launched from the inner B ring ($r_L = 1.55\,R_S$). As for the simulations further out, grains within the instability region ($1.525 - 1.625\,R_S$) take longer to collide with the planet at higher latitudes: Figure 5.14 shows a grain falling into the equatorial region within 3 hours, while Figures 5.15 and 5.16 show mid-latitude deposition taking about an order of magnitude longer.

Figures 5.17 - 5.21 show grain trajectories for the C ring ($r_L = 1.4\,R_S$). The time taken for grains to fall onto the planet is shorter, as to be expected for shorter travel distances. Again,

equatorial influx is quicker than for mid-latitudes, although Figure 5.19 shows that grains can fall onto southern latitudes within fewer than ten hours. Collision with the ring plane (Figure 5.17) versus collision with the planet (Figure 5.18) can come down to a single charging event – all other simulation parameters were identical in the simulations shown by Figures 5.17 and 5.18 apart from the random seed used by the stochastic charging algorithm. Figure 5.21 shows a high velocity initial condition ($\Delta v_z = +5\,\mathrm{kms}^{-1}$), which results in the grain falling onto the planet at northern mid-latitude within 8 hours.

The results of this section are summarised in Table 5.1. A discussion of these, including further work to be done, is presented in Chapter 6.

Figure	$r_L(R_S)$	$\Delta v_z\,(\mathrm{ms}^{-1})$	Launch Azimuth (local time)	Collisional Outcome	Time to Impact (hours)	Latitude of Planetary Impact
5.8	1.7	-200	Noon	Main rings	255	–
5.9	1.7	-200	Midnight	Main rings	320	–
5.10	1.7	-100	Midnight	Planet	700	42°S
5.11	1.7	$+100$	Midnight	Planet	4.5	1°N
5.12	1.7	$+100$	Noon	Planet	17	38°S
5.13	1.55	-100	Midnight	Main rings	2.5	–
5.14	1.55	$+100$	Noon	Planet	3	1.5°N
5.15	1.55	-100	Noon	Planet	51	42°S
5.16	1.55	-100	Midnight	Planet	26	40°S
5.17	1.4	$+100$	Noon	Main rings	1.3	–
5.18	1.4	$+100$	Noon	Planet	1.6	1.5°N
5.19	1.4	-100	Midnight	Planet	9	40°S
5.20	1.4	$+200$	Midnight	Planet	27	33°S
5.21	1.4	$+5000$	Noon	Planet	8	49°N

Table 5.1: Summary of simulations for initially uncharged $10\,\mathrm{nm}$ grains around Saturn, with plasma parameters: $T_e = T_i = 1\,\mathrm{eV}, T_\nu = 2.5\,\mathrm{eV}, n_\alpha = 1\,\mathrm{cm}^{-3}$; launched from the outer B ring ($1.7R_S$), the instability region ($1.55R_S$), and the C ring ($1.4R_S$).

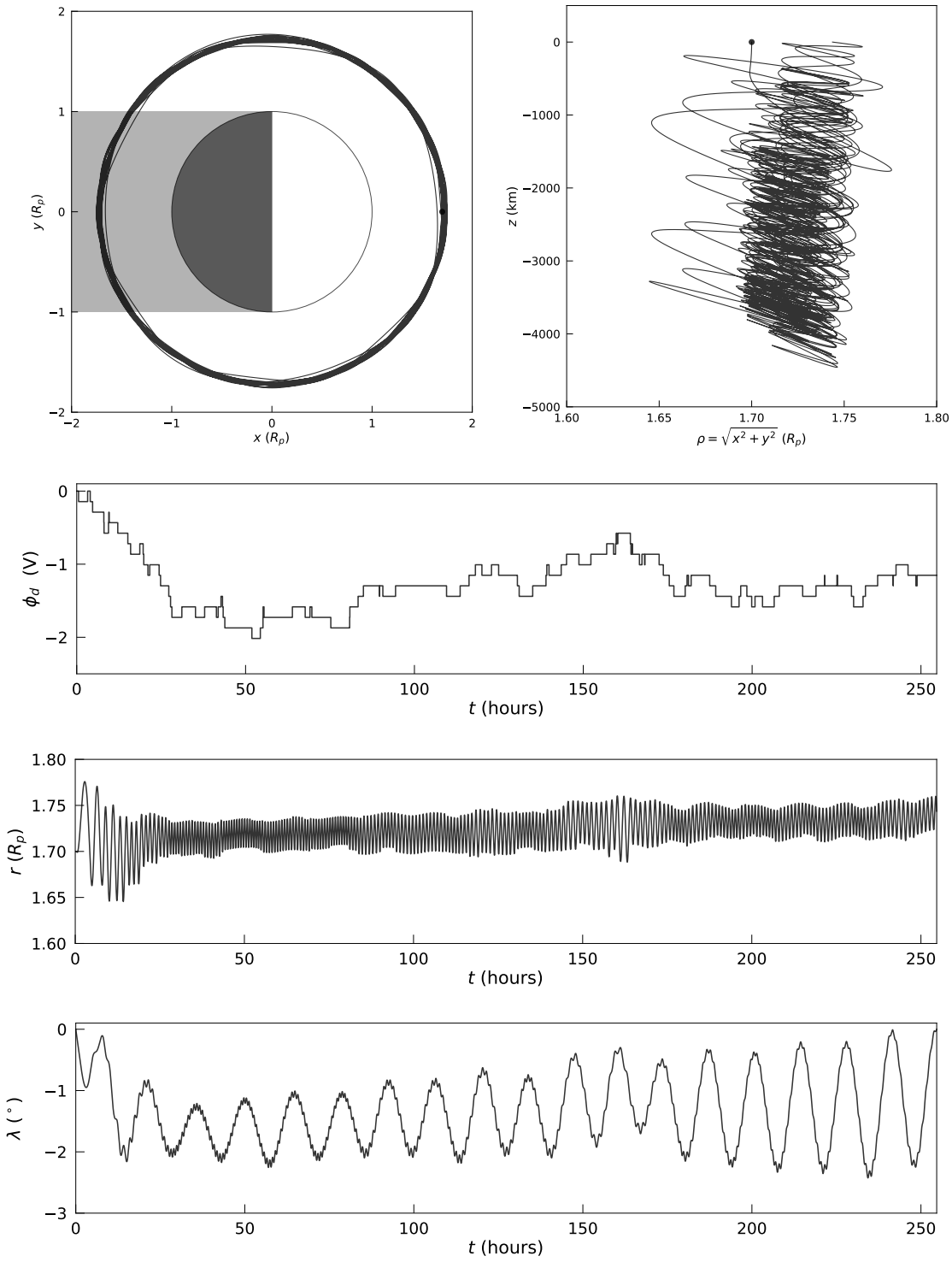

Figure 5.8: Following an initially uncharged $10\,\mathrm{nm}$ grain's trajectory around Saturn until it crashes into the ring plane, with initial conditions: $r_L = 1.7\,R_\mathrm{S}$, $\Delta v_z = -200\,\mathrm{m\,s^{-1}}$, and O^+ plasma parameters: $T_e = T_i = 1\,\mathrm{eV}$, $T_\nu = 2.5\,\mathrm{eV}$, $n_\alpha = 1\,\mathrm{cm^{-3}}$. The top row shows the grain's spatial trajectory, with a black circle indicating its initial launch at local noon; the bottom three rows show the grain surface potential, radial range and latitudinal temporal evolution.

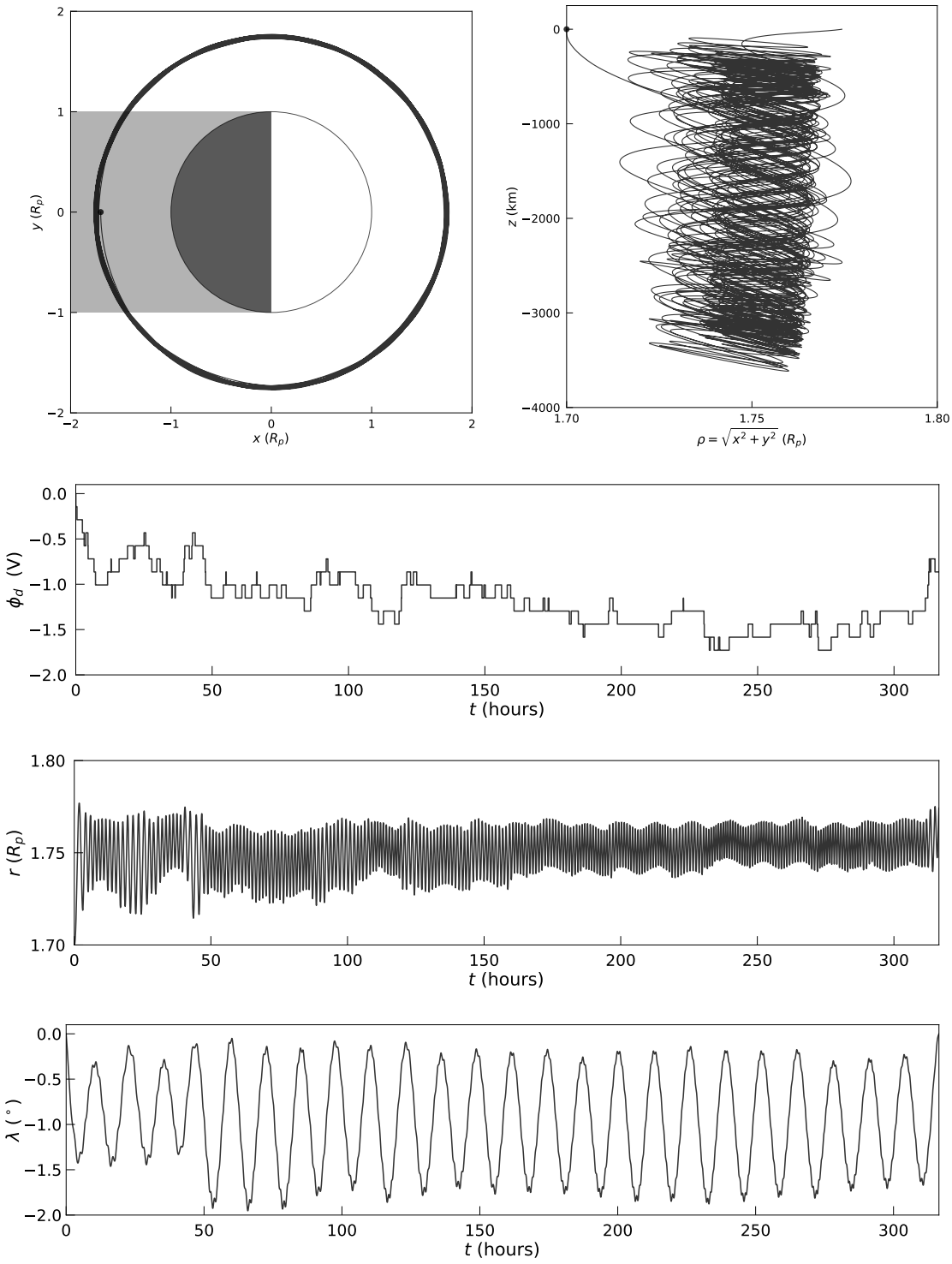

Figure 5.9: Following an initially uncharged $10\,\mathrm{nm}$ grain's trajectory around Saturn until it crashes into the ring plane, with initial conditions: $r_L = 1.7\,R_\mathrm{S}$, $\Delta v_z = -200\,\mathrm{m\,s^{-1}}$, and O^+ plasma parameters: $T_e = T_i = 1\,\mathrm{eV}$, $T_\nu = 2.5\,\mathrm{eV}$, $n_\alpha = 1\,\mathrm{cm^{-3}}$. The top row shows the grain's spatial trajectory, with a black circle indicating its initial launch at local midnight; the bottom three rows show the grain surface potential, radial range and latitudinal temporal evolution.

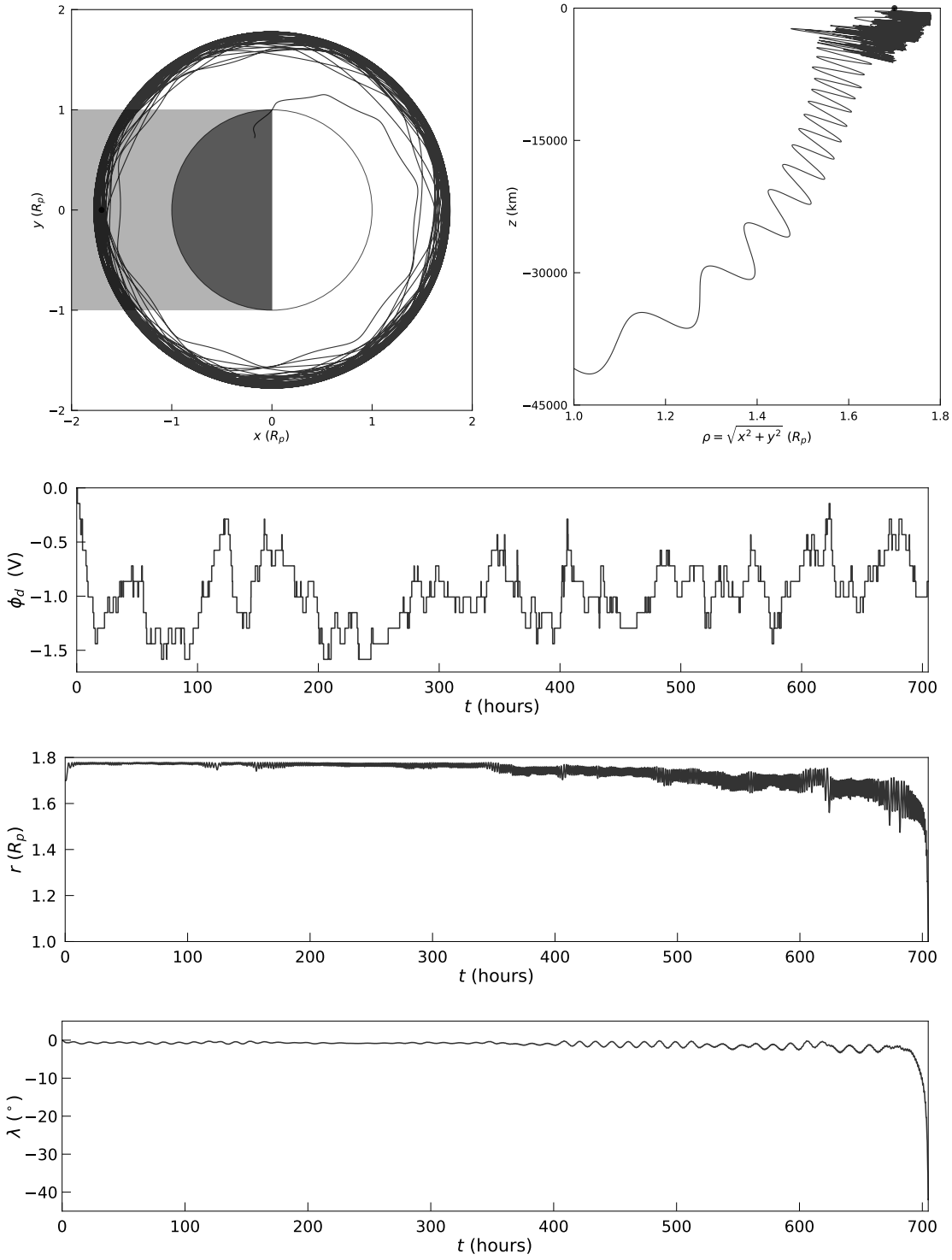

Figure 5.10: Following an initially uncharged $10\,\mathrm{nm}$ grain's trajectory around Saturn until it crashes into the planet at $\lambda \approx 42°\mathrm{S}$, with initial conditions: $r_L = 1.7\,R_\mathrm{S}$, $\Delta v_z = -100\,\mathrm{m\,s^{-1}}$, and O^+ plasma parameters: $T_e = T_i = 1\,\mathrm{eV}$, $T_\nu = 2.5\,\mathrm{eV}$, $n_\alpha = 1\,\mathrm{cm^{-3}}$. The top row shows the grain's spatial trajectory, with a black circle indicating its initial launch at local midnight; the bottom three rows show the grain surface potential, radial range and latitudinal temporal evolution.

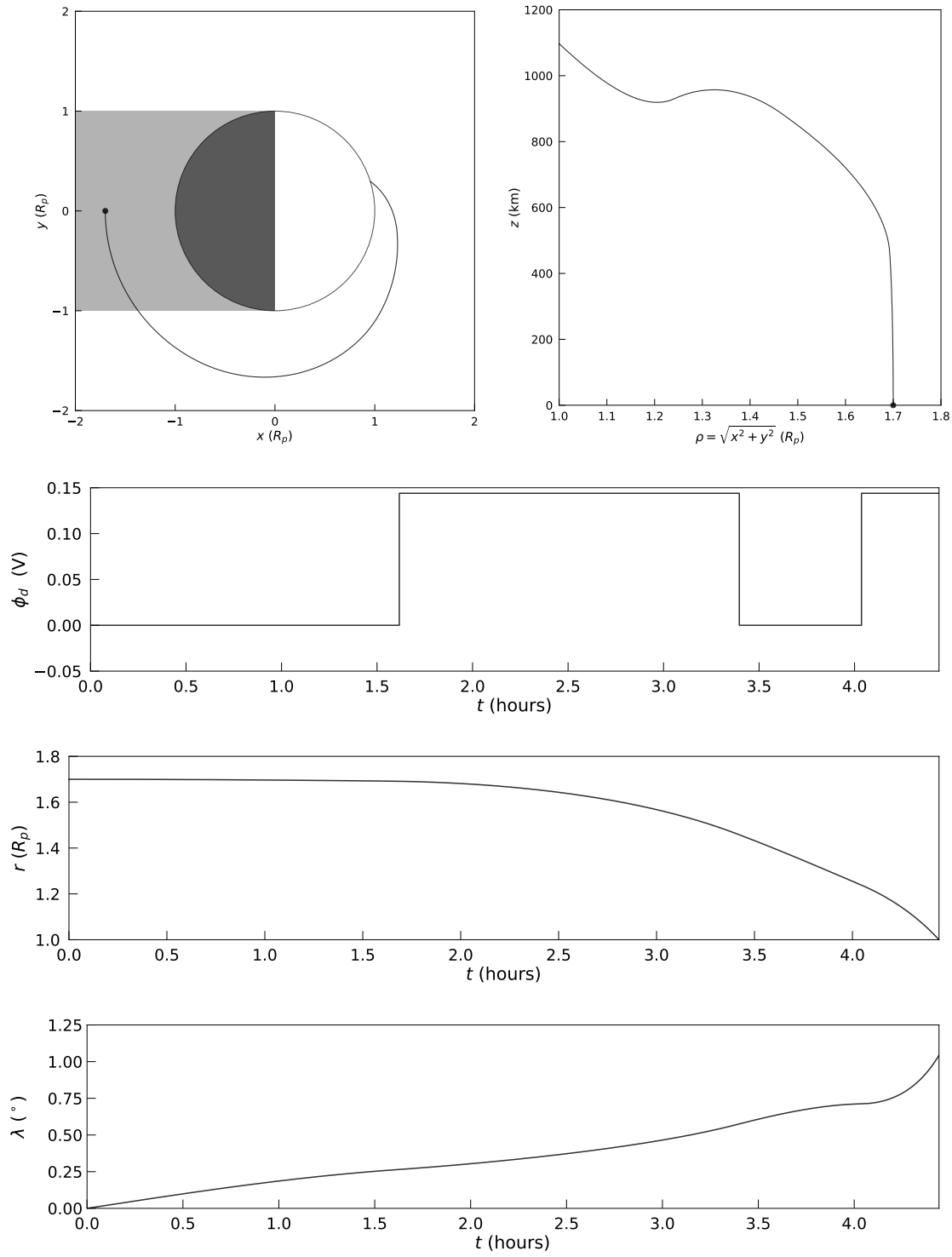

Figure 5.11: Following an initially uncharged $10\,\mathrm{nm}$ grain's trajectory around Saturn until it crashes into the planet's equatorial region, with initial conditions: $r_L = 1.7\,R_\mathrm{S}$, $\Delta v_z = +100\,\mathrm{m\,s^{-1}}$, and O^+ plasma parameters: $T_e = T_i = 1\,\mathrm{eV}$, $T_\nu = 2.5\,\mathrm{eV}$, $n_\alpha = 1\,\mathrm{cm^{-3}}$. The top row shows the grain's spatial trajectory, with a black circle indicating its initial launch at local midnight; the bottom three rows show the grain surface potential, radial range and latitudinal temporal evolution.

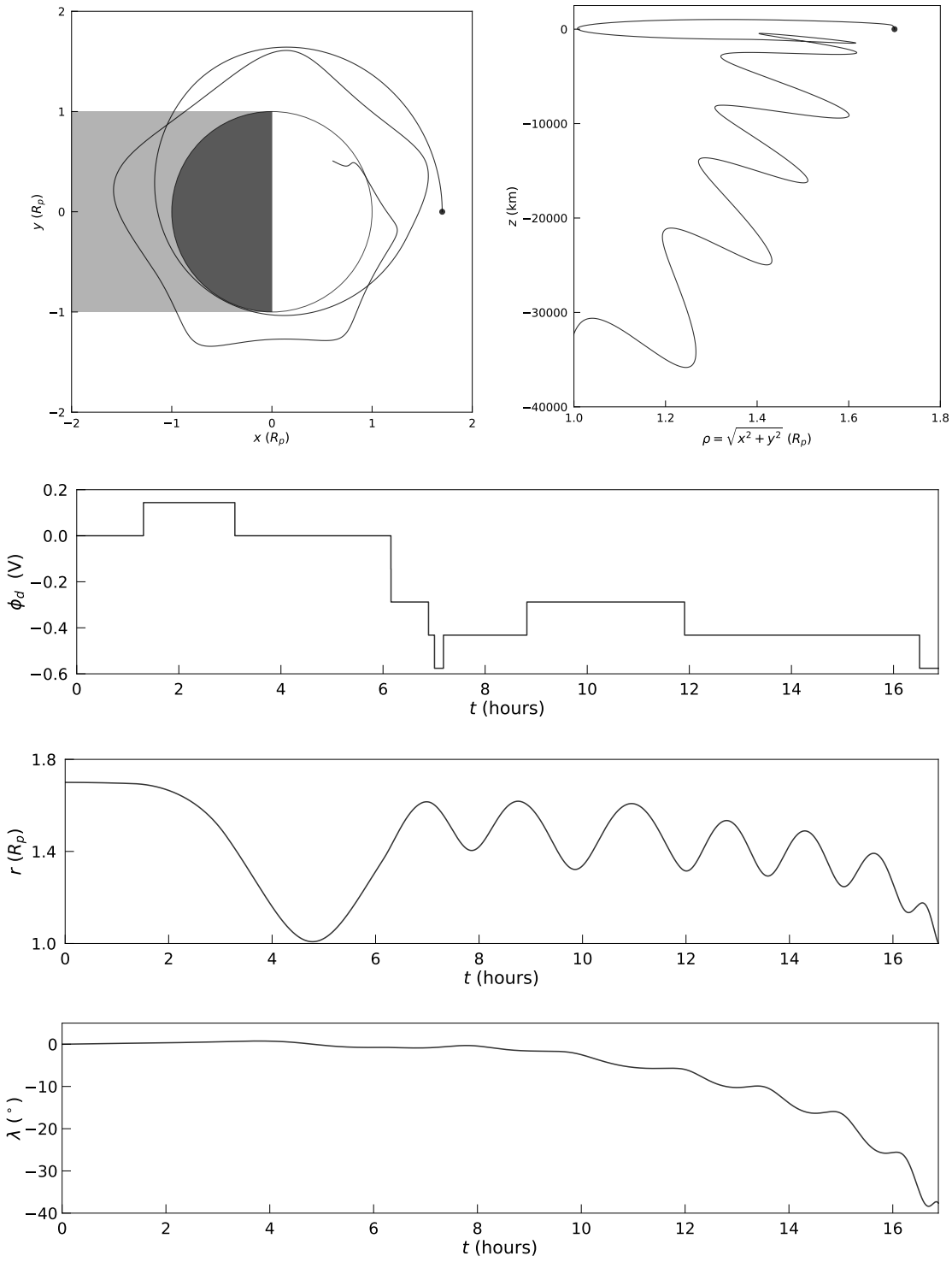

Figure 5.12: Following an initially uncharged $10\,\mathrm{nm}$ grain's trajectory around Saturn until it crashes into the planet at $\lambda \approx 38°\mathrm{S}$, with initial conditions: $r_L = 1.7\,R_\mathrm{S}$, $\Delta v_z = +100\,\mathrm{m\,s^{-1}}$, and O^+ plasma parameters: $T_e = T_i = 1\,\mathrm{eV}$, $T_\nu = 2.5\,\mathrm{eV}$, $n_\alpha = 1\,\mathrm{cm^{-3}}$. The top row shows the grain's spatial trajectory, with a black circle indicating its initial launch at local noon; the bottom three rows show the grain surface potential, radial range and latitudinal temporal evolution.

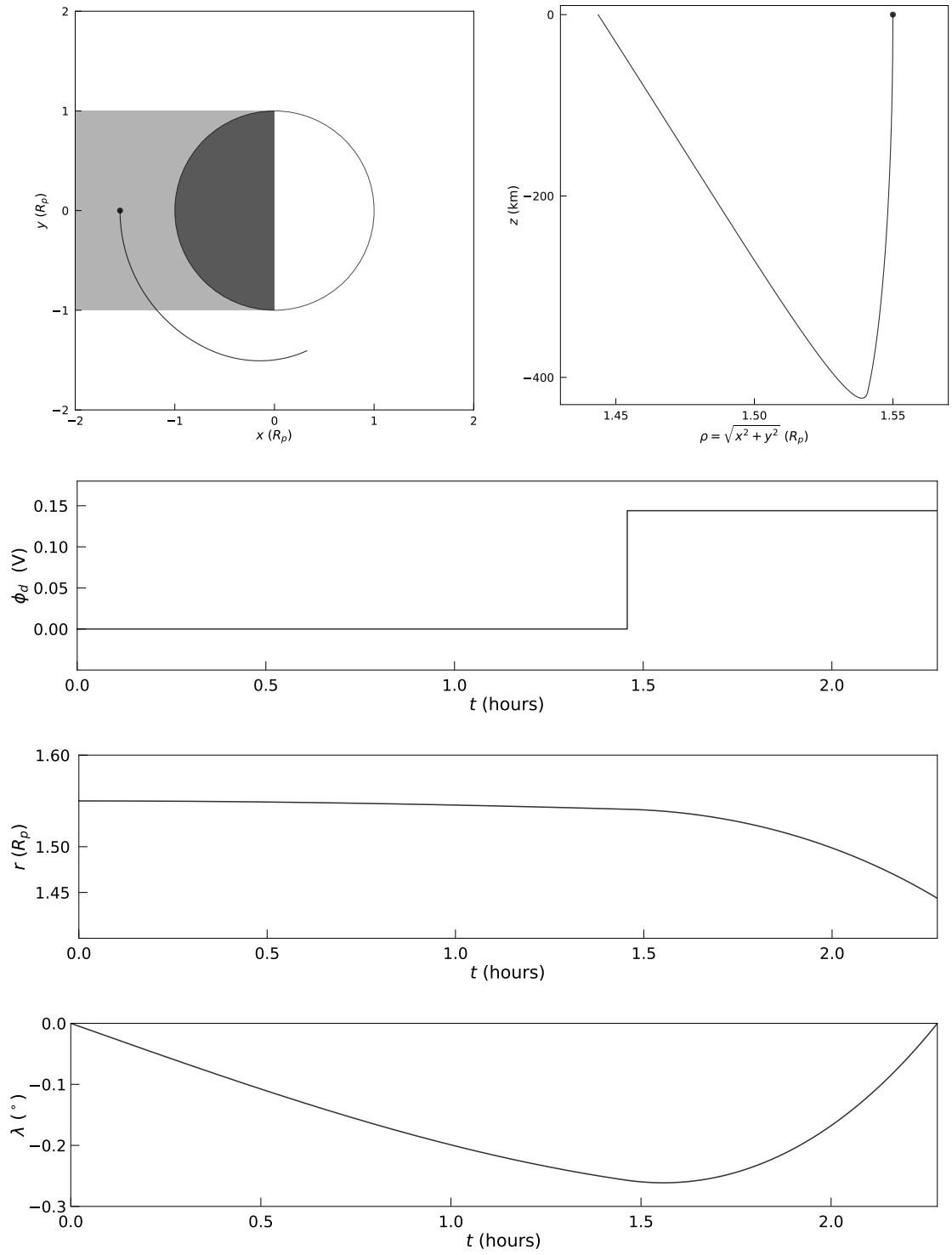

Figure 5.13: Following an initially uncharged $10\,\mathrm{nm}$ grain's trajectory around Saturn until it crashes into ring plane, with initial conditions: $r_L = 1.55\,R_\mathrm{S}$, $\Delta v_z = -100\,\mathrm{m\,s^{-1}}$, and O^+ plasma parameters: $T_e = T_i = 1\,\mathrm{eV}$, $T_\nu = 2.5\,\mathrm{eV}$, $n_\alpha = 1\,\mathrm{cm^{-3}}$. The top row shows the grain's spatial trajectory, with a black circle indicating its initial launch at local midnight; the bottom three rows show the grain surface potential, radial range and latitudinal temporal evolution.

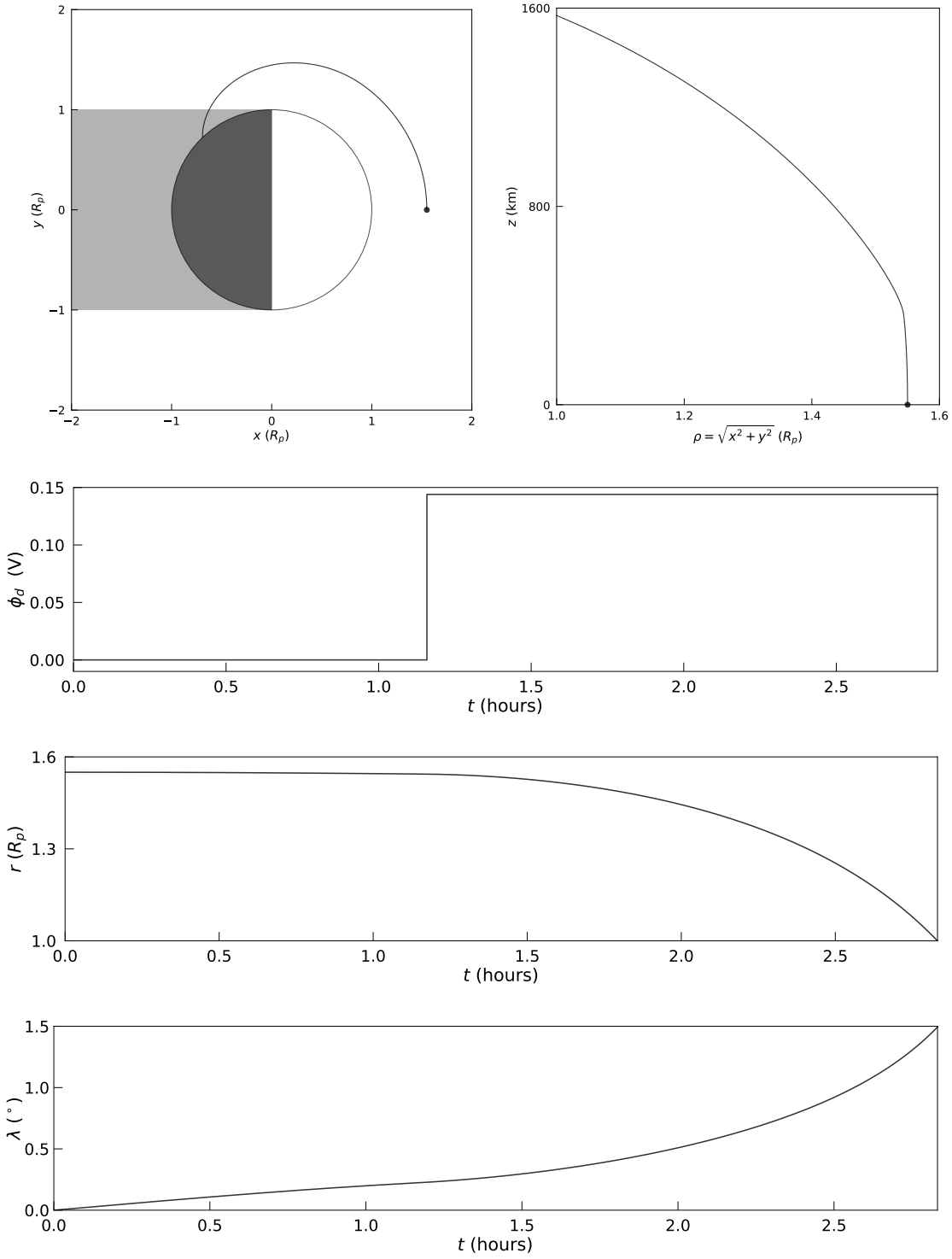

Figure 5.14: Following an initially uncharged $10\,\mathrm{nm}$ grain's trajectory around Saturn until it crashes into the planet's equatorial region, with initial conditions: $r_L = 1.55\,R_\mathrm{S}$, $\Delta v_z = +100\,\mathrm{m\,s^{-1}}$, and O^+ plasma parameters: $T_e = T_i = 1\,\mathrm{eV}$, $T_\nu = 2.5\,\mathrm{eV}$, $n_\alpha = 1\,\mathrm{cm^{-3}}$. The top row shows the grain's spatial trajectory, with a black circle indicating its initial launch at local noon; the bottom three rows show the grain surface potential, radial range and latitudinal temporal evolution.

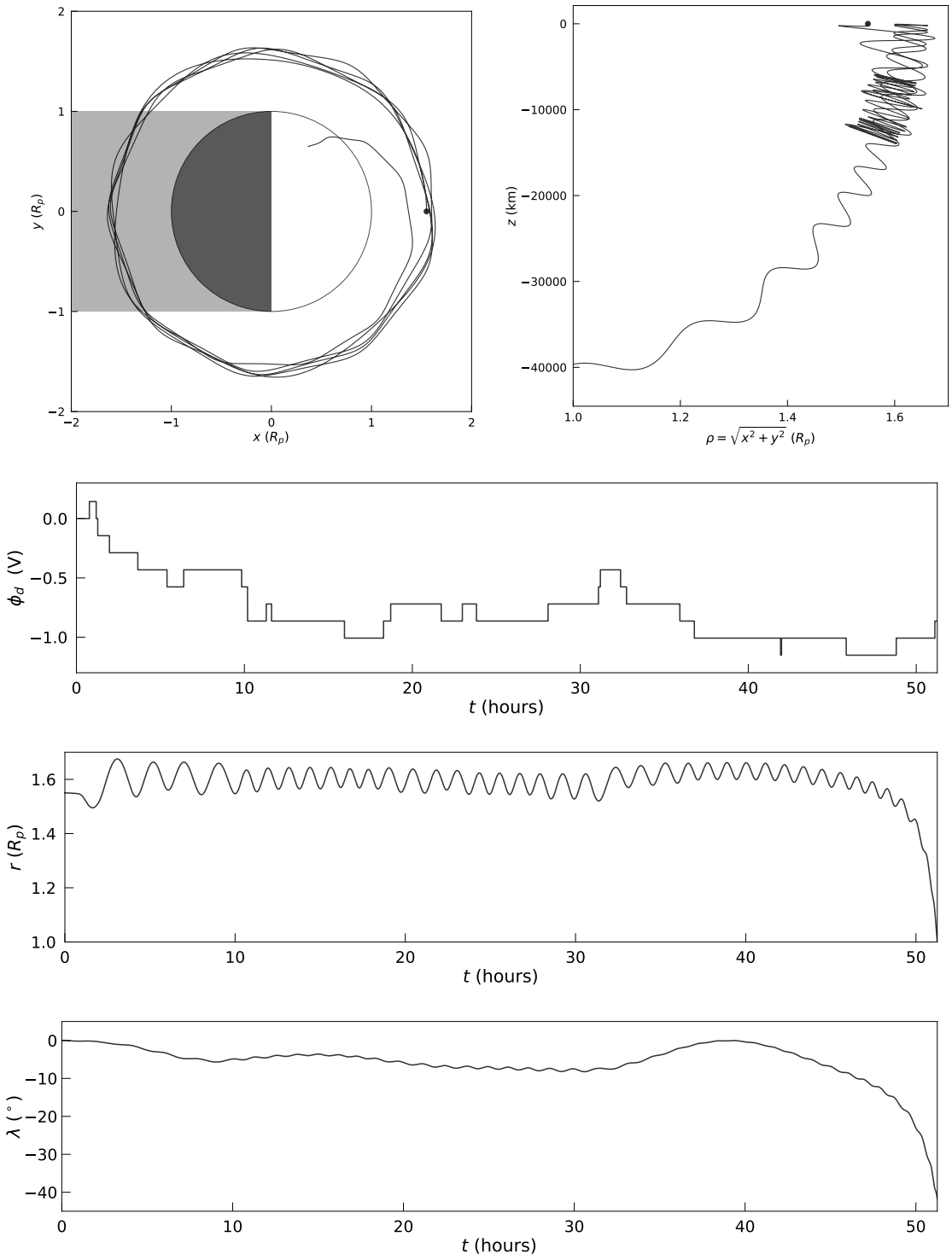

Figure 5.15: Following an initially uncharged $10\,\mathrm{nm}$ grain's trajectory around Saturn until it crashes into the planet at $\lambda \approx 42°\mathrm{S}$, with initial conditions: $r_L = 1.55\,R_\mathrm{S}$, $\Delta v_z = -100\,\mathrm{m\,s^{-1}}$, and O^+ plasma parameters: $T_e = T_i = 1\,\mathrm{eV}$, $T_\nu = 2.5\,\mathrm{eV}$, $n_\alpha = 1\,\mathrm{cm^{-3}}$. The top row shows the grain's spatial trajectory, with a black circle indicating its initial launch at local noon; the bottom three rows show the grain surface potential, radial range and latitudinal evolution.

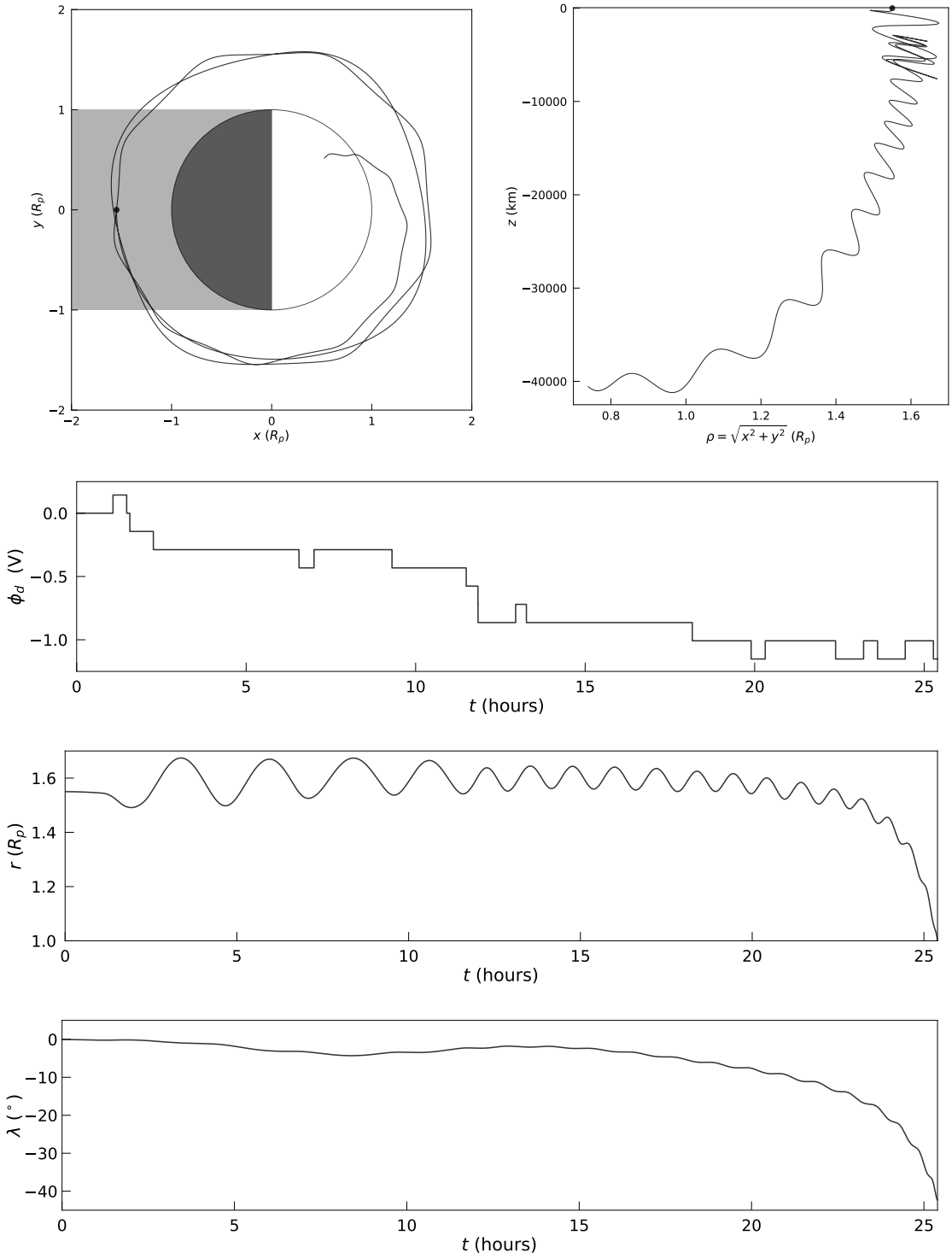

Figure 5.16: Following an initially uncharged $10\,\mathrm{nm}$ grain's trajectory around Saturn until it crashes into the planet at $\lambda \approx 40°\mathrm{S}$, with initial conditions: $r_L = 1.55\,R_\mathrm{S}$, $\Delta v_z = -100\,\mathrm{m\,s^{-1}}$, and O^+ plasma parameters: $T_e = T_i = 1\,\mathrm{eV}$, $T_\nu = 2.5\,\mathrm{eV}$, $n_\alpha = 1\,\mathrm{cm^{-3}}$. The top row shows the grain's spatial trajectory, with a black circle indicating its initial launch at local midnight; the bottom three rows show the grain surface potential, radial range and latitudinal temporal evolution.

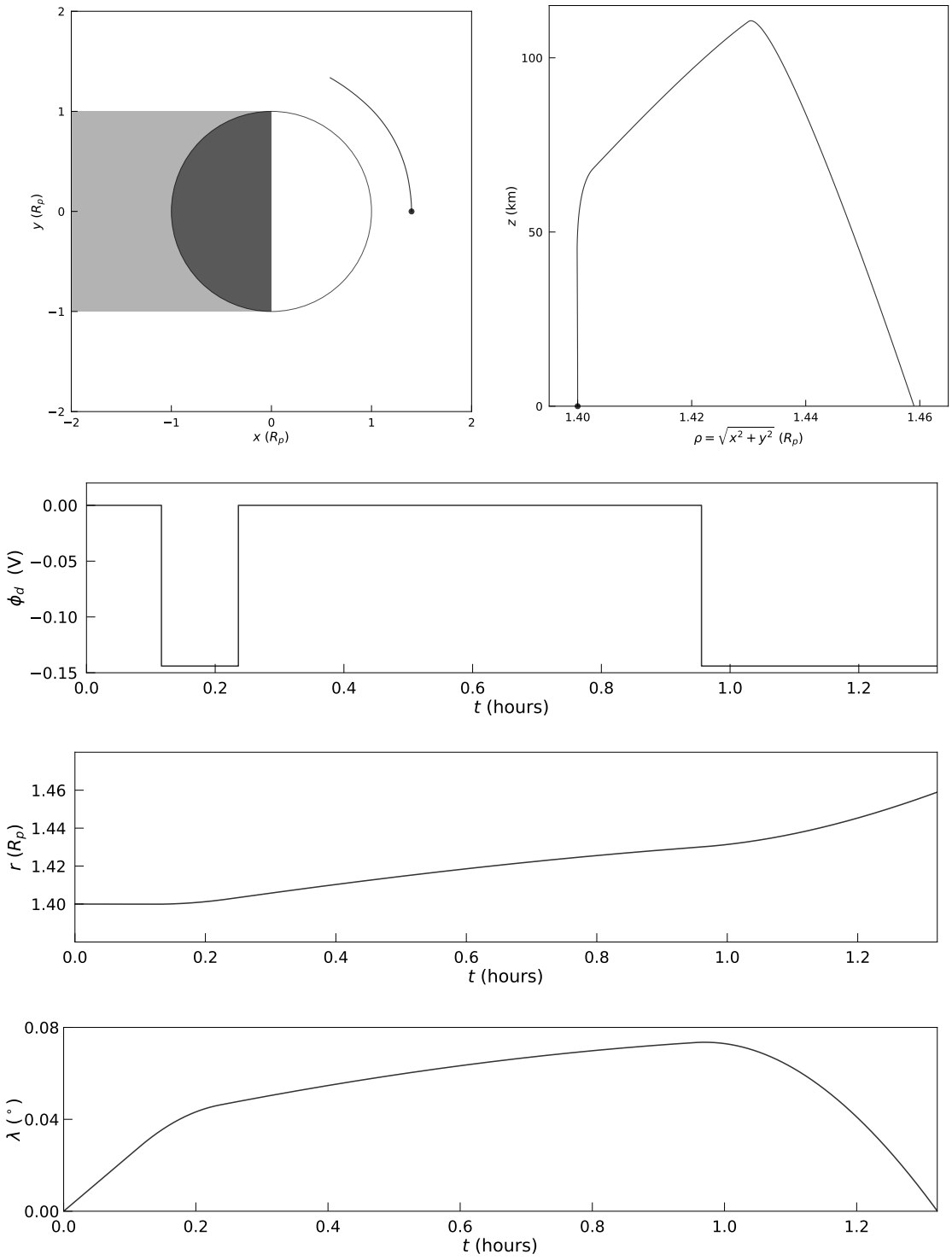

Figure 5.17: Following an initially uncharged $10\,\mathrm{nm}$ grain's trajectory around Saturn until it crashes into the C ring, with initial conditions: $r_L = 1.4\,R_\mathrm{S}$, $\Delta v_z = +100\,\mathrm{m\,s^{-1}}$, and O^+ plasma parameters: $T_e = T_i = 1\,\mathrm{eV}$, $T_\nu = 2.5\,\mathrm{eV}$, $n_\alpha = 1\,\mathrm{cm^{-3}}$. The top row shows the grain's spatial trajectory, with a black circle indicating its initial launch at local noon; the bottom three rows show the grain surface potential, radial range and latitudinal temporal evolution.

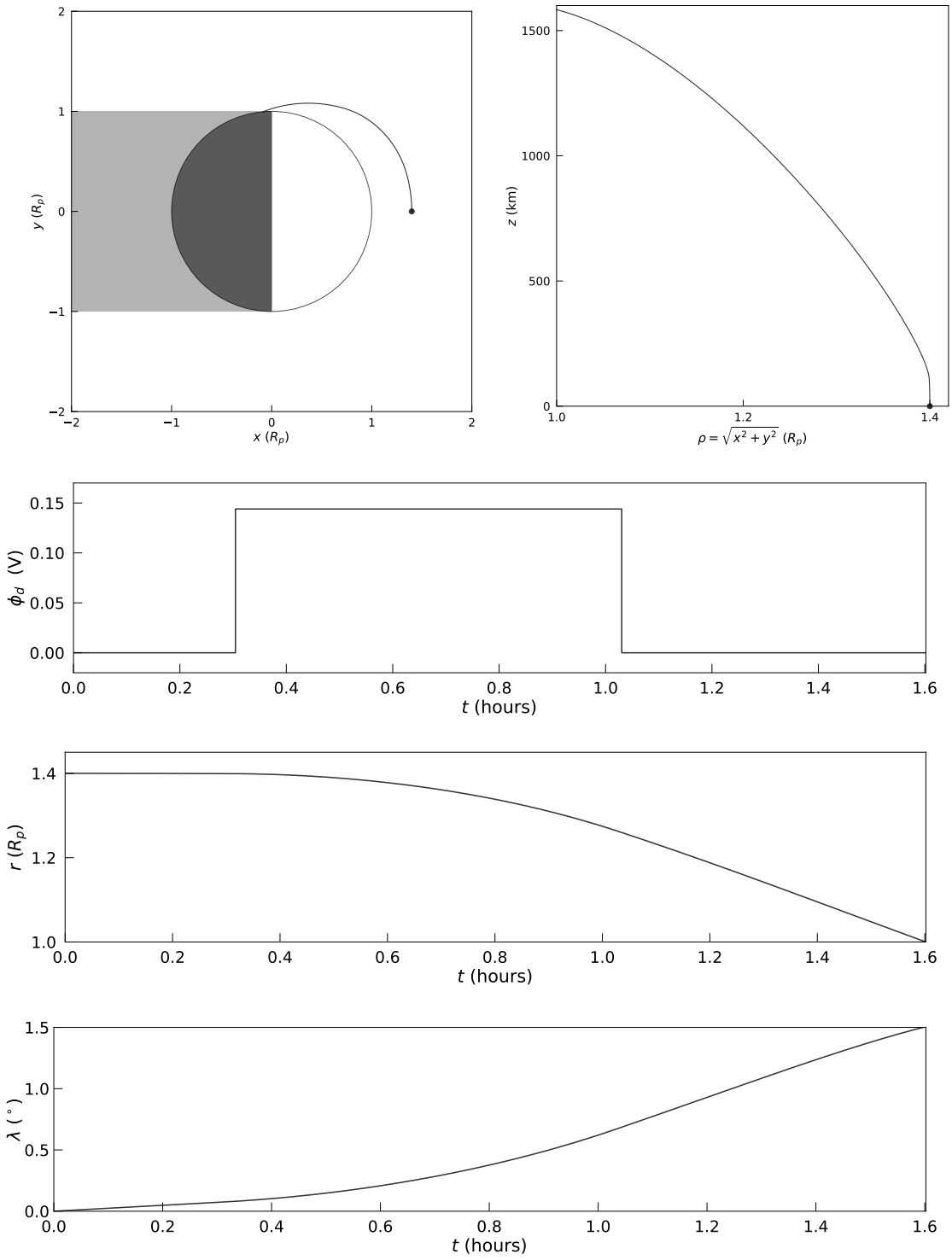

Figure 5.18: Following an initially uncharged $10\,\mathrm{nm}$ grain's trajectory around Saturn until it crashes into the planet's equatorial region, with initial conditions: $r_L = 1.4\,R_\mathrm{S}$, $\Delta v_z = +100\,\mathrm{m\,s^{-1}}$, and O^+ plasma parameters: $T_e = T_i = 1\,\mathrm{eV}$, $T_\nu = 2.5\,\mathrm{eV}$, $n_\alpha = 1\,\mathrm{cm^{-3}}$. The top row shows the grain's spatial trajectory, with a black circle indicating its initial launch at local noon; the bottom three rows show the grain surface potential, radial range and latitudinal temporal evolution.

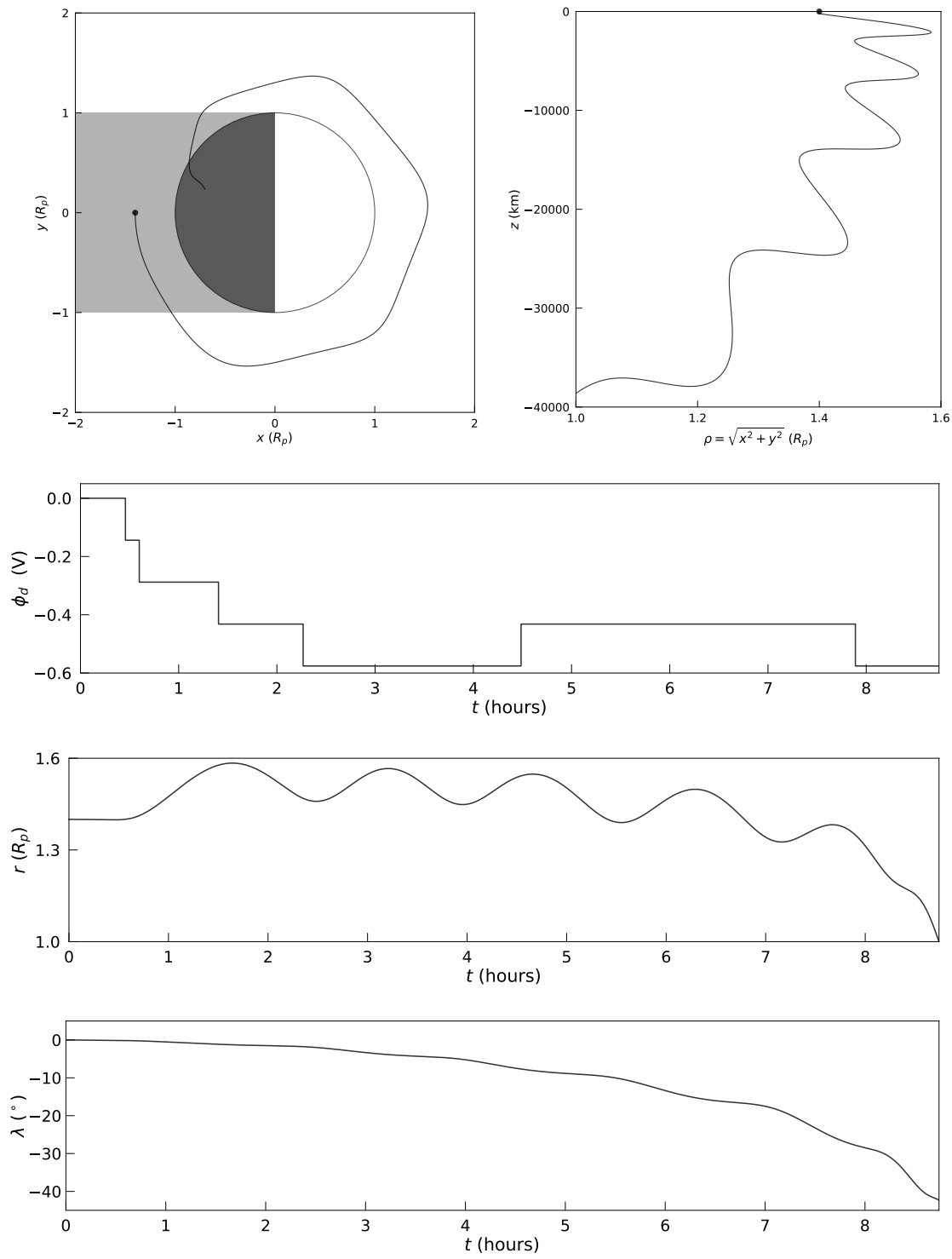

Figure 5.19: Following an initially uncharged $10\,\mathrm{nm}$ grain's trajectory around Saturn until it crashes into the planet at $\lambda \approx 40°\mathrm{S}$, with initial conditions: $r_L = 1.4\,R_\mathrm{S}$, $\Delta v_z = -100\,\mathrm{m\,s^{-1}}$, and O^+ plasma parameters: $T_e = T_i = 1\,\mathrm{eV}$, $T_\nu = 2.5\,\mathrm{eV}$, $n_\alpha = 1\,\mathrm{cm^{-3}}$. The top row shows the grain's spatial trajectory, with a black circle indicating its initial launch at local midnight; the bottom three rows show the grain surface potential, radial range and latitudinal temporal evolution.

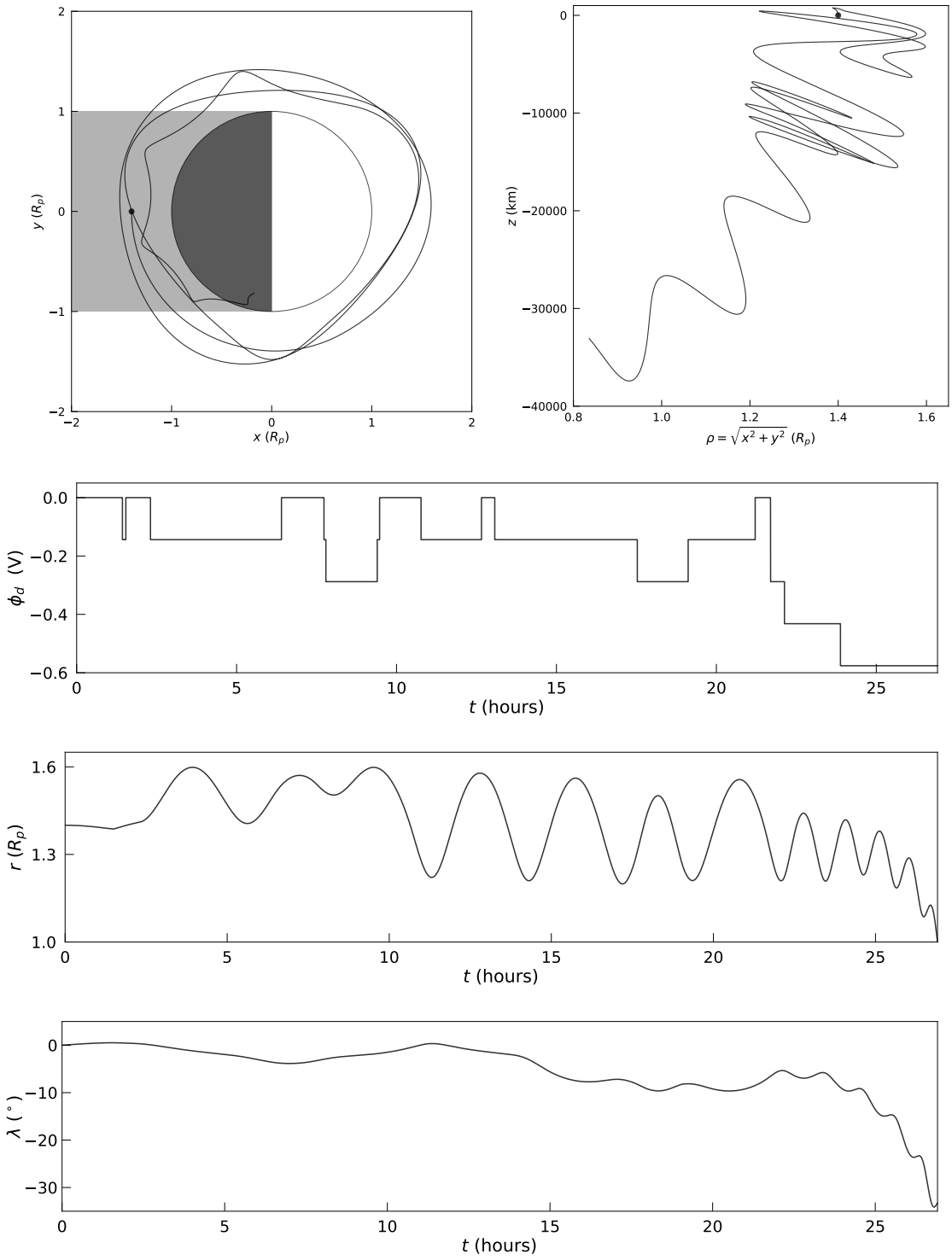

Figure 5.20: Following an initially uncharged $10\,\mathrm{nm}$ grain's trajectory around Saturn until it crashes into the planet at $\lambda \approx 33°\mathrm{S}$, with initial conditions: $r_L = 1.4\,R_\mathrm{S}$, $\Delta v_z = +200\,\mathrm{m\,s^{-1}}$, and O^+ plasma parameters: $T_e = T_i = 1\,\mathrm{eV}$, $T_\nu = 2.5\,\mathrm{eV}$, $n_\alpha = 1\,\mathrm{cm^{-3}}$. The top row shows the grain's spatial trajectory, with a black circle indicating its initial launch at local midnight; the bottom three rows show the grain surface potential, radial range and latitudinal temporal evolution.

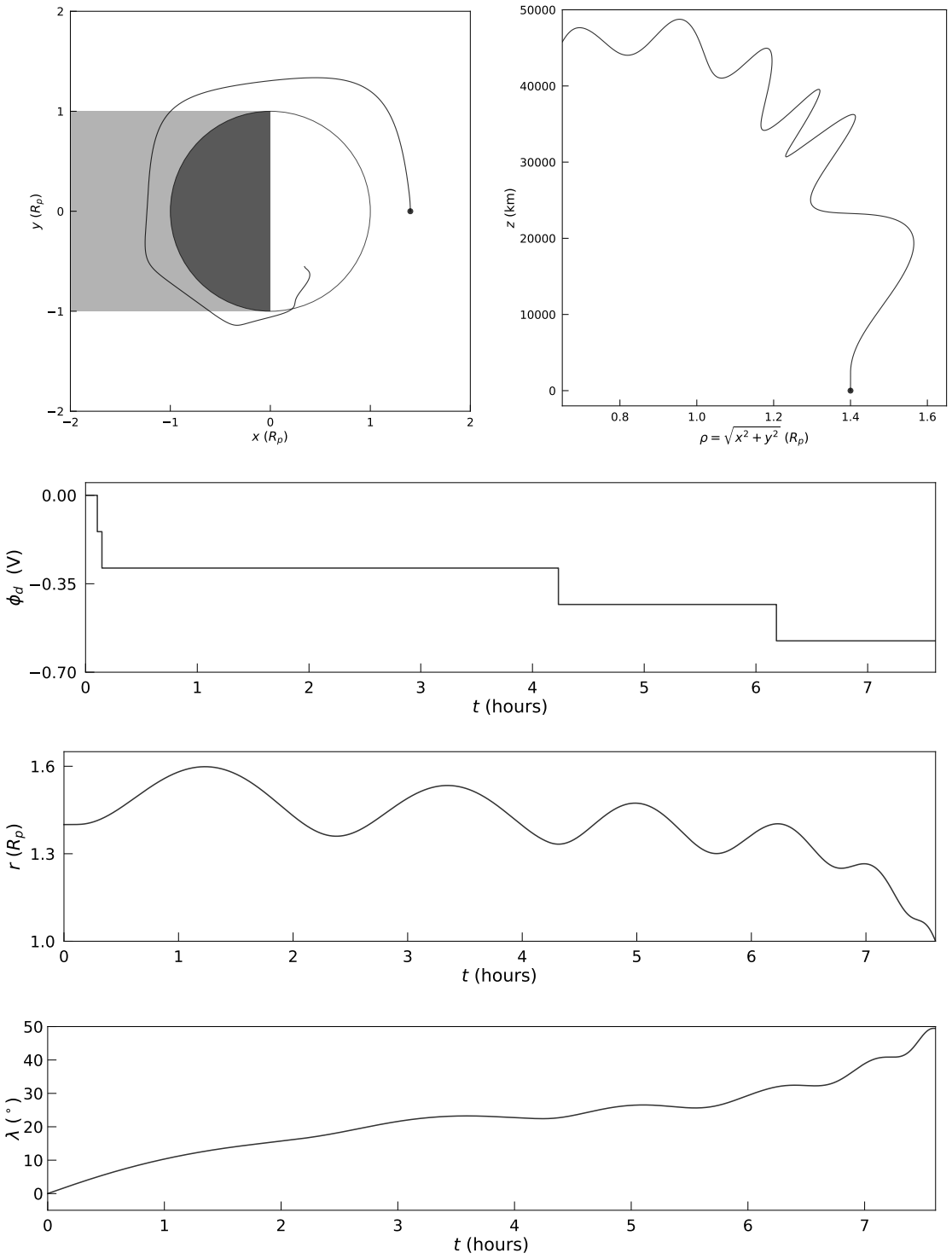

Figure 5.21: Following an initially uncharged $10\,\mathrm{nm}$ grain's trajectory around Saturn until it crashes into the planet at $\lambda \approx 49°$N, with initial conditions: $r_L = 1.4\,R_\mathrm{S}$, $\Delta v_z = +5\,\mathrm{km\,s^{-1}}$, and O^+ plasma parameters: $T_e = T_i = 1\,\mathrm{eV}$, $T_\nu = 2.5\,\mathrm{eV}$, $n_\alpha = 1\,\mathrm{cm^{-3}}$. The top row shows the grain's spatial trajectory, with a black circle indicating its initial launch at local noon; the bottom three rows show the grain surface potential, radial range and latitudinal temporal evolution.

6

Conclusions

In this thesis, the dynamics of charged dust in Saturn's main rings has been studied. Here, I describe the findings of the ring rain simulations of Chapter 5, discussing further work that can be undertaken, and review the key results of previous chapters.

6.1 Summary of Work

In Chapter 2, adaptive integrators for solving the equations of motion of grains with constant charge-to-mass ratios were developed and tested. The derivation and verification of analytical results for grains in planetary gravitational and magnetic fields were presented in Chapter 3, and extensive simulations were run and compared to literature. In Chapter 4, a novel stochastic charging algorithm was described, that was used to integrate the charging equations for nanograins. This was applied to the study of ring rain, Chapter 5.

The results presented in §5.4 (Table 5.1) hint at the complexity still to be explored in ring rain, highlighting the chaotic nature of the nanograins' trajectories through their sensitivity to initial conditions, and also provide a useful step towards independently verifying the results of Hsu et al. (2018b). Grains were launched from different regions of the main rings and their equations of

motion and stochastic charging integrated. Grains launched from the outer B ring took hundreds of hours to reach southern mid-latitudes (Figure 5.10), whilst equatorial deposition occurred on much shorter timescales (Figure 5.11). This corroborates Hsu (2020)'s hypothesis that the higher silicate fraction in the observed dust at mid-latitudes is due to photo-evaporation of water-ice. Although further simulations must be run to confirm this, it suggests that ring rain may not be a cleansing mechanism for the rings (Crida et al. 2019), and the rings may indeed be youthful (millions of years old as opposed to coeval with the formation of the Solar System), assuming certain interplanetary pollution fluxes.

The dust's initial velocity distribution appears to be a significant factor influencing the distribution of ring rain's latitudinal deposition. Liu & Ip (2014) assumed a population of nanograins produced by low-velocity mutual collisions between ring particles, whilst Ip et al. (2016) set $|\Delta v_z| = 1.5\,\mathrm{km\,s^{-1}}$ based on high-velocity impacts from laboratory experiments, to model ejecta from micro-meteoroid bombardment of the rings. Hsu et al. (2018b) also assumed an impactor-ejecta process, with the ejecta speed distribution treated as a free parameter, characterised by a range and power-law slope, to be fit to the measured *CDA* profiles. Jontof-Hutter (2012) studied the effect of varied launch speeds on the stability of dust and found that a vertical impulse of $|\Delta v_z| = 0.5\,\mathrm{km\,s^{-1}}$ leads to additional instability, however, their assumption of constant charge-to-mass ratios precludes a direct comparison to grains whose charge varies stochastically. Figure 5.21 hints that northern mid-latitudinal influx occurs for grains with faster northward vertical velocities ($\Delta v_z \sim \mathrm{km\,s^{-1}}$), in order to overcome the Lorentz force directed southwards arising from the vertical offset of Saturn's magnetic dipole. Otherwise, the modest vertical velocity boosts explored by Figures 5.8 - 5.20 result in southern or equatorial deposition (or collision with the main rings).

Grains can exhibit wide radial excursions (Figure 5.20), if they are not initially highly-charged, and so the radial opacity profile (Figure 1.8) may not be straightforwardly explained by magnetically conjugate ring locations with H_3^+ emission peaks (Figure 1.18).

6.2 Future Work

To study ring rain further, a statistically significant sample of simulations needs to analysed. As identified in §5.3, a sensitivity analysis, through running batches of test grains whilst varying a single parameter (in particular, plasma density, plasma temperature, impact ejection speed and grain radius) systematically and iterating through parameters, would be a more informative approach rather than finely tuning a single complex plasma model. Even *Cassini* measurements (e.g. Tokar et al. 2005; Young et al. 2005; Waite et al. 2005) give snapshots of the plasma environment within a restricted space and time, for which simulations could provide a quantitative measure of the effect of small perturbations to initial conditions, as well as exploring a wider range of input parameters to predict ring rain at other seasons and examine the effect of ring tilt angle and shadowing.

During micro-meteoroid bombardment of the rings, high density impact plasma is generated (e.g. Northrop & Connerney 1987). Hsu et al. (2018b) allow the initial grain charge to be variable ($|q_{d0}| = 0 - 50e$), with the initial charge distribution proportional to $(1 + |q_{d0}|)^{-0.5}$, to account for the electrons/ions collected by the grains from the impact plasma. This parameter is something to be explored further in a sensitivity analysis, alongside other environmental and grain parameters. Recalling that a significant factor in a grain's charging history is its size (e.g. $I_\alpha \propto a_d^2$, Eq. 4.1), an important caveat to note is that a grain is subject to sputtering, solar radiation and other erosive processes that would change its size and therefore its orbital trajectory.

The inclusion of grain composition in the dynamical model would allow an analysis of the silicate to water-ice ratio of ring rain, to compare to the photo-evaporation interpretation, which explains the lower water-ice fraction in ring rain by long integration times leading to water loss (§5.1.1). Using the approach of Cui & Goree (1994), who describe charge distribution functions (§4.1.5), the fraction of grains having a certain charge at a given time could be quantified, to investigate any differences in the average charge and the magnitude of charge fluctuations of silicate versus water-ice grains, that could lead to orbital instability (Chapter 3).

Together with a detailed systematic investigation of the influx of dust onto Saturn across latitudes, by varying grain and environmental parameters, the effect of ring rain on the structure of the rings can be investigated further; to examine how the relative proportions of dust from the

distinct regions of the main rings (Figure 5.1) varies, to review whether compositional differences in ring rain occur due to dynamical sorting from the bulk rings. The contribution of grains from Enceladus' orbit (E ring) needs to be studied, which may necessitate the inclusion of the secondary electron emission current, to ascertain the proportion of silicate nanograins able to cross synchronous orbit from outside. Given that grains can exhibit wide radial excursions, the mapping from ring locations to H_3^+ profiles can be further investigated; as well as considering the mechanism of ballistic transport.

The results cannot be predicted with certainty at this stage, but the path has been mapped out and the journey awaits.

Bibliography

Aarseth, S., Brackbill, J., & Cohen, B. 1985, in Methods for N-body Simulations (Academic Press New York), 377–418

Acuña, M. H., Behannon, K. W., & Connerney, J. E. P. 1983, Jupiter's Magnetic Field and Magnetosphere, ed. A. J. Dessler, Cambridge Planetary Science Old (Cambridge University Press), 1–50

Acuña, M. H. & Ness, N. F. 1980, Science, 207, 444

Alfvén, H. 1940, Ark. f. Mat., Astr. o. Fysik, 27A

Alfvén, H. 1950, Cosmical Electrodynamics (International Series of Monographs on Physics)

André, N., Blanc, M., Maurice, S., et al. 2008, Reviews of Geophysics, 46

Archinal, B., Acton, C., A'hearn, M., et al. 2018, Celestial Mechanics and Dynamical Astronomy, 130, 1

Arridge, C., Achilleos, N., Dougherty, M., Khurana, K., & Russell, C. 2006, Journal of Geophysical Research: Space Physics, 111

Atreya, S. & Donahue, T. 1975, Icarus, 24, 358

Atreya, S. & Waite, J. 1981, Nature, 292, 682

Atreya, S., Waite Jr, J., Donahue, T., Nagy, A., & McConnell, J. C. 1984, Saturn, 239

Baines, K. H., Flasar, F. M., Krupp, N., & Stallard, T. 2018, Saturn in the 21st Century, Vol. 20

(Cambridge University Press)

Barnes, J. & Hut, P. 1986, Nature, 324, 446

Bastin, J. A. 1981, The Moon and the Planets, 24, 467

Birkeland, K. 1913, The Norwegian Aurora Polaris Expedition 1902-1903, Vol. 1, Sec. II (H. Aschelhoug & Co.)

Birmingham, T. J. & Northrop, T. G. 1979, Journal of Geophysical Research: Space Physics, 84, 41

Borderies, N., Goldreich, P., & Tremaine, S. 1982, Nature, 299, 209

Borderies, N., Goldreich, P., & Tremaine, S. 1984, in IAU Colloq. 75: Planetary Rings, Vol. 1, 713–734

Broadfoot, A., Atreya, S., Bertaux, J., et al. 1989, Science, 246, 1459

Broadfoot, A., Herbert, F., Holberg, J., et al. 1986, Science, 233, 74

Broadfoot, A., Sandel, B., Shemansky, D., et al. 1981, Science, 212, 206

Bulirsch, R. & Stoer, J. 1966, Numerische Mathematik, 8, 93

Bunce, E., Cowley, S., & Wild, J. 2003, Annales Geophysicae, 21, 1709

Burns, J. A. 1991, in Origin and Evolution of Interplanetary Dust (Springer), 341–348

Burns, J. A., Hamilton, D. P., & Showalter, M. R. 2001, Dusty Rings and Circumplanetary Dust: Observations and Simple Physics, ed. E. Grün, B. Å. S. Gustafson, S. Dermott, & H. Fechtig (Berlin, Heidelberg: Springer Berlin Heidelberg), 641–725

Burns, J. A., Lamy, P. L., & Soter, S. 1979, Icarus, 40, 1

Burns, J. A., Lamy, P. L., & Soter, S. 2014, Icarus, 232, 263

Canup, R. M. 2010, Nature, 468, 943

Cao, H., Dougherty, M. K., Hunt, G. J., et al. 2019, Icarus, 113541

Cao, H., Russell, C. T., Christensen, U. R., Dougherty, M. K., & Burton, M. E. 2011, Earth and

Planetary Science Letters, 304, 22

Cao, H., Russell, C. T., Wicht, J., Christensen, U. R., & Dougherty, M. K. 2012, Icarus, 221, 388

Carbary, J. F., Bythrow, P. F., & Mitchell, D. G. 1982, Geophysical Research Letters, 9, 420

Cassini Final Mission Report. NASA/JPL 2019, Mission Overview, Science Objectives and Results, https://pds-rings.seti.org/cassini/report/Cassini%20Final%20Report%20-%20Volume%201.pdf

Chambers, J. E. 1999, Monthly Notices of the Royal Astronomical Society, 304, 793

Chen, R. H. 1983, The Moon and the Planets, 28, 37

Chow, V. W., Mendis, D. A., & Rosenberg, M. 1993, Journal of Geophysical Research: Space Physics, 98, 19065

Christensen, U. R. & Wicht, J. 2008, Icarus, 196, 16

Ciarniello, M., Filacchione, G., D'Aversa, E., et al. 2019, Icarus, 317, 242

Clark, R. N., Cruikshank, D. P., Jaumann, R., et al. 2012, Icarus, 218, 831

Clark, R. N. & McCord, T. B. 1980, Icarus, 43, 161

Colwell, J., Cooney, J., Esposito, L., & Sremčević, M. 2009a, Icarus, 200, 574

Colwell, J. E., Nicholson, P. D., Tiscareno, M. S., et al. 2009b, in Saturn from Cassini-Huygens (Springer), 375–412

Connerney, J. 2013, Nature, 496, 178

Connerney, J. E. P. 1986, Geophys. Res. Lett., 13, 773

Connerney, J. E. P. 1993, Journal of Geophysical Research: Planets, 98, 18659

Connerney, J. E. P., Ness, N. F., & Acuna, M. H. 1982, Nature, 298, 44

Connerney, J. E. P. & Waite, J. H. 1984, Nature, 312, 136

Cooper, J. F. 1983, Journal of Geophysical Research: Space Physics, 88, 3945

Cowling, T. G. 1933, Monthly Notices of the Royal Astronomical Society, 94, 39

Crida, A., Charnoz, S., Hsu, H.-W., & Dones, L. 2019, Nature Astronomy, 1

Cui, C. & Goree, J. 1994, IEEE Transactions on Plasma Science, 22, 151

Cuzzi, J., Clark, R., Filacchione, G., et al. 2009, Ring Particle Composition and Size Distribution, ed. M. K. Dougherty, L. W. Esposito, & S. M. Krimigis, 459

Cuzzi, J. N. & Durisen, R. H. 1990, Icarus, 84, 467

Cuzzi, J. N. & Estrada, P. R. 1998, Icarus, 132, 1

Cuzzi, J. N., French, R. G., Hendrix, A. R., et al. 2018, Icarus, 309, 363

Deuflhard, P. 1983, Numerische Mathematik, 41, 399

Dionne, G. F. 1975, Journal of Applied Physics, 46, 3347

Dormand, J. & Prince, P. 1980, Journal of Computational and Applied Mathematics, 6, 19

Dougherty, M., Esposito, L., & Krimigis, S., eds. 2009, Saturn from Cassini-Huygens (Springer Science & Business Media)

Dougherty, M. K., Cao, H., Khurana, K. K., et al. 2018, Science, 362

Draine, B. T. & Salpeter, E. E. 1979, ApJ, 231, 77

Durisen, R. H. 1984, in IAU Colloq. 75: Planetary Rings, 416–446

Durisen, R. H., Cramer, N. L., Murphy, B. W., et al. 1989, Icarus, 80, 136

Dzhanoev, A. R., Schmidt, J., Liu, X., & Spahn, F. 2016, A&A, 591, A147

Epstein, E. E., Janssen, M. A., & Cuzzi, J. N. 1984, Icarus, 58, 403

Esposito, L. 2014, Planetary Rings: A Post-Equinox View, 2nd edn. (Cambridge University Press)

Esposito, L. W., Colwell, J. E., Larsen, K., et al. 2005, Science, 307, 1251

Estrada, P. R., Durisen, R. H., Cuzzi, J. N., & Morgan, D. A. 2015, Icarus, 252, 415

Farmer, A. J. & Goldreich, P. 2005, Icarus, 179, 535

Farrell, W. M., Desch, M. D., Kaiser, M. L., Kurth, W. S., & Gurnett, D. A. 2006, Geophysical Research Letters, 33, 7203

Fehlberg, E. 1969, NASA Technical Report R-315

Filacchione, G., Ciarniello, M., Capaccioni, F., et al. 2014, Icarus, 241, 45

Fillius, W., Ip, W., & McIlwain, C. 1980, Science, 207, 425

French, R. G., Salo, H., McGhee, C. A., & Dones, L. 2007, Icarus, 189, 493

Giguere, P. & Huebner, W. 1978, The Astrophysical Journal, 223, 638

Goertz, C. & Ip, W.-H. 1984, Geophysical Research Letters, 11, 349

Goertz, C. K. 1989, Reviews of Geophysics, 27, 271

Goertz, C. K. & Morfill, G. 1983, Icarus, 53, 219

Goldreich, P. & Tremaine, S. 1978, Icarus, 34, 240

Goldstein, H., Poole, C., & Safko, J. 2014, Classical Mechanics, New International edn. (Pearson Education Limited), 134–183

Göller, J. & Grün, E. 1989, Planetary and Space Science, 37, 1197

Gombosi, T. I., Armstrong, T. P., Arridge, C. S., et al. 2009, in Saturn from Cassini-Huygens (Springer), 203–255

Gombosi, T. I. & Ingersoll, A. P. 2010, Science, 327, 1476

Goree, J. 1994, Plasma Sources Science and Technology, 3, 400

Gragg, W. 1964, PhD thesis, University of California, Los Angeles

Gragg, W. B. 1965, Journal of the Society for Industrial and Applied Mathematics, Series B: Numerical Analysis, 2, 384

Graps, A. & Grün, E. 2002, COSPAR Colloquia Series, 15, 168

Graps, A., Grün, E., Krüger, H., Horányi, M., & Svedhem, H. 2001, in ESA Special Publication, Vol. 495, Meteoroids 2001 Conference, ed. B. Warmbein, 601–608

Graps, A. L., Grün, E., Svedhem, H., et al. 2000, Nature, 405, 48

Graps, A. L., Jones, G. H., Juhász, A., Horányi, M., & Havnes, O. 2008, Space Science Reviews, 137, 435

Grün, E. 1984, in Planetary Rings, ed. A. Brahic

Grün, E., Baguhl, M., Hamilton, D. P., et al. 1996, Nature, 381, 395

Grün, E., Hamilton, D., Baguhl, M., et al. 1994, Geophysical Research Letters, 21

Grün, E., Morfill, G. E., & Mendis, D. A. 1984, in IAU Colloq. 75: Planetary Rings, ed. R. Greenberg & A. Brahic, 275–332

Grün, E., Morfill, G. E., Terrile, R. J., Johnson, T., & Schwehm, G. 1983, Icarus, 54, 227

Grün, E., Pater, I., Showalter, M., Spahn, F., & Srama, R. 2006, Planetary and Space Science, 54, 837

Grün, E., Zook, H. A., Baguhl, M., et al. 1993, Nature, 362, 428

Grün, E., Zook, H. A., Baguhl, M., et al. 1992, Science, 257, 1550

Gurnett, D., Kurth, W., Hospodarsky, G., et al. 2005, Science, 307, 1255

Hamilton, D., Yuxi, L., Moye, C., Davies, A., & Hedman, M. M. 2020, postponed 13^{th} Meeting on Cosmic Dust, Kitakyushu International Conference Center, Kitakyushu, Japan

Hamilton, D. P. 1993, Icarus, 101, 244

Hamilton, D. P. 2006, in Bulletin of the American Astronomical Society, Vol. 38, AAS/Division for Planetary Sciences Meeting Abstracts #38, 578

Hamilton, D. P. & Burns, J. A. 1993, Nature, 364, 695

Hamilton, D. P. & Burns, J. A. 1993, Advances in Space Research, 13, 241

Hamilton, D. P. & Krivov, A. V. 1996, Icarus, 123, 503

Hamilton, D. P. & Krüger, H. 2008, Nature, 453, 72

Handel, P. H. & James, P. B. 1983, Geophysical Research Letters, 10, 1

Havnes, O., Aslaksen, T., Melandsø, F., & Nitter, T. 1992a, Physica Scripta, 45, 491

Havnes, O., Morfill, G., & Goertz, C. 1984, Journal of Geophysical Research: Space Physics, 89, 10999

Havnes, O., Morfill, G., & Melandsø, F. 1992b, Icarus, 98, 141

Hedman, M., Nicholson, P., Cuzzi, J., et al. 2013, Icarus, 223, 105

Hedman, M. M., Nicholson, P. D., Baines, K. H., et al. 2009, The Astronomical Journal, 139, 228

Herbert, F. & Sandel, B. R. 1999, Planetary and Space Science, 47, 1119

Hill, G. W. 1878, American Journal of Mathematics, 1, 5

Hill, J. R. & Mendis, D. A. 1981, The Moon and Planets, 24, 431

Horányi, M. 1996, Annual Review of Astronomy and Astrophysics, 34, 383

Horányi, M. 2000, Physics of Plasmas, 7, 3847

Horányi, M. & Burns, J. A. 1991, Journal of Geophysical Research: Space Physics, 96, 19283

Horányi, M., Burns, J. A., Hedman, M., Jones, G., & Kempf, S. 2009, Diffuse Rings, ed. M. K. Dougherty, L. W. Esposito, & S. M. Krimigis (Springer), 459

Horányi, M. & Cravens, T. E. 1996, Nature, 381, 293

Horányi, M., Juhász, A., & Morfill, G. E. 2008, Geophysical Research Letters, 35

Horányi, M., Morfill, G., & Grün, E. 1993a, Journal of Geophysical Research: Space Physics, 98, 21245

Horányi, M., Morfill, G., & Grün, E. 1993b, Nature, 363, 144

Horányi, M., Morfill, G. E., & Cravens, T. E. 2010, IEEE Transactions on Plasma Science, 38, 874

Howard, J., Horányi, M., & Stewart, G. 1999, Physical Review Letters, 83, 3993

Hsu, H.-W. 2010, PhD thesis, Ruprecht-Karls-Universität Heidelberg

Hsu, H.-W. 2020, private communication

Hsu, H.-W., Horányi, M., & Kempf, S. 2018a, in Astronomical Society of the Pacific Conference Series, Vol. 513, Serendipities in the Solar System and Beyond – – Celebrating Prof. Wing-Huen Ip's 70th birthday, ed. C.-M. Ko, P.-C. Yu, & C.-K. Chang, 177–181

Hsu, H.-W., Kempf, S., & Jackman, C. M. 2010, Icarus, 206, 653

Hsu, H.-W., Postberg, F., Kempf, S., et al. 2011, Journal of Geophysical Research: Space Physics, 116

Hsu, H.-W., Schmidt, J., Kempf, S., et al. 2018b, Science, 362

Huebner, W. & Carpenter, C. 1979, Los Alamos, NM

Iñarrea, M., Barrasa, V.L. Palacian, J., Salas Ilarraza, J., & Pascual, A. 2004, Monografías de la Real Academia de Ciencias Exactas, Físicas, Químicas y Naturales de Zaragoza, 159

Iess, L., Militzer, B., Kaspi, Y., et al. 2019, Science, 364

Ip, W.-H. 1983, Icarus, 54, 253

Ip, W.-H. 1984, Journal of Geophysical Research: Space Physics, 89, 8843

Ip, W.-H. 1995, Icarus, 115, 295

Ip, W.-H. 1997, Icarus, 126, 42

Ip, W.-H. 2005, Geophysical Research Letters, 32

Ip, W.-H., Liu, C.-M., & Pan, K.-C. 2016, Icarus, 276, 163

Johnson, R., Luhmann, J., Tokar, R., et al. 2006, Icarus, 180, 393

Johnson, T. V., Morfill, G., & Grün, E. 1980, Geophysical Research Letters, 7, 305

Jones, G. H., Arridge, C. S., Coates, A. J., et al. 2009, Geophysical Research Letters, 36

Jones, G. H., Krupp, N., Krüger, H., et al. 2006, Geophysical Research Letters, 33, 21202

Jontof-Hutter, D. 2012, PhD thesis, University of Maryland

Jontof-Hutter, D. & Hamilton, D. P. 2012a, Icarus, 218, 420

Jontof-Hutter, D. & Hamilton, D. P. 2012b, Icarus, 220, 487

Juhász, A. & Horányi, M. 2002, Journal of Geophysical Research: Space Physics, 107, 1066

Julian, W. H. & Toomre, A. 1966, Astrophysical Journal, 146, 810

Kaiser, M., Desch, M., & Connerney, J. 1984, Journal of Geophysical Research: Space Physics, 89, 2371

Kanal, M. 1962, Scientific Report JS-5, Space Physics Research Lab., Univ. of. Michigan, College of Engineering, Space Physics Research Laboratory,

Keeler, J. E. 1895, ApJ, 1, 416

Kempf, S., Srama, R., Horanyi, M., et al. 2005, Nature, 433, 289

Khrapak, S. A., Nefedov, A. P., Petrov, O. F., & Vaulina, O. S. 1999, Phys. Rev. E, 59, 6017

Kliore, A. J., Nagy, A., Asmar, S., et al. 2014, Geophysical Research Letters, 41, 5778

Kliore, A. J., Patel, I. R., Lindal, G. F., et al. 1980, Journal of Geophysical Research: Space Physics, 85, 5857

Kollmann, P., Roussos, E., Kotova, A., Paranicas, C., & Krupp, N. 2017, Nature Astronomy, 1, 872

Koschny, D. & Grün, E. 2001, Icarus, 154, 391

Koskinen, T., Sandel, B., Yelle, R., et al. 2015, Icarus, 260, 174

Kovalevskaya, S. 1948, Scientific Works (Izd. Akad. Nauk SSSR, Moscow)

Krimigis, S., Armstrong, T., Axford, W., et al. 1981, Science, 212, 225

Krimigis, S., Armstrong, T., Axford, W., et al. 1982, Science, 215, 571

Krüger, H., Grün, E., Graps, A., & Lammers, S. 1998, Astrophysics and Space Science, 264, 247

Krüger, H., Horányi, M., & Grün, E. 2003, Geophysical Research Letters, 30

Krupp, N., Kollmann, P., Mitchell, D. G., et al. 2018, Global Configuration and Seasonal Variations of Saturn's Magnetosphere, ed. K. Baines, F. M. Flasar, N. Krupp, & T. Stallard (Cambridge University Press, Cambridge, UK), 126

Kurth, W. S., Bunce, E. J., Clarke, J. T., et al. 2009, Auroral Processes, ed. M. K. Dougherty, L. W. Esposito, & S. M. Krimigis (Dordrecht: Springer Netherlands), 333–374

Lamy, L., Zarka, P., Cecconi, B., et al. 2008, Journal of Geophysical Research: Space Physics, 113

Lane, A. L., Hord, C. W., West, R. A., et al. 1982, Science, 215, 537

Laplace, P. S. 1966, Celestial Mechanics, ed. N. Bowditch, Vol. 2 (Chelsea Publishing Company)

Lehnert, B. 1964, Dynamics of Charged Particles (North-Holland)

Lew, J. S. 1961, Journal of Geophysical Research, 66, 2681

Lillie, C. F., Hord, C. W., Pang, K., Coffeen, D. L., & Hansen, J. E. 1977, Space Science Reviews, 21, 159

Lissauer, J. J. 1984, Icarus, 57, 63

Liu, C.-M. & Ip, W.-H. 2014, The Astrophysical Journal, 786, 34

Marouf, E. A., Tyler, G. L., Zebker, H. A., Simpson, R. A., & Eshleman, V. R. 1983, Icarus, 54, 189

Matthews, L. 1998, PhD thesis, Baylor University

Matthews, L. & Hyde, T. 2004, Advances in Space Research, 33, 2292

Matthews, L. S. & Hyde, T. W. 2003, Journal of Physics A: Mathematical and General, 36, 6207

Maxwell, J. C. 1859, On The Stability of the Motion of Saturn's Rings

McCoy, J. E. & Criswell, D. R. 1974, in Lunar and Planetary Science Conference Proceedings, Vol. 5, 2991–3005

McElroy, M. B. 1973, Space Science Reviews, 14, 460

McGhee, C. A., French, R. G., Dones, L., et al. 2005, Icarus, 173, 508

Mendis, D., Houpis, H. L., & Hill, J. R. 1982, Journal of Geophysical Research: Space Physics, 87, 3449

Mendis, D. & Rosenberg, M. 1994, Annual Review of Astronomy and Astrophysics, 32, 419

Meyer-Vernet, N. 1982, A&A, 105, 98

Meyer-Vernet, N. 1984, Icarus, 57, 422

Migliorini, A., Dinelli, B., Moriconi, M., et al. 2019, Icarus, 329, 132

Mignard, F. 1984, in IAU Colloq. 75: Planetary Rings, 333–366

Miller, K., Waite, J., Perryman, R., et al. 2020, Icarus, 339, 113595

Mitchell, C., Porco, C., Dones, L., & Spitale, J. 2011, in Bulletin of the American Astronomical Society, Vol. 43, AAS/Division of Dynamical Astronomy Meeting #42, 8.07

Mitchell, C. J., Horányi, M., Havnes, O., & Porco, C. C. 2006, Science, 311, 1587

Mitchell, C. J., Horányi, M., & Howard, J. E. 2003, Journal of Geophysical Research: Space Physics, 108, 1179

Mitchell, C. J., Porco, C. C., Dones, H. L., & Spitale, J. N. 2013, Icarus, 225, 446

Mitchell, D. G., Perry, M. E., Hamilton, D. C., et al. 2018, Science, 362

Moore, L., Galand, M., Kliore, A. J., Nagy, A. F., & O'Donoghue, J. 2018, Saturn in the 21st Century, 20, 196

Moore, L., O'Donoghue, J., Müller-Wodarg, I., Galand, M., & Mendillo, M. 2015, Icarus, 245, 355

Morfill, G., Grün, E., & Johnson, T. 1980, Planetary and Space Science, 28, 1087

Morfill, G. E. & Thomas, H. M. 2005, Icarus, 179, 539

Mott-Smith, H. M. & Langmuir, I. 1926, Phys. Rev., 28, 727

Nagy, A. F., Kliore, A. J., Mendillo, M., et al. 2009, Upper Atmosphere and Ionosphere of

Saturn, ed. M. K. Dougherty, L. W. Esposito, & S. M. Krimigis (Dordrecht: Springer Netherlands), 181–201

NASA/JPL. 2020, Planets and Pluto: Physical Characteristics https://ssd.jpl.nasa.gov/?planet_phys_par

Ness, N. F., Acuna, M. H., Behannon, K. W., et al. 1982, Science, 215, 558

Ness, N. F., Acuna, M. H., Lepping, R. P., et al. 1981, Science, 212, 211

Nicholson, P. D., Hedman, M. M., Clark, R. N., et al. 2008, Icarus, 193, 182

Nitter, T., Havnes, O., & Melandso, F. 1998, Journal of Geophysical Research, 103, 6605

Northrop, T. & Birmingham, T. 1990, Planetary and Space Science, 38, 319

Northrop, T. & Connerney, J. 1987, Icarus, 70, 124

Northrop, T. & Hill, J. R. 1982, Journal of Geophysical Research: Space Physics, 87, 6045

Northrop, T. & Hill, J. R. 1983, Journal of Geophysical Research: Space Physics, 88, 6102

Northrop, T. & Morfill, G. 1984, Advances in Space Research, 4, 63

Northrop, T. G. 1992, Phys. Scr, 45, 475

O'Donoghue, J., Melin, H., Stallard, T. S., et al. 2016, Icarus, 263, 44

O'Donoghue, J., Moore, L., Connerney, J., et al. 2018, Icarus, 322, 251

O'Donoghue, J., Moore, L., Connerney, J. E. P., et al. 2017, Geophysical Research Letters, 44, 11,762

O'Donoghue, J., Stallard, T., Melin, H., et al. 2013, Nature, 496, 193

O'Donoghue, J., Stallard, T. S., Melin, H., et al. 2014, Icarus, 229, 214

Okuzumi, S. 2009, The Astrophysical Journal, 698, 1122

Perry, M. E., Waite Jr., J. H., Mitchell, D. G., et al. 2018, Geophysical Research Letters, 45, 10,093

Pilcher, C. B., Chapman, C. R., Lebofsky, L. A., & Kieffer, H. H. 1970, Science, 167, 1372

Polyakhova, E. N. 2004, in Order and Chaos in Stellar and Planetary Systems, Vol. 316, 303

Porco, C. A. & Danielson, G. E. 1982, Astronomical Journal, 87, 826

Porco, C. C., Helfenstein, P., Thomas, P. C., et al. 2006, Science, 311, 1393

Postberg, F., Kempf, S., Srama, R., et al. 2006, Icarus, 183, 122

Poulet, F., Cruikshank, D., Cuzzi, J., Roush, T., & French, R. 2003, Astronomy & Astrophysics, 412, 305

Poulet, F. & Cuzzi, J. 2002, Icarus, 160, 350

Prangé, R., Fouchet, T., Courtin, R., Connerney, J., & McConnell, J. C. 2006, Icarus, 180, 379

Press, W. H., Teukolsky, S. A., Vetterling, W. T., & Flannery, B. P. 2007, Numerical Recipes in C, The Art of Scientific Computing, 3rd edn. (Cambridge University Press), 899–954

Price, O., Jones, G. H., Morrill, J., et al. 2019, Icarus, 319, 540

Quinn, T., Perrine, R. P., Richardson, D. C., & Barnes, R. 2010, The Astronomical Journal, 139, 803

Reffet, E., Verdier, M., & Ferrari, C. 2015, Icarus, 254, 276

Rennilson, J. & Criswell, D. R. 1974, The Moon, 10, 121

Richardson, D. C. 1993a, Monthly Notices of the Royal Astronomical Society, 261, 396

Richardson, D. C. 1993b, PhD thesis, University of Cambridge

Richardson, D. C. 1994, Monthly Notices of the Royal Astronomical Society, 269, 493

Richardson, D. C., Quinn, T., Stadel, J., & Lake, G. 2000, Icarus, 143, 45

Röntgen, W. C. 1895, Wurzburg Physico-Médical Society on December, 28

Ross, S. M. 2014, Introduction to Probability and Statistics for Engineers and Scientists, 5th edn. (Academic Press), 177–183

Roussos, E., Kollmann, P., Krupp, N., et al. 2018, Science, 362

Roussos, E., Krupp, N., Armstrong, T. P., et al. 2008, Geophysical Research Letters, 35

Russell, C. T. 1993, Reports on Progress in Physics, 56, 687

Saha, P. & Tremaine, S. 1992, The Astronomical Journal, 104, 1633

Sandel, B., Shemansky, D., Broadfoot, A., et al. 1982, Science, 215, 548

Sanz-Serna, J. M. 1992, Acta Numerica, 1, 243

Schaffer, L. & Burns, J. A. 1994, Journal of Geophysical Research: Space Physics, 99, 17211

Schmidt, J., Ohtsuki, K., Rappaport, N., Salo, H., & Spahn, F. 2009, in Saturn from Cassini-Huygens (Springer), 413–458

Serigano, J., Hörst, S., He, C., et al. 2020, Journal of Geophysical Research: Planets, e2020JE006427

Shemansky, D. E., Matheson, P., Hall, D. T., Hu, H. Y., & Tripp, T. M. 1993, Nature, 363, 329

Shimizu, M. 1980, The Moon and the Planets, 22, 521

Shkuratov, Y., Starukhina, L., Hoffmann, H., & Arnold, G. 1999, Icarus, 137, 235

Shohet, J. L. 2017, Encyclopedia of Plasma Technology-Two Volume Set, Vol. 2 (CRC Press), 895

Smith, B. A., Soderblom, L., Batson, R. M., et al. 1982, Science, 215, 504

Smith, B. A., Soderblom, L., Beebe, R. F., et al. 1981, Science, 212, 163

Smith, E. J., Davis, L., Jones, D. E., et al. 1980, Science, 207, 407

Smith, K. T. 2018, Science, 362, 44

Spahn, F., Krivov, A. V., Sremčević, M., Schwarz, U., & Kurths, J. 2003, Journal of Geophysical Research: Planets, 108

Spilker, L. J. 2019, Geophysical Research Letters, 46, 5754

Spitzer, L., J. 1962, Physics of Fully Ionized Gases, 2nd edn. (Interscience (Wiley), New York)

Spitzer, Jr., L. 1941, ApJ, 93, 369

Springel, V. 2016, in Star Formation in Galaxy Evolution: Connecting Numerical Models to

Reality, ed. Y. Revaz, P. Jablonka, R. Teyssier, & L. Mayer (Springer), 251–358

Srama, R., Ahrens, T. J., Altobelli, N., et al. 2004, Space Science Reviews, 114, 465

Stadel, J. G. 2001, PhD thesis, University of Washington

Stallard, T., Miller, S., Ballester, G. E., et al. 1999, The Astrophysical Journal, 521, L149

Stallard, T., Miller, S., Lystrup, M., et al. 2008, Nature, 456, 214

Stallard, T. S., Melin, H., Miller, S., et al. 2012, Philosophical Transactions of the Royal Society A: Mathematical, Physical and Engineering Sciences, 370, 5213

Stanley, S. 2010, Geophysical Research Letters, 37

Stanley, S. & Bloxham, J. 2016, Physics of the Earth and Planetary Interiors, 250, 31

Steinpilz, T., Joeris, K., Jungmann, F., et al. 2020, Nature Physics, 16, 225

Stevenson, D. 1982, Geophysical & Astrophysical Fluid Dynamics, 21, 113

Stoer, J. & Bulirsch, R. 2013, Introduction to Numerical Analysis, 2nd edn., Vol. 12 (Springer Science + Business Media LLC), 428–569

Størmer, C. 1930, Terrestrial Magnetism and Atmospheric Electricity, 35, 193

Tagger, M., Henriksen, R. N., & Pellat, R. 1991, Icarus, 91, 297

Terrile, R., Yagi, G., Cook, A., & Porco, C. 1981, in Bulletin of the American Astronomical Society, Vol. 13, 728

Thomsen, M., Goertz, C., Northrop, T., & Hill, J. 1982, Geophysical Research Letters, 9, 423

Thomsen, M. F. & Van Allen, J. A. 1980, Journal of Geophysical Research: Space Physics, 85, 5831

Tiscareno, M. S., Burns, J. A., Hedman, M. M., et al. 2006, Nature, 440, 648

Tiscareno, M. S. & Murray, C. D. 2018, Planetary Ring Systems: Properties, Structure, and Evolution (Cambridge University Press)

Tiscareno, M. S., Nicholson, P. D., Cuzzi, J. N., et al. 2019, Science, 364

Tokar, R., Johnson, R., Thomsen, M., et al. 2005, Geophysical Research Letters, 32

Toomre, A. 1964, The Astrophysical Journal, 139, 1217

Tyler, G., Eshleman, V., Anderson, J., et al. 1981, Science, 212, 201

Tyler, G., Eshleman, V., Anderson, J., et al. 1982, Science, 215, 553

Van Allen, J., Thomsen, M., Randall, B., Rairden, R., & Grosskreutz, C. 1980, Science, 207, 415

Verheest, F. 2000, Waves in Dusty Space Plasmas (Dordrecht: Kluwer Academic)

Virtanen, P., Gommers, R., Oliphant, T. E., et al. 2020, Nature Methods, 17, 261

Wahlund, J.-E., Morooka, M. W., Hadid, L. Z., et al. 2018, Science, 359, 66

Waite, J., Cravens, T., Ip, W.-H., et al. 2005, Science, 307, 1260

Waite, J. H., Combi, M. R., Ip, W.-H., et al. 2006, Science, 311, 1419

Warwick, J. W. 1989, Journal of Geophysical Research: Space Physics, 94, 8757

Warwick, J. W., Pearce, J. B., Evans, D. R., et al. 1981, Science, 212, 239

Weinheimer, A. J. & Few, A. A. 1982, Geophysical Research Letters, 9, 1139

Welch, P. 1967, IEEE Transactions on Audio and Electroacoustics, 15, 70

West, R. A., Tomasko, M. G., Smith, B. A., et al. 1982, Icarus, 51, 51

Whipple, E. C. 1981, Reports on Progress in Physics, 44, 1197

Wieczorek, M. 2015, in Treatise on Geophysics, 2nd edn., ed. G. Schubert (Oxford: Elsevier), 153 – 193

Wilson, G. & Waite, J. 1989, Journal of Geophysical Research: Space Physics, 94, 17287

Wisdom, J. & Tremaine, S. 1988, The Astronomical Journal, 95, 925

Ye, S.-Y., Fischer, G., Kurth, W. S., Menietti, J. D., & Gurnett, D. A. 2016, Journal of Geophysical Research: Space Physics, 121, 11,714

Young, D., Berthelier, J.-J., Blanc, M., et al. 2005, Science, 307, 1262

Zhang, Z., Hayes, A., Janssen, M., et al. 2017a, Icarus, 294, 14

Zhang, Z., Hayes, A., Janssen, M., et al. 2017b, Icarus, 281, 297

Zook, H. A., Grün, E., Baguhl, M., et al. 1996, Science, 274, 1501